Radio and infrared interferometry of stellar and substellar objects

Memoria para optar al título de Doctor en Física

Juan Bautista Climent Oliver

Departmento de Astronomía y Astrofísica
Universidad de Valencia
Junio 2020

Director:
José Carlos Guirado Puerta

A ma mare, Teresa.

A Elena.

Acknowledgements

Me gustaría expresar, en primer lugar, el profundo agradecimiento que siento por mi tutor, José Carlos. Por supuesto que este trabajo no hubiese sido posible sin su ayuda y su sabiduría pero es que su amabilidad y buen humor han traspasado más allá de lo profesional. Gracias por hacer de estos años un periodo inolvidable.

Este mismo agradecimiento se extiende para los enormes profesionales que me han acompañado a lo largo de estos años. Gracias a Jon por compartir conmigo una pequeña parte de su conocimiento y por su buena disposición. Gracias a la gente del Observatorio Astronómico porque desde el primer momento me he sentido arropado y como en casa. Gracias Sofía, Esther, Pablo, Lorena, Rebecca, Fernando, Alberto, Amelia, Juan, Vicent Martínez, Xusa, Iván, Rafa, Óscar, Vicent Peris, Miquel, Carlos y Julia. Contagiáis el amor por la ciencia (siempre con una buena taza de té o café). Y hablando de ciencia, gracias a todos y cada uno de los miembros del Departamento de Astronomía y Astrofísica por permitirme formar parte de este gran grupo de investigadores, y por el apoyo continuo. Gracias a Feli, Manel y Lupe por su eterna paciencia con mis mil y una dudas. Gracias a Toni y a Pepe porque me han animado a mejorar como docente y siempre han estado ahí a la mínima necesidad. También quiero agradecer los buenos ratos en las comidas con Fabrizio, Sergio, Miquel, Tomek, Isa, Jose, Nico, Álex, Jose Lopez, Alejandro Mus, Pancho y Alejandro Cruz.

Durante estos años he tenido la oportunidad de viajar y conocer a mucha gente que también me gustaría reconocer. Gracias a Miguel Ángel Pérez-Torres, Eduardo Ros y a Antxon Alberdi que son la parte externa del grupo de radioastronomía de la universidad de Valencia pero una parte externa que no se siente nada lejos. Gracias por vuestra calidez y vuestras divertidas anécdotas. A Tirna, Elia, Mengyuan y tantos otros que han hecho que cada congreso sea único, irrepetible y tremendamente divertido. Y no me olvido de mi tutor alemán, Markus Wittkowski, que me ha guiado por los desconocidos caminos de la interferometría infrarroja y me ha acogido durante mis estancias en ESO. Danke schön, Markus!

Como se suele decir: ”Si he podido ver más allá es porque me encaramé a hombros de gitantes”. Por ello no quiero que caiga en el olvido y me gustaría dar las gracias a toda la comunidad científica y los que la han hecho posible, así como al Gobierno de España y a la Universidad de Valencia por darme esta oportunidad.

Más allá del ámbito científico esta tesis merece el reconocimiento de mi familia. He tenido la suerte de disfrutar de vuestra maravillosa compañía desde el día que nací y os mereceríais que escribiese una tesis sobre cada uno de vosotros y sobre lo mucho que os aprecio. A mis tíos y tías que viven cerca: María y Rodolfo, Milagrín y Jose, Elisa y Salvador, Amparo y Rafa, y a mi tío Juan que vive un poco más lejos; un enorme GRACIAS a cada uno de vosotros. A mis abuelos, Juan y Milagros, que ya no están pero se siguen sintiendo. No soy sino el fruto del amor y las enseñanzas que entre todos me habéis dado.

Y una mención aparte se merecen mis primos: Jose y Maribel, por enseñar el camino a los que seguíamos y guiarnos con paciencia; Clara y Casto, porque, aunque yo era demasiado pequeño para darme cuenta, me criastéis como a un hijo; Miguel Ángel, por abrirme la mente al arte; Rodol por quererme de forma desbordada (y ”de nada” por ayudarte a saltarte alguna clase cuando eras pequeño); Salva y María, porque juntos formamos el trío de mi infacia que siempre recordaré; Pablo, mi hermano de otra madre, ya sabes cuánto te quiero; Álex, por esas tardes echando unas risas y canastas; Carlos, porque me enseñaste que un físico se dedica a montar microondas; Víctor, porque siempre me meto contigo pero, al final, siempre pasamos un buen rato juntos. Y también me gustaría incluir aquí a Joan, Diego, Laia y Clareta. A todos vosotros, os digo ”gracias” desde lo más puro de mi corazón.

Gracias a mis amigos y amigas por compartir risas y alegrías pero también lágrimas y tristezas. Gracias a Carmensin, Antonio, Anja, Gema y a Luz. Gracias también a Juan

Carlos y Fernando. A mis amigos canarios: Carlos, Alberto, Loreto, Paloma, Patri e Izabella, gracias por una de las etapas favoritas de mi vida. También quiero agradecer a aquellos amigos que me han moldeado aunque hoy nos hayamos distanciado: Sam, Carlos, Borja, Ángel, Voro, Eric, Willy, David, Josan, Ramón, Raúl y Sara. A todos os llevo muy adentro y os tengo en gran estima.

A Celia, Mauro, Marcos, Manuel, María y el resto de mi segunda familia: gracias por adoptarme como uno más. Vuestro ánimo siempre alegre se contagia, vuestras historias y anécdotas me atrapan y vuestros brazos siempre abiertos no puedo sino corresponderlos con un abrazo y un ”gracias”.

A mi madre, Teresa. Mi piedra ángular en esta vida sobre la que todo lo demás se construye. Gracias por tu apoyo incondicional, por tu seguridad, por compartir y enseñarme tus valores, por escucharme y quererme. A ti, consciente del significado de cada palabra, te puedo decir sin titubear: ”gracias por todo”, porque, así es, me lo has dado todo.

Y, por supuesto, a ella. Elena. Las palabras se quedan cortas para expresar todo mi agradecimiento, pero tú eso ya lo sabes. Aun así, quiero intentarlo: gracias por tu apoyo, gracias por tu comprensión, gracias por tu alegría y tus locuras, gracias por hacernos un gran equipo, y sobretodo, gracias por quererme.

Abstract

In the work presented here, we have used interferometry as a Swiss knife allowing us to make contributions in a number of relevant astrophysical scenarios of research where high angular resolution provides a privileged insight. Both stellar and substellar objects are the targets of our studies, which cover from asymptotic giant branch (AGB) and red supergiant (RSG) stars with very extended and cool atmospheres to ultracool low-mass objects which show extreme magnetic activity. The extraordinary resolution provided by present instrumentation, both in radio and infrared, along with their increasing sensitivity allow us to investigate, with unprecedented details, the following cases:

The first object we investigated was the substellar triple system VHS 1256-1257. This young and nearby system is composed by an equal-magnitude M7.5 binary with separation of $0.1''$ and an L7 object located $8''$ from the central binary. It is the third multiple system known to date in which all three components may be substellar and the separation between components makes it a perfect target for high resolution interferometry in order to determine the dynamical masses of the individual components. Additionally, the L7 source belongs to one intriguing (not yet understood) population of very red L dwarfs with likely high content of atmospheric dust or high metallicity. With such motivations, we performed multi-epoch, multi-frequency observations of this intriguing system making use of the Very Large Array (VLA) and the European VLBI Network (EVN) at 1.4 GHz (L band), 8.4 GHz (X band), and 34 GHz (K$_a$ band). Our observations discovered radio emission at X band originating in the central binary. We also estimated the spectral index between 8 and 12 GHz by making use of the 4 GHz recorded bandwidth in our X band VLA observations, giving us an indication of the spectral behavior of this sys-

tem. We found an spectral index of $\alpha = -1.1 \pm 0.3$, indicating a non-thermal, optically thin, synchrotron, or gyrosynchrotron radiation. Were this behaviour to continue down to L band, we should have detected radio emission in VHS 1256-1257 with a flux density above 300 μJy. However, we did not detect any emission from the central binary at such frequency in any of our four epochs, placing a strong upper limit of 20 μJy. At first, we attributed our lack of detection at L band either to a strong variability that weakened the radio emission in all of our epochs of observation, or to self-absorption. The first hypothesis however seems highly unlikely and, consequently, we further explored the second one arriving at the conclusion that the turnover frequency must be in the interval 5-8.5 GHz, which implies the presence of strong magnetic fields (~ kG) in the M7.5 binary. Our data also imposes a 3σ upper bound to the radio emission of the L7 object of 9 μJy at 10 GHz. Remarkably, we have also detected K_a band (26-40 GHz) radio emission coincident with the expected position of the central binary with a peak flux of 65 μJy. This value seems to be way above the flux expected for a dusty disk model. Additionally, this hypothesis does not seem to fit with ALMA band 7 (275-373 GHz) observations in which no emission from this object was detected.

The second object of our study was the M7, low-mass companion to AB Dor A, AB Dor C. This object is important in the calibration of stellar evolution models since such models have had some difficulties in their predictions in the case of low- and very low-mass pre-main-sequence stars, and only well-known objects with dynamically determined masses and precise photometry can be used to test and check the predictions of such models. We performed infrared interferometric observations of this object using the VLTI/AMBER instrument at J, H and K infrared bands. We found that both the visibilities and closure phases of this object at K band are compatible with a binary brown dwarf system with flux ratio of $5 \pm 1\%$. This implies that the masses of components AB Dor Ca and AB Dor Cb would be $0.072 \pm 0.013 M_\odot$ and $0.013 \pm 0.001 M_\odot$, respectively. The disagreement between observed magnitudes and theoretical mass-luminosity relationships would be partially alleviated by this binarity.

The third contribution we made was in the field of red supergiants. These objects undergo an impressive amount of mass loss but the physical mechanisms that contribute to and dominate this mass loss are still unclear. It is thought that photospheric convection may be a crucial factor of the levitation of the outer atmospheric layers in these objects. This is why we observed the RSG V602 Car with the VLTI/PIONIER instrument. With the great quality of the data obtained we were able to reconstruct images of the surface of this star at two different epochs, 2016 and 2019. In the first epoch, the reconstructed image revealed a bright arc-like feature toward the northern rim of the photospheric surface. In 2019, an arc-like feature was also seen but at a different orientation and a new peak of emission was detected on the opposite side. 3D RHD models predict substructures similar to the observed surface features of V602 Car, however, they do not successfully reproduce the observed visibility data. These results imply that convection alone may not be the only relevant process to levitate the atmospheres on RSGs.

Our final contribution comes back to the AB Dor system, in this case to the main star, AB Dor A. This PMS star is known to be a strong and persistent radio emitter. We used the Australian VLBI Network (LBA) to obtain high angular resolution data at 1.4, 8.4 and 22.3 GHz over a decade. Our 8.4 GHz images showed a double core-halo morphology, similar at all epochs, with emission extending at heights between 5 and 18 stellar radii. When further analyzing these images, we found that there was a clear variation of the source structure within the observing time. We hypothesized that the origin of such features may be: a possible companion to AB Dor A, emission from the stellar polar caps, a flaring, magnetically-driven loop structure, or the presence of helmet streamers. Our current observations can only discard the companion scenario. We also detected AB Dor A at 1.4 GHz with the image showing a structure compatible with an unresolved source. Finally, we placed strong upper limits of 0.11 mJy, 0.04 mJy, 0.10 mJy, 0.04 mJy and 0.07 mJy for the radio emission of AB Dor C in 2007 (8.4 GHz), 2010 (8.4 GHz), 2013 (8.4 GHz), 2017 (22.3 GHz) and 2018 (1.4 GHz), respectively.

Resumen

En el trabajo presentado aquí hemos usado la interferometría a modo de navaja suiza, lo cual nos ha permitido hacer contribuciones relevantes a diversos campos donde una gran resolución angular proporciona una gran ventaja. Hemos estudiado tanto objetos estelares como sub-estelares: desde gigantes rojas con atmósferas muy extensas y frías hasta enanas ultra-frías con una actividad magnética extrema. Todo gracias a la gran resolución que proporcionan los instrumentos actuales, tanto en radio como en infrarrojo, junto con su gran sensibilidad.

La técnica interferométrica

La técnica de interferometría astronómica nació del deseo de mejorar la resolución angular que ofrecían los telescopios o antenas y es que, incluso en las mejores circunstancias imaginables, la máxima resolución angular de una observación está limitada por difracción a λ/D, donde λ es la longitud de onda de observación y D es el diámetro del telescopio. Esta relación pone en clara desventaja a las observaciones realizadas a frecuencias bajas (como aquellas en radio) y fue la que motivó el temprano desarrollo de esta técnica.

La interferometría se basa en el siguiente *modus operandi*: en primer lugar, los telescopios (término que se utiliza en el domino infrarrojo) o las antenas (término reservado para el domino de radio frecuencias) recogen los fotones procedentes de nuestro objeto de interés al que estamos apuntando. Estos fotones se llevan posteriormente a una localización central que recibe el nombre de correlador (en radio frecuencias) o de combinador (en el infrarrojo) donde las señales de diferentes elementos serán combinadas de forma

coherente. Como resultado de este proceso obtendremos las franjas interferométricas. Así, combinando la luz de varias antenas o telescopios, la interferometría permite simular un telescopio con un diámetro igual a la máxima separación entre los elementos. El extremo representativo de esta técnica es lo que se conoce como VLBI (por sus siglas en inglés Very Large Baseline Interferometry), donde las antenas que observan en radio frecuencias están separadas por cientos o miles de kilometros, permitiendo obtener la mayor resolución angular en el mundo de las observaciones astronómicas.

Es importante tener en cuenta que, aunque el principio físico que hay detrás de la interferometría es el mismo independientemente de si se observa en el infrarrojo o o en radio, existe también un buen número de diferencias. Algunas de estas diferencias son debidas a que la inteferometría en radio le lleva más de un cuarto de siglo de ventaja a la inteferometría en infrarrojo, en cuanto al desarrollo se refiere. Otras sin embargo, están relacionadas con las limitaciones más restrictivas que la atmósfera impone sobre la técnica en el domino infrarrojo.

Tras obtener los observables interferométricos (fases y amplitudes de las visibilidades), éstos deben ser corregidos por los errores instrumentales introducidos en el sistema de recepción de señales, así como, por todos los errores que introduce la atmósfera. En el caso de VLBI, estos últimos son especialmente relevantes, puesto que al tener elementos con separaciones de hasta miles de kilómetros, la atmósfera afecta de forma muy diferente a cada antena. Además, los errores instrumentales aquí deben incluir un modelo geométrico que incluye una gran cantidad y variedad de fenómenos como son la nutación, la precesión, el movimiento tectónico, etc. En radio frecuencias, la atmósfera tiene un tiempo de coherencia de unos pocos minutos incluso en las peores circunstancias. Es por esto por lo que se puede utilizar la técnica conocida como referencia de fase, basada en la observación de forma alternante de un calibrador de fase y del objeto de interés. Esta técnica nos permite obtener las correcciones necesarias para el calibrador de fase y, posteriormente, extender esas correcciones a nuestro objeto de interés. Sin embargo, en el dominio de infrarrojo, el tiempo de coherencia de la atmósfera puede llegar a ser de unos pocos milisegundos. Esto, obviamente, imposibilita la referencia de fase tal y como se realiza en radio y se debe optar con una técnica alternativa denominada ”fringe-tracking” que permite estabilizar las franjas interferométricas y así aumentar el tiempo de exposición en nuestro objeto de interés.

Una vez tenemos los datos completamente calibrados ha llegado el momento de extraer la información científica. De nuevo, este proceso depende de la calidad de los datos. Hoy en día una gran parte de las observaciones interferométricas en radio permiten la obtención de una imagen astronómica. Sin embargo, en el caso de la interferometría en infrarrojo esto no siempre es así. Así pues, la forma más básica de extraer información en cualquiera de los casos es analizando las visibilidades y las clausuras de fase. El primer paso para realizar este ajuste consiste en crear un modelo geométrico o físico y obtener sus visibilidades. Este modelo puede ser tan sencillo como un disco uniforme o una gaussiana, o modelos físicos con mucha complejidad. A continuación, podemos ajustar el modelo para que represente de la forma más fidedigna las visibilidades y clausuras de fase que hemos medido observacionalmente.

Si los datos son suficientemente buenos, tal y como hemos comentado, podemos obtener una imagen de nuestro objeto de interés. Esto se hace de forma diferente en los dominios de radio y de infrarrojo. En el primero, se suele utilizar un algoritmo conocido como CLEAN y que está incluido en los paquetes de reducción de datos como AIPS o DIFMAP. En el segundo, se debe usar diferentes observables como las clausuras de fase, el ”bispectrum” o las clausuras de amplitudes para reconstruir la imágen. Afortunadamente, existe un gran número de paquetes de software que realizan este procedimiento con buenos resultados y grandes funcionalidades: BSMEM, MACIM, MIRA, WISARD y SQUEEZE.

Metodología

Para la parte de nuestro trabajo realizada con interferometría en el infrarrojo hemos utilizado el Very Large Telescope Interferometer (VLTI) que se encuentra en Cerro Paranal, Chile. El VLTI combina las señales procedentes de varios telescopios que tienen un diámetro de 8.2 metros (UTs) o de 1.8 metros (ATs). Si se opta por observar con los UTs, hay que tener en cuenta que estos telescopios están fijos, mientras que los ATs permiten ser recolocados en 30 estaciones diferentes. El VLTI ofrece varios instrumentos.

En nuestro trabajo presentado aquí hemos hecho uso de AMBER y de PIONIER (y parcialmente de GRAVITY).

AMBER (por sus siglas en inglés, Astronomical Multi-BEam combineR) combina la luz de 3 telescopios, permitiendo la medida no solo de las visibilidades, también de las clausuras de fase. Opera en las bandas inteferométricas J, H y K (de 1.1 a 2.4 μm) y permite obtener una máxima resolución angular de 2 milisegundos de arco (mas) con los UTs o de 50 mas con los ATs. Aunque ahora ya no se ofrece para su uso en el VLTI, AMBER proporcionó la opción de observar con tres resoluciones espectrales diferentes: baja (R=35), media (R=1500) y alta (R=120000).

PIONIER (Precision Integrated-Optics Near-infrared Imaging ExpeRimen), por su parte, combina la luz de 4 telescopios y, por tanto, produce visibilidades de seis líneas de base diferentes, así como cuatro medidas de las clausuras de fase con una resolución espectral baja (R=40). Opera en la banda infrarroja H, con una magnitud límite de H= 9 en el mejor de los escenarios. Puede integrar la luz de toda la banda espectral con la intención de mejorar la sensibilidad del instrumento o, alternativamente, puede obtener las medidas en seis longitudes de onda diferentes dentro de la banda H, mejorando de esta forma el cubrimiento del plano *uv*.

Para la parte de nuestro trabajo realizada con interferometría en radio hemos utilizado varios instrumentos: el Very Large Array (VLA), el European VLBI Network (EVN) y el Australian VLBI Network (LBA).

El VLA es un instrumento formado por 28 antenas (27 de las cuales están operativas) de 25 metros de diámetro. Está localizado en Socorro, New Mexico, Estados Unidos. Fue diseñado y construido como un array reconfigurable de forma que permite ofrecer cuatro configuraciones diferentes: configuración A con un tamaño de 36.40 Km, configuración B con un tamaño de 11.40 Km, configuración C con un tamaño de 3.40 Km y, finalmente, configuración D con un tamaño de 1.03 Km. Puede observar en frecuencias que van desde 1.0 GHz hasta 50 GHz, ofreciendo un resolución angular máxima que varía desde $0.2''$ hasta $0.04''$.

El EVN es un array de antenas esparcidas a lo largo y ancho del planeta, con la gran mayoría de ellas localizadas en europa. Debido a la gran colección de antenas y al tamaño de las mismas, el EVN es el array de VLBI más sensible del mundo en el momento actual. Puede observar en frecuencias que van desde 1.664 GHz hasta 22.230 GHz en todas las antenas y con algunas frecuencias extras que solamente se pueden observar en un número reducido de antenas.

El LBA es un array de VLBI localizado en el hemisferio sur, lo cual permite observaciones de objetos que, de otra forma, resultarían inaccesibles por otros arrays. Sus antenas están repartidas entre Australia, Nueva Zelanda y Sudáfrica. Puede observar en frecuencias que van desde 1.4 GHz hasta 22.2 GHz, aunque no todas las antenas pueden observar a todas las frecuencias ofertadas.

La reducción de los datos astronómicos se ha realizado usando diferentes paquetes de software. En el caso de los datos obtenido con el instrumento AMBER, hemos utilizado el paquete de software específico para este instrumento: *amdlib*. Este algoritmo utiliza las matrices ”pixel-to-visibilities” (P2VM) para extraer las visibilidades complejas para cada una de las líneas de base y canales espectrales del interferograma obtenido por AMBER. Una vez que se han obtenido las visibilidades complejas, hemos de corregir los diferentes errores instrumentales y atmosféricos. Esto se hace observando en la misma noche nuestro objeto de interés y un calibrador con diámetro estelar bien determinado. De esta forma, uno corrige primero las visibilidades del calibrador y, a continuación, corrige las del objeto de interés dividiendo las visibilidades del objeto entre las visibilidades del calibrador.

En el caso de los datos obtenidos con PIONIER el proceso es similar. Este instrumento también cuenta con su paquete de software específico: *pndrs*. De forma similar a lo que ocurre con las observaciones de AMBER, este software también utiliza las visibilidades de una estrella de calibración (cuyas observaciones se deben intercalar con observaciones del objeto de interés) para corregir los efectos instrumentales y atmosféricos.

Tanto para datos obtenidos con el EVN como para aquellos obtenidos con el LBA hemos utilizado el software de reducción de datos AIPS y, posteriormente, para obtener y analizar las imágenes finales, DIFMAP. Los datos del VLA se han reducido utilizando el software específico CASA. En cualquiera de los casos, la reducción de datos interferométricos en radio suele empezar con la calibración en amplitud para convertir las amplitudes de las visibilidades en densidades de flujo, y también para corregir algunos de los efectos instrumentales en las antenas y en el correlador. La estrategia más común para llevar a cabo dicha calibración es observar una estrella de calibración bien conocida, corregir los errores de amplitud en esta estrella y aplicar estas correcciones también a nuestra fuente de interés. Alternativamente, también se puede realizar la calibración en amplitud utilizando la temperatura de sistema de las antenas individuales. Esta temperatura resume las contribuciones que no provienen directamente del objeto observado: amplificadores, receptores, etc.

El siguiente paso consiste en la calibración de fase. Los errores en las fases medidas tienen diferentes procedencias: el retraso geométrico entre dos antenas, la contribución de la instrumentación de las propias antenas, la contribución debida a efectos atmosféricos y, finalmente, la contribución debida a efectos ionosféricos. La primera corrección de fase que se realiza ocurre en el correlador donde se intenta corregir utilizando un modelo de la rotación de la Tierra, la atmósfera, los relojes en cada antena, etc. La siguiente corrección se denomina ”fringe-fitting” e intenta, usando un cuadrícula de dos dimensiones con el ”fringe rate” en un eje y el retraso en el otro, determinar el pico de la transformada de Fourier de las visibilidades. Además, uno debe tener en cuenta varias correcciones adicionales: el ángulo paraláctico, debido a la rotación del patrón de respuesta de la antena en el cielo según avanza la observación, y la corrección por la ionosfera que afecta al retraso de la señal de forma diferente según la hora y localización de cada antena.

Con los datos completamente calibrados uno puede empezar el análisis bien ajustando a las visibilidades y clausuras de fase o bien investigando la imagen resultante, tal y como se ha descrito con anterioridad.

Resultados y conclusiones

El primer objeto que hemos investigado es el sistema triple, subestelar VHS 1256-1257. Este sistema es relativamente joven (150-300 millones de años) y se encuentra próximo a nosotros (12.7-17.1 pc). Está compuesto por una binaria con separación de $0.1''$ y cuyas componentes son dos objetos de tipo espectral M7.5. A $8''$ de esta binaria central se encuentra un objeto muy frío con tipo espectral L7. Este sistema es el tercer sistema que se conoce en el que todas las tres componentes son subestelares. Además de esto, la separación entre componentes hace de VHS 1256-1257 una fuente tremendamente interesante para observar con interferometría en radio ya que permite distinguir si la emisión proviene de la binaria central y/o del objeto L7. Observaciones con VLBI podrían incluso, en el mejor de los casos, distinguir si la emisión central proviene de una de las componentes, de las dos y/o de la interacción entre ambas. Con una campaña de detecciones en diferentes épocas, podríamos observar el movimiento en este sistema y determinar así sus masas dinámicas. Como última motivación para estudiar este sistema, es necesario poner de manifiesto que la población de enanas rojas frías de tipo espectral L no se conoce con mucho detalle y, por tanto, detecciones en este objeto L7 serían muy interesantes.

Observamos este sistema usando el VLA primeramente, en banda X (8.4 GHz) en mayo del 2015 y en banda L (1.4 GHz) en julio del 2016. Además, también hicimos uso del EVN en banda L durante 3 épocas diferentes (marzo, mayo y noviembre del 2016). Gracias a estas observaciones descubrimos por primera vez radio emisión en banda X proveniente de la binaria central VHS 1256-1257 AB. Además, utilizando el gran ancho de banda proporcionado por las observaciones con el VLA, pudimos fraccionar los 4 GHz de ancho de banda en 4 segmentos de 1 GHz cada uno, con la intención de obtener una idea del comportamiento espectral de este sistema. Pudimos estimar un índice espectral de $\alpha = -1.1 \pm 0.3$, lo cual indica que el origen de esta emisión detectada es no térmico, sincrotrón o girosincrotrón. Si este mismo mecanismo de emisión se mantuviese a bajas frecuencias, entonces nuestras observaciones en banda L deberían detectar emisión en radio proveniente de la binaria central de VHS 1256-1257 con una densidad de flujo mayor a 300 μJy. Sin embargo, no detectamos emisión alguna por encima de los 20 μJy en la posición esperada en ninguna de las 4 épocas de observación en banda L. Formulamos la hipótesis de que una variabilidad fuerte del mecanismo de emisión podría ser el responsable. Sin embargo, pronto nos vimos obligados a considerar hipótesis adicionales, puesto que es bastante improbable que la variabilidad explique la no detección en 4 épocas. Aunque no es posible descartar esta opción, investigamos también la posibilidad de que la emisión en radio se encuentre "auto-absorbida" a estas frecuencias bajas.

Utilizando las expresiones analíticas para la emisión en radio girosincrotrón en enanas dMe en condiciones ”quiescent”, obtuvimos la estimación de que la frecuencia de ”turnover” se debía encontrar en el intervalo de 5 GHz a 8.5 GHz. Esto implica que en la binaria central de VHS 1256-1257 existirían campos magnéticos muy fuertes, con intensidades ~kG. Esto está en buen acuerdo con los modelos teóricos desarrollados para enanas M, así como con el valor promedio de la intensidad del campo magnético medido en una muestra de enanas con tipo espectral M7-9.5. Nuestros datos también imponen una cota superior de 3σ de 9μJy para la emisión en radio del objeto L7 a 10 GHz.

Finalmente, nuestro análisis preliminar de observaciones de este sistema triple con el VLA en banda K_a (26-40 GHz) muestran una clara detección coincidente con la posición esperada para la binaria central con un pico de 65 μJy. Este flujo parece estar muy por encima del predicho por un modelo de disco de escombros, hipótesis que además no encaja con las observaciones de ALMA banda 7 (275-373 GHz) en las que no se detectó emisión alguna proveniente de este sistema.

El siguiente objeto que hemos estudiado es AB Dor C. Este objeto forma parte de un sistema de 4 objetos (dos binarias: AB Dor A/C y AB Dor Ba/Bb) que se encuentra aproximadamente a 15 pc de distancia de nosotros. Con un compendio de observaciones VLBI y datos de Hipparcos se descubrió la existencia de AB Dor C (0.090 $M_{\odot}$) orbitando AB Dor A a una distancia promedio de $0.2''$ y se catalogó con tipo espectral M8. El estudio de la naturaleza de este objeto es especialmente relevante debido a que los modelos teóricos de evolución estelar muestran ciertas dificultades a la hora de predecir características física de objetos de baja masa en pre-secuencia principal. Solamente aquellos objetos bien conocidos y con masas debidamente determinadas pueden ser utilizados para comprobar las predicciones de estos modelos teóricos. AB Dor C es un candidato ideal para ser uno de estos objetos. Sin embargo, existe la hipótesis de que este objeto en realidad es binario.

Con la intención de comprobar o desmentir esta posible binariedad de AB Dor C, observamos este objeto con el instrumento AMBER en el VLTI en modo de baja resolución. Debido a problemas técnicos, la banda J no se observó de forma correcta y solamente se empleó la banda K para el análisis y la obtención de resultados. Las observaciones se tomaron el 28 de Diciembre del 2012 utilizando los UT1-UT2-UT4. Por la debil emisión de AB Dor C, empleamos una técnica de observación no estándar basada en utilizar AB Dor A para fijar las franjas interferométricas y así poder integrar sobre más tiempo en AB Dor C. Esto lo pudimos realizar gracias al conocimiento previo de la órbita de AB Dor C y AB Dor A proveniente de observaciones con VLBI.

Tanto las visibilidades como las clausuras de fase obtenidas con AMBER son compatibles con una binaria con cociente de flujo en banda K de un 5% y con una separación de 38 mas. Según los modelos, esto implicaría que las componentes AB Dor Ca y AB Dor Cb tendrían masas de $0.072 \pm 0.013 M_{\odot}$ y $0.013 \pm 0.001 M_{\odot}$, respectivamente. En este caso, AB Dor C estaría formado por una enana marrón cerca del límite de la quema de hidrógeno en el caso de AB Dor Ca, y por un objeto que se encontraría en la frontera entre las enanas marrones y los exoplanetas en el caso de AB Dor Cb. Además comprobamos que esta binariedad aliviaría el desacuerdo visto entre las magnitudes observacionales y las predichas por las relaciones teóricas masa-luminosidad.

La tercera aportación de nuestro trabajo ha sido al campo de las estrellas supergigantes rojas (RSGs por sus siglas en inglés). De acuerdo con el escenario aceptado de evolución de estrellas masivas, las RSGs son los descendentes de estrellas de secuencia principal masivas ($10M_{\odot} \leq M \leq 40M_{\odot}$). Se encuentran fusionando helio y su destino dependerá de su masa y del ritmo de pérdida de masa: bien acabarán como supernovas o bien volverán al diagrama H-R para finalmente explotar como supergigantes azules o estrellas Wolf-Rayet (W-R). Las supergigantes rojas representan un caso extremo en la evolución estelar, puesto que son las estrellas más grandes del universo en cuanto a tamaño y también son las más luminosas de las estrellas frías.

Durante su vida, las RSGs pierden gran cantidad de masa. Sin embargo, los mecanismos físicos que contribuyen y dominan esta gran pérdida son un misterio para la comunidad científica actual. Se sabe que esta pérdida de masa contribuye a producir una gran cantidad de polvo y también que juega un papel principal a la hora enriquecer el medio interestelar. Sin embargo, a día de hoy solamente tenemos hipótesis no corroboradas que tratan de explicar este fenómeno. Entre las más populares está la interacción entre pulsación y convección. Sin embargo, hay bastantes mecanismos alternativos como (i) el descenso de la gravedad efectiva causado por movimientos convectivos, combinado con la presión radiativa en líneas moleculares; (ii) campos magnéticos contribuyendo al calentamiento de las capas externas de la atmósfera y a la pérdida de masa; (iii) un escenario que incluya aceleración radiativa en líneas moleculares corridas por el efecto Doppler; (iv) campos magnéticos y ondas de Alfvén; (v) la presencia de ”hot spots” gigantes.

Con la intención de arrojar algo de luz sobre los posibles mecanismos comentados y sabiendo que la convección en la fotosfera estelar puede ser un factor crucial a la hora de levitar las capas más externas de la atmósfera de una RSG, hemos observado la supergigante roja V602 Carinae (V602 Car) con el instrumento PIONIER en el VLTI. Hemos obtenido observaciones con 3 configuraciones diferentes con los ATs, realizadas entre el 7 de abril del 2016 y el 27 de junio del 2016, y entre el 29 de abril del 2019 y el 8 de julio del 2019. Gracias a la buena calidad de los datos obtenidos, pudimos utilizar el paquete de software SQUEEZE para reconstruir imágenes tanto en 2016 como en 2019 y así analizar la evolución temporal de la estrella. En la primera época, la imagen obtenida muestra un emisión característica en forma de arco hacia el borde norte de la superficie de la fotosfera. En 2019 también se ve una emisión en forma de arco pero en este caso tiene una orientación diferente y, además, aparece un nuevo pico de emisión en el lado opuesto. Al comparar estos resultados observacionales con modelos 3D RHD hemos encontrado que, efectivamente, las simulaciones predicen correctamente las sub-estructuras vistas en la superficie de V602 Car en dos épocas diferentes. Sin embargo, no consiguen reproducir las visibilidades observadas y, por tanto, necesitamos la presencia de una componente molecular extendida. De este estudio hemos podido concluir que la convección solamente puede que no sea el único proceso relevante a la hora de hacer levitar las atmósferas de las supergigantes rojas.

La última aportación presentada en esta tesis está relacionada de nuevo con el sistema AB Dor. En este caso, nos centramos en la emisión en radio de la estrella principal AB Dor A. Esta estrella con tipo espectral K0 tiene una rotación muy rápida (0.51 días de periodo) y presenta emisión en todas las longitudes de onda desde radio hasta rayos X. La edad exacta de esta estrella está, a día de hoy, en discusión, con la gran mayoría de estimaciones cubiertas por un rango de entre 30 y 200 millones de años.

Solamente en número limitado de objetos, las observaciones de VLBI han conseguido resolver la emisión estelar en radio frecuencias. Estos casos pueden ser un buen indicativo de los procesos que pueden ocurrir en AB Dor A. En estrellas ”weak-lined T Tauri” (WTTs) se han detectado casos con estructuras extendiéndose más allá de los 20 $R_\star$. También en el caso de V773 Tau A la emisión detectada pudo haber sido producto del equivalente solar de los ”helmet streamers”. Así pues, la magnetosfera de AB Dor A puede ser bastante compleja y llena de emisión coronal girosincrotrón, ”loops” gigantes con duraciones de horas o incluso eventos similares a los ”helmet streamers” solares.

Hemos observado este sistema usando el LBA a 1.4 (época 2018), 8.4 (épocas 2007, 2010 y 2013) y 22.3 GHz (época 2017) a lo largo de más de una década. Nuestras imágenes a 8.4 GHz muestran una morfología ”double core-halo”, similar en las 3 épocas observadas a esta frecuencia, y con la emisión extendiéndose a alturas entre 5 y 18 radios estelares. Lo que resulta todavía más intrigante ese que, en estas imágenes, existe una clara variación temporal de la estructura de la fuente durante el tiempo de observación. Hemos considerado varios modelos que tratan de explicar las características observadas en nuestros mapas, a saber: una posible compañera orbitando alrededor de AB Dor A, emisión estelar al estilo ”polar-cap”, una estructura de loops que emite en radio frecuencias debido a la reconexión magnética y la presencia de ”helmet streamers”. Nuestras observaciones actuales solamente nos permiten descartar la primera de estas hipótesis, esto es, la posible compañera orbitando alrededor de AB Dor A. Además de esto, también hemos detectado emisión de AB Dor A a 1.4 GHz compatible con una fuente no resuelta. Finalmente, hemos puesto cotas superiores de emisión en radio para AB Dor C en 0.11 mJy, 0.04 mJy, 0.10 mJy, 0.04 mJy y 0.07 mJy para 2007, 2010, 2013, 2017 y 2018, respectivamente.

Contents

List of Figures

List of Tables

Chapter 1

Introduction to interferometry

The technique of interferometry is the backbone of this dissertation. It has allowed us to investigate stellar and sub-stellar objects at high angular resolution and at both infrared (IR) and radio wavelengths. As such, a general overview of the technique should be provided firstly, emphasizing the relevant aspects for the work we have conducted in this dissertation. We will do our best to describe the common aspects between IR and radio interferometry but, when necessary, a clear distinction will be made. Despite this, for a more much detailed treatment of radio interferometry the reader is encouraged to visit the classic text by Thompson et al. (2001) or the series of lectures on Synthesis Imaging from the NRAO Summer School. For the optical/infrared interferometry basics several resources are more than appropriate: Monnier (2003); Labeyrie et al. (2006); Malbet & Perrin (2007); Glindemann (2011); Saha (2011); Buscher & Longair (2015).

We have organized this chapter as follows: (i) we will begin by introducing the technique of interferometry, from its necessary origin to a basic mathematical formulation. (ii) We will then focus on IR interferometry while discussing some of the main differences with the radio counterpart. In this section we will also introduce the infrared instruments used during the work presented here and their data reduction process. (iii) A similar treatment will be given to the very-long-baseline interferometry (VLBI) technique so that the reader has a profound understanding of the cornerstone of our work at radio wavelengths. And finally, (iv) we will end this chapter by describing the imaging techniques employed both in radio and IR interferometry.

1.1 Interferometry basics

Even under the best imaginable observational circumstances, the angular resolution, θ, of any telescope is limited by diffraction to

$$\theta \approx \frac{\lambda}{D} \tag{1.1}$$

where λ is the observing wavelength and D is the diameter of the telescope.

The technique of astronomical interferometry originated from the desire to image with higher angular resolution and to improve the precision of the positions of celestial objects. Equation 1.1 implies that the lower the wavelength of observation, the bigger the diameter of the telescope should be in order to keep the same angular resolution. This relationship clearly hinders lower frequency observations and motivated the development of early interferometry, specially at radio-wavelengths. Combining the light of multiple telescopes of reasonable sizes and synchronizing its signals, this technique can simulate a telescope with a much larger diameter ($\theta \approx \frac{\lambda}{b}$, where b is the separation between telescopes), allowing lower wavelengths not only to keep up with the angular resolution of optical observations but, in most cases, to surpass it. Prominent examples of the exquisite angular resolutions achieved through this technique are arrays such as the European VLBI Network (EVN), and the Very Long Baseline Array (VLBA) among others that we shall discuss later and that are able to reach sub-milliarcsecond resolutions. In this simulated telescope the angular resolution can be indeed much higher than the angular resolution of the real telescope but the flux recollected still depends on the diameter and technical characteristics of the real telescope.

It is worth noting that the technological development for the IR technique started more than 50 years ago at radio wavelengths. However, at optical and IR wavelengths the first successful direct interference from light collected by two different telescopes happened in 1974 (Labeyrie 1975) and it was not until the 1990s when the first optical synthesis image from three different telescope was obtained (Baldwin et al. 1996). Nowadays, arrays as such the Very Large Telescope Interferometer (VLTI) are capable of combining the infrared light from four different telescopes.

As an overview of the interferometry technique: the telescopes (infrared term) or antennas (radio term) collect photons coming from our target of observation which are then brought together to a central location. This central location is called correlator (radio term) or combiner (optical/infrared term) and it is where the different signals are combined coherently in order to create fringes. However, the coherent combination happens differently at these two wavelengths:

- For wavelengths longer than ~0.2 mm, the electric field measured by the antenna gets converted into cabled electrical signals and amplified. It is then combined with a reference signal of high coherence (conserving the amplitude and the phase of the coming electric field) and sent to the correlator. The correlator is a multiplicative interferometer that, as we shall see in the next section, multiplies the signals and takes the time average.

- For shorter wavelengths, the information travels from the telescopes to the combiner through mirrors and optical elements. The combiner can be classified as an additive interferometer that sums the signals coherently. In this case, one does not preserve the phase of the electric field and the fringes need to be coded.

For an array observing at a central wavelength of λ_0, the coherence length is $\lambda_0^2/\Delta\lambda$ (Thompson et al. 2001). If the path difference between the collectors of an interferometer is a significant fraction of this coherence length then one must introduce an additional time delay that needs to be adjusted as the geometry of the collectors continually changes. This time delay is important since it defines the phase center (radio term) or point of zero optical path delay (OPD; infrared term) as the location on the sky where the adjusted time delay is matched perfectly. Adjusting this phase center is the equivalent of pointing the interferometer.

1.1.1 The two-element interferometer

Let us now present the very simple but illustrative example of a two element multiplier interferometer in response to a point source and for which the rotation of the Earth and the atmosphere are not considered. To develop the mathematical formulae, let us focus this example on radio wavelengths although most of the principles and reasoning that we will discuss directly translate to the IR regime.

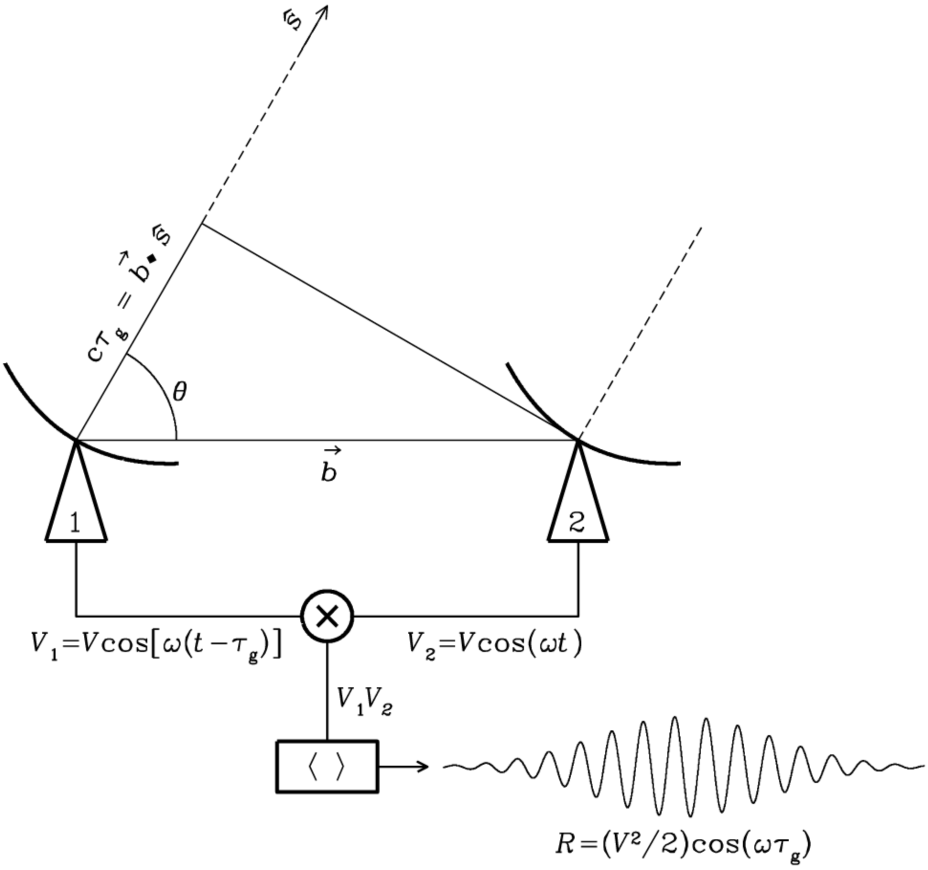

Figure 1.1: Structure of a two element multiplier interferometer. Credit: National Radio Astronomy Observatory (NRAO).

As illustrated in Fig. 1.1, this basic interferometer consists of two antennas separated by a vector $\vec{b}$ called baseline. $\hat{s}$ represents the unit vector in the direction of a distant point source. The output voltage V_1 of antenna 1 is the same as the output voltage V_2 of antenna 2, but it is retarded by what is known as the geometric delay τ_g. This delay occurs when the wavefront that comes from a source in the direction $\hat{s}$ first reaches antenna 2 and afterwards antenna 1. From the trigonometry of Fig. 1.1, one can obtain the mathematical expression for the geometric delay:

$$\tau_g = \frac{\vec{b} \cdot \hat{s}}{c} \tag{1.2}$$

In the case of a quasi-monochromatic two element interferometer observing in a very narrow frequency range centered on $\nu = \omega/(2\pi)$, the voltages measured by the antennas 1 and 2 can be written as

$$V_1 = V \cos\left[\omega\left(t - \tau_{\mathrm{g}}\right)\right] \tag{1.3}$$

$$V_2 = V \cos(\omega t) \tag{1.4}$$

where V is the maximum amplitude of the voltage and t is time.

After the measurement of the output voltages, the correlator first multiplies these voltages

$$V_1 V_2 = V^2 \cos(\omega t) \cos\left[\omega\left(t - \tau_{\mathrm{g}}\right)\right] = \frac{V^2}{2}\left[\cos\left(2\omega t - \omega\tau_{\mathrm{g}}\right) + \cos\left(\omega\tau_{\mathrm{g}}\right)\right] \tag{1.5}$$

and then takes a time average giving the final output R_1:

$$R_1 = \langle V_1 V_2 \rangle = \frac{V^2}{2} \cos\left(\omega\tau_{\mathrm{g}}\right) \tag{1.6}$$

The time average must be taken during $\Delta t \gg (2\omega)^{-1}$ in order to remove the high-frequency term. This final output R_1 provided by the interferometer is proportional to the point-source flux density. The sinusoidal dependence of the correlator output voltage with the change of the source direction creates fringes with a phase of

$$\phi = \omega\tau_{\mathrm{g}} = \frac{\omega}{c} b \cos\theta \tag{1.7}$$

This observable can be a very sensitive measure of the source position. Finally, it is worth noting that the final correlator output does not show any uncorrelated noise from the receivers.

If we now apply a $\frac{\pi}{2}$ phase shift to the output from one of the telescopes, the new response of the interferometer is:

$$R_2 = \frac{V^2}{2} \sin\left(\omega\tau_{\mathrm{g}}\right) \tag{1.8}$$

Euler's formula allows us to construct a new and very useful function called the visibility function $\mathcal{V}$ by combining R_1 and R_2 as follows:

$$\mathcal{V} = R_1 + iR_2 = \frac{V^2}{2} e^{i\omega\tau_{\mathrm{g}}} \tag{1.9}$$

1.1.2 Extended sources and the *uv* plane

When observing a spatially incoherent extended source with sky brightness distribution $I(\hat{s})$, the two-element interferometer response can be considered as the sum of the visibilities of independent point sources:

$$\mathcal{V} = \frac{1}{2} \int_{4\pi} I(\hat{s}) e^{i\omega\tau_g} d\Omega = \frac{1}{2} \int_{4\pi} I(\hat{s}) e^{i\frac{2\pi\nu}{c}\vec{b}\hat{s}} d\Omega \tag{1.10}$$

where $d\Omega$ is the differential solid angle subtended by the source.

In practice, we would like to recover the value of the intensity from the value of the visibility measured by our interferometer. In order to do this, we must assume a reference point of the extensive source also known as the phase center. $\hat{s}_0$ would be the vector pointing to such phase center and, by definition, would be orthogonal to the baseline vector $\vec{b}$. All other observed points would have an offset vector $\vec{\sigma}$ such that $\vec{s} = \hat{s}_0 + \vec{\sigma}$. Let us define now a coordinate system (u,v,w) where the w axis is parallel to $\hat{s}_0$ and, consequently, the u and v axes are in the plane orthogonal to $\hat{s}_0$. This coordinate system is sketched in Fig. 1.2.

In this coordinate system, the scalar product between the vectors $\vec{s} = (x, y, z)$ and

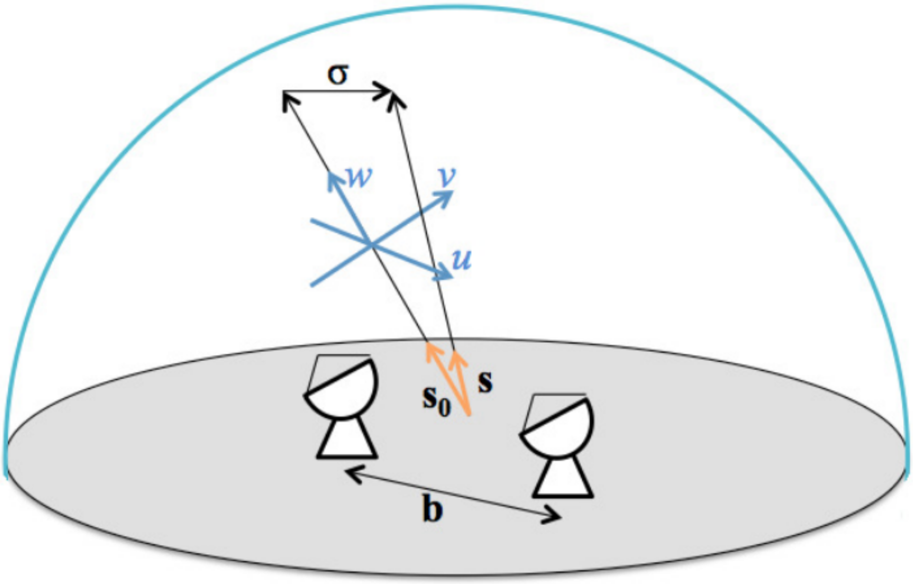

Figure 1.2: Definition of the coordinate system (*u*,*v*,*w*). Credit: figure adapted from Avison & George (2013).

$\vec{b} = (u, v, 0)$ would be

$$\vec{b} \cdot \vec{s} = ux + vy \tag{1.11}$$

The solid angle subtented by the source, $d\Omega$, would be:

$$d\Omega = \frac{dxdy}{\sqrt{1 - x^2 - y^2}} \tag{1.12}$$

In the case where $x^2 + y^2 \ll 1$, that is, when the source is compact, the visibility function is the inverse Fourier transform of $I(\hat{s})$ and, therefore, to obtain $I(\hat{s})$ one simply needs to compute the Fourier transform of the measured visibility function:

$$\mathcal{V}(u, v) = \frac{1}{2} \int_{-\infty}^{+\infty} \int_{-\infty}^{+\infty} I(\hat{s}) e^{i \frac{2\pi\nu}{c}(ux+vy)} dxdy \tag{1.13}$$

As defined above, the *u* and *v* axes are within a plane orthogonal to the vector $\hat{s}_0$. This is known as the *uv* plane. As the earth rotates, the projected baselines on the *uv* plane describe ellipses (called *uv-tracks*) as the vector $\vec{b}$ changes in length and orientation. The interferometer is, therefore, sampling the visibility function at different (*u*,*v*) points in the *uv* plane. These sampled points define what is known as the *transfer function* of the observation. This is the cornerstone of the aperture synthesis technique, designed by Martin Ryle and Anthony Hewish and awarded the Nobel Prize in Physics in 1974. The better the transfer function of an observation, that is, the better the *uv* plane is sampled, the more reliable would be the intensity distribution $I(\hat{s})$ computed from the Fourier transform of the measured visibility function.

In addition to the aperture synthesis technique, one can also increase the number of antennas involved in the observation in order to improve the sampling of the *uv* plane. However, there are a few points to consider when extending the mathematical treatment we have considered here for the two-element interferometer to an array of telescopes. An interferometer with N telescopes or antennas contains $N(N-1)/2$ baselines that can be interpreted as $N(N-1)/2$ two-element interferometers. The synthesized beam of the array, that is the point-source response, tends to a Gaussian profile as the number of elements increases (see Fig. 1.3) approaching an angular resolution of λ/b. However, not all of the energy is collected by the main Gaussian. A small part of it creates sidelobes which need to be considered when analizing the data.

1.2 Infrared interferometry

The same interferometry technique that has been discussed for radio wavelengths applies for other wavelength domains, such as IR and optical. However, although both radio and IR interferometry share the same fundamentals and the same objectives, they exhibit some significative differences that we shall discuss briefly. Some of these differences are due to observing at different wavelengths while others reflect the more advanced state of maturity of the radio interferometry field.

The first difference is that, in radio interferometry the signal detection occurs at the antenna where it is digitized and the combination of signals from multiple antennas takes place in the correlator. However, in IR interferometry this technique is typically not sensitive enough. The interferometry is then achieved by propagating the light beams through delay lines from each telescope to a central laboratory, where the optical path is equalized

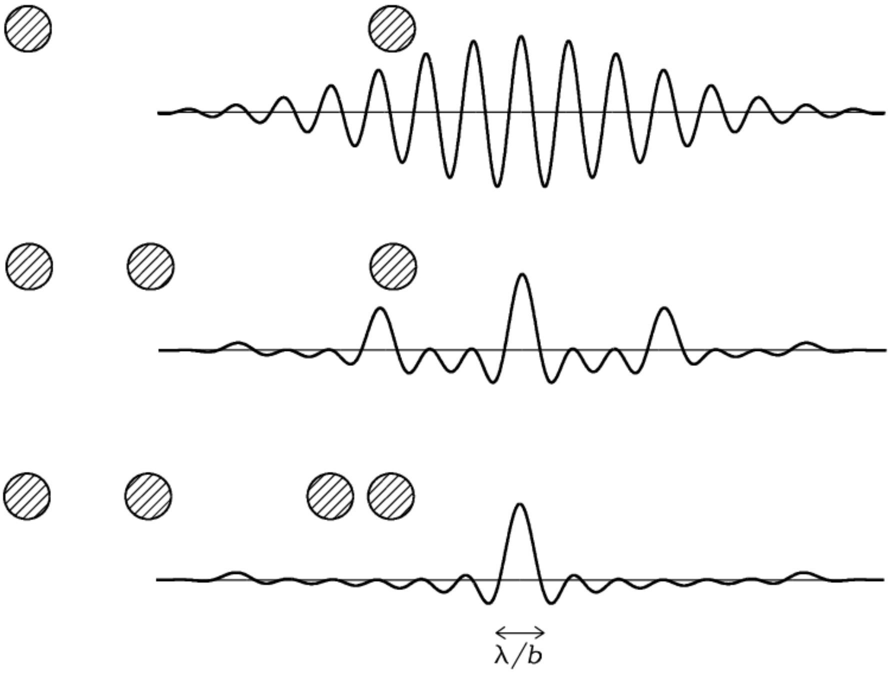

Figure 1.3: Synthesized beam of different arrays of telescopes/antennas. *(Top panel):* two-element interferometer with projected baseline length *b*; *(middle panel):* three-element interferometer with projected baseline lengths: $b/3$, $2b/3$, and b; *(bottom panel):* four-element interferometer with projected baselines lengths: $b/6$, $2b/6$, $3b/6$, $4b/6$, $5b/6$, and b. Credit: National RadioAstronomy Observatory (NRAO).

and the light beams are combined to form interferences. To avoid losses due to diffraction in the delay lines, the mirror of the telescope must be larger than about $\sqrt{B \times \lambda}$. That is why this technique is not used at mm-interferometry.

Since optical/infrared detectors can only measure the power of the electric field, the fringes need to be coded. Mathematically, since IR interferometry uses additive interferences, the signal measured from the combination of two antennas would be:

$$I_{12} = I_1 + I_2 + 2\sqrt{I_1 I_2}\, V_o\, |\mathcal{V}_{12}| \cos\Phi_{12} \tag{1.14}$$

where I_i is the intensity of the signal measured by telescope i, and $\mathcal{V}_{12}$ is the visibility of the source, with amplitude $|\mathcal{V}_{12}|$ and phase Φ_{12}. V_o is the contrast that takes into account the calibration of the entire system: both instrument and atmosphere. To obtain the visibility of the source, one must modulate the signal in order to measure both the amplitude and the phase of the visibility:

$$I\left(\Phi_{\text{mod}}\right) = I_1 + I_1 + 2\sqrt{I_1 I_2} V_o \left|\mathcal{V}_{12}\right| \cos\left(\Phi_{12} + \Phi_{\text{mod}}\right) \tag{1.15}$$

which can be done by measuring the variation of $I\left(\Phi_{\text{mod}}\right)$ as a function of Φ_{mod}. Although we will not discuss them further, there are mainly two types of fringe coding: temporal or spatial coding.

The second important difference is related to the atmosphere. Even in bad conditions, the atmosphere has a coherence time of a few minutes at radio frequencies, which allows for the use of a phase calibrator and the phase-referencing technique described in Sect. 1.4.1. In the infrared domain, however, the coherence time can be as small as a few milliseconds. This together with the fact that the angular scale over which the atmospheric phase is coherent is very small, renders the phase-referencing technique completely impractical for IR interferometry observations. Consequently infrared interferometry makes use of closure phases relations in order to retrieve the astronomical phase and of a system called fringe-tracking (Shao & Staelin 1977) to allow for longer exposures by stabilizing the interferometric fringes to a fraction of the wavelength.

Another difference is that, although both radio and IR interferometers must delay the signals from some telescopes to match the optical paths, this is achieved by different methods. In a radio interferometer switchable lengths of coaxial cable can be employed whereas for an IR interferometer this is not possible due to losses and glass dispersion. Alternatively, these interferometers use a retroreflector moving on a long track to introduce the desired delays. This element must be stabilized through laser metrology to compensate for air path disturbances and vibrations in the building.

The type of noise encountered in each interferometer are different as well. While the main source of noise in radio interferometry is the thermal noise, at infrared frequencies one must consider various type of noises: the photon noise, the read-out noise of the detectors, the background noise (coming either from thermal emission or from the sky brightness), and also noise from the atmosphere turbulence.

Finally, radio interferometers measure correlated flux density of the source in units of Jansky, whereas at infrared wavelenghts the interferometers tend to always measure a normalized visibility that can be then converted to correlated flux density by an amplitude calibration process. A summary of all the differences discussed here can be found in Table. 1.1.

Table 1.1: Main differences between radio and infrared interferometry.

Radio interferometry	Infrared interferometry
Antennas	Telescopes
Correlator	Combiner
Preserves phase of electric field	Does not preserve phase of electric field
Delay signals through coaxial cable	Delay signals through stabilized retroreflector
Measures correlated flux density in Jy	Measures normalized visibilities (can be converted to correlated flux density via calibratrion)
Can use phase-referencing technique	Fringe-tracking
Phase center	Point of zero optical path delay (OPD)
Dominated by thermal noise	Dominated by a combination of photon, read-out, background, and atmospheric noises.

Let us now introduce the two infrared instruments used during the work presented in this dissertation. Both instruments are operated at the Very Large Telescope Interferometer (VLTI) in Cerro Paranal in the Chilean Atacama Desert. The VLTI consists in combining the light coming from various 8.2-m Unit Telescopes (UTs) or from various 1.8-m Auxiliary Telescopes (ATs) (see Fig. 1.4). The UTs are set on fixed locations while the ATs can be relocated on 30 different stations. The two instruments we have employed during the work presented here are AMBER and PIONIER, which combine the light coming from 3 and 4 telescopes at the VLT, respectively.

1.2.1 AMBER

The Astronomical Multi-BEam combineR (AMBER) focal instrument (Petrov et al. 2007) at the VLTI combines coherently three telescopic beams, allowing to measure not only visibilities but also closure phases. It operates in the J, H and K infrared bands (i.e. 1.1 to

Figure 1.4: Aerial view of the ESO Very Large Telescope. Credit: J.L. Dauvergne & G. Hüdepohl (atacamaphoto.com)/ESO

2.4 μm) and is able to achieve an angular resolution of 2 milli-arcsecond (mas) with the UTs and 50 mas with the ATs.

Now a decommissioned instrument, AMBER offered the observer three spectral resolution options ranging from the low (R = 35), to the medium (R = 1500) and, finally, to the highest resolution (R = 120000). This instrument was offered in combination with the external fringe tracker FINITO (Fringe-Tracking Instrument of NIce and TOrino) such that, on the UTs, it was able to reach magnitude $K = 9$ in the best conditions and in low spectral resolution. If used on the ATs, the limiting magnitude was $K = 6.5$.

For the reduction of AMBER data, a dedicated software is provided: *amdlib* (Tatulli et al. 2007; Chelli et al. 2009). This software uses the pixel-to-visibilities matrix (P2VM) to extract complex visibilities for each baseline and each spectral channel of an AMBER interferogram. Once the complex visibilities have been obtained, one can obtain the amplitudes and the closure phases. As explained above, the visibilities need to be corrected

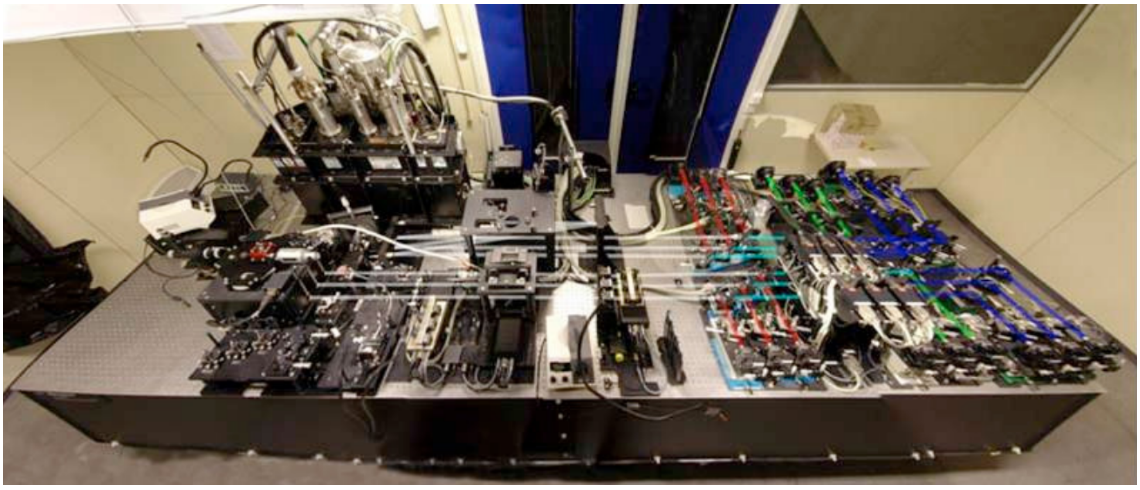

Figure 1.5: AMBER instrument in the integration room of the Laboratoire d'Astrophysique de Grenoble in 2003. Credit: Petrov et al. (2007)

for atmospheric and instrumental effects. To achieve this correction, the observation is planned so that a calibrator star is observed on the same night. Knowing or estimating the diameter of this calibrator star is extremely important since one must first correct the calibrator visibility by dividing it by the expected calibrator star visibility. The next step is then correct the target source by dividing the visibility of the target source through the visibility of the calibrator. Once this process is finished, the observer has now the calibrated visibilities and closure phases of the target object and can fit some models or, if the quality of the data allows it, proceed to an image reconstruction using other packages.

1.2.2 PIONIER

The Precision Integrated-Optics Near-infrared Imaging ExpeRiment (PIONIER) instrument at the VLTI (Le Bouquin et al. 2011) combines the light of the 4 UTs or the 4 ATs to provide visibilities of six different baselines, together with four closure phase measurements with low spectral resolution ($R \approx 40$). It operates in the H infrared band and has a limiting magnitude of $H = 9$ in the best scenario possible. It can either integrate the light of the entire H band for sensitivity enhancement or take measurements at six different wavelengths within the H band, increasing the *uv* coverage.

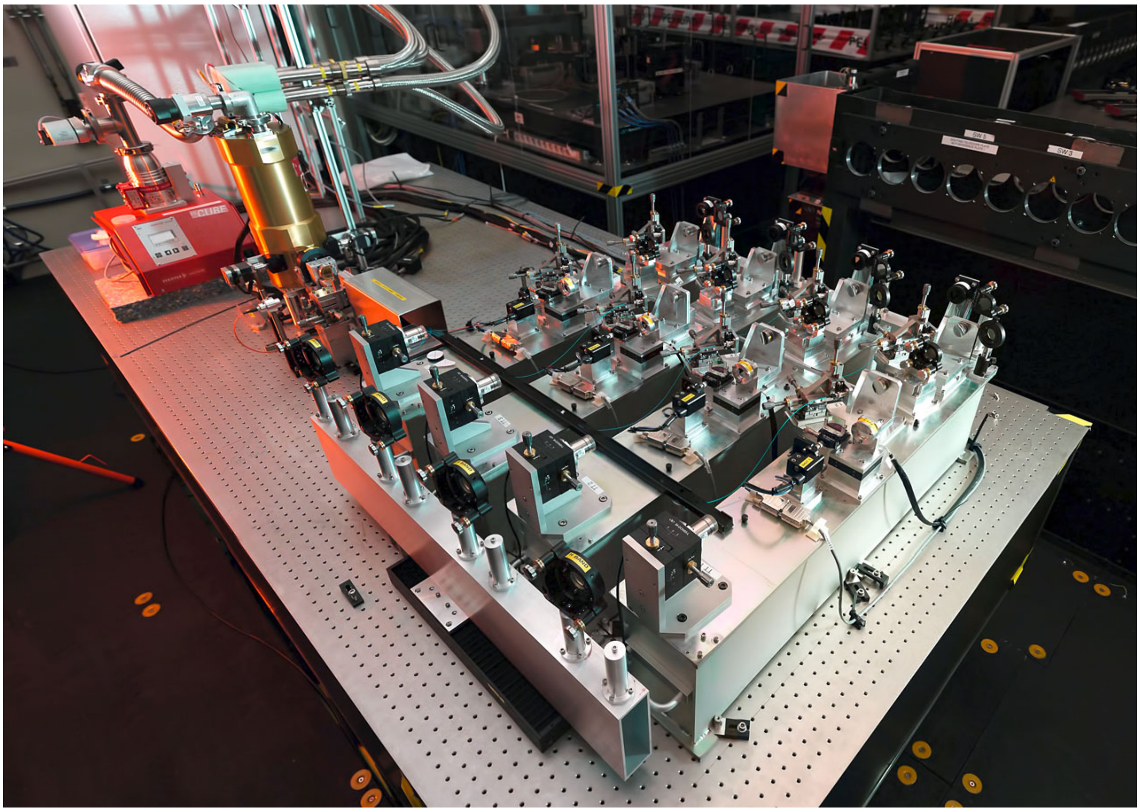

Figure 1.6: PIONIER instrument. Credit: ESO & B. Lazareff (LAOG)

For the reduction of PIONIER data, a similar process to the AMBER data reduction is followed. In this case, the dedicated package *pndrs* (Le Bouquin et al. 2011) also uses the visibilities of a calibrator star (whose observations must be interleaved with observations of the target source) to correct the instrumental and atmospheric effects of the data. *pndrs* converts the raw FITS file produced by the instrument into calibrated visibilities and closure phase measurements written in the standard OIFITS format (Pauls et al. 2005). As with the final AMBER data, these OIFITS files are science-ready and can be further analyzed by external packages such as the reconstruction package SQUEEZE (Baron et al. 2010) or the model fitting package LITpro (Tallon-Bosc et al. 2008).

1.3 Very-long-baseline interferometry

Originally developed in the 1960s, the Very-Long-Baseline Interferometry or VLBI technique refers to the special case when the different elements that form an interferometric network are separated by such large distances that it is impractical to connect them physically. For short baselines arrays, all the elements of the interferometric network can be connected via coaxial cables, waveguides, optical fibers, or other types of transmission lines to a computer where appropriate computations will take place. However, in the case of VLBI, where baselines lengths may reach up to thousands of kilometres, a novel strategy must be considered, i.e.: each station records the received signals on tapes or disks with the help of an extremely precise atomic clock. Later on, these tapes or disks will be sent for processing at a central processor or correlator where the signals from each pair of antennas will be correlated using the precise time difference between the arrivals of the radio signal at different antennas to estimate the baseline lengths accurately. In practice, there may be no need for physically sending the disks or tapes to a central correlator since the substantial increase in bandwidth for data transmission has allowed real-time VLBI in what is known as e-VLBI (electronic VLBI).

Let us now briefly introduce the arrays employed for the radio-wavelength part of this dissertation.

1.3.1 The Very Large Array

The Very Large Array (VLA) consists of an array of 28 antennas (27 active), each with a diameter of 25 meters, located in Socorro, New Mexico. It was constructed as a reconfigurable array so that it can offer four different configurations: A configuration with size of 36.40 km, B configuration with size of 11.40 km, C configuration with size of 3.40 km and D configuration with size of 1.03 km. The central frequency available for observations ranges from 1.0 GHz to 50 GHz. In this sense, the maximum resolution that can be achieved with the VLA varies from 0.2 arcseconds to 0.04 arcseconds.

Figure 1.7: Aerial view of the Very Large Array. Credit: National RadioAstronomy Observatory (NRAO).

1.3.2 The European VLBI network

The European VLBI network (EVN) is an array of radio telescopes spread around the globe with the majority of them located in Europe (see Fig. 1.8). The participant antennas, commonly used for independent radio astronomical observations, are scheduled three times per year for several weeks together as a VLBI array. As a result of the collection of extremely large telescopes, the EVN is currently the most sensitive VLBI array in the world. The main frequencies/wavelengths that can be observed are: 1.664 GHz (18 cm), 2.268 GHz (13 cm), 4.992 GHz (6 cm), 6.030 MHz (5 cm), 6.668 GHz (5 cm), 8.418 GHz (4 cm), and 22.230 GHz (1 cm). Moreover, at some stations it is also possible to observe at: 0.327 GHz (90 cm), 0.610 GHz (50 cm), 1.416 GHz (21 cm), 15.362 GHz (2 cm), and 43.214 GHz (7 mm). Finally, the EVN often offers the possibility of joint proposals, i.e.: observations in conjunction with other arrays of radio telescopes such as the VLBA in the

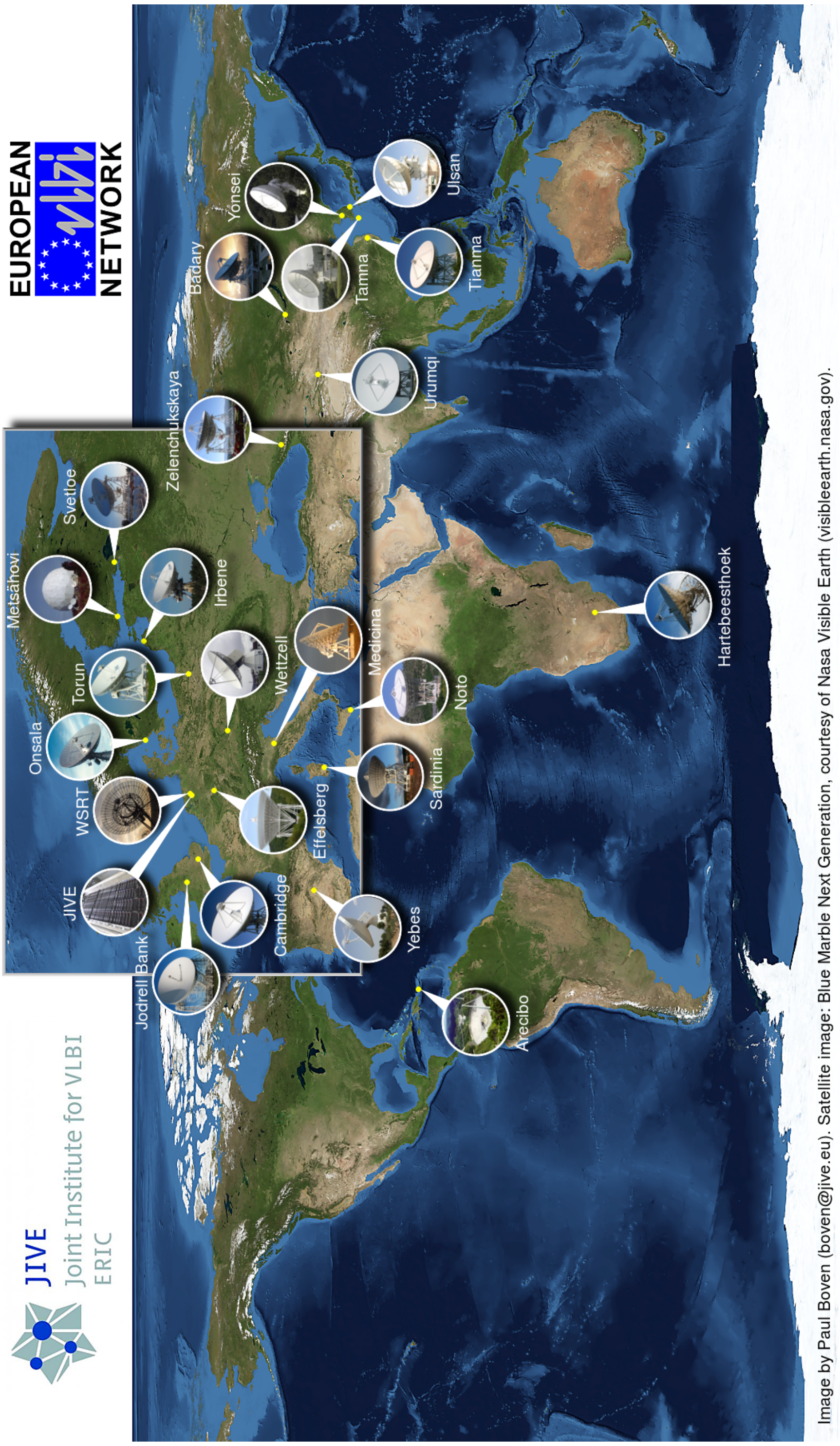

Image by Paul Boven (boven@jive.eu). Satellite image: Blue Marble Next Generation, courtesy of Nasa Visible Earth (visibleearth.nasa.gov).

Figure 1.8: Location of the main antennas used by the EVN. Miyun is a new station not yet fully participating (not shown). Robledo and Ny Alesund are non-EVN stations that sometimes participate (not shown). Credit: European VLBI Network.

USA or MERLIN in Great Britain.

1.3.3 The Australian VLBI network

The Long Baseline Array (LBA) is a VLBI network located in the southern hemisphere which allows for observations on objects inaccessible from the northern hemisphere instruments. As can be appreciated in Fig. 1.9, the stations are spread across Australia, New Zealand, and South Africa. The central frequency available for observations ranges from 1.4 GHz to 22.2 GHz, but not all antennas can observe at all available frequencies. The radio telescopes of the Australia Telescope National Facility (ATNF) are the core of the LBA. These are: ATCA (Australian Telescope; in turn, a connected interferometer), Parkes, and Mopra, and the antennas in Hobart and Ceduna, belonging to the University of Tasmania.

1.3.4 Data reduction in VLBI observations

The fact that the individual elements of a VLBI array are separated by hundreds and thousands of kilometres allows for superior angular resolution, as detailed above, but it also comes with a cost: phase errors introduced by the earth's atmosphere. However, these are not the only errors to consider. Other sources of error in VLBI observations are mainly uncertainties in the geometry of the array and instrumental errors. This is a very complex topic that we shall not cover in detail here since it includes the development of a VLBI geometrical model that takes into account nutation, precession, tectonic motion, post-glacial rebound, etc. The interested reader is encouraged to see the work of Walker (1999).

Let us now discuss the mathematical formulation behind the calibration of VLBI data. Due to the numerous errors that we have just mentioned in the paragraph above, the visibility measured by the antennas i and j, $\tilde{V}_{ij}(t, \nu)$, at a certain time t and frequency ν is different from the true visibility, $V_{ij}(t, \nu)$. Let us introduce the gain factors $G_i(t, \nu)$ and

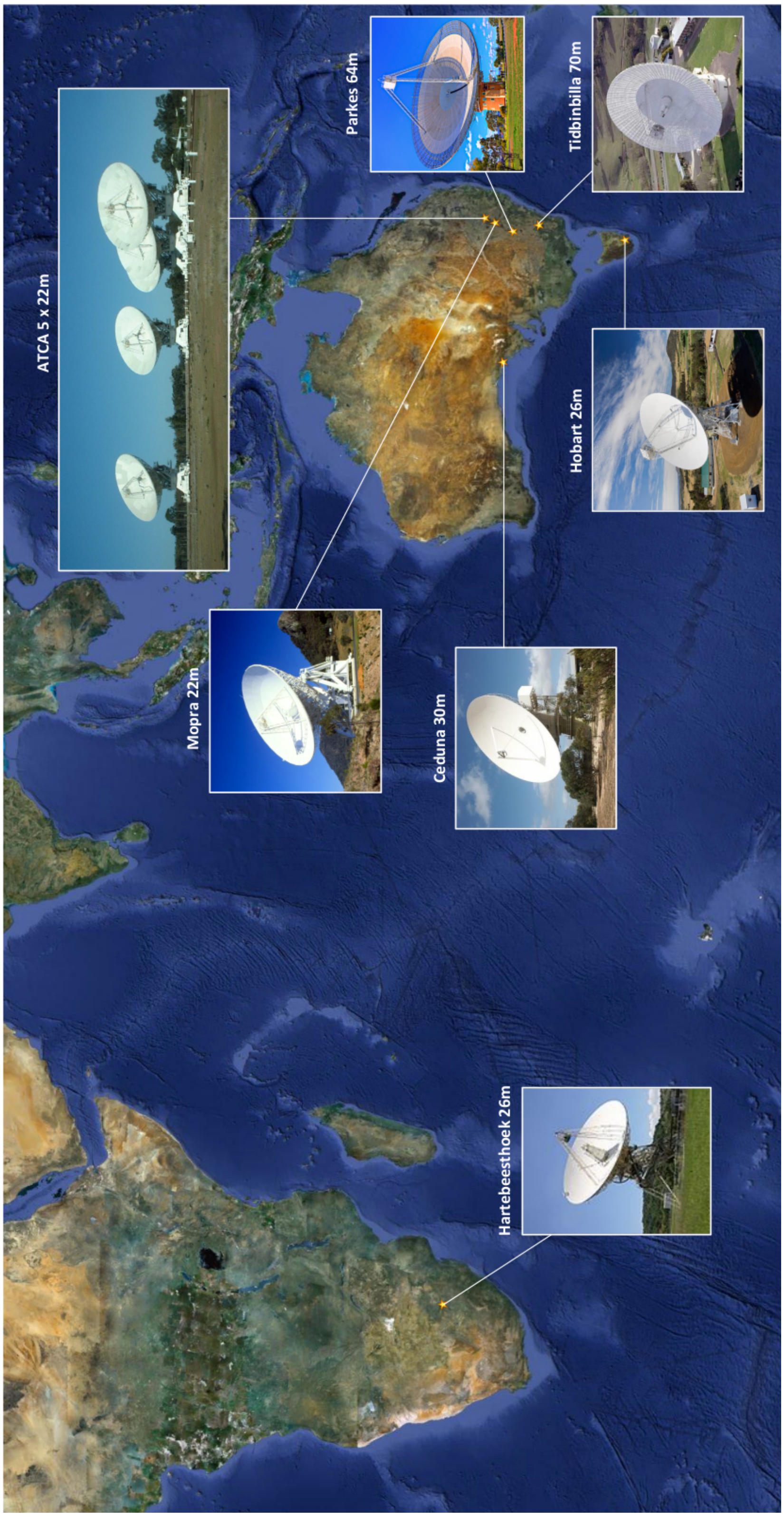

Figure 1.9: Location of the main antennas used by the LBA.

$G_j(t, \nu)$ such that

$$\tilde{V}_{ij}(t, \nu) = G_i(t, \nu) G_j^*(t, \nu) V_{ij}(t, \nu) + \epsilon_{ij} \tag{1.16}$$

where ϵ_{ij} is a thermal noise term. In this fashion, the gain factors represent the amplitude and phase errors corresponding to each antenna, and are defined as:

$$G_i(t, \nu) = a_i(t, \nu) e^{i\phi_i(t,\nu)} \tag{1.17}$$

where $a(t, \nu)$ is known as the amplitude calibration and $\phi(t, \nu)$ the phase calibration of a given telescope.

Let $A_{ij}(t, \nu)$ and $\phi_{ij}(t, \nu)$ be the amplitude and phase of the true visibility $V_{ij}(t, \nu)$, Eq. 1.16 can be rewritten as:

$$\tilde{A}_{ij}(t, \nu) e^{i\tilde{\theta}_{ij}(t,\nu)} = a_i(t, \nu) a_j(t, \nu) A_{ij}(t, \nu) e^{i\left[\phi_i(t,\nu) - \phi_j(t,\nu) + \theta_{ij}(t,\nu)\right]} \tag{1.18}$$

Our task now is to estimate the amplitude and phase calibration terms for each telescope while also correcting for the contribution due to the ionosphere and the effects of the parallactic angle.

Amplitude calibration

The measured visibility amplitudes have no physical units and need to be converted into flux densities (in Jy). Additionally, the amplitude calibration also corrects for errors produced by instrumental factors at the antennas and in the correlator. To do this, the common strategy consists in observing a well-known calibrator source alternatively with the target source. In this manner, one can correct for all the amplitude errors and also calibrate the flux for the calibrator. Later on, these corrections are applied to the target source. However, for VLBI observations the assumption that the calibration sources are unresolved no longer holds and an alternative approach must be considered.

This alternative approach for amplitude calibration in such high angular resolution observations involves the use of the system temperature (T_{sys}) of the individual antennas.

The T_{sys} sums up all the contributions to the antenna temperature (T_a) that do not come from the astronomical source. These include noises from the amplifiers, the receivers, etc.

Let S be the observed flux of the astronomical source (expressed in Jy), the antenna gain g is defined as follows:

$$g = \frac{T_a}{S} \quad \text{(in K/Jy)} \tag{1.19}$$

We then define the system equivalent flux density (SEFD) as:

$$\text{SEFD} = \frac{T_{sys}}{g} \tag{1.20}$$

which represents the total temperature of the receiver in Jy (Moran & Dhawan 1995). The continuous measurement of system temperatures for each station together with accurate gain curves characterising the variation of the gain versus the elevation allows for a precise amplitude calibration by following the relationship proposed by Cohen et al. (1975):

$$A_{ij} = \tilde{A}_{ij} b \sqrt{(\text{SEFD})_i (\text{SEFD})_j} = \tilde{A}_{ij} b \sqrt{\frac{T^i_{sys} T^j_{sys}}{g_i g_j}} \tag{1.21}$$

where $T^i_{sys}, T^j_{sys}, g_i, g_j$ are the system temperatures and the antenna gains for the antennas i and j, respectively. The coefficient b includes some necessary corrections such as digitisation losses or corrections on the internal structure of the correlator.

Phase calibration

Phase errors will disperse the measured flux of individual visibilities away from the correct locations in the image. Were these errors not corrected, they would severely affect the SNR of the observations or, even, the detection of the source. These errors arise from different sources, mainly: the geometric delay τ between two antennas, the contribution due to the antennas instrumentation, the contribution due to atmospheric effects and, finally, the contribution due to ionospheric effects. They can be sum up in the total delay as follows:

$$\tilde{\theta}(t,\nu) = \tilde{\theta}_{geo}(t,\nu) + \tilde{\theta}_{ins}(t,\nu) + \tilde{\theta}_{atm}(t,\nu) + \tilde{\theta}_{ion}(t,\nu) + 2\pi n \tag{1.22}$$

where $2\pi n$ is an integer number of cycles. For VLBI observations each of the terms that contribute to the total delay is much larger than for smaller networks like the VLA.

An initial correction of the phase errors is applied at the correlator by making use of a model of earth's rotation, atmosphere, and station clocks, among other effects. However, further treatment is required for the residual delays. The process for this additional correction is known as fringe-fitting (Beasley & Conway 1995). A mathematical description of this procedure is beyond the scope of this Section, hence, we will only provide a qualitative overview of such procedure.

We first need to make some assumptions: (i) through the time and frequency interval considered, $a(t,\nu)$ and $\left|V_{ij}\right|$ can be considered constant; (ii) the thermal noise term, ϵ_{ij}, is small or, in other words, each baseline has a high SNR; (iii) the phases vary linearly with time and frequency and, consequently can be expanded as:

$$\tilde{\theta}_{ij}(t,\nu) = \phi_i\left(t_0,\nu_0\right) - \phi_j\left(t_0,\nu_0\right) + \theta_{ij}\left(t_0,\nu_0\right) + \left[\dot{\tau}_{ij}\left(t-t_0\right) + \tau_{ij}\left(\nu-\nu_0\right)\right] \tag{1.23}$$

for a baseline ij at the reference point (t_0,ν_0) within the interval considered. The quantities

$$\dot{\tau}_{ij} \equiv \left.\frac{\partial\left(\phi_i - \phi_i + \theta_{ij}\right)(t,\nu)}{\partial t}\right|_{(t_0,\nu_0)} \tag{1.24}$$

and

$$\tau_{ij} \equiv \left.\frac{\partial\left(\phi_i - \phi_i + \theta_{ij}\right)(t,\nu)}{\partial \nu}\right|_{(t_0,\nu_0)} \tag{1.25}$$

are known as the fringe rate and delay, respectively, and are of extreme importance for the fringe-fitting procedure.

Using a two-dimensional grid with the fringe rate in one axis and the delay in another, the fringe-fitting method aims to determine the peak of the Fourier transform of the visibility in this grid and, therefore, find the corrected values of τ and $\dot{\tau}$ (see Fig. 1.10).

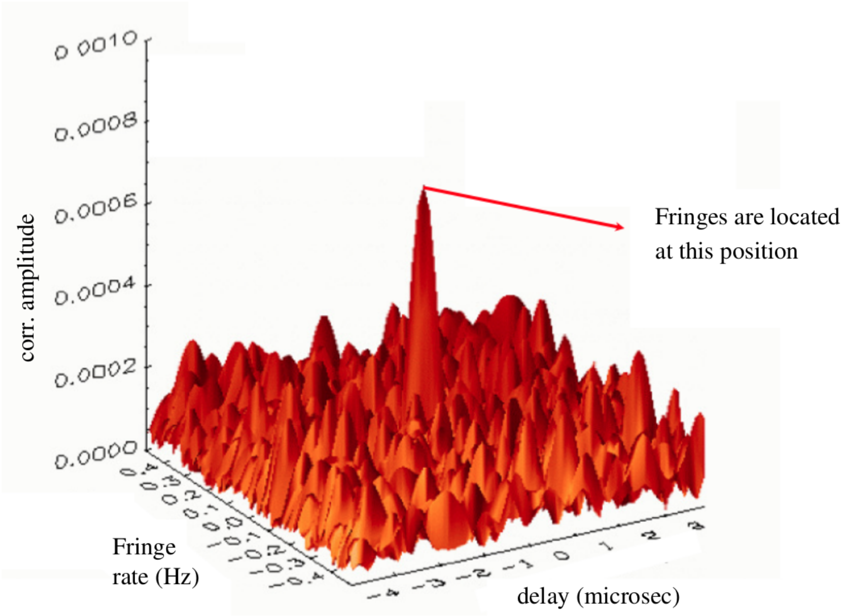

Fringes are located at this position

Figure 1.10: Fringe-fitting finding the maximum peak of the Fourier transform of observed visibilities in delay, delay-rate space. Credit: K. Kingham, United States Naval Observatory.

This procedure we have just described is applied to each baseline. However, one can also apply the same methodology in the case of low SNR data by solving for antenna-dependent delays and delay-rates. This is known as Global Fringe Fitting (Schwab & Cotton 1983).

Parallactic angle

For antennas on altazimuth mounts, the variation of the parallactic angle with hour angle causes the antenna response pattern to rotate on the sky. This parallactic angle can be expressed as follows (Taylor et al. 1999):

$$\chi(t) = \arctan\left(\frac{\cos\lambda\sin(h(t))}{\sin\lambda\cos\delta - \cos\lambda\sin\delta\cos(h(t))}\right) \tag{1.26}$$

where δ is the source declination, $h(t)$ is the source hour angle and λ is the latitude of the antenna.

Due to the nature of VLBI observations, the large baselines between antennas result in different parallactic angles, which then introduce an additional phase that needs to be corrected.

Ionospheric correction

Forming the uppermost part of the earth's atmosphere is the ionosphere which is ionised by the sun and, consequently, undergoes diurnal and seasonal changes. The ionospheric plasma, characterized mainly by its content of free electrons and ions, delays the signal coming from the observational source. Because of the large distances between antennas, in VLBI observations the effect that the ionosphere has on the observational phases needs to be taken into account, specially at low GHz frequencies.

Changes in the electron content (TEC) of the ionosphere along the line of sight introduce phase errors and measurements of this quantity are, therefore, extremely important in radio interferometry. TEC is mathematically defined as:

$$\mathrm{TEC} = \int_0^{h_0} N \cdot dh \tag{1.27}$$

where N is the number of electrons, h is the coordinate of propagation of the wave, an h_0 is the value that represents the end of the ionosphere.

This quantity describes the number of electrons in a column along the ray path of one square meter cross section. As stated above, it depends on multiple factors, such as local time, location, season, and solar activity. However, five different ionospheric models are available each day through NASA's crustal dynamics data interchange system (CDDIS). With this model, one can estimate the excess delay of a radio wave propagating through the ionosphere:

$$\Delta\tau_{\mathrm{ion}} = \pm\frac{\kappa}{c\nu^2} \cdot \mathrm{TEC} \tag{1.28}$$

with a positive sign for the group delays and a negative sign for phase delays, and where $\kappa \approx 40.3 \left(\mathrm{m}^3\mathrm{s}^2\right)$, ν is the frequency in Hz, and c is the speed of light in meters per second.

Once our VLBI data has been calibrated both in amplitude and in phase, the ionospheric effect has been taken into account, and the parallactic angle has been corrected, we can proceed to image our sources.

1.4 Imaging

1.4.1 Imaging VLBI data

The technique known as hybrid mapping allows us to, iteratively, obtain the model that best fits our observational data. The process of hybrid mapping iterates two different techniques: image deconvolution and self-calibration.

Firstly, since the number of visibilities in the uv plane is finite, the Fourier transform of Eq. 1.13 that would yield the intensity distribution $I(x, y)$, can only be evaluated at the measured uv points. That is, the first model of the intensity distribution is obtained by applying the discrete Fourier transform to the visibilities, $I_D(x, y)$

$$I_D(x, y) = \int_{-\infty}^{+\infty} \int_{-\infty}^{+\infty} W(u, v)V(u, v)S(u, v)e^{-i\frac{2\pi\nu}{c}(ux+vy)}dudv \tag{1.29}$$

where $W(u, v)$ is the weighting function that we shall describe later, and $S(u, v)$ is known as the sampling function with value of one where there is visibility data and of zero in the rest of the uv plane. Before gridding the image, each visibility is multiplied by a certain weight. There are a great number of weighting functions: natural, uniform, radial, Briggs, etc. The two more widely used are the natural weighting and the uniform weighting. The first one gives constant weights to all visibilities (inversely proportional to the noise variance of a visibility) and provides optimum sensitivity and good SNR, but lower angular resolution. The latter gives a weight inversely proportional to the sampling density function and, therefore, provides better resolution although with a higher rms image noise.

The function $I_D(x, y)$ is known as the dirty map while the Fourier transform of the sampling function is known as the diry beam:

$$B(x, y) = \int_{-\infty}^{+\infty} S(u, v) e^{-i\frac{2\pi v}{c}(ux+vy)} du dv \tag{1.30}$$

This is our first in the imaging procedure. Once we have obtained the dirty map, we must compensate the insufficient coverage of the *uv* plane. The most commonly used algorithm for this, although certainly not the only one, was developed by Jan Högbom in 1974 and is known as CLEAN. The steps provided here are a schematic view of this image deconvolution technique:

1. Find the point of maximum emission on the dirty map.
2. Subtract the dirty beam from the dirty map, centered on the coordinates of the point of maximum intensity and multiplied by a gain factor. We will now save both the coordinates of the point of maximum intensity and the gain value of the scaled intensity.
3. Repeat last step until negative residuals are comparable to positive residuals.
4. Convolve the entire set of coordinate values of maximum emission peaks and gain values with the clean beam. This ideal beam is a Gaussian with FWHM equal to the FWHM of the central lobe of the dirty beam.

After this iterative process, we now have what is known as the clean map of our source. However, there are still calibration errors and noise in our image that we need to treat. This is done in the self-calibration part.

Phase self-calibration consists in minimizing the difference between observed phases and model phases based on a trial image (Cornwell 1995; Walker 1995). In practice one must minimize the following expression:

$$\chi^2 (g_1, \ldots, g_n) = \sum_{i<j}^{N} \omega_{ij} \left| V_{ij}^{obs} - g_i g_j^* V_{ij}^{\mathrm{mod}} \right|^2 \tag{1.31}$$

where g_i is the gain of the antenna *i*, *N* is the number of antennas, ω_{ij} represent the baseline weights, and V_{ij}^{obs} and V_{ij}^{mod} are the observed and model visibilities for the baseline ij, respectively. We then apply these gain corrections obtained to the initial data set to improve the quality of the visibilities. Once the self-calibration has ended, we can now start again the cycle of deconvolving and self-calibrate until a convergent model is reached.

Self calibration should only be done if the target source has sufficient SNR in the self calibration time interval, otherwise one may introduce artificial sources in the data. If the target is not sufficiently strong for self-calibration, then an alternative approach must be followed. This approach consists in observing a phase reference source frequently during the observing time. A calibrator source that must be within a few degrees of the target region, ideally unresolved, and with enough flux density to obtain a good signal-to-noise in a short time. This technique is known as phase-referencing and can be sum up in the following steps: i) observe in an alternative fashion both the target and calibrator source ii) estimate the antenna gains using only the calibrator data, iii) interpolate these gain solutions from the calibrator onto the target data.

1.4.2 Fitting and imaging infrared interferometric data

Although the ultimate goal of interferometry is to have sufficient data quality and *uv* coverage to make a synthesis image, this is not always possible, specially at IR wavelengths and one may have to be content with fitting a model to the visibility data. This rarely happens in radio nowadays.

Fitting visibilities

The first step in this process consists in creating a model and compute its visibilities. One can use geometrical models without any physics involved, such as point sources, Gaussians, or uniform disks or, alternatively, physical models that allow to connect the observed data with physical quantities like densities and temperatures. It is worth noting that size scales can be extracted with any of these two types of model. As an illustrative example, the visibility of a uniform disk (UD) with diameter Θ can be expressed as:

$$V(u, v) = 2\frac{J_1(\pi\Theta r)}{\pi\Theta r} \tag{1.32}$$

where $r = \sqrt{u^2 + v^2}$. A visual illustration of this can be found in Fig. 1.11.

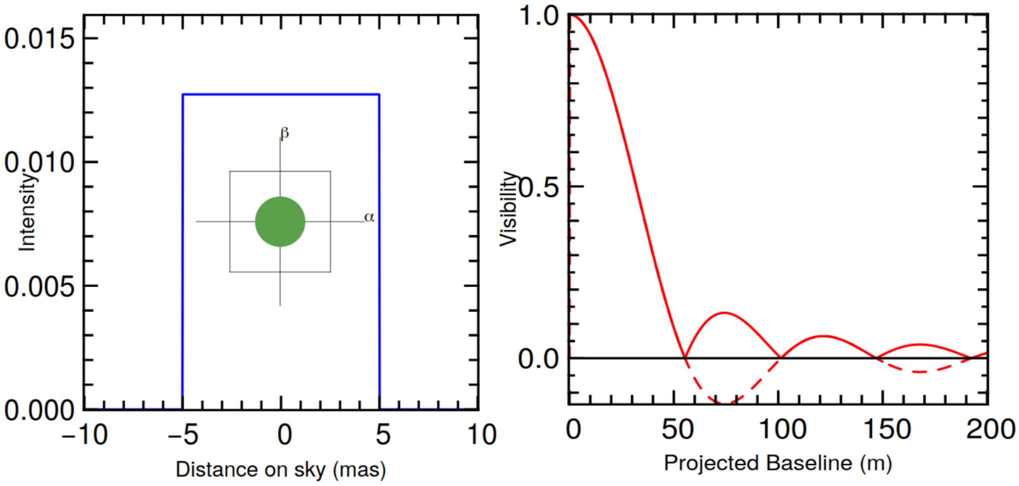

Figure 1.11: Left: brightness distribution of a uniform disk model with Θ = 10 mas. The green disk would represent the geometrical shape while the blue line would represent a radial cut across the brightness distribution. Right: Corresponding visibility curve as a function of baseline for $\lambda = 2.4$ μm. The dashed red line is complex visibility amplitude while the solid red line is the visibility amplitude. Credit: Berger & Segransan (2007).

With the visibilities of the model constructed the next step is to fit the various parameters (size, distance, density...) to the observational data. For this one can use an in-house software or other alternatives like LITpro (Lyon Interferometric Tool prototype), developed by the Jean-Marie Mariotti Center (JMMC, Tallon-Bosc et al. 2008). In some cases due to the quality of the data it is impossible to distinguish between some models, e.g.: without long enough baselines a uniform disk and a Gaussian may yield the same results. In such cases, it is useful to make use of the previous knowledge of the object, e.g.: in the IR regime, a G star should closely resemble a UD while in the sub-mm regime a young stellar object may be better fitted by a Gaussian. This has been a mere overview of the fitting process. For an in-depth introduction, the reader is encouraged to read Berger & Segransan (2007).

Imaging infrared interferometric data

As pointed out in Sect. 1.4.1, the CLEAN technique uses the phases in order to create a model of the intensity image. However, in the IR domain atmospheric turbulence changes the fringes phases so quickly that phase referencing is not practical. Although one can use the visibilities amplitudes to fit some models and extract information (as we have just discussed), an alternative method allows us to recover some of the lost phase information.

In order to image our data, we must construct the observable known as closure phases. These observables are independent of phase shifts caused by the instruments and the atmosphere and are formed by summing the visibility phases around a triangle of baselines (see Fig. 1.12).

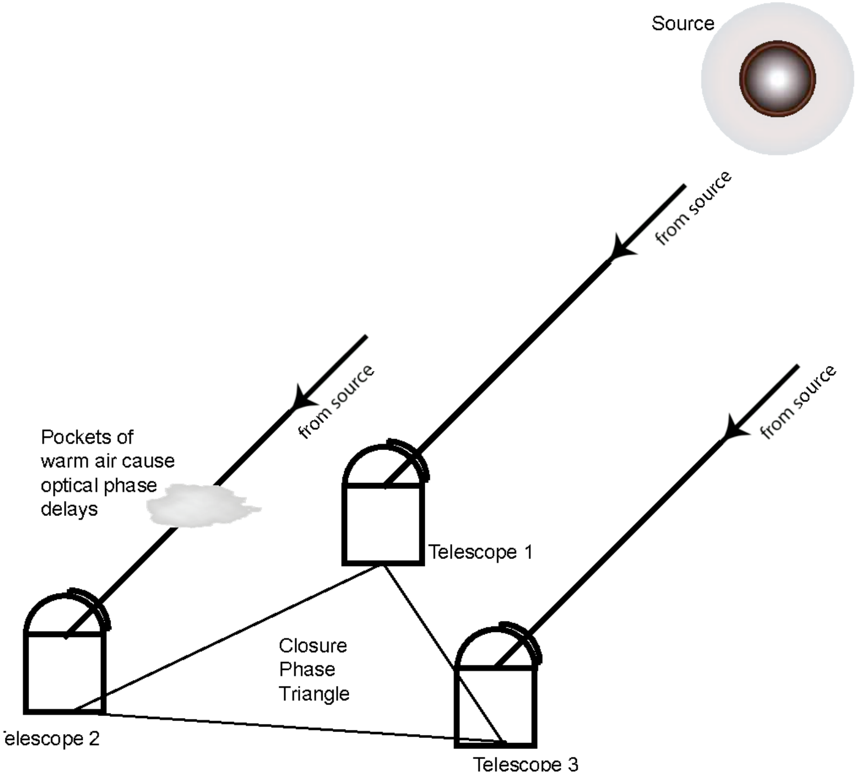

Figure 1.12: Telescope geometry for closure phase measurement. Credit: Monnier et al. (2006)

Let φ_{ij} be visibility phase measured by the baseline ij and expressed as:

$$\varphi_{ij} \equiv \phi_i - \phi_j + \theta_{ij} \tag{1.33}$$

where

$$\theta_{ij} = \vec{B}_{ij} \cdot \vec{S} + \psi_{ij} \tag{1.34}$$

with $\vec{B}_{ij}$ being the baseline vector between telescopes ij, $\vec{S}$ the unit vector in the direction of the source, and ψ_{ij} the contribution of the structure of the source.

The closure phases are then:

$$\begin{aligned}
C_{ijk} &= \varphi_{ij} + \varphi_{jk} + \varphi_{ki} \\
&= \left(\phi_i - \phi_j + \theta_{ij}\right) + \left(\phi_j - \phi_k + \theta_{jk}\right) + (\phi_k - \phi_i + \theta_{ki}) \\
&= \theta_{ij} + \theta_{jk} + \theta_{ki} \\
&= \left(\vec{B}_{ij} + \vec{B}_{jk} + \vec{B}_{ki}\right) \cdot \vec{S} + \psi_{ij} + \psi_{jk} + \psi_{ki} \\
&= \psi_{ij} + \psi_{jk} + \psi_{ki}
\end{aligned} \tag{1.35}$$

and, indeed, is an observable independent of any instrumental effects and dependent on the structure of the source.

As promised, the closure phases can recover some of the lost phase information. Take, for example, a 3 telescope array. We can only construct one closure phase but we had 3 Fourier phases available using phase referencing. However, if one considers an array with 7 telescopes the number of independent closure phases increases to 70% of the total Fourier phases available through phase referencing (15 out of 21). An array like the VLA with 27 antennas would be able to recover 93% of the phase information through the use of closure phases. Note, however, that astrometry requires phase-referencing. For the interested reader, more detailed information on using the closure phases on optical/IR interferometry can be found in Monnier (2007).

In order to obtain an image, algorithms like BSMEM (Buscher 1994), MACIM (Ireland et al. 2006), MIRA (Thiébaut 2008), WISARD (Meimon et al. 2008) and SQUEEZE (Baron et al. 2010) make use of the closure phases and/or other observables such as the bispectrum and closure amplitudes. The bispectrum is formed through triple products of the complex visibilities around a closed triangle (Weigelt 1977). The closure amplitude uses 4 telescopes and can be used to compensate for unstable amplifier gains and varying antenna efficiencies (Readhead et al. 1980). A comparison between these algorithms can be found in Malbet et al. (2010).

Chapter 2

Stellar radio emission

The study of radio emission opens a new window for probing the universe, as it contains telltale information exclusive to this wavelength regime. In particular, stellar radio emission traces a wide variety of phenomena: magnetic reconnection in the stellar corona, stellar winds, disks and radio jets in pre-main sequence stars, interacting binaries, and auroras in brown dwarfs, to name a few (see Güdel 2002, for a review). Our Sun occupies a privileged and dominant place in the radio astronomy literature, as detailed and even *in situ* observations are plausible in this case (for reviews on this subject see Dulk 1985; Bastian et al. 1998). Several types of thermal, incoherent types of radio emission are known to occur in our Sun: thermal bremsstrahlung from the chromosphere, gyroresonance emission above active regions, blackbody radiation, and coronal bremsstrahlung near coronal loops (Gary & Hurford 1994). Additionally, the activity of the Sun produces flares dominated by gyrosynchrotron, plasma, and electron cyclotron maser radiation.

Beyond our Sun, the first radio stars surveyed were the numerous and nearby M dwarfs. However, these studies soon expanded to K stars, late-type binaries, solar analog G stars, RS Canun Venaticorum (RS CVn) and Algol-type binaries, T Tauri stars (TTSs), chemically peculiar Ap/Bp stars, and O, B and Wolf-Rayet (WR) stars (Güdel 2002, and references therein). The structure and evolutionary phase of each of these objects are closely associated with the features of their radio emission. Let us give a brief overview of the responsible mechanisms that are expected to occur on each of these objects and, following this discussion, we will detail the most relevant radiation mechanisms for this thesis. An in depth discussion of all the mechanisms presented here can be found in Güdel (2002).

2.1 Radiation mechanisms

Stellar radio emission is typically classified as continuum or line emission. During our work, the most relevant radio emission is the continuum one, which in turn, can be divided into *thermal emission* and *non-thermal emission*. The former occurs when the emitting particles have a thermal equilibrium distribution of energies while the latter is associated to particles with a non-thermal equilibrium distribution of energies. The most common thermal mechanisms are *bremsstrahlung* or free-free emission, and gyroresonance emission or cyclotron whereas gyrosynchotron, and synchrotron emission are the most common non-thermal mechanisms (for a detailed discussion on thermal and non-thermal radiation see Rybicki & Lightman 1979).

Bremsstrahlung emission

When a charged particle is deflected by another charged particle is decelerates and this loss of kinetic energy is emitted as electromagnetic radiation (see Fig. 2.1). This emission is known as Bremsstrahlung or free-free emission.

Simplified expressions for the emission and absorption coefficients derived from Dulk (1985) can be found in Güdel (2002). These expressions are valid for free-free emission in a thermal plasma, assuming a cosmic abundance of 90% H and 10% He, and for frequencies much greater than the plasma frequency. The absorption coefficient is given by:

$$\kappa_\nu \approx 0.01 n_e^2 T^{-3/2} \nu^{-2} \times \begin{cases} \ln\left(5\times10^7 T^{3/2}/\nu\right), T \leqslant 3.2\times10^5\mathrm{K} \\ \ln\left(4.7\times10^{10} T/\nu\right), T > 3.2\times10^5\mathrm{K} \end{cases} \tag{2.1}$$

where T = T_{eff}, the upper equation is used for singly ionized species and the lower

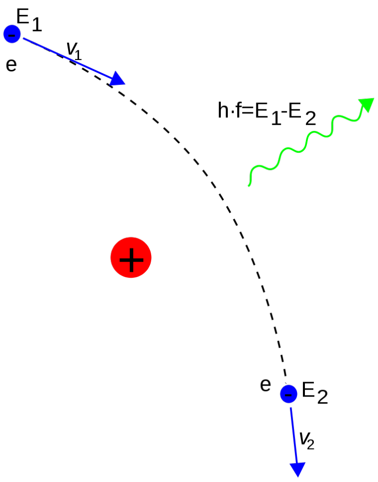

Figure 2.1: Sketch of free-free emission occurring as the electric field of an atomic nucleus deflects a moving electron with initial energy E_1 and final energy E_2.

equation for fully ionized plasma. The emissivity is, in turn, given by:

$$\frac{\eta_\nu}{\kappa_\nu} = \frac{2kT_{\text{eff}}\nu^2}{c^2} \tag{2.2}$$

In the optically thick regime, bremsstrahlung emission presents a ν^2 dependence. Meanwhile, optically thin flux is nearly independent of the frequency with a $\nu^{0.1}$ dependence.

Gyrosynchrotron emission

When electrons are in presence of magnetic fields, they travel drawing circles or spirals around the field lines. Due to this movement, an angular acceleration is produced which induces emission of energy. Depending on the speed of the electrons ($\gamma = 1/\sqrt{1-(v^2/c^2)}$), this emission is known as cyclotron, gyrosynchrotron or synchrotron emission for non-relativistic ($\gamma \approx 1$), mildly relativistic ($\gamma \leq 2-3$) or ultra-relativistic ($\gamma \gg 1$) electrons, respectively.

For non-relativistic electrons, the gyrofrequency is given by:

$$\nu_e \equiv \frac{\omega_e}{2\pi} = \frac{eB}{2\pi m_e c} \approx 2.8 \times 10^6 B \quad [\text{Hz}] \tag{2.3}$$

where e is the electron charge, m_e is the electron rest mass, B is the magnetic field (in Gauss) and c is the speed of light.

In the relativistic case, the gyrofrequency is:

$$\nu_{e,rel} = \nu_e/\gamma \tag{2.4}$$

The various parameters of the gyrosynchrotron emission (mainly the emission and absorption coefficients) can be found in Ramaty (1969). These expressions are fairly complex since no simplifications of the non-relativistic and ultrarelativistic limits are made. Using the previous work of Dulk (1985), Güdel (2002) simplied the expressions for the emission and absorption coefficients for the case of an angle between the line of sight and the magnetic field equal to $\pi/3$.

The Güdel's expressions presented here are valid under two asumptions:

1. A gas in which the emitting electrons have an isotropic pitch angle distribution and a power-law distribution in energy given by:

   $$N(E)dE = CE^{-p}dE \tag{2.5}$$

   where p is the electron power-law index and C is a quantity that varies with pitch angle

2. A range of $2 \leq p \leq 7$ and $10 \leq \nu/\nu_e \leq 100$

Under this assumptions, the expressions are:

$$\begin{aligned} j_\nu &\approx 10^{-31.32+5.24p} N B^{-0.22+0.90p} \nu^{1.22-0.90p} \\ \alpha_\nu &\approx 10^{-0.47+6.06p} N B^{0.30+0.98p} \nu^{-1.30-0.98p} \end{aligned} \tag{2.6}$$

where N is the total non-thermal electron number density above the low-energy cutoff E_0 = 10keV = 1.6×10^{-8} ergs.

These expressions are very useful since they inform us that the spectral index $\alpha \sim 1.22 - 0.9\ p$ at the optically-thin regime and, approximately, 5/2 at the optically-thick regime. Combining the two spectral limits, one can obtain the spectrum of a source with a power-law distribution (see Fig. 2.2).

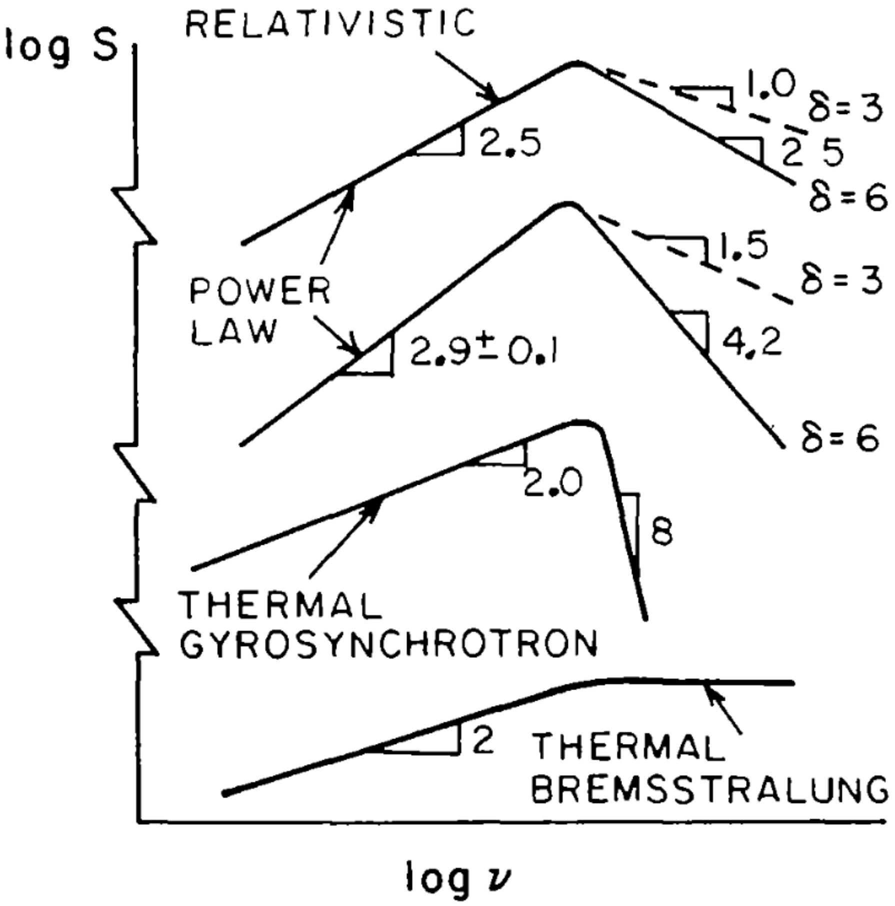

Figure 2.2: Schematic spectra of flux density for various mechanisms. From top to bottom: gyrosynchrotron for a power-law distribution of highly relativistic electrons, gyrosynchrotron for a power-law distribution of mildly relativistic electrons, thermal gyrosynchrotron and bremsstrahlung emission. Credit: Dulk (1985)

The Electron Cyclotron Maser Instability

Within a plasma, high-frequency electromagnetic waves are amplified by a resonant interaction between the charged electrons within the plasma at the Doppler shifted electron cyclotron frequency (Treumann 2006). The theory behind the electron cyclotron maser instability (ECMI) was discovered independently by three physicists: Twiss (1958); Gaponov (1959); Schneider (1959).

A detail model for how the electron cyclotron maser operates can be found in Chu (2004). Here we will only discuss the underlying principle. Although it has ”maser” in its name, this phenomenon is not the result of quantum effects and inverted particle populations. The electrons participating in this mechanism are bunched together in momentum space, such that the slight detuning (instability) of the ambient electric field stimulates the electrons to emit (or absorb) radiation in a way that leads to linear amplification of the emission.

This mechanisms emits radiation at a wavelength that depends on the strength of the magnetic field and not on the dimension of some resonant cavity. It is also important to know that the ECMI emission produces coherent radiation that is detected is typically detected in radio observations as emission with very high brightness temperatures, strongly circularly polarized and with short duration.

2.2 Radio stars through the HR diagram

Due to the ionized mass loss, in the massive and young O, B and WR stars, thermal free-free emission is typically the invoked mechanism. However, ultra-relativistic electrons travelling along the magnetic fields of the wind can also produce non-thermal synchrotron emission in these stars (Abbott et al. 1984; Leitherer & Robert 1991). A dearth of radio detections is expected (and observed) in the B-F stars as a consequence of the absence of magnetic dynamo action in these objects. Only a few of them present radio emission originating at the interaction of the magnetic field with the stellar wind. One particular case of these main sequence stars are the chemically peculiar Ap/Bp stars, characterized by overabundances of some metals, and whose strong magnetic fields produce non-thermal radio emission. Finally, entering the late-type stars we find flaring stars, whose expected radio emission mechanism is gyrosynchrotron emission occurring in the intense flares.

In RS CVn, Algol-type and W Ursae Majoris stars the tidal influence of the components produces an intense mass loss and, consequently, a strong stellar wind in both components. It is the collision of these winds that is thought to produce the non-thermal gyrosynchrotron emission detected in these objects.

T Tauri stars typically display great activity in terms of magnetism and variability and rotate with a period of a few days. This rapid rotation and the youth of these objects, along with the fact that most TTSs are fully convective, is thought to produce strong magnetic fields and, consequently, radio emission. If a circumstellar disk is still present, free-free radio emission could occur from the ionized gas of this disk. As a consequence of the magnetic reconnection that may occur on magnetic loops, TTSs may also present flaring events (López-Santiago et al. 2016) and magnetospheric accretion bursts (Alencar et al. 2012; Stauffer et al. 2014). More evolved than TTSs but within the pre-main sequence (PMS), low-mass K and M stars also display radio emission triggered by a dynamo mechanism induced by the very fast rotation of these objects. This radio emission is thought to originate due to mildly relativistic electrons spiraling around the magnetic field lines and radiating gyrosynchrotron emission.

2.3 Radio emission in ultracool dwarfs

With the CCD revolution it became possible to systematically study the coolest, lowest-mass objects: the ultra-cool dwarfs (UCDs). From the first observational studies (Basri & Marcy 1995; Drake et al. 1996) it quickly became a consensus that magnetic activity faded out in the UCDs. The explanation was thought to be related to the loss of the tachocline, the shearing layer between a star's radiative inner core and its convective outer envelope. With such low masses, UCDs would not posses a tachocline and, consequently, it would be very difficult to explain any strong magnetic field in these objects (Mohanty et al. 2002).

These first results, however, would soon be challenged by the detection of flares from very late M dwarfs in the ultraviolet (Linsky et al. 1995), Hα (Reid et al. 1999; Liebert et al. 1999), and X-ray (Fleming et al. 2000). It was the detection of another X-ray flare from LP 944-20, a M9.5 object (Rutledge et al. 2000), what triggered VLA observations of this object and the detection of both bursting and quiescent radio emission (Berger et al. 2001). The detection of quiescent emission demonstrated that: (i) UCDs can generate stable magnetic fields and (ii) they can source the highly-energetic, non-thermal electrons needed to produce observable radio emission.

Since this discovery, radio observations have been the best available tool to probe the magnetism in the UCD regime. They have revealed both bursting and non-bursting emission. The former in the form of bright, circularly polarized radio bursts at GHz frequencies which are thought to be related to synchrotron emission mechanisms in some cases (e.g. Berger et al. 2001) or ECMI emission in others (e.g. Burgasser & Putman 2005; Hallinan et al. 2007). The latter is generally steady over the timescales of individual observations, usually about an order of magnitude fainter than the peak observed burst luminosity, and with low or moderate circular polarization. It is consistent with gyrosynchrotron emission and as such its spectrum is broadband, peaking around 1-10 GHz and with shallow spectral indices on both sides of the peak.

The rotation of the UCD seems to be an important magnitude both in some bursting and non-bursting detections. In the non-bursting cases, it has been observed that the circular polarization measured may vary with the rotation period of the UCD (see Fig. 2.3 Williams et al. 2015).

In many cases the bursts have been observed to have certain periodicity, a periodicity that matches that of the rotation period. An exceptional example of this case is the L dwarf binary LSPM J0746+2000 (see Fig. 2.4; Berger et al. 2009).

Past radio surveys of UCDs only detected about 10% of the objects studied (Berger 2006; McLean et al. 2012; Antonova et al. 2013; Lynch et al. 2016). However, this detection rate could have been higher it the authors employed biased surveys as proposed by Kao et al. (2016): select dwarfs with prior Hα detection and/or optical variability. Following this strategy the authors detected 4 out of 5 late-L and T dwarfs. Additionally, when considering this 10% number one must take into account that the radio detectability of individual objects varies over time in a not yet well-understood manner.

Finally, radio studies of UCDs are the only effective way to observe the magnetic properties of cool, extrasolar bodies and, as such, are in a privileged position for contributing to exoplanetary science. While no exoplanet has been yet detected at radio wavelengths, understanding the phenomenology and the physical mechanisms involved in the radio emission of UCDs is crucial for planet discovery around them (Robertson et al. 2014)

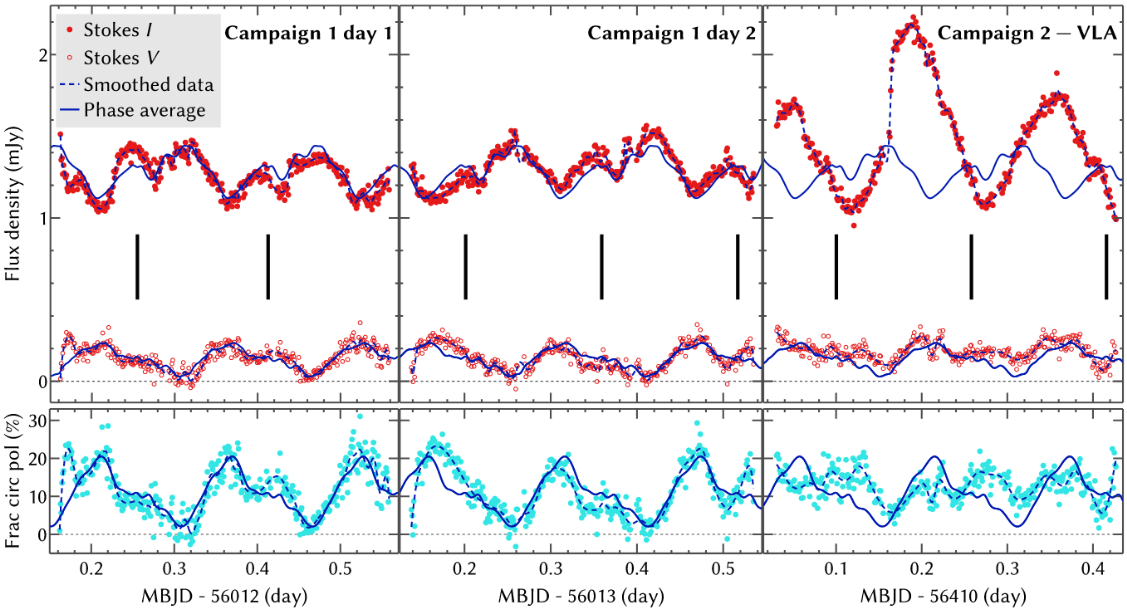

Figure 2.3: Radio light curve of NLTT 33370 B showing periodic variation and moderate polarization in the non-bursting radio emission. In the upper panels, filled and empty points show Stokes I and V components, respectively. The lower panels show the fractional circular polarization derived from these values. Vertical black lines indicate times that the dwarf's periodically-modulated optical emission reaches maximum. Credit: Williams et al. (2015)

and for the atmosphere and habitability of these planets (Jakosky et al. 2015; Shields et al. 2016) which could be abundant and observationally accessible (e.g. TRAPPIST-1 system, see Gillon et al. 2016, 2017).

2.4 Radio emission in RSGs

Since the first detection of radio emission from a RSG (Kellermann & Pauliny-Toth 1966), the field of radio emission in RSGs has seen an increasing amount or research both observationally and theoretically. For completeness, we will present here some remarkable results.

In thermodynamic equilibrium, the spectral radio flux density can be obtained using

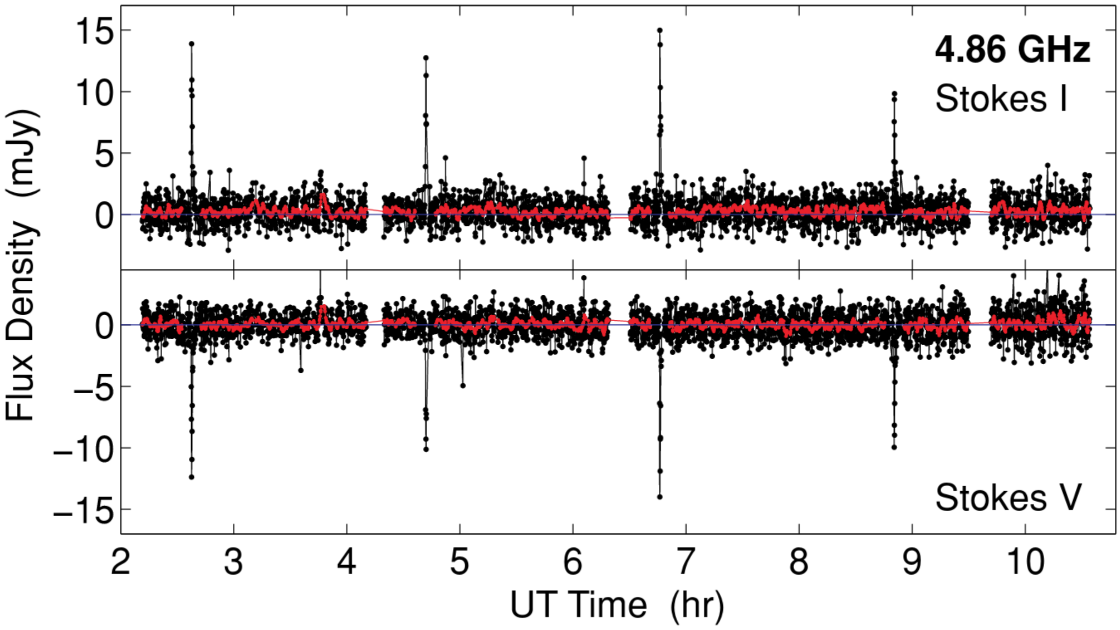

Figure 2.4: Radio Light curve of LSPM J0746+2000 showing periodic, highly polarized bursts. The black and red points show the data averaged into 5- and 60-second bins, respectively. In this case, the bursts have ~100% left circular polarization with a periodicity of ~2 hours. Credit: Berger et al. (2009)

the Rayleigh-Jeans approximation on the Planck function:

$$S_\nu = \frac{2kT_b\nu^2}{c^2}\frac{A}{d^2} \approx 0.1\left(\frac{T_b}{10^6\mathrm{K}}\right)\left(\frac{\nu}{1\mathrm{GHz}}\right)^2\left(\frac{r}{10^{11}\mathrm{cm}}\right)^2\left(\frac{1\mathrm{pc}}{d}\right)^2 \mathrm{mJy} \tag{2.7}$$

where T_b is the brightness temperature. Since the outer atmospheres of RSGs are optically thick at radio wavelengths, $T_b = T_{eff}$, and so spatially resolved observations can act as an approximate linear thermometer. Indeed, this method has been successfully applied to Betelgeuse (O'Gorman et al. 2017, and references therein) showing that the mean gas temperature of Betelgeuse's extended atmosphere declines from ~ 3600 K at $2R_\star$ to ~ 1400 K at $6R_\star$ (see Fig. 2.5). The same authors obtained a high-resolution continuum image of this RSG using the Atacama Large Millimeter/submillimeter Array (ALMA) discerning the thermal structure, including a region ~ 1000 K brighter than the mean disk, indicating localized heating (see Fig. 2.6).

The great mass loss rates that are seen in RSGs imply the presence of strong winds

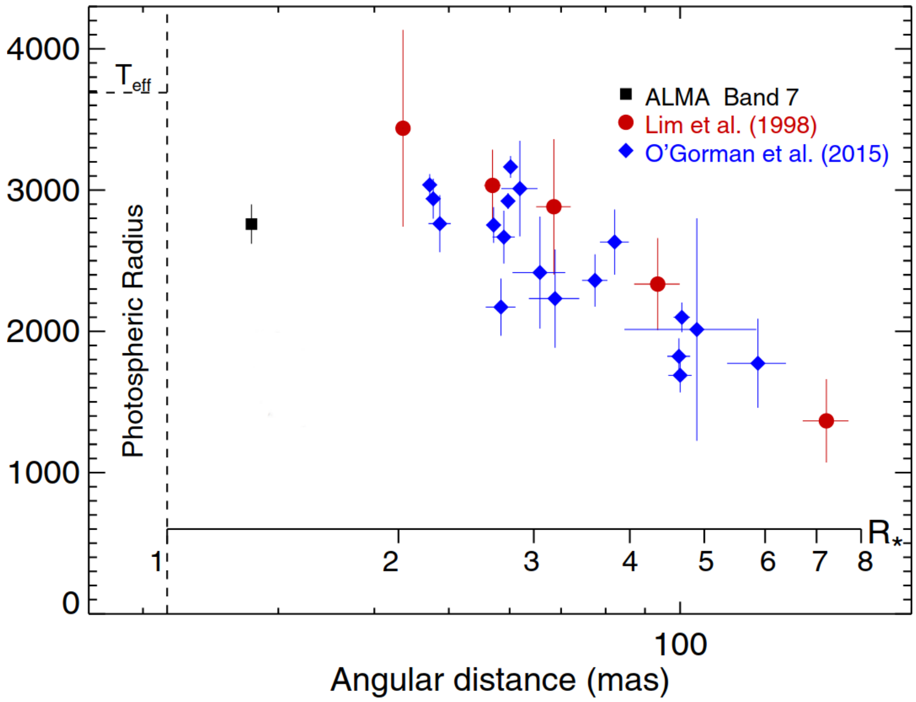

Figure 2.5: Temperature profile of Betelgeuse's extended atmosphere. The red filled circles, blue filled diamonds, and black filled square represent the gas temperature derived from spatially resolved radio observations by Lim et al. (1998). O'Gorman et al. (2015), O'Gorman et al. (2017), respectively. Credit: adapted from O'Gorman et al. (2017)

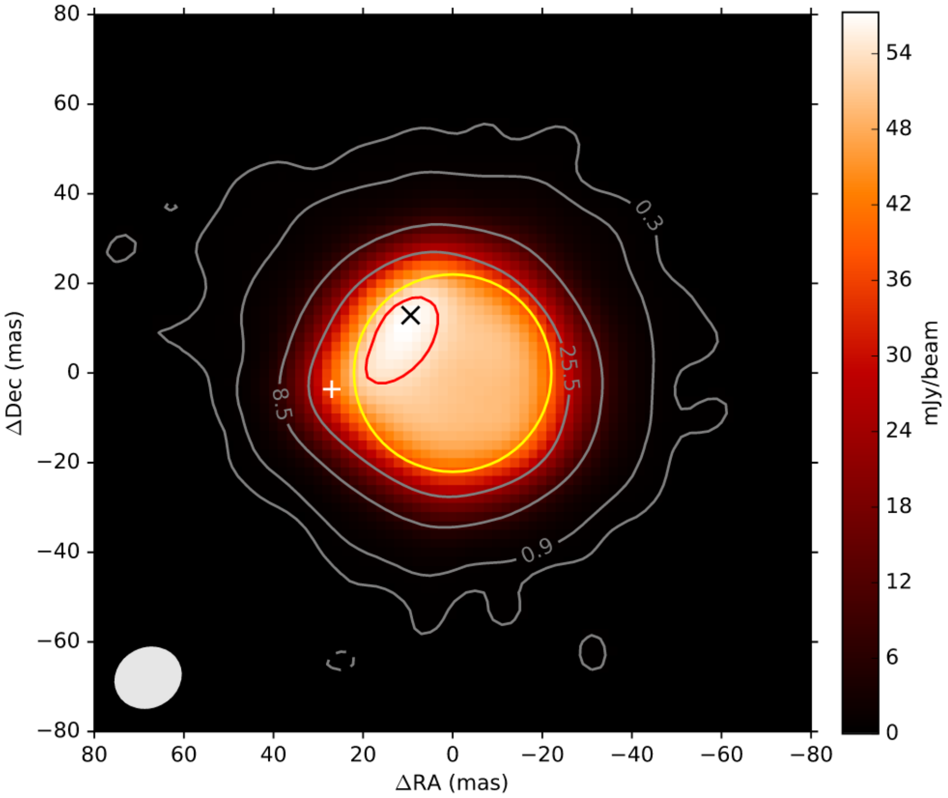

Figure 2.6: ALMA 338 GHz continuum image of Betelgeuse. The numbers within the contours are the flux density values in mJy. The yellow circle is the size of the infrared H-band photosphere from Montargès et al. (2016). The authors detected a clear peak in the north-east direction (marked with a cross) and an east-extension (marked with a plus sign). Credit: O'Gorman et al. (2017).

in these objects. As explained in Sect. 3.3, the mechanisms that drive the stellar winds remain uncertain and the study of RSG winds and outflows based on the detailed analysis of circumstellar masers can supply constraints on models for the shaping and acceleration of such winds.

A wide variety of maser transitions lie within bands accessible with ALMA. Observed with high enough angular resolution, these lines can help us to constrain the kinematics and physical conditions (such as temperature or density) across the extended atmospheres of RSGs (see Gray et al. 2016). Some notable work done in this area comes from Richards et al. (2014). The authors found that although the maser distribution is broadly consistent with excitation models (see Fig. 2.7), phenomena such as wind collisions, clumping, and asymmetries complicates the conditions and the kinematics. Since this topic is beyond the reach of this dissertation, the interested reader is encouraged to read this brief review of masers around evolved start that can be found in Richards (2012) and references therein.

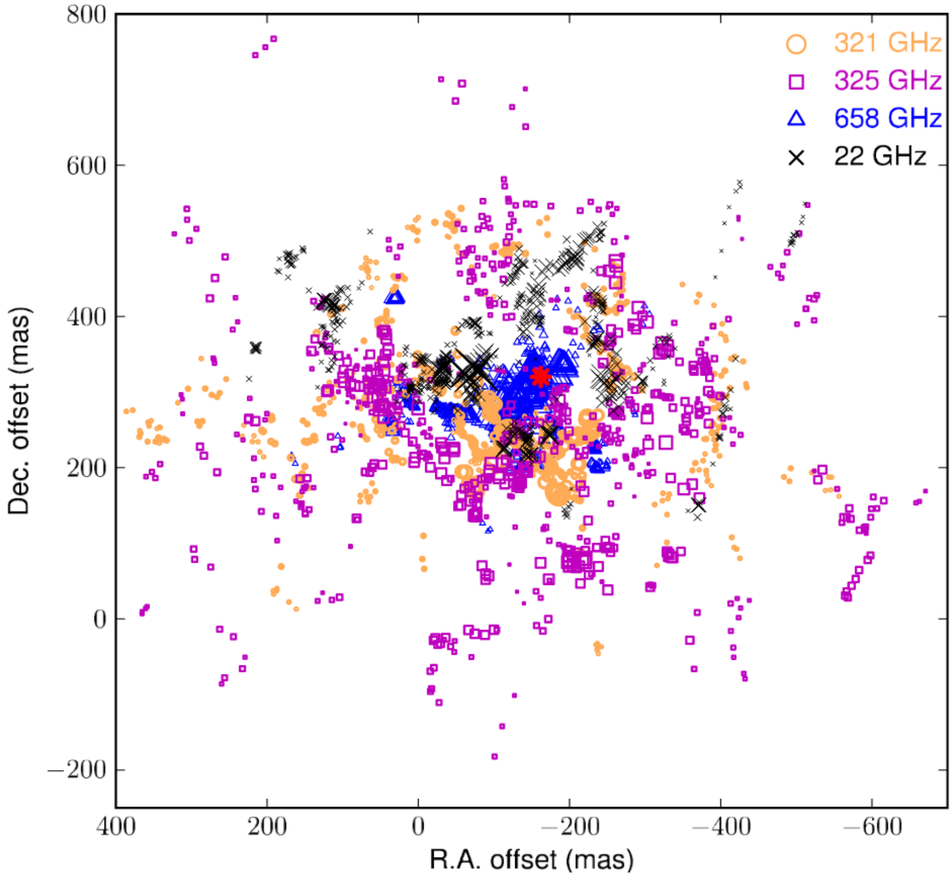

Figure 2.7: Relative positions of all imaged maser components of VY CMa. The RSG is represented as a red star. The maser symbol size proportional to $\sqrt{flux\,density}$. Credit: Richards et al. (2014).

Chapter 3

Objects of study

3.1 The AB Doradus system

Located approximately 15 pc away from us, the AB Doradus (AB Dor) system was first discovered as a single star, AB Dor. This K0 dwarf star is a fast rotator (period of ~0.51 days; Innis et al. 1988) that presents strong emission at all wavelengths, from radio (Slee et al. 1984, 1986; Lim et al. 1992; Guirado et al. 1997, and more recent observations) to X-rays (Lalitha et al. 2013; Drake et al. 2015, and references therein). Subsequent observations (Innis et al. 1985) associated the young low-mass star, Rossiter 137B (separated by $9''$), to AB Dor and renamed them as AB Dor B and AB Dor A, respectively. Infrared observations revealed that AB Dor B is a tight binary itself (Close et al. 2005) separated by an angular distance of $0.06''$(Guirado et al. 2006) : AB Dor Ba and AB Dor Bb, with spectral types M5 and M5-6, respectively (Close et al. 2007). Finally, VLBI and Hipparcos data revealed the presence of a low-mass companion to AB Dor A, AB Dor C (0.090 $M_{\odot}$; Guirado et al. 1997) orbiting AB Dor A at an average angular distance of $0.2''$(see Fig. 3.1). These pairs (AB Dor A/C and AB Dor Ba/Bb) are of great importance since stellar evolution models (used to infer fundamental parameters of objects such as radius, mass and/or age) require dynamically determined masses and, in the case of low and very low-mass stars, only a few have been reported (e.g. Hillenbrand & White 2004; Stassun et al. 2004; Mathieu et al. 2007).

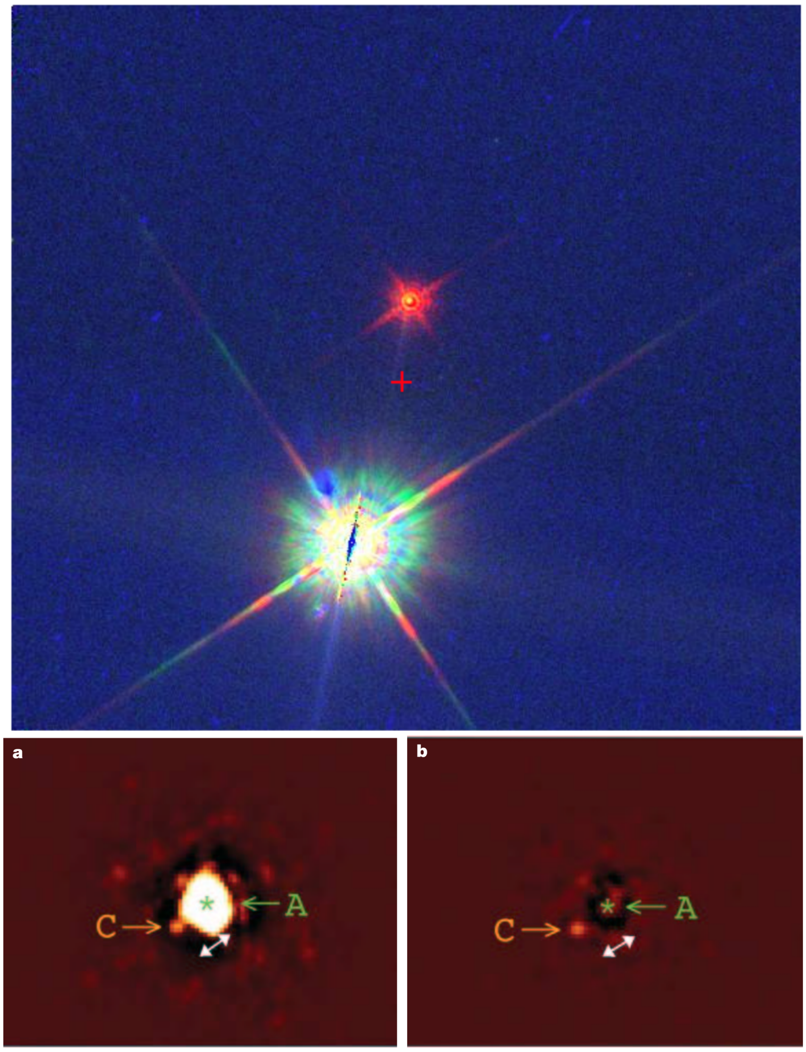

Figure 3.1: The AB Doradus system. The top panel shows the binary AB Dor A/B with the main star at the bottom. The image was taken by the instrument WFPC2 of the Hubble Space Telescope (HST). The bottom panel shows the discovery image of AB Dor C with the VLT NACO SDI high contrast camera (**a**) and the same image after subtraction of the scattered light from AB Dor A (**b**). Credits: HST archive and Close et al. (2005).

Interestingly, the AB Dor quadruple system gives name to the closest group of coeval stars that move coherently through the galaxy: the AB Doradus moving group (AB Dor MG Zuckerman et al. 2004; Malo et al. 2013; Gagné et al. 2014). With approximately 90 bona fide members (although this number is subjected to change) across the northern and the southern hemispheres, this moving group would have a radius of about 100 pc were the position of the members be approximated by a sphere (Fig. 3.2; Torres et al. 2008). Although a few A, B and M spectral type objects have been discovered in this moving group, the majority of the members are of spectral type F, G, or K, with very short rotation periods and active chromospheres.

The exact age of both the moving group and the AB Dor system are a current subject of discussion. Let us focus on the system we will be studying in detail. Some of the estimates for the age of AB Dor are: 40–50 Myr for AB Dor A and 25–120 Myr for AB Dor C in Azulay et al. (2017), 40-60 Myr in Zuckerman et al. (2004) and López-Santiago et al. (2006), 30-100 Myr in Close et al. (2005), 40-100 Myr in Nielsen et al. (2005), 75-150 Myr in Luhman & Potter (2006), 50-100 Myr in Janson et al. (2007) and Boccaletti et al. (2008), 40-50 Myr in Guirado et al. (2011), >110 Myr for the AB Dor nucleus star in Barenfeld et al. (2013) and 130-200 Myr in Bell et al. (2015).

3.1.1 Radio emission in the AB Doradus system

Slee et al. (1984) were the first to detect radio emission from AB Dor system, finding a clear modulation in its flux and continuous absence of circular polarization (Slee et al. 1986). They interpreted this modulation as spot groups on the star that may have lifetimes of the order of 2 years or more. A more detailed study of the modulation in radio emission (Lim et al. 1992) found that the peaks in emission coincided with the two stellar longitudes at which starspots preferentially form and detected a large spot at one of these active longitudes. These starspots were also the interpretation adopted by other authors that managed to deduce a model of them based on optical photometry and spectroscopy (see Figure 5 in Budding et al. 2009). Subsequent monitoring of the AB Dor A/C system with the Australia Telescope Compact Array (ATCA) showed a baseline flux of 2 mJy and flare events up to 8 mJy with a half-brightness duration of about 3 hours (Slee et al. 2014) indicating that the modulation is still present even 23 years after the discovery of radio emission from this star. Finally, VLBI multiepoch observations of AB Dor A and AB Dor B showed the first high resolution images of these stars as unresolved point sources (Azulay et al. 2015, 2017).

Only in a handful of cases have VLBI observations resolved the stellar radio emission of young objects. These cases, however, are of extreme importance to better understand

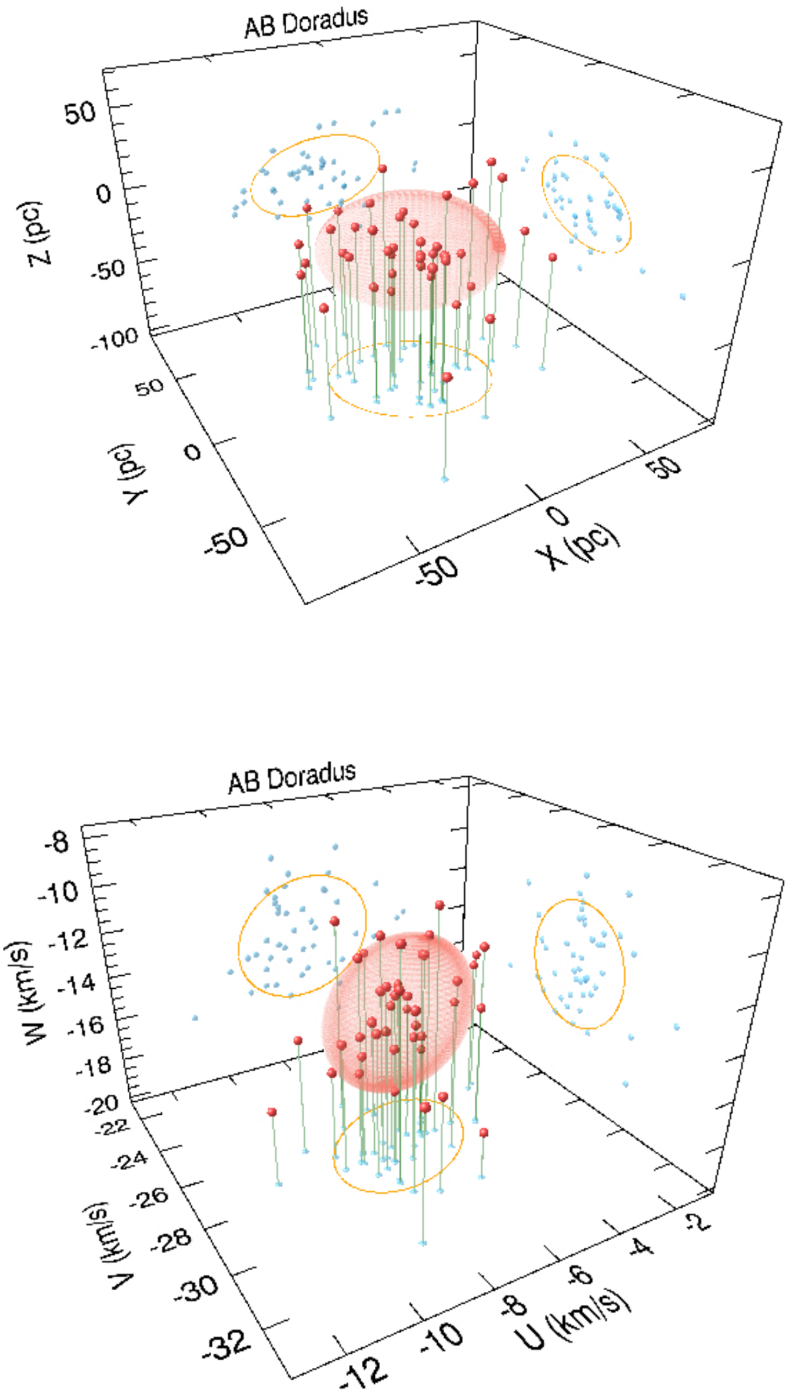

Figure 3.2: Representation of the galactic positions (top panel) and spatial velocities (bottom panel) of the well-defined members of the AB Dor MG. The red dots represent the members and the red ellipsoids represent the models. The projections of both members and models are represented by blue dots and orange ellipsoids, respectively. Credit: Gagné et al. (2014)

the different scenarios that may be present in AB Dor A. The first reported VLBI detection of a young star is from the binary star θ^1 Orionis A (Felli et al. 1989) that not only was detected but slightly resolved. From the study of six weak-lined T Tauri (WTT) stars, Phillips et al. (1991) found that the radio structure on these stars is in continuous evolution, reflected by both the changing combinations of unresolved flares within $2R_\star$ and by the presence of giant loops extending to $20R_\star$ and persisting for hours or more in the case of the variable star DoAr 21. Andre et al. (1991) found that the young binary star ρ Oph (HIP 80473) was most likely resolved, with VLBI visibilities well adjusted by a 1.7 mas diameter Gaussian. Andre et al. (1992) expanded the VLBI observations to 9 other young objects in the same molecular cloud ρ Oph, finding five detections from which the T Tauri WL 5 appeared to be resolved with extensions up to $25R_\star$. Phillips et al. (1996) presented one of the first reported VLBI images of a resolved magnetic structures in a young object, in this case the PMS multiple system HD 283447. The double radio source detected at one epoch was hypothesized to be the result of the inner binary where each star would have an active radio-emitting region of a few stellar radii. One exceptional case of resolving the magnetosphere using VLBI observations is the binary system V773 Tau A. This system exhibits a persistent radio emission that varies in intensity depending on the separation between components, indicating some interaction between the individual magnetospheres (Torres et al. 2012). Massi et al. (2008) linked this emission to solar-like helmet streamers anchored to the top of a closed loop at a few stellar radii above the stellar surface and extending up to the upper mirror points located 30 stellar radii away. Although posterior observations did not confirm the detection of these mirror magnetic points (Torres et al. 2012), the interaction between individual magnetospheres was confirmed. From all this past work, one can expect the magnetosphere of AB Dor A to be fairly complex where a variety of phenomena could occur: from coronal gyrosynchrotron emission to giant loops lasting hours, or even solar-like helmet streamers.

Other objects exhibiting extended magnetospheres include RS CVn (Massi et al. 1988; Trigilio et al. 2001; Ransom et al. 2002, 2003), Algol-like binaries (Mutel et al. 1998; Peterson et al. 2010), M dwarfs (Benz et al. 1998) and chemically peculiar Bp/Ap stars (Phillips & Lestrade 1988). The radio emission detected in these objects is believed to

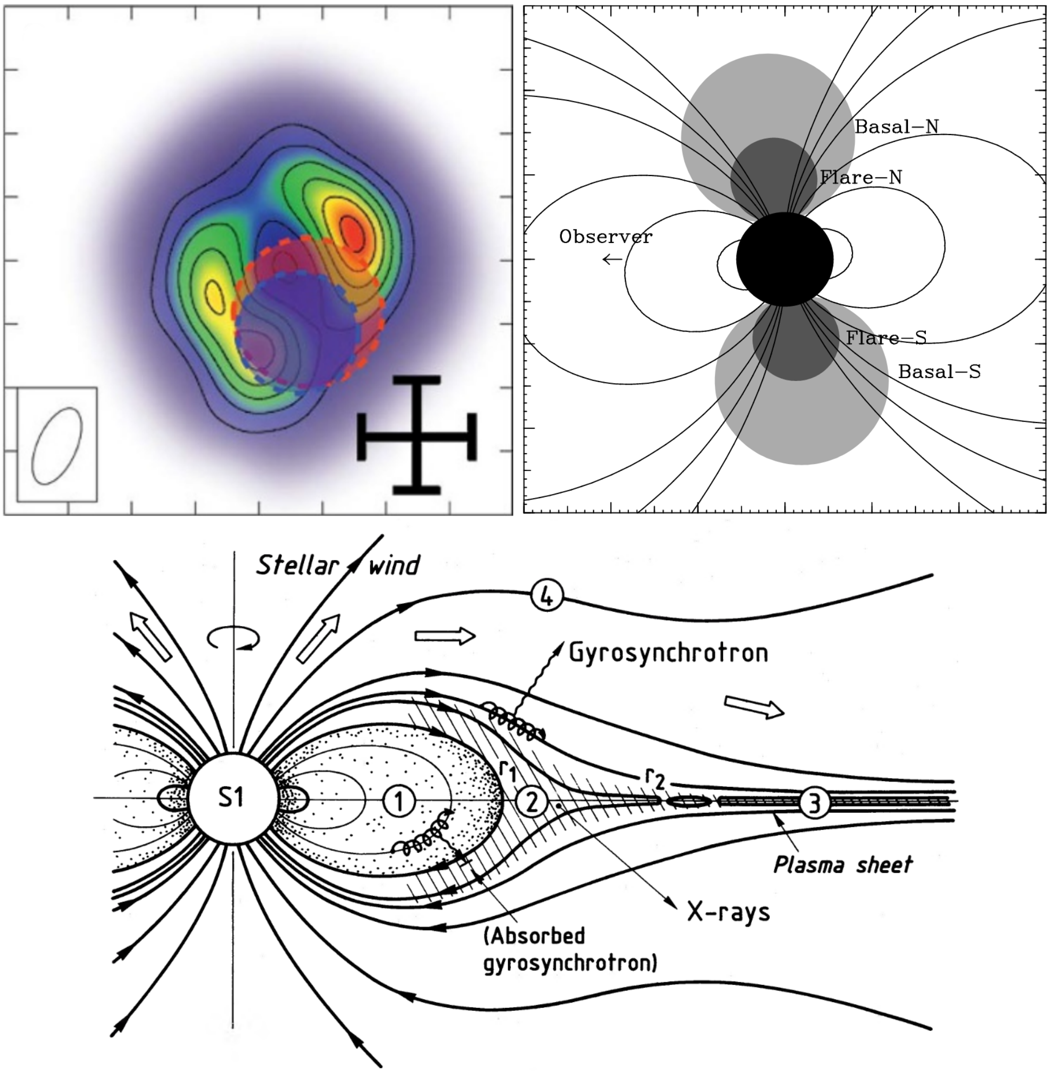

Figure 3.3: (Top left): VLBI image of Algol at epoch 2008.5 with positions of Algol B (red dashed circle) and Algol A (blue dashed circle) overlaid. The black cross represents the 1σ uncertainty in position. (Top right): Polar cap model for the radio magnetosphere of a young star, after the observations of Algol by Mutel et al. (1998). (Botton): Magnetospheric model after Andre et al. (1988). Credits: Peterson et al. (2010), Mutel et al. (1998), Andre et al. (1988), respectively.

come from synchrotron or gyrosynchrotron radiation from energetic electrons accelerated by magnetic reconnections. Most of the radio emission would originate in: i) the magnetic equator line at a distance where the stellar wind opens the closed magnetic field lines and creates a current sheet of plasma where electrons are continuously accelerated (see Fig. 3.3); ii) close to the polar caps where the wind flows almost unrestrained; and iii) a combination of the previous two places. A version of this model has successfully explained the two radio lobes of opposite circular polarization seen in Algol (Mutel et al. 1998) and UV Cet B (Benz et al. 1998) where each lobe would be located in a different polar cap region (see Fig. 3.3).

Regarding AB Dor C, observations with different near-infrared instruments at the Very Large Telescope (VLT) (Close et al. 2005, 2007; Boccaletti et al. 2008) allowed independent photometry of this object and determined a spectral type of M8. As discussed in Sect. 2.3, objects with this spectral type are classified as UCDs and are not typically expected to present radio emission although a few interesting exception exists. Up to this date, AB Dor C has not presented detectable radio emission at any of the observed frequencies and epochs with the strongest upper limit being 0.07 mJy at 8.4 GHz (Azulay et al. 2017).

3.2 The VHS 1256-1257 system

While searching for common proper motion companions using the VISTA Hemisphere Survey (VHS) and the 2MASS catalogs, Gauza et al. (2015) discovered a low mass L7 companion to the binary system VHS J125601.92-125723.9 (hereafter VHS 1256-1257). This binary system is composed by an equal-magnitude M7.5 binary with separation of 0.1″ imaged by Stone et al. (2016) for the first time, using the Keck telescope (see Fig. 3.4). The L7 object is located at a projected angular separation of 8″ from the central binary.

The system is known to be relatively young (150-300 Myr), and nearby, with the closest estimation to be 12.7 pc from parallax distance (Gauza et al. 2015) while the furthest estimation yields 17.1 pc (Stone et al. 2016) from spectrophotometric data. Another hint at the age of the system comes from the strong lithium depletion observed in the high resolution spectra of the M7.5 binary (Gauza et al. 2015).

With an estimate of the distance to the system, one can make use of bolometric corrections available for M7-M8 and red L dwarfs (Golimowski et al. 2004; Filippazzo et al. 2015) and the luminosity-mass-age relationship of Chabrier et al. (2000) to infer the mass of each object in this multiple system. Indeed, with this procedure the estimated masses

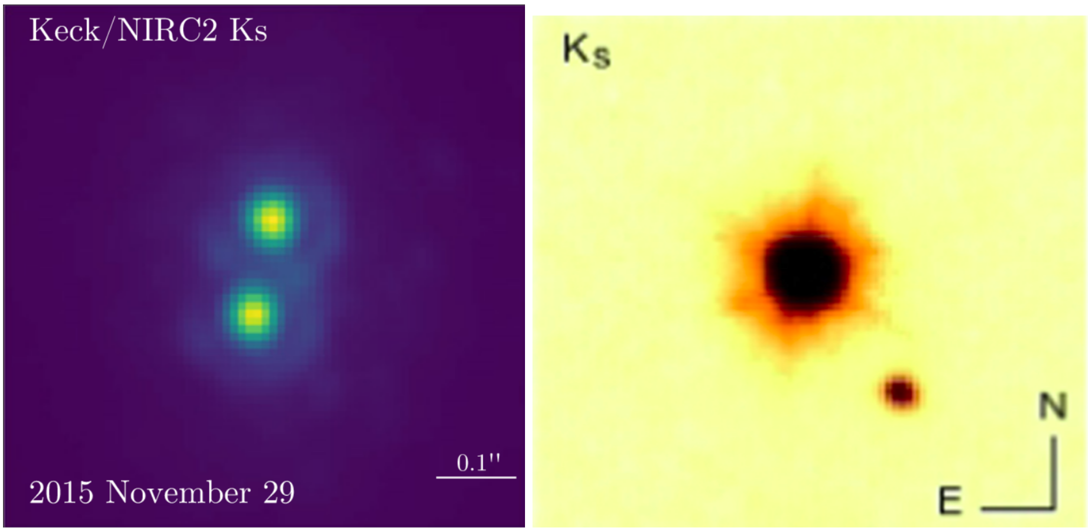

Figure 3.4: (Left): Keck image of the central binary in the VHS 1256-1257 system at K_s band. North is up, and east is left. (Right): Discovery of the L7 object orbiting the central binary (not resolved in the image). Credit: Stone et al. (2016) and Gauza et al. (2015), respectively.

intervals are: 10-20 $M_{\rm Jup}$ and 50-80 $M_{\rm Jup}$ for the L7 object and for each of the component of the central binary. Correcting the projected separation measured in Stone et al. (2016) by using the projected separation-semimajor axis correction factor (Dupuy & Liu 2011) one can find that the period interval for the central binary is 5.7-8.7 years (Stone et al. 2016).

The importance of this multiple is threefold: (i) it is the third multiple system known to date in which all three components may be substellar (see Bouy et al. 2005; Radigan et al. 2013); (ii) The very red L dwarf population is not very well-understood and the study of this L7 object with high content of atmospheric dust or high metallicity (Rich et al. 2016) can be extremely useful to this field; (iii) With an 8″ separation between the central pair and the L7 object, the system is accessible to most wavelengths and, with special importance, to radio wavelength where high resolution multi-epoch images can help with the determination of the dynamical masses.

3.3 Red supergiants. V602 Carinae

According to the accepted scenario for the evolution of massive stars, red supergiants (RSGs) are the helium-fusing descendants of moderately massive main-sequence stars ($10M_\odot \lesssim M \lesssim 40M_\odot$). They are the end result of a nearly horizontal evolution across the top of the Hertzsprung-Russell diagram: since their H-burning predecessors left the main sequence and crossed the yellow void until passing through the very short-lived yellow supergiant stage. From here, the star may end its life as a RSG before transitioning toward a core-collapse supernovae or, in some massive cases, it will spend a portion of their He-burning lifetimes as RSGs before evolving back across the H-R diagram, passing once again through the brief yellow supergiant phase and exploding as either a blue supergiant or a Wolf-Rayet (W-R) star, depending on its initial masses and mass loss rate.

RSGs represent an extreme case in stellar evolution since they have the largest physical size of any stars and are the most luminous cool stars in the universe. During their time as RSGs they undergo an impressive amount of mass loss. As an extreme case, a 100 $M_\odot$ very high mass star may lose up to 50% of its mass during its evolution which, inevitably, deeply affect its path in the H-R diagram (De Loore et al. 1977, 1978; Chiosi et al. 1978, 1979, and subsequent works). The physical mechanisms that contribute to and dominate this mass loss are still unclear but observational evidence has demonstrated that this mass loss contributes to RSGs producing substantial amounts of dust, while also playing a major role in the enrichment of the interstellar medium (ISM) via returning the elements synthesised during their life to the ISM.

The most commonly proposed mechanism to explain the origin of mass loss in RSGs has been an interplay of pulsation and convection (e.g., Yoon & Cantiello 2010). However, there are alternative mechanisms such as (i) a decrease of the effective gravity, caused by convective motions, combined with radiative pressure on molecular lines (Josselin & Plez 2007); (ii) magnetic fields contributing to the heating of the outer atmosphere and to the mass loss (Aurière et al. 2010); (iii) a scenario that includes radiative acceleration on Doppler-shifted molecular lines (Arroyo-Torres et al. 2015); (iv) magnetic fields and Alfvén waves (e.g. Airapetian et al. 2010; Cranmer & Saar 2011; Thirumalai & Heyl

2012; Rau et al. 2019; Yasuda et al. 2019); (v) the presence of giant dominating hot spots (Montargès et al. 2016). Although the processes that initiate the mass loss from RSG stars are not currently known, the mass loss itself has been tightly linked to the initial metallicity of the gas out of which they form since mass-loss rates scales with metallicity (e.g. Abbott 1982; Lamers & Cassinelli 1996; Kudritzki et al. 1989; Puls et al. 2000). The primary effect of metallicity is due to its influence on radiatively driven stellar winds and the resulting mass loss.

3.3.1 Interferometry in red supergiants

Interferometric studies spanning different wavelength ranges, from visual to mid-infrared, went from measuring simple RSGs diameters (approximately two decades ago) to produce the first images of stellar surfaces on these objects. Let us briefly review some of the relevant work done in this field.

Measuring the radius of RSGs

The determination of the stellar radius of a RSG is crucial in order to derive fundamental stellar parameters like effective temperature and luminosity, which are, in turn, important to calibrate stellar evolutionary models for massive stars and to understand their further evolution toward WR stars and supernovae (e.g., Dessart et al. 2013; Groh et al. 2013, 2014; Smith 2014; Meynet et al. 2015). However trivial one might think it is, the definition of stellar radius of a RSGs is not easy because of the complex geometries of the stellar atmospheres (Scholz 1997). There are a few definitions of the stellar diameter used in the literature and that the reader should be familiarized with (a visual representation of some of them can be found in Fig. 3.5):

1. Rosseland radius: It corresponds to the atmospheric layer where the Rosseland-mean optical depth is 2/3. By definition, it is independent of wavelength and physically the most meaningful definition. However it has some issues since it can be contaminated by extended molecular and dusty layers, and additionally, it is not a

direct observable. The best way to determine its value may be arguably by comparing the observations with model atmosphere predictions, such as the PHOENIX model (Hauschildt & Baron 1999) or the ATLAS 9 model (Kurucz 1993) among others.

2. Uniform disk (UD) radius: obtained from a fit of a uniform disk model to the measured visibility data, it needs to be corrected for the limb-darkening effect. As a disadvantage, this radius depends on the wavelength and therefore does not correspond to a certain physical layer of the RSG.

3. 0% intensity radius. As its name implies, it corresponds to the radius where the intensity drops to zero. Although, for a spherical geometry, the intensity never drops to zero it is set to zero at an arbitrary distance. In this case, it is obtained by fitting a model atmosphere to interferometric data.

4. 50% radius or FWHM. Similarly to the previous one, this radius corresponds to the radius where the intensity drops 50%. However, the same issue arises here, since this radius also depends on the wavelength.

The limb-darkening effect

Thanks to the high angular resolution provided by the interferometry technique, one can measure the limb-darkening effect on some RSG, which happens as a consequence of the vertical temperature stratification of the stellar atmosphere and, also, our line of sight. Since along any line of sight the observer will see an optical depth of 1, when looking at the center of the star deeper (and hotter) atmospheric layers are seen, contrary to what happens when looking toward the limb of the star where shallower (and colder) atmospheric layers are seen (see Fig. 3.6 for illustrative purposes). Using this effect, one can constrain the vertical temperature stratification of the atmosphere and compare to model atmospheres (see the early works of Quirrenbach et al. 1996; Hajian et al. 1998; Wittkowski et al. 2001, 2004).

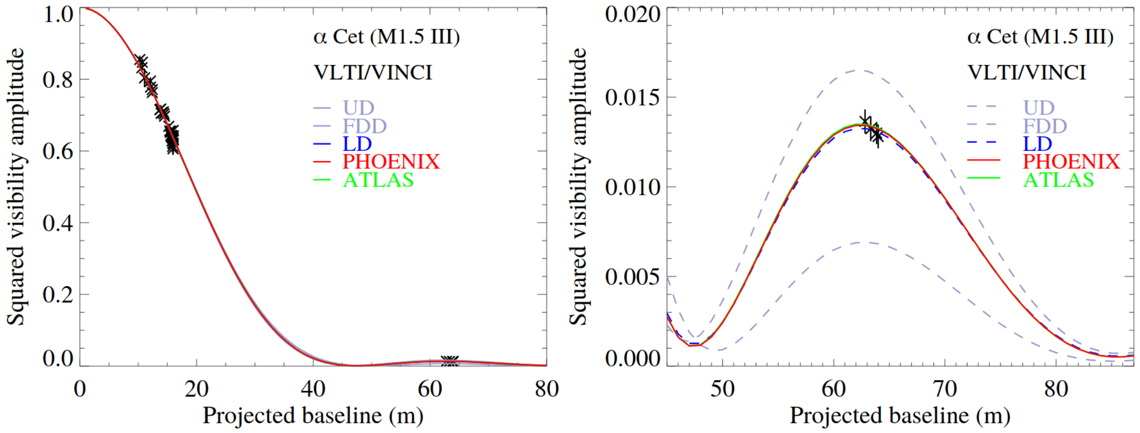

Figure 3.5: Squared visibility amplitudes of α Ceti obtained with VLTI/VINCI, and the best-fitting models of a uniform disc (upper dashed light blue line), a fully darkened disc (lower dashed light blue line), a limb-darkening model (dashed blue line), and of PHOENIX and ATLAS 9 model atmosphere predictions (solid red and green lines). The left panel shows the full range of the visibility function, while the right panel shows an enlargement of the low squared visibility function in the 2nd lobe. Credit: Wittkowski et al. (2006).

Fig. 3.5 shows the measurement of the limb-darkening effect of the M giant Menkar (α Ceti) obtained by Wittkowski et al. (2006) using the VINCI instrument at the VLTI. It is only in the second lobe where different models yield different results. The peak of the visibility of the second lobe is a measure of the strength of the limb-darkening effect and directly probes the shape of the intensity profile. To probe the wavelength-dependent strength of the limb-darkening effect, one could measure the variation of a UD diameter as a function of the wavelength. In this sense, the closer that the limb-darkening model and the UD prediction are the weaker the effect.

Imaging the stellar surface

Schwarzschild predicted that the stellar surface of RSGs would not be populated by a large amount of granules (as happens in the Sun) but by only a few convective cells (Schwarzschild 1975). Since gravity and temperature are the main parameters controlling the convection, when the main-sequence star becomes a RSG and, consequently the gravity decreases, only a few convective patterns are expected to populate the stellar sur-

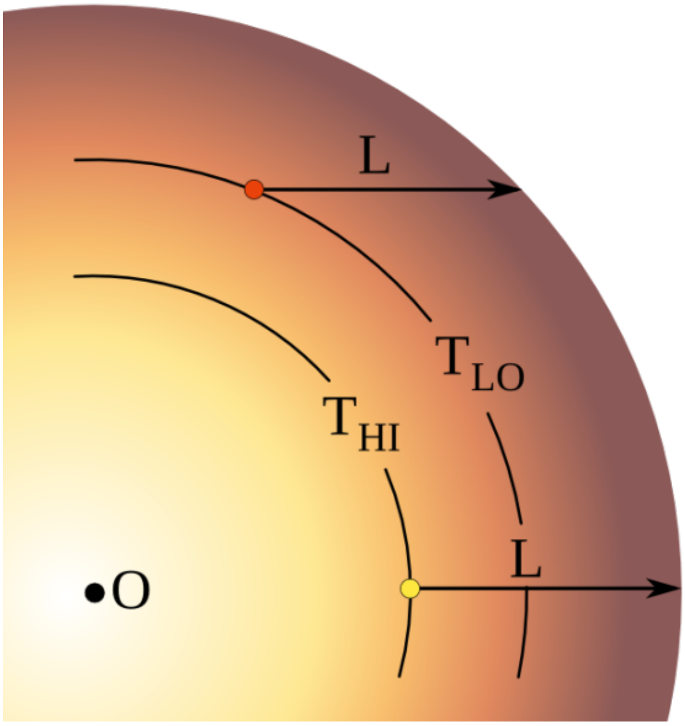

Figure 3.6: Illustration of the limb-darkening effect. Depending on the line of sight, the geometrical depth corresponding to an optical depth of unity (L in the figure) varies. When the line of sight corresponds to the center of the star our instruments will receive information from the inner layer with higher temperature (T_{HI}) whereas when the line of sight corresponds to the limb of the star we will receive information from an outer layer of the star with lower temperature (T_{LO}).

face as seen in simulations (Chiavassa & Freytag 2015). Indeed, this behaviour has been observed in all of the RSG images so far, with the detection of at least one large convective spot (e.g. Haubois et al. 2009; Chiavassa et al. 2010b; Baron et al. 2014; Monnier et al. 2014; Wittkowski et al. 2017b).

With the confirmation of this prediction, new questions aroused regarding the timescales of convective patterns, the role of the magnetic field, and the interplay between convection and pulsation. Current 1D pulsation models do not reproduce interferometric measurements (Arroyo-Torres et al. 2015), nor do 3D radiative-hydrodynamics (RHD) models which seem to be too compact to reproduce the observed extension of RSG stars in the near-IR (Arroyo-Torres et al. 2013, 2014, 2015). These questions are currently still open for discussion.

3.3.2 V602 Carinae

V602 Carinae (V602 Car, HD 97671) is a RSG with Simbad spectral type M3-M4 I. It is one of the largest known stars with a radius of 1050±165 $R_\odot$, an effective temperature of 3432±280 K, a surface gravity $\log g$ = -0.30±0.16, and an initial mass of 20-25 $M_\odot$ corresponding to a current mass of 10-13 $M_\odot$ (Arroyo-Torres et al. 2015). V602 Car is a semiregular variable star with ranging magnitude from 9.1 to 7.6 (Kazarovets et al. 2006) and a period of $\sim$ 672 days (Samus et al. 2009). It has an estimated mass loss rate of $1.9 \times 10^{-6} M_\odot$ per year (Mauron & Josselin 2011).

This RSG has been studied with spectro-interferometric observations (VLTI/AMBER) at K infrared band (1.92-2.47 μm) by Arroyo-Torres et al. (2015). The authors found that the PHOENIX model atmosphere does a good job in reproducing the flux spectra measured. However, the PHOENIX model was unable to predict the large observed extensions of molecular layers and so were the 3D convection models and 1D pulsation models.

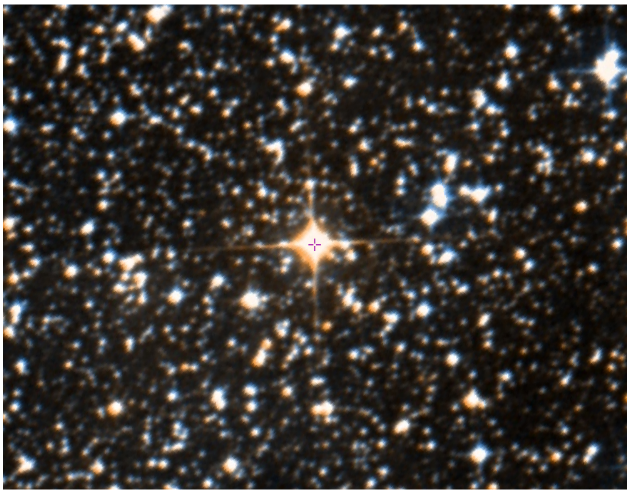

Figure 3.7: V602 Car optical image from the DSS2 survey.

Chapter 4

The milliarcsecond-scale radio structure of AB Dor A

This chapter is based on the homonymous manuscript accepted for publication in Astronomy and Astrophysics.

4.1 Introduction

Young stellar objects (YSOs) present radio emission due to a wide range of mechanisms. One of the most common mechanism detected observationally (see Forbrich et al. 2011, and references therein) occurs when electrons gyrate in the magnetic fields of these objects producing non-thermal continuum emission called cyclotron, gyro-synchrotron, or synchrotron emission depending on the velocity of such electrons (Dulk 1985). The majority of YSOs with non-thermal radio emission detected are pre-main-sequence (PMS) stellar objects with the notable exception of a few Class I protostars (Forbrich et al. 2006; Deller et al. 2013). The radio emission in these objects is thought to originate in and be confined to the magnetosphere (with a typical size of a few stellar radii; see Bouvier et al. 2007) and, consequently, usually remains unresolved at the current very long baseline interferometry (VLBI) resolution (milli-arcsecond), as demonstrated by the largest existing sample of VLBI detections of PMS stars (Ortiz-León et al. 2017).

In a few cases, VLBI observations of PMS stars revealed resolved magnetospheres with sizes up to several times the stellar radii (Phillips et al. 1991; Andre et al. 1991, 1992). Other objects exhibiting extended magnetospheres include RS CVn (Massi et al. 1988; Trigilio et al. 2001; Ransom et al. 2002, 2003), Algol-like binaries (Mutel et al. 1998; Peterson et al. 2010), M dwarfs (Benz et al. 1998) and chemically peculiar Bp/Ap stars (Phillips & Lestrade 1988). Based on some of these VLBI results, together with measured radio spectra and polarization measurements, a magnetospheric model consisting in a global dipole-like structure was suggested (see Fig. 3 in Andre et al. 1988). The radio emission detected in these objects is believed to come from synchrotron or gyrosynchrotron radiation from energetic electrons accelerated by magnetic reconnections. Most of the radio emission would originate in: i) the magnetic equator line at a distance where the stellar wind opens the closed magnetic field lines and creates a current sheet of plasma where electrons are continuously accelerated; ii) close to the polar caps where the wind flows almost unrestrained; and iii) a combination of the previous two places. A version of this model has successfully explained the two radio lobes of opposite circular polarization seen in Algol (Mutel et al. 1998) and UV Cet B (Benz et al. 1998) where each lobe would be located in a different polar cap region.

Of particular interest to our work is the case of the young binary system V773 Tau A. This system exhibits a persistent radio emission that varies in intensity depending on the separation between components, indicating some interaction between the individual magnetospheres (Torres et al. 2012). More remarkably, the detected radio emission in this object may be explained by the presence of solar-like helmet streamers. Those streamers would be anchored to the top of a closed loop at a few stellar radii above the stellar surface. However, they would extend up to the upper mirror points located 30 stellar radii away (Massi et al. 2008). Posterior observations did not confirm the detection of these mirror magnetic points (Torres et al. 2012); however, the interaction between individual magnetospheres was confirmed and the hypothesis of helmet streamers should be added to the list of possible scenarios occurring in these PMS stars.

Radio emission has also been detected in ultracool dwarfs (UCDs). The discovery of the first radio emission from an UCD proved the existence of powerful magnetic fields

(~kG) on these objects (Berger et al. 2001). The presence of mildly relativistic electrons accelerating along the lines of these magnetic fields may produce what is known as electron cyclotron maser instability (ECMI) emission in a similar fashion to the auroral radio bursts observed in Solar System planets (Zarka et al. 2001). This emission is then detected as bright, highly-polarized radio bursts and, in some cases, with periodicity equal to the rotation period (Berger et al. 2009; Doyle et al. 2010; Harding et al. 2013; Wolszczan & Route 2014). Additionally, these electrons spiraling in an ambient magnetic field may produce non-bursting radio emission (quiescent emission) via gyrosynchrotron mechanism. This emission varies on timescales of weeks (and longer) but is typically steady over the observing time (Antonova et al. 2007; McLean et al. 2012). The only known exception is the most radio-bright UCD, NLTT 33370 B, with consistent level of radio emission for more than a decade (McLean et al. 2011). These scenarios are not mutually exclusive and some of the known radio-active UCDs present both quiescent and bursting emission (Berger et al. 2005; Hallinan et al. 2006, 2008; Williams et al. 2015). Understanding the phenomenology and the physical mechanisms involved in the radio emission of UCDs is crucial for planet discovery around them (Robertson et al. 2014) and for the atmosphere and habitability of these planets (Jakosky et al. 2015; Shields et al. 2016) which could be abundant and observationally accessible (e.g. TRAPPIST-1 system, see Gillon et al. 2016, 2017). The number of UCD with detected radio emission has been increasing over the last years, with objects with spectral type as late as T6.5 (Kao et al. 2016), including a likely planetary-mass T2.5 object (Kao et al. 2018).

About 15 pc away, AB Doradus (AB Dor) is one of the most active and extensively studied PMS objects. It is a multiple system formed by two pairs of stars separated by $9''$, AB Dor A/C and AB Dor Ba/Bb (Close et al. 2005; Guirado et al. 2006), giving name to the AB Dor moving group (AB Dor-MG). The main star of this system, the K0 dwarf AB Dor A, is a fast rotator (period of 0.5 days; see Table 4.1) which presents strong emission at all wavelengths, from radio to X-rays (see Schmitt et al. 2019, and references therein). It has been well studied by the *HIPPARCOS* satellite (Lestrade et al. 1995; Lindegren & Kovalevsky 1995) and VLBI arrays (Lestrade et al. 1995; Guirado et al. 1997). This joined effort revealed the presence of AB Dor C, a low-mass companion with 0.090 $M_{\odot}$, orbiting AB Dor A at an average angular distance of 0.2″. The pair AB Dor A/C has also been observed by different near-infrared instruments at the VLT (Close et al. 2005, 2007; Boccaletti et al. 2008) allowing independent photometry of AB Dor C which, along with the dynamical mass determination, served as a benchmark for stellar evolutionary models. Recent evidence indicates that AB Dor C may be a binary system itself (Climent et al. 2019) consisting of two brown dwarfs, AB Dor Ca/Cb, with 72 and 13 Jovian masses, respectively. The exact age of the system is a current subject of discussion: 40–50 Myr for AB Dor A and 25–120 Myr for AB Dor C in Azulay et al. (2017), 40-60 Myr in Zuckerman et al. (2004) and López-Santiago et al. (2006), 30-100 Myr in Close et al. (2005), 40-100 Myr in Nielsen et al. (2005), 75-150 Myr in Luhman & Potter (2006), 50-100 Myr in Janson et al. (2007) and Boccaletti et al. (2008), 40-50 Myr in Guirado et al. (2011), >110 Myr for the AB Dor nucleus star in Barenfeld et al. (2013) and 130-200 Myr in Bell et al. (2015).

Slee et al. (1984) were the first to detect radio emission from AB Dor finding a clear modulation in its flux and an absence of circular polarization (Slee et al. 1986). They interpreted this modulation as spot groups on the star that may have lifetimes of the order of 2 years or more. A more detailed study of the modulation in radio emission (Lim et al. 1992) found that the peaks in emission coincided with the two stellar longitudes at which starspots preferentially form and detected a large spot at one of these active longitudes. These starspots were also the interpretation adopted by other authors that suggested a model of them based on optical photometry and spectroscopy (see Fig. 5 in Budding et al. 2009). Subsequent monitoring of the AB Dor A/C system with the Australia Telescope Compact Array (ATCA) has shown a baseline flux of 2 mJy and flare events up to 8 mJy with a half-brightness duration of about 3 hours (Slee et al. 2014) indicating that the modulation is still present even 23 years after the discovery of radio emission from this star. Finally, from VLBI multiepoch observations of AB Dor A (Azulay et al. 2017) reported both revised orbital elements and dynamical masses for the AB Dor A/C system.

Here we present the study of new 1.4 GHz and 22.3 GHz VLBI observations of AB Dor A. In addition we re-analysed the 8.4 GHz VLBI data from Azulay et al. (2017) finding an extended, fastly evolving, coronal structure around AB Dor A. Our field of

Table 4.1: Physical properties and orbital parameters of AB Dor A/C

Parameter	Value	Ref.
Abs. position AB Dor A[a]		
α_0 (h m s)	5 28 44.79483	1
δ_0 (° ′ ″)	-65 26 55.91774	1
Parallax (mas)	66.4 ± 0.3	1
Distance (pc)	15.06 ± 0.10	1
Orbital elements AB Dor A[b]		
P (years)	11.78 ± 0.10	1
a_A (mas)	31 ± 1	1
e	0.59 ± 0.05	1
i (°)	65 ± 1	1
ω_A (°)	114 ± 5	1
Ω (°)	132 ± 2	1
T_0	1991.9 ± 0.2	1
Relative position AB Dor C[c]		
Separation (″)	0.156 ± 0.10	2
P.A (°)	127 ± 1	2
Stellar properties		
Spectral Type A	K0V	3
Mass A ($M_\odot$)	0.89 ± 0.08	1
Radius A ($R_\odot$)	0.96 ± 0.06	5
Rot. Period A (days)	0.51479 ± 0.00001	4
Spectral Type C	M8	2
Mass C ($M_\odot$)	0.090 ± 0.008	1

Notes.
(a) The reference epoch for AB Dor A is 2000.0.
(b) We consider the pair AB Dor A and AB Dor C with the origin of coordinates placed at the center of mass of this system. P, a_A, e, i, ω_A, Ω, and T_0 represent the period of the orbit, the semi-major axis of AB Dor A apparent orbit in the sky, the ellipticity of the orbit, the inclination of the orbit on the sky, the longitude of the periastron of the orbit, the longitude of the ascending node, and the time of periastron passage, respectively.
(c) The values of AB Dor C orbital parameters are given for epoch 2004.093.

References. (1) Azulay et al. (2017); (2) Close et al. (2005); (3) Torres et al. (2006); (4) Innis et al. (1988); (5) Guirado et al. (2011)

view allowed us to also probe the UCD binary AB Dor Ca/Cb and place strong upper limits to the radio emission in this object. We describe the observations in Section 2 and the data reduction and analysis in Section 3. Then, we present the results from this analysis in Section 4. In Section 5 we discuss our results considering different scenarios that might explain them. Finally, in Section 6 we present our conclusions.

Table 4.2: Journal of observations

Frequency (GHz)	Observing Date	Array Configuration[a]	UT range	Beam Size (mas)	P.A (°)
8.4	11 Nov. 2007	At, Cd, Hh, Ho, Mp, Pa	10:00-22:00	2.5×0.9	-3
8.4	25 Oct. 2010	At, Cd, Ho, Mp, Pa	11:00-23:00	3.2×2.8	-26
8.4	16 Aug. 2013	At, Cd, Hh, Ho, Mp, Pa, Ti, Ww	15:00-03:00	2.2×0.7	4
22.3	14 Jun. 2017	At, Cd, Ho, Mp, Pa	20:40-07:40	4.7×3.4	-74
1.4	6 Feb. 2018	At, Ho, Cd, Pa	03:24-14:00	19.8×15.3	-55

Notes. [a] Australia Telescope Compact Array (At), Hobart (Ho), Ceduna (Cd), Hartebeesthoe (Hh), Mopra (Mp), Parkes (Pa), DSS43 – NASA's Deep Space Network Tidbinbilla (Ti), and Warkworth (Ww).

4.2 Observations

We observed the binary system AB Dor A/C using the Australian Long Baseline Array (LBA) at 1.4 GHz (21 cm) and at 22.3 GHz (1.3 cm). During February 6th, 2018 we observed at 1.4 GHz for a total duration of 10 hours. The system was observed in phase referencing mode using the source BL Lac PKS 0516-621 (about 3.6° away) as a phase calibrator. The sequence calibrator-target lasted 3.5 minutes (2.5 minutes on source and 1 minute on the calibrator). Both right and left circular polarizations were recorded using four 16 MHz bandwidth subbands per polarization. The same strategy was followed with the 22.3 GHz LBA observations carried out on June 14th, 2017 with the same phase-referencing calibrator but with a sequence calibrator-target lasting 3 minutes (2 minutes on source and 1 minute on the calibrator).

Previous observations of the AB Dor system at 8.4 GHz, already reported in Azulay et al. (2017), were reanalyzed along with the new 1.4 GHz and 22.3 GHz data. See Table 4.2 for further details of these observations.

4.3 Data reduction and imaging procedure

We reduced the data shown in Table 4.2 using the Astronomical Image Processing System (AIPS) of the National Radio Astronomy Observatory (NRAO) following standard routines. Firstly, we calibrated the ionospheric delay and corrected the instrumental phases. We then calibrated the visibility amplitudes using the nominal sensitivity for each antenna and corrected the phases for parallactic angles. Finally, we performed a fringe-search on the phase calibrator to minimize the residual contributions to the phases and applied these new corrections to our target. The phase-referenced channel-averaged images were obtained using the Caltech imaging program DIFMAP (Shepherd et al. 1994) with the clean algorithm while selecting the polarization of interest in each case. We firstly centered a box at the maximum emission peak and used the DIFMAP task *clean*. After this, if additional flux was still present in the image above the noise level then we repeated the procedure by centering an additional box at the new maximum peak. We repeated these steps until no new peaks were distinguishable from the noise. This procedure was done interactively. The AB Dor A image for each epoch and frequency is shown at Fig. 4.1.

In addition to producing an image of AB Dor A/C for each LBA dataset, we also fitted circular Gaussians to the interferometric visibilities (*uv* plane) using the DIFMAP task *modelfit* (the use of elliptical Gaussians resulted in null non-physical FWHM values). To estimate the errors in the fitted parameters (i.e, size, density flux of each component and distance between components) we followed the expressions described in Fomalont (1999). The fitting results are shown in Table 4.3.

Table 4.3: Model components of the fit of circular Gaussians on the uv-plane for VLBI observations

Epoch	Comp.[a]	S (mJy)	θ (mas)	T_b (10^5K)
2007.863	1	3.4 ± 0.5	1.41 ± 0.18	420
	2	1.3 ± 0.2	0.60 ± 0.10	890
2010.816	1	2.31 ± 0.17	1.30 ± 0.09	340
	2	1.20 ± 0.16	1.51 ± 0.18	130
2013.625	1a	2.7 ± 0.2	0.90 ± 0.08	830
	1b	0.80 ± 0.15	0.40 ± 0.07	1200
	2	1.48 ± 0.19	0.65 ± 0.08	870
2017.452[b]	1	1.2 ± 0.6	4.9 ± 1.3	1.5
2018.101	1	4.8 ± 0.8	11 ± 2	350

Notes. [a] We adopt the convention that the central component will be denoted by subindex 1. In case of detection, the subindex 2 will indicate the presence of a second component to the east. In 2013, subindices 1a and 1b indicate the central and the closest component to the east, respectively, while subindex 2 the furthest one. S represents the flux density, θ the FWHM diameter of the circular Gaussian component and T_b the minimum brightness temperature. [b] 22.3 GHz data show a low signal-to-noise ratio (~5) and should be treated carefully.

4.4 Results

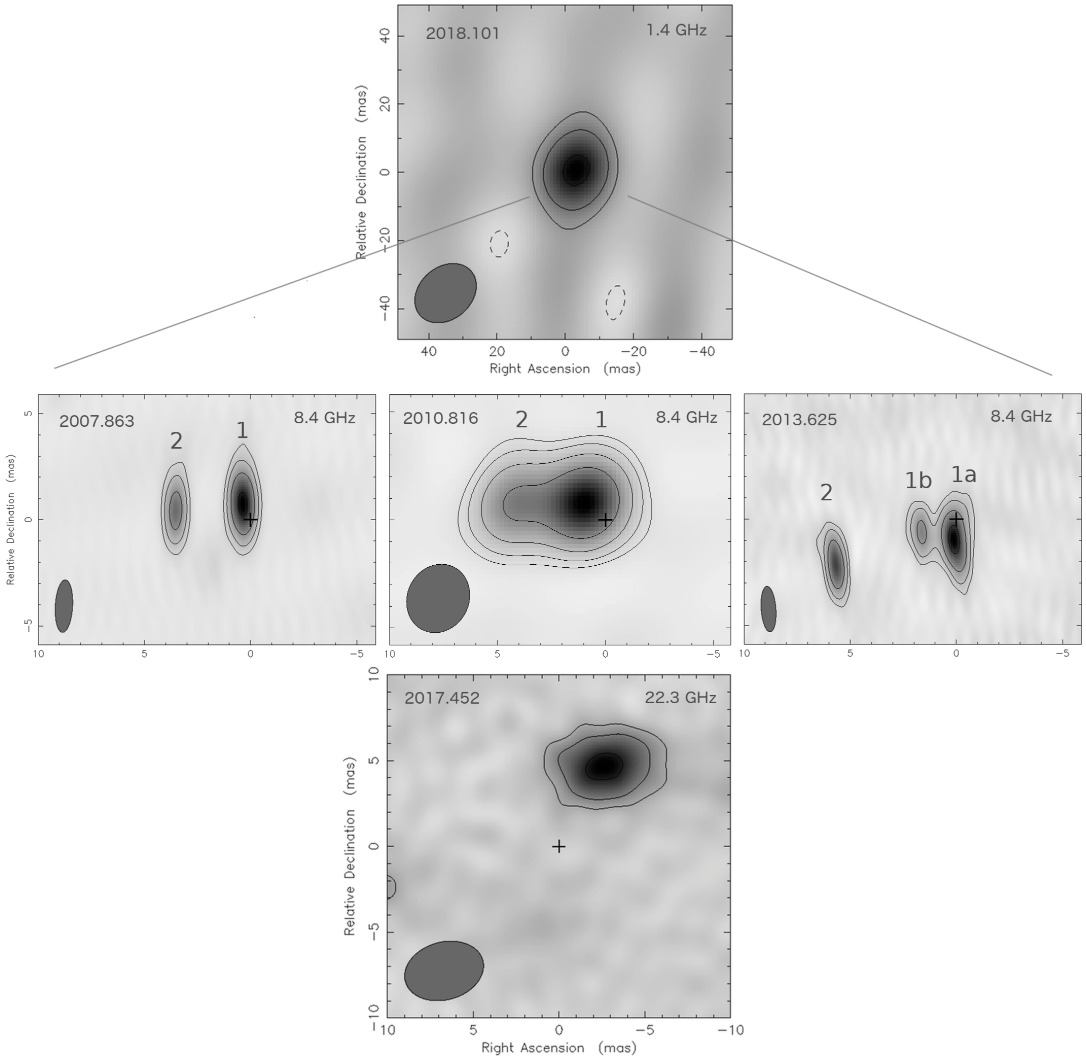

Figure 4.1: LBA images of all our observations of AB Dor A. Here and hereafter north is up and east to the left. Numbers (if any) indicate the index assigned to each component. For each image, the synthesized beam is shown at the bottom left corner (see Table 4.2). The lowest contour level (the remaining levels are spaced by factors of 2), the peak brightness, and background rms noise for each image are as follows: *(2007)*: 11%, 2.35 mJy beam^{-1}, 0.06 mJy beam^{-1}; *(2010)*: 6%, 2.16 mJy beam^{-1}, 0.05 mJy beam^{-1}; *(2013)*: 10%, 1.80 mJy beam^{-1}, 0.05 mJy beam^{-1}; *(2017)*: 22%, 0.714 mJy beam^{-1}, 0.05 mJy beam^{-1}; *(2018)*: 22%, 5.84 mJy beam^{-1}, 0.6 mJy beam^{-1}. All the images are centered, and cross-marked, at the expected positions of AB Dor A according to its proper motion, parallax, and orbital wobble.

4.4.1 VLBI imaging and model fitting of AB Dor A

Fig. 4.1 shows the maps of AB Dor A at all observed frequencies and epochs. At 8.4 GHz, the brightest peak of emission is located at the map center, coincident (to within one beam size) with the expected position of AB Dor A, according to the kinematics reported in Azulay et al. (2017). In Fig. 4.1, the 8.4 GHz images show a complex structure around AB Dor A (which was unnoticed in Azulay et al. 2017, see Section 5). In 2007 and 2010, two emission peaks or components can be identified, separated by 3.1 ± 0.2 mas (~10 R_{star}) and clearly oriented east-west. In the latter epoch, the double structure is not as clearly separated as in 2007 resulting in a double core-halo morphology.

Later on, in 2013, the double structure is still seen (separation of 5.7 ± 0.3 mas, ~18 R_{star}) although component 1 seems to be split in two close features, labeled as 1a and 1b in Fig. 4.1. However, we should remark that our visibility amplitudes and phases are similarly well fitted by a component 1a with a slight elongation towards the east. The reality of 1b as an independent feature should be taken with caution. The possible nature of the detected structures at 8.4 GHz is discussed in Sect. 4.5.

At 1.4 GHz, AB Dor A appears as a clear unresolved source with an estimated size of 11 ± 2 mas, whose position is also coincident with that expected by the orbit determination of Azulay et al. (2017). Our 1.4 GHz data show no circular polarization (with an upper limit of 10%) and minimum brightness temperature $\gtrsim 10^7$ K, indicating non-thermal radio emission.

Finally, at 22.3 GHz (Fig. 4.1), AB Dor A shows an extended component located 5.5 mas away (17.5 R_{star}) from the expected orbital position (marked with a cross). No significant circular polarization is found and the minimum brightness temperature is $\sim 10^5$ K. Considering the low SNR (~5) and large disagreement between expected and measured peak position, we consider that the validity of this detection may require further confirmation. No background sources are expected at the peak position. The origin of this emission, if real, remains unclear.

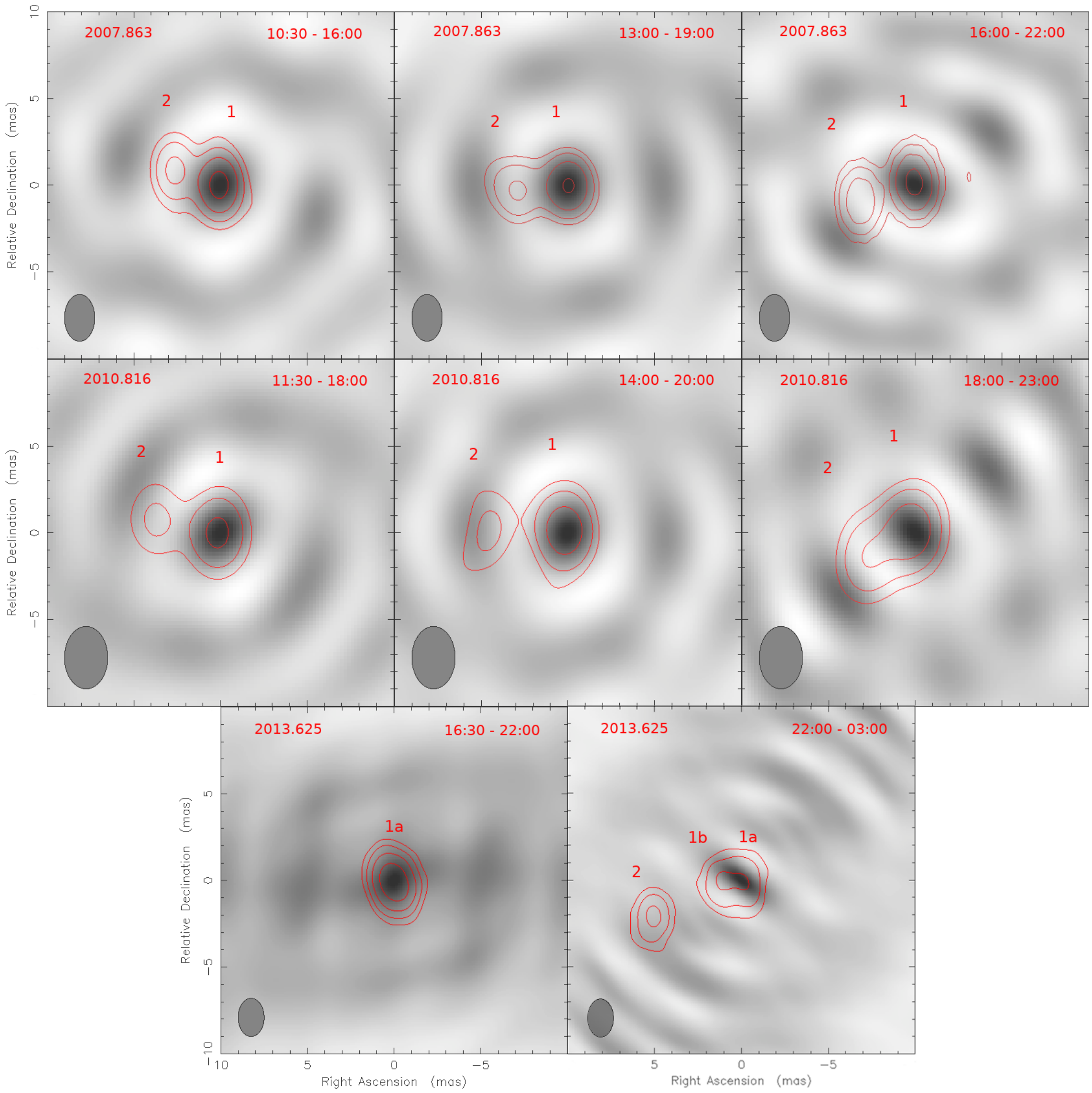

Figure 4.2: LBA snapshot images of AB Dor A at 8.4 GHz (as defined in the text) in red contours while the dirty beam of the corresponding snapshot is shown in gray scale. Different epochs are shown in different rows. Within the same epoch, the contour levels are the same and the beam size represents the average of the beam sizes of all the snapshots of such epoch, with 0° inclination for easier visualization. The FWHM beam size, its orientation and lowest contour level (the remaining levels are spaced by factors of 2) for each epoch are as follows: *(2007)*: 1.7 × 2.7 mas at 0°, 10% of 3.01 mJy beam^{-1}; *(2010)*: 2.5 × 3.6 mas at 0°, 15.5% of 2.46 mJy beam^{-1}; *(2013)*: 1.5 × 2.2 mas at 0°, 8% of 3.84 mJy beam^{-1}.

4.4.2 Time analysis of AB Dor A images

The images shown in Fig. 4.1 correspond to the structure of AB Dor A obtained with the full interferometric data set extending throughout the complete duration of each observation (typically 10 hr), which actually covers nearly one rotation period of the star (~12 hr). If the morphology of AB Dor A happens to vary within the duration time of each observation, the observed structure seen at VLBI scales should show a time dependence within a rotation period. To further investigate this dependence we divided the 2007 and 2010 VLBI observations into three time intervals, each corresponding to 5–6 hr, which allowed us to obtain three ”snapshot” images. The same procedure was applied to the 2013 data. However, only two snapshot images could be obtained for this epoch since shorter time intervals resulted in very sparse *uv* coverage and, therefore, maps of degraded quality with unreliable structures. The time covered by each snapshot is defined in Table 4.4. Fig. 4.2 shows the snapshot maps corresponding to the same observational epoch (but different UT ranges) and the remarkable changes in the structure of AB Dor A. Epochs 2007 and 2010 start at similar rotational phases of the star (with the epoch of zero rotation phase at JD 2444296.575; Pakull 1981): 0.30 for 2007 and 0.39 for 2010, and, indeed, their snapshot images corresponding to the same time interval are similar, showing a double core-halo morphology, a feature also visible in the entire data set images. However, the details of the structures change significantly on timescales of a few hours: the easternmost component seems to have rotated (from snapshot 1 to snapshot 3) with respect to the brightest emission peak an angle of 40 ± 3° (47 ± 3°) at epoch 2007 (2010). We should emphasize that each snapshot image conserves its own astrometric information (referenced to the external quasar), that is, the snapshot images are properly registered. This allows us to measure the absolute motion of both components between snapshots 1 and 3 registering a total 0.6 mas (1.8 mas) movement for component 1 and 1.8 mas (2.0 mas) movement for component 2 in 2007 (2010). We investigated whether these rotation of component 2 could be an artifact of the intrinsic rotation in the dirty beam. As seen in Fig. 4.2, despite the similarity between images and dirty beams, the position and rotation rate of the east side lobe and component 2 do not match. Yet, we should admit that some contamination may be present in our data, so our findings in terms of time analysis should be taken with caution.

Finally, the appearance of the snapshots at epoch 2013 (see Figure 4.2) shows a very different behaviour (although this epoch starts at a very similar phase to the 2010 data, i.e, 0.40) with significant changes between the two snapshot images: the first snapshot, corresponding to the first half of the observation, shows a unique central component coincident with the brightest peak found in the maps constructed with the entire data set. Following the naming convention in Fig. 4.1, this will be component 1a. However, in the second snapshot we recover the binary structure with the presence of component 2, being component 1a elongated due to component 1b. The absence of this double structure during the first half of the observations makes the behaviour of AB Dor A in the 2013 epoch look different than that in 2007 or 2010. Perhaps significantly, the separation between components during the second half of 2013 also differs from the separation measured in 2007 and 2010 data (see Sect. 4.4.1).

Table 4.4: Flux density of the components present in the snapshots (Fig. 4.2).

Epoch	Snapshot	$S_{1,1a}$ (mJy)	S_{1b} (mJy)	S_{2} (mJy)
11 Nov. 2007				
10:30-16:00	1	3.6 ± 0.3		1.1 ± 0.2
13:00-19:00	2	3.0 ± 0.5		1.3 ± 0.3
16:00-22:00	3	3.5 ± 0.6		1.5 ± 0.3
25 Oct. 2010				
11:30-18:00	1	1.8 ± 0.3		0.8 ± 0.3
14:00-20:00	2	2.3 ± 0.4		1.1 ± 0.3
18:00-23:00	3	1.7 ± 0.4		1.3 ± 0.4
16 Aug. 2013				
16:30-22:00	1	5.4 ± 0.3		
22:00-03:00	2	1.5 ± 0.2	1.6 ± 0.3	2.3 ± 0.4

Following the same procedure described in Sect. 4.3, we fitted circular Gaussians to the interferometric visibilities for each time interval (Table 4.4). Due to the resemblance with the entire data set image and in order to make the comparison easier, we fixed the component sizes to those measured in Table 4.3. Both in 2007 and 2010, the brightest component flux remains constant (within errors) during the entire observation while the second component might be slightly increasing in flux during the second half. Regarding epoch 2013, we notice that the flux density of the three components is, in some cases, larger in the snapshot maps (Table 4.4) than that measured in the entire data set image (Table 4.3), likely a consequence of the time averaging over the complete observing time in the latter maps.

4.4.3 Radio emission of AB Dor C

We found no emission at the expected position of AB Dor C, according to the well-known orbit of the system (Azulay et al. 2017) in any of our epochs. The non-detections place upper limits of 0.11 mJy, 0.04 mJy, 0.10 mJy, 0.04 mJy and 0.07 mJy for the radio emission of this ultracool dwarf in 2007, 2010, 2013, 2017 and 2018, respectively.

4.4.4 Orbit

We analyzed the orbital motion of the system in a similar fashion to Azulay et al. (2017), making use of previously reported VLBI, optical (*HIPPARCOS*), infrared and our new VLBI measurement (epoch 2018). We used a Bayesian approach with a model based on the definitions of Wright & Howard (2009). Our estimates of the astrometric and orbital parameters are in agreement with the values provided by Azulay et al. (2017). Indeed, we obtained dynamical masses of 0.91 ± 0.06 $M_\odot$ and 0.091 ± 0.005 $M_\odot$ for AB Dor A and AB Dor C, respectively.

4.5 Discussion

How do our images compare with previous VLBI observations of AB Dor A? Azulay et al. (2017) imaged for the first time AB Dor A at VLBI resolution. Their main objective was astrometric, providing precise positions of the peak emission of AB Dor A, which appeared in all maps as an unresolved source. In our analysis, we used a different weighting scheme to gain more sensitivity (at the expense of a worse resolution), and, in practice, self-calibration was not used. Following this procedure, we have been able to resolve the internal structure of AB Dor A, finding several sub-structures (see Fig. 4.1). We notice that we are able to reproduce the images presented in Azulay et al. (2017) by following the procedure described therein. Therefore, the images presented in this work supersede those reported in Azulay et al. (2017), and provide visual evidence of substructures around AB Dor A at radio frequencies.

There have been a few mechanisms proposed to explain the radio emission detected in active PMS stars like AB Dor A, as stated in the Introduction. The usual explanation consists in synchrotron or gyrosynchrotron emission from large-scale magnetic structures or loops within a dipolar magnetosphere. Phillips et al. (1996) presented an alternative explanation for the case of HD 283447 (a binary system) modelled as a combination of smaller magnetospheres around each star and a common magnetic structure. These structures would be associated with the process of interacting magnetospheres that could form solar-like helmet streamers as reported by Massi et al. (2008) in the young binary system V773 Tau A, although not confirmed by more recent observations (Torres et al. 2012). Recently, Lanza (2018) considered that the flares observed in some systems could be produced via the interaction between the magnetic field of the star and its close-by planets, although recent observations have not been able to find evidence of such interactions (Bower et al. 2016). Slingshots prominences might be another possible explanation for substructures around this star. However, although their presence in AB Dor A is well known (Collier Cameron & Robinson 1989), these corotating clouds are mostly made of neutral plasma that is not expected to emit at the observed frequencies.

As mentioned in Sect. 4.4.1, the radio emission detected in our 1.4 GHz image could be interpreted as synchrotron or gyrosynchrotron emission likely originated in relativistic electrons spiraling around the magnetic field lines in the outer layers of the corona. On the contrary, the 8.4 GHz images (Fig. 4.1 and Fig. 4.2) present a challenge to the models considered, since they must account for the following observed properties:

a) A complex internal structure consisting of compact features located at 10 R_{star} (in 2007 and 2010) and at 18 R_{star} (in 2013) away from the central component in the east direction.

b) Variability of the components positions on a timescale of hours (see Fig. 4.2).

c) Low degree of circular polarization (¡10%).

d) Brightness temperatures between 10^7 K and 10^8 K.

Any successful model must also be consistent with the dynamical configuration of the system, that is, with the well-known inclination of the rotation axis ($\sim$60°; Kuerster et al. 1994) with respect to our line of sight. We notice that the position angle of the rotation axis in the plane of the sky, $\mathrm{PA_{rot}}$, is unknown. As a reference, we show in Fig. 4.3 the configuration resulting from a rotation axis perpendicular to the orbital plane of AB Dor A/C, as shown in Fig. 2 of Azulay et al. (2017), which corresponds to a position angle $\mathrm{PA_{rot}}=42\,^{\circ}$. However, there is no observational evidence supporting this particular value of $\mathrm{PA_{rot}}$; therefore, any orientation of the rotation axis in the plane of the sky can be assumed in the following discussion.

On the other hand, the astrometric results of Azulay et al. (2017) successfully predict the position of the brightest peak of our 8.4 GHz images (Fig. 4.1). Given the scatter of 1.1 mas ($\sim$3 stellar radii) of the astrometric measurements, it is reasonable to assume that the peak of emission at each epoch corresponds to a radio emitting region near, but not necessarily coincident with, the stellar photosphere. Accordingly, the photosphere could be located several stellar radii away from the brightness peak. This is relevant for the discussion that follows.

4.5.1 Polar cap hypothesis

Previous studies of Algol (Mutel et al. 1998) and UV Ceti (Benz et al. 1998) found that a strong, large-scale, dipolar field could be consistent with the double-lobe structure observed in VLBI images of these objects. In these cases, each VLBI component would correspond to an emission region located above each one of the polar caps of the star. In this model (e.g. Kellett et al. 2002), electrons are accelerated at the equatorial region by the flaring activity of the star, then they move along the (dipole-like) magnetic field lines

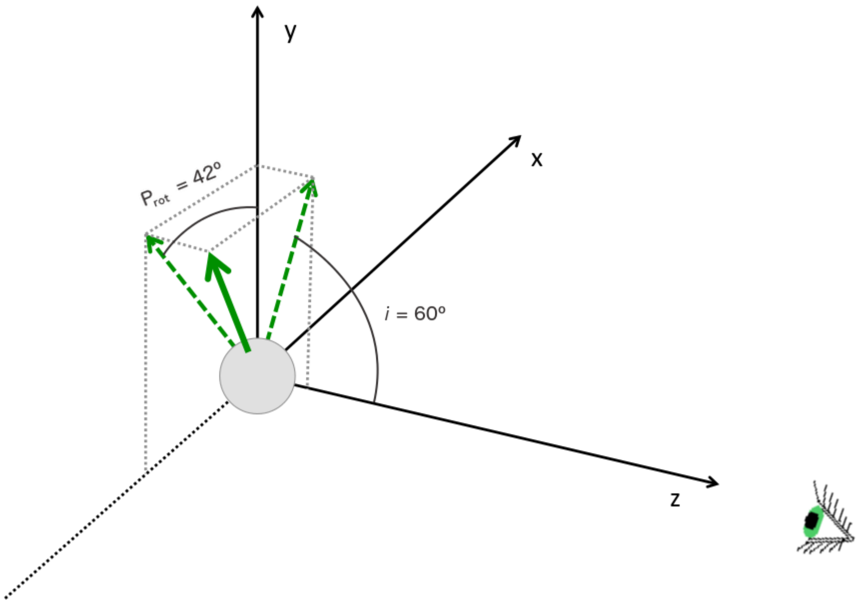

Figure 4.3: AB Dor A represented as a gray sphere with its rotation axis plotted in solid green, assuming the rotation axis is perpendicular to the orbital plane of the binary system AB Dor A/C. The dashed lines represent the projection of the rotation axis on the xy plane (plane of the sky) and on the zy plane. In this sketch, the rotation axis is inclined 60° with respect to our line of sight, here represented by the z axis.

towards the magnetic poles. Our 8.4 GHz images (see Fig. 4.1) posses a great morphological resemblance with the double-lobe structure detected in Algol and UV Ceti. Hence, is a polar cap model consistent with our 8.4 GHz observations?

Although the magnetic field of AB Dor A extrapolated from Zeeman-Doppler images is known to be much more complex than a simple dipole (e.g. Cohen et al. 2010), the dipole-like contribution could also be significant in this star and similar polar emission to Algol and UV Ceti could occur. Under this polar cap hypothesis, the magnetic dipole axis must be oriented east-west to explain the preferred direction for the radio emission of Fig. 4.1. Zeeman-Doppler images of the surface of AB Dor A showed that there is a misalignment between magnetic and rotation axes. Observations from 1995 to 2007 revealed that the latitude of the dipole component axis ranged from -35° to 57° indicating that this misalignment varies significantly with time (see Table 1 in Jardine et al. 2019). Therefore, it is plausible that the magnetic dipole axis was oriented east-west during our

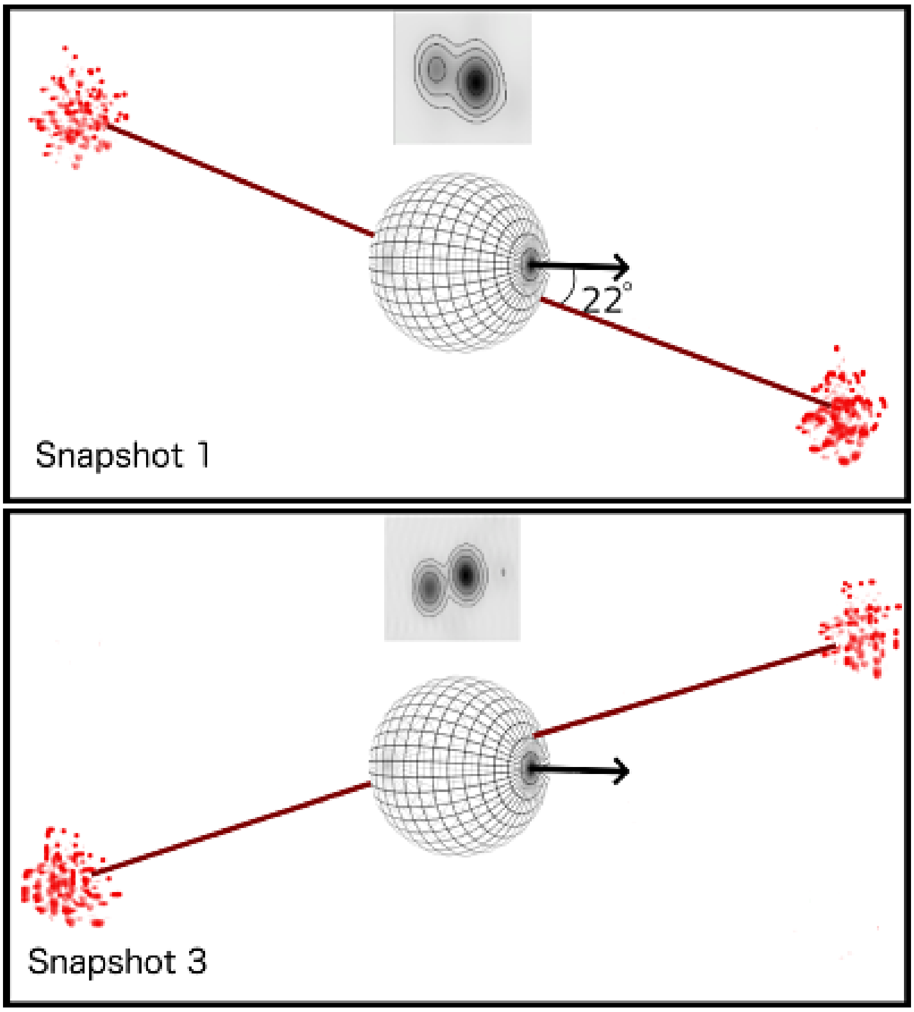

Figure 4.4: Polar-cap model applied to 2007 data: the rotation axis (black arrow) is inclined 60° towards the observer but east-west oriented with $\mathrm{PA_{rot}}\sim270°$; the magnetic axis (red line) is misaligned by ~22° with respect to the rotation axis. The rotation of the star would result in different orientations of the magnetic axis, effectively reproducing snapshot 1 (top panel) and snapshot 3 (bottom panel). The intermidiate stage would correspond to snapshot 2.

observations.

Under this assumption, the stellar disk in 2007 and 2010 (2013) would be located between components 1 (1a) and 2, which would be readily associated to radio emission above each of the polar caps at projected distance of $\sim5\ \mathrm{R_{star}}$ ($\sim9\ \mathrm{R_{star}}$) above the stellar surface, high enough to avoid, at least partially, the emission to be hidden by the stellar photosphere.

This polar-cap hypothesis can be further checked using the snapshot images of Fig. 4.2.

To explain the temporal variation shown in these images it is necessary to invoke a rotation axis oriented east-west ($\mathrm{PA}_{\mathrm{rot}} \sim 270°$) with a misaligned magnetic axis, as sketched in Fig. 4.4. According to this model, as the star rotates, emission coming from above the magnetic polar regions would create the different snapshots explaining the relative motion between components 1 and 2 in epochs 2007 and 2010. Snapshots at epoch 2013 would represent a special case. During the first half of the 2013 observations, emission coming from only one of the polar caps would be detected (component 1a) and during the second half of the observations the emission from both polar caps would be detected. On the other hand, were snapshots 1 and 3 of 2007 and 2010 representing the time of maximum apparent separation between magnetic and rotation axes then the estimated misalignment of the magnetic axis would be $\sim 22°$ for both 2007 and 2010. This misalignment is also compatible with the maps at epoch 2013.

The difference in flux between components might be either an intrinsic effect and/or a geometrical one, however, the fact that the brightest peak of emission permanently (at the three epochs) coincides with the westernmost component may be favoring a geometrical explanation for this effect. A possible scenario that would account for this difference in flux would be that, as Fig. 4.4 shows, the rotation axis of the star is inclined towards our line of sight so that polar emission coming from above this region would be directed towards us while emission from the opposite pole is pointing away from us, perhaps partially hidden, and thus detected as a weaker emission. This also may explain why only the westernmost component (polar cap pointing to the observer) is seen at the first snapshot of epoch 2013, although, certainly, the limited dynamic range of our snapshot images may not be enough to detect both sides of the emission (even more considering that component 1a was more than three times brighter in snapshot 1; see Table 4.4).

Regarding the (absence of) polarization in our maps, we should mention that both polarized and non-polarized polar-cap emission have been reported for other radio stars. It was found that Algol possesses two lobes of opposite circular polarization (Mutel et al. 1998) whereas a low circular polarization was found in the pair of giant synchrotron lobes of UV Ceti (Benz et al. 1998). In principle, AB Dor A would be similar to the latter case, although further observations and a deeper understanding of the mechanisms involved in

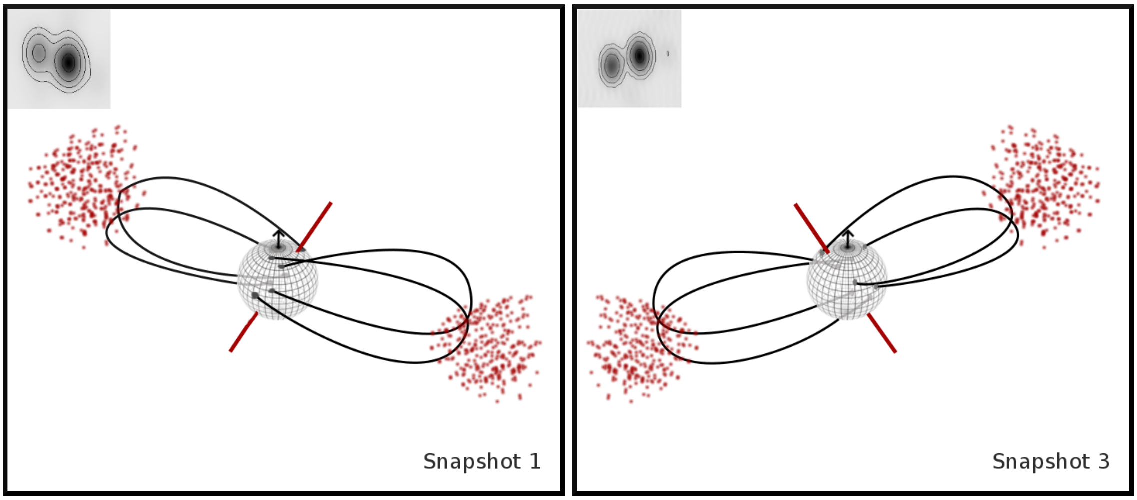

Figure 4.5: Flaring loop model applied to 2007 data. AB Dor A is represented as a sphere with its rotation axis indicated by an arrow ($i \sim 60°$, $\mathrm{PA_{rot}} \sim 0°$) and a slightly misaligned magnetic axis ($\sim 20°$) which is plotted as a red line. The radio emission is originated by magnetic reconnection and/or interaction at top of the loop system surrounding the star. As discussed in the main text, the rotation of the star would create snapshot 1 (left panel) and snapshot 3 (right panel).

this type of emission may be necessary to clarify this point.

Therefore, the polar cap hypothesis can explain our results considering 1) a rotation axis oriented east-west ($\mathrm{PA_{rot}} \sim 270°$ in the plane of the sky), and 2) a misalignment between the magnetic and rotation axis of ~22°. This is a fairly stringent, but certainly possible scenario to explain the complex internal structure of AB Dor A.

4.5.2 Flaring loops hypothesis

A great number of flaring events are known to occur in AB Dor A (see Schmitt et al. 2019, and references therein). From these and previous studies, it is well established that the corona of this star presents evidence for both compact and extended structures. Typically, X-ray observations tend to detect small closed loops near the surface (Maggio et al. 2000) while Hα absorption transients reveal cool condensations of neutral hydrogen trapped within the corona by the star magnetic field extending several stellar radii away from the rotation axis of the star (Collier Cameron & Robinson 1989), indicating the possible presence of giant loops in AB Dor A. On the other hand, Cohen et al. (2010) carried out detailed numerical simulations finding that the corona of AB Dor A must be dominated by strong azimuthal tangling of the magnetic field due to its ultra-rapid rotation. This azimuthal wrapping of the magnetic field lines could lead to strongly curved, and eventually interacting, magnetic loops which may extend up to $\sim 10\,R_{\rm star}$. Rather than episodic events (which are not excluded), and following the scenario proposed by Lim et al. (1992), these loops could constitute a quasi-permanent structure azimuthally distributed (following the magnetic field wrapping as modeled by Cohen et al. (2010) where magnetic reconnection and/or interaction events may occur. These interactions would produce a permanent acceleration of the plasma electrons which would justify the permanent radio emission. The idea of an extended corona in AB Dor A is also justified by the above-mentioned presence of massive prominences at large distances from the stellar disk, in turn associated to the existence of large and energetic loops (Villarreal D'Angelo et al. 2018, and references therein). The morphological similarity between the images at 8.4 GHz in Fig. 4.1 (east-west radio emission) certainly seems to support the presence of a long-lived, extended loop structure.

Under this hypothesis, component 1 and 2 in epochs 2007 and 2010 (Fig. 4.1) would correspond, respectively, to the east and west side of such a flaring structure at a height of $\sim 5R_{\rm star}$ around AB Dor A (see Fig. 4.5 for easier visualization). We notice that a $PA_{\rm rot}\sim 0^\circ$ and a slightly misaligned magnetic field (~20°) would successfully reproduce the snapshot maps in 2007 and 2010: considering the star rotation after 6 hours (time difference between snapshots 1 and 3) the magnetic axis would have rotated ~180° around the rotation axis which, translated to our images, would correspond to the different orientation of the emission seen between snapshot 1 and 3 (see Fig. 4.5). This model is also compatible with the snapshot images in 2013, assuming that the easternmost (in principle, weaker) side of the flaring structure is not seen or detected during the first part of the observations. We notice that the registration of the snapshot images seems to support this hypothesis as both component 1 and 2 (in 2007 and 2010) move in opposite directions (see Fig. 4.2) as it would correspond to the motion of the azimuthally-distributed emission region due to the rotation of the misaligned magnetic field axis. On the other hand, the fact that component 1 is permanently brighter that component 2 does not have a unique answer in this model, although it could be explained by a combination of 1) inhomogeneities in the radio emission region, 2) orientation effects of a clockwise rotation, given the high directivity of the radio emission (as corresponds to synchrotron emission), and 3) occultation and/or absorption due to the stellar disk or slingshot prominences.

Helmet streamers hypothesis

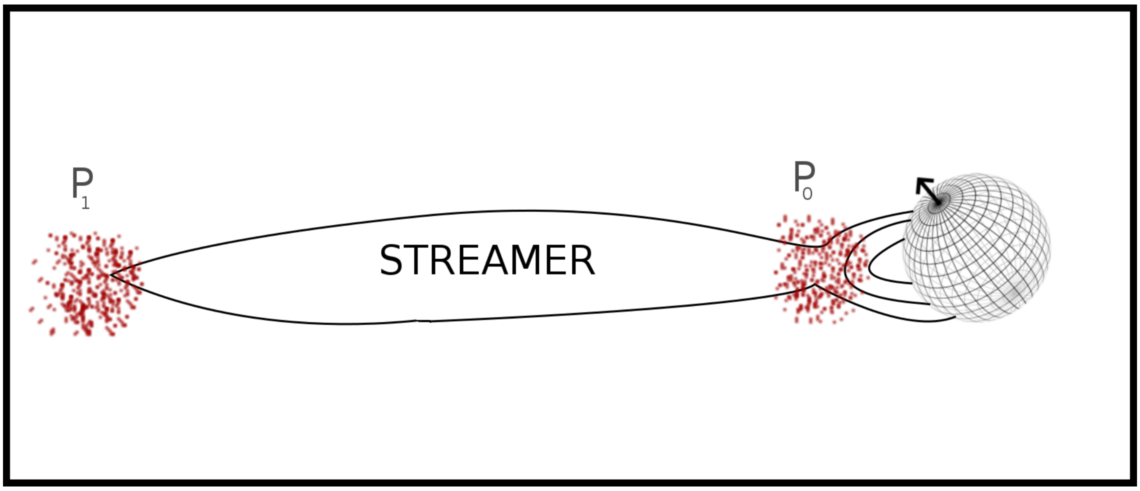

Figure 4.6: Sketch of the emission and magnetic structure of a helmet streamer in AB Dor A. P_0 and P_1 denote the lower and upper mirror points, respectively, where the radio emission is generated. See text.

As introduced in the previous Section, the slingshot prominences detected by Collier Cameron & Robinson (1989) are corotating condensations of mostly neutral gas whose physics has been abundantly studied (Ferreira 2000; Jardine & van Ballegooijen 2005; Jardine & Collier Cameron 2019; Waugh & Jardine 2019; Villarreal D'Angelo et al. 2019; Jardine et al. 2019). Similarly to the solar case, helmet streamers and flares are expected to occur at the top of such prominences (although not exclusively) triggered by magnetic reconnection of the coronal loops. Evidence of stellar helmet streamers has been reported for the binary system V773 Tauri A via VLBI observations (Massi et al. 2008) which revealed a complex magnetic structure around this object, although more recent observations did not confirmed such structures (Torres et al. 2012). The well-known presence of frequent slingshot prominences at large height in AB Dor A led us to consider that its internal mas-scale structure in radio could be the observational evidence of the formation of helmet streamers on top of magnetic loops. Supporting this hypothesis, and only one month after our 2007 observations, Jardine et al. (2019) reported two unusually big slingshot prominences in AB Dor A, which may have been the consequence of a very energetic event. Although the lifespans of these phenomena are 2–3 days, the formation and ejection of prominences is thought to be a continuous process in AB Dor A (up to 18 events per day; Villarreal D'Angelo et al. 2018) and so will be the presence of associated helmet streamers. This recurrent scenario would justify the permanent extended structure seen in Fig. 4.1.

Within a helmet streamer, confined particles travel along the streamer and are reflected back between both lower and upper mirror points (see Fig. 4.6; Melrose & Brown 1976), both of which would constitute the radio emitter regions. Under this hypothesis, component 2 in our images of epochs 2007 and 2010 would be interpreted as the upper mirror point, meanwhile the brighter component 1 would correspond to the lower mirror point blended together with the coronal emission produced near the stellar disk. In the particular case of epoch 2013, the presence of the streamer would be detected only during the second half of the observation, which would create component 2. As can be seen in Fig. 4.1, the streamer would not corotate with the star, otherwise we would have detected its emission coming from the west-side of the star during the 12 hours of observation. This is reinforced by our snapshots images (Fig. 4.2) showing that, during the entire observation, component 2 had an apparent rotation of only 40° (47°) in 2007 (2010) between snapshot 1 and 3, separated by 6 hours.

Is a non-corotating helmet streamer an acceptable scenario? According to our images, the streamer would extend up to 9–10 R_{star} (18 R_{star}) in 2007 and 2010 (2013). These values are considerably lower than the Alfvén radius (distance below which the magnetic field dominates the gas pressure and forces the material to co-rotate with the star) for AB Dor A, which is estimated to be 24 R_{star} (Villarreal D'Angelo et al. 2018). These values do not favor a non-corotating streamer in AB Dor A. However, there is no clear evidence that helmet streamers must co-rotate with the star; actually, the observed positions of the tentative helmet streamers in V773 Tau A do not correspond to those predicted by the stellar rotation (Massi et al. 2008). After all, once the helmet streamer has been produced, it is no longer attached to the star surface and may be subjected to curve following the strongly wrapped magnetic field of AB Dor A. Even more, in correspondence with the continuous ejection of slingshot prominences, the upper mirror points may also be expelled due to the fast rotation. Yet, the preference for eastward helmet streamers at the three epochs would have an unclear origin.

4.5.3 Close companion hypothesis

Although it may be tempting to interpret the 8.4 GHz images (Fig. 4.1) as a binary system (identifying AB Dor A as component 1 and the companion as component 2), the temporal analysis of Fig. 4.2 makes this scenario highly unlikely. Assuming that the axis of the orbital plane is parallel to the rotational axis of AB Dor A (left panel in Fig. 4.3), at only 3 mas of separation, the fast orbital motion of component 2 (both in 2007 and 2010) would imply unacceptable large values of the radial velocity semi-amplitude of the stellar reflex motion, much greater than the precision of previously-reported radial velocity measurements of AB Dor A (32.4 ± 2.2 $\mathrm{km \cdot s^{-1}}$; Gontcharov 2006).

4.5.4 AB Dor C

Our non-detections at any of the observed frequencies put a strong upper bound to the flux density of the ultracool dwarf AB Dor C (see Sect. 4.4.3). The study of samples of ultracool dwarfs (McLean et al. 2012; Route & Wolszczan 2013) has showed that these kind of objects are not typically expected to present radio emission. Nonetheless, some authors have detected radio emission from late M, L and T objects (Matthews 2013; Hallinan et al. 2015; Guirado et al. 2018) which has been associated with an electron cyclotron maser emission mechanism. They might have benefited from the strong correlation between auroral radio emission and the presence of H_α line (Kao et al. 2016). In spite of the fact that there is no current evidence for H_α line emission in AB Dor C, there are some facts that might indicate radio emission in this ultracool dwarf:

a) Young and late M-dwarfs, like AB Dor C, tend to present H_α emission (West & Hawley 2008) which may be indicative of auroral radio emission.

b) The model of Reiners & Christensen (2010) and the scaling law reported in Christensen et al. (2009) (magnetic field ∝ energy flux, valid for fully convective, rapid rotating objects) predict magnetic fields ¿10^3 G for an object with mass as low as 72 M_J.

c) AB Dor A is know to possess a strong magnetic field and H_α emission (Lalitha et al. 2013, and references therein). Since the system could have been formed from collapse and fragmentation of the same rotating cloud, AB Dor C may have retained some of the characteristics of AB Dor A, i.e, high rotational velocity and strong magnetic field. These features could then be responsible for radio emission in this ultracool dwarf, although variable in time and/or fainter than expected, explaining our non-detection.

More sensitive observations would be necessary to address the possible radio emission of this object. The radio detection of AB Dor C would be of great importance to probe its emission mechanism and might provide some insights on its structure.

4.6 Conclusions

Our multi-epoch, multi-frequency observations of the binary system AB Dor A/C revealed an intriguing scenario in the main star of the system. At 1.4 GHz, AB Dor A was detected as a point-like unresolved source with no flux variability during the 12 hours that our observation lasted and with circular polarization lower than 10%. With a minimum brightness temperature of 3.5×10^7 K, the origin of this emission seems to be non-thermal gyrosynchrotron or synchrotron emission coming from accelerated electrons located in the outer layers of the corona. A tentative detection (with SNR $\sim$ 5) was also made at 22.3 GHz with emission located ~18 R_{star} away from the expected position, and whose origin remains unclear. Reanalysis of the 8.4 GHz data resulted in the detection of an extended and variable structure, morphologically similar at all epochs. We considered four different scenarios in order to explain the 8.4 GHz observations:

a) A polar cap model with emission coming from above the polar regions of the star. Under this hypothesis, the rotation axis would be oriented east-west, and the magnetic axis would be slightly misaligned with respect to the rotation axis. This model is able to successfully explain the 2007 and 2010 preferred east-west orientation of the emission, the relative motion between components and the fact that the western component seems to be always the brightest. One of the polar cap regions is not seen (or not detected) in the first snapshot image of epoch 2013. Although the geometric requirements are stringent, this model explains the observational features seen in our 8.4 GHz images.

b) A flaring loop model where the emission would originate due to magnetic reconnection of a coronal loop structure distributed azimuthally following the magnetic field lines, in turn wrapped by the rapid rotation of AB Dor A. Counting with a nearly north-south rotation axis, a slightly misaligned magnetic axis would rotate reproducing the different snapshot images with the emission coming from magnetic reconnection events at heights 5–9 R_{star}. Again, in the case of 2013, during the first half of the observation, only one side of the loop structure was detected. It is not clear how this model may justify why the westernmost component is the brightest one, although a combination of orientation and absorption effects could produce such an effect.

c) A helmet streamer model where the radio emission is originated at the upper and lower mirror points, the latter likely merged with coronal emission of AB Dor A itself. Helmet streamers are in principle associated to large and continuously produced slingshot prominences; our maps suggest that the streamers may be curved due to fast rotation and may not necessarily corotate with the star. Helmet streamers could successfully explain most of the observed characteristics of our data; yet, the preferred eastwards orientation of the radio emission needs to be properly explained under this model.

d) A close companion to AB Dor A, which would readily justify the binary radio morphology. This model is, however, highly unlikely: the small separation between both components would produce unacceptable large radial velocity values, incompatible with previously published observational measurements of AB Dor A.

Whichever model is correct for AB Dor A, our results confirm the extraordinary coronal magnetic activity of this star, able to produce compact radio structures at very large heights, so far only seen in interacting binary systems. Finally, no emission was found at the expected position of the ultracool dwarf AB Dor C, placing strong upper limits to this binary brown dwarf. New data will provide an excellent opportunity to further investigate this remarkable system.

Chapter 5

Radio emission in ultracool dwarfs: The nearby substellar triple system VHS 1256-1257

This chapter is based on the homonymous publication that appeared on Astronomy and Astrophysics, 610, A23, 2018 with DOI: 10.1051/0004-6361/201732130 and published on February 2018.

5.1 Introduction

Radio observations play an important role to understand the processes involved in the formation and evolution of stellar and substellar objects. In particular, radio emission studies of ultracool objects (late M, L, and T objects; e.g., Matthews 2013; Kao et al. 2016, and references therein) are relevant to probe the magnetic activity of these objects and its influence on the formation of disks or planets. Moreover, the study of ultracool dwarfs may open a suitable route to the detection of radio emission of exoplanets: meanwhile no exoplanet has been yet detected at radio wavelengths, an increasing number of ultracool objects (McLean et al. 2012) show substantial evidence of radio emission at

GHz-frequencies in objects with spectral types as cool as T6.5 (Kao et al. 2016). But radio detection of ultracool dwarfs is still a relatively rare phenomenon, and new candidates are needed to improve the statistics of active cool objects. One of these targets is the system VHS J125601.92–125723.9 (hereafter VHS 1256–1257; Gauza et al. 2015); this system is composed by a 0.1″ equal-magnitude M7.5 binary (components A and B; Stone et al. 2016) and a lower-mass L7 companion (component b) separated 8″ from the primary pair. The system is relatively young, 150–300 Myr, and nearby (12.7–17.1 pc), which locate the low-mass object b near the deuterium burning limit (Stone et al. 2016). Recently, Zapatero Osorio et al. (2017, in preparation) have determined a new trigonometric distance of $15.8^{+1.0}_{-0.8}$ pc for the system using optical and near-infrared images spanning a few years. This distance is compatible with a likely age of 300 Myr, which agrees with the strong lithium depletion observed in the high resolution spectra of the M7.5 binary and the recent age determinations of Stone et al. (2016) and Rich et al. (2016). In this work, we will adopt these values of distance and age. Using the bolometric corrections available for M7-M8 and red L dwarfs (Golimowski et al. 2004; Filippazzo et al. 2015) and the new distance, the luminosities are determined at $\log L/L_\odot = -4.91 \pm 0.10$ dex for the faint L7 companion VHS 1256−1257 b and $\log L/L_\odot = -3.24 \pm 0.10$ dex for each member of the M7.5 binary. By applying the luminosity-mass-age relationship of Chabrier et al. (2000), we infer masses in the interval 10-20 $M_{\rm Jup}$ (VHS 1256−1257 b) and 50-80 $M_{\rm Jup}$ (A and B components) for the age range 150-300 Myr, with most likely values of 15-20 $M_{\rm Jup}$ and 70-80 $M_{\rm Jup}$ at 300 Myr. The interest in VHS 1256–1257 is obvious for several reasons: first, it is only the third multiple system in which all three components may be substellar (Bouy et al. 2005; Radigan et al. 2013); second, the L7 source belongs to one intriguing (not yet understood) population of very red L dwarfs with likely high content of atmospheric dust or high metallicity (Rich et al. 2016); third, given their large separation (8″), unambiguous observations of the substellar object b and the central pair AB are accessible by instruments at virtually all wavelengths, including radio; and fourth, the binarity of the host system AB will permit the determination of their dynamical masses in a few years, which is essential to fully characterize the system. Additionally, Gauza et al. (2015) reports detection of the H_α line emission (656.3 nm) in the primary, which indicates the existence of chromospheric activity in this M7.5 low-mass binary, therefore showing ability to sustain significant magnetic fields, and hence, radio emission.

Table 5.1: VLA and VLBI Observations of VHS 1256–1257

Telescope / Configuration	Epoch	Frequency band	UT Range	Beam size	P.A. [°]	rms [μJy]	Peak [μJy]
VLA / BnA	15 May 2015	X	05:10 - 06:10	$0.78'' \times 0.45''$	−51	3	60
VLA / B	28 Jul 2016	L	00:00 - 01:00	$5.66'' \times 3.38''$	−12	7	<21
EVN[a]	4 Mar 2016	L	22:30 - 04:30	3.1 × 2.4 mas	−64	22	<66
”	27 May 2016	”	15:30 - 23:30	11.9 × 2.2 mas	−78	30	<90
”	2 Nov 2016	”	05:00 - 13:00	3.2 × 2.3 mas	−73	31	<93

Notes. [a]: European VLBI Network using the following antennas: Jodrell Bank, Westerbork, Effelsberg, Medicina, Noto, Onsala85, Tianma65, Urumqi, Torun, Zelenchukskaya, Hartebeesthoek, Sardinia, Irbene, and DSS63.

In this paper we present Karl G. Jansky Very Large Array (VLA) and European VLBI Network (EVN) observations of VHS 1256−1257. We describe our observations and report the principal results, consisting in the discovery of the radio emission of the central components of the VHS 1256−1257 system. We also present a study of the spectral behaviour of the detected emission and set an upper bound to the possible radio emission of the very low-mass companion VHS 1256–1257 b.

5.2 Observations and data reduction

5.2.1 VLA observations

We observed with DDT/Exploratory Time with the VLA the system VHS 1256−1257 at X- and L-band on 2015 May 15 and 2016 Jul 28, respectively. The observation at X-band lasted 2 hours and was carried out in BnA configuration, using an effective bandwidth of 4 GHz (8−12 GHz) in dual polarization. The observation at L-band lasted 1 hour, in B configuration, and using an effective bandwidth of 1 GHz (1−2 GHz) in dual polarization (see Table 5.1). We used 3C286 as absolute flux calibrator meanwhile we performed amplitude and phase calibration using interleaved observations of the radio source J1254−1317. Data reduction and imaging were carried out using the CASA[a] software package of the NRAO. The standard procedure of calibration for continuum VLA data was applied. Special care was taken to flag data contaminated by radio frequency interferences (RFI) at *L*-band. The resulting images are shown in Fig. 5.1.

5.2.2 VLBI observations

The VLA observations explained above confirmed the radio emission of VHS 1256−1257. This detection triggered VLBI observations that were carried out with the EVN at *L*-band (1.6 GHz; see Table 5.1) with the purpose of constraining both the origin and properties of the radio emission. Each observation lasted 6–7 hr and both polarizations were recorded with a rate of 1024 Mbps (two polarizations, eight subbands per polarization, 16 MHz per subband, two bits per sample). We used the phase-reference mode and the selected calibrators were J1254−1317 (as primary calibrator, separated 0.5° from VHS 1256−1257), and J1303−1051 (as secondary calibrator, separated 2.7°). The duty cycle was 1 min on the primary calibrator, 3 min on the target, and 1 min on the secondary calibrator, with a total integration time at the target of ∼3.5 hr per epoch.

The data reduction was realized using the program Astronomical Image Processing System (AIPS) of the National Radio Astronomy Observatory (NRAO) with standard routines. Once the final data were obtained, the images were made with the Caltech imaging program DIFMAP (Shepherd et al. 1994). We did not detect neither the central M7.5 binary nor the very-low mass substellar companion at any epoch, establishing an average flux density upper limit of $\sim 80\,\mu$Jy (3σ). The interpretation of these non-detection will be discussed in next Section.

---

[a] http://casa.nrao.edu

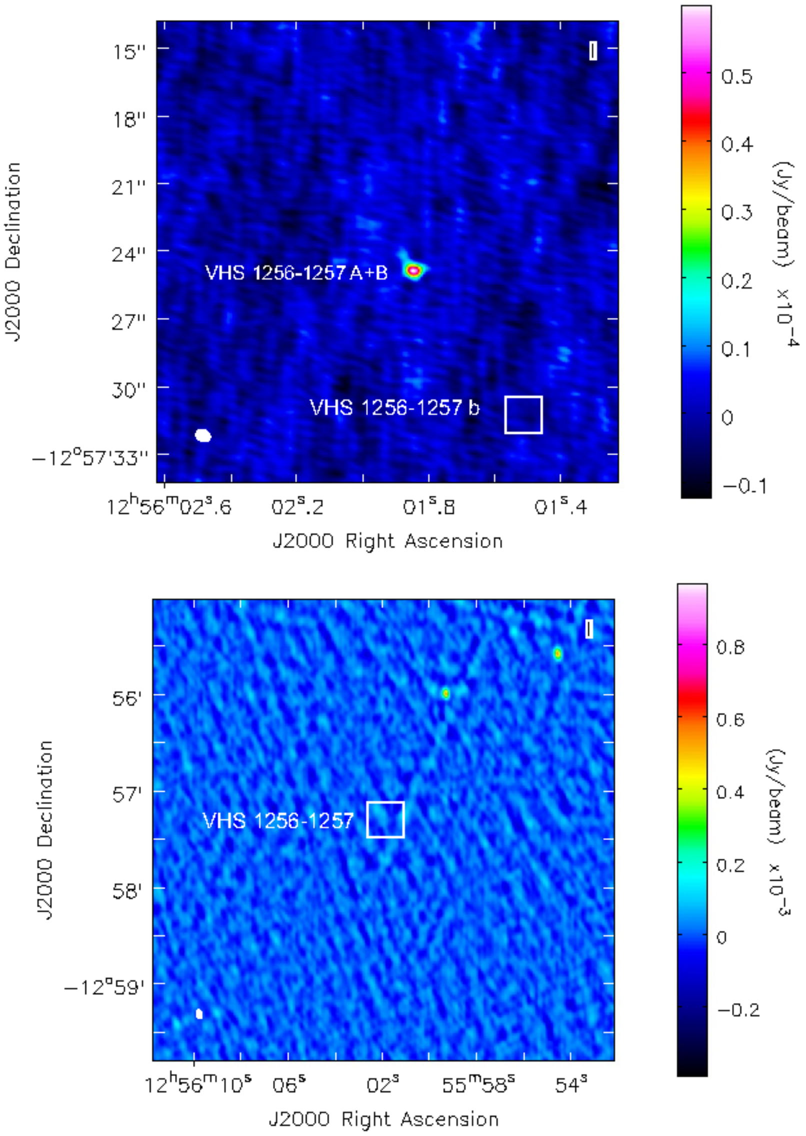

Figure 5.1: *Top.* VLA image of the VHS 1256−1257 field at X-band. The detected source is readily assigned to the M7.5 binary VHS 1256−1257 AB. The location of the (undetected) L7-object b is marked with a solid white box. The $3\,\sigma$ threshold detection is $9\,\mu$Jy. The restoring beam, shown at the bottom left corner, is an elliptical Gaussian of 0.78×0.45 arcsec (P.A. −51°). At 15.8 pc, the separation between components AB and b corresponds to 128.4 AU. *Bottom.* VLA image of the VHS 1256−1257 field at L-band. A solid box, with size that of the X-band image, is centered at the position of the X-band detection. None of the VHS 1256−1257 components is detected at this frequency band. The $3\,\sigma$ threshold detection is $20\,\mu$Jy. The two bright knots seen in the map at the NW correspond to known extragalactic radio sources. The restoring beam, shown at the bottom left corner, is an elliptical Gaussian of 5.66×3.38 arcsec (P.A. −12°).

5.3 Results and Discussion

5.3.1 The radio emission of the central pair VHS 1256–1257 AB

Figure 5.1 revealed a clear detection on 2015 May 15 (*X*-band) of an unresolved source with a peak flux density of $60\,\mu$Jy, which can be assigned to the primary of VHS 1256−1257, the equal-mass M7.5 binary. We confirmed this identification by using both the coordinates and proper motion given in Gauza et al. (2015) to find the expected position of component AB at the time of our observation; this expected position differs only $0.18''$, about one third of the synthesized beam, from the measured position in the VLA *X*-band map in Fig. 5.1 (the source has moved ~$6.3''$ between Gauza's epoch and ours). A noise floor of $\sim 3\,\mu$Jy imposes a strong upper bound to the radio emission at the expected position of the low-mass companion VHS 1256–1257 b. In contrast, we found no detection in any of the components of the system on 2016 July 28 (*L*-band), with a 3σ threshold detection of $20\,\mu$Jy. The flux density measured at *X*-band implies a radio luminosity of 1.95×10^{-13} erg s^{-1} Hz^{-1} at 15.8 pc. Assuming that the flux is originated at only one of the central components of VHS 1256–1257, this luminosity is similar to other single ultracool dwarfs detected with comparable spectral types (M7.5; McLean et al. 2012). We notice that the figures above are halved if we consider both components to contribute equally to the radio flux. We did not detect significant traces of variability or pulsed emission in the flux density throughout the 2 hr duration of our observations, which suggests that the detected radio emission is produced either in quiescent conditions or, alternatively, during a long-duration, energetic flare. However, the latter possibility seems unlikely given the low frequency rate of energetic flares in late M dwarfs (~0.1/day) recently reported by Gizis et al. (2017).

Obtaining an estimate of the brightness temperature is difficult since the resolution of our observations does not provide a precise estimate of the size of the emitting region. Additionally, as said above, the fraction of the radio emission which is originated at each component of the central binary is unknown. Under the assumption that radio emission comes from a single object of size $0.12\,R_\odot$ (derived from the models of Chabrier et al. (2000)), we calculate a brightness temperature of 5.4×10^7 K ($\times1/2$ for equal binary contribution), which is consistent with synchrotron or gyrosynchrotron non-thermal radio emission (Dulk 1985). In principle, the low degree of circular polarization (less than 15%) seems to discard coherent mechanisms predicted for ultracool dwarfs (i.e., auroral emissions; Hallinan et al. 2015; Kao et al. 2016), normally associated to a high degree of polarization; however, in case that both components A and B contribute to the radio emission, we notice that the degree of circular polarization above would be the result of the combination of both radio emitters, not reflecting properly the polarization properties of each one. Further information about the emission mechanism acting on this object can be obtained from the 4 GHz recorded bandwidth of our *X*-band VLA observations. In practice, we produced four narrower-band images of VHS 1256-1257 by deconvolving adjacent 1 GHz-bandwidth data sets separately (see Fig. 5.2), from which we could obtain an indication of the spectral behaviour of this system between 8 and 12 GHz. The corresponding spectral index is $\alpha = -1.1\pm0.3$ ($S \propto \nu^{\alpha}$), compatible with optically thin non-thermal synchrotron or gyrosynchrotron emission from a power-law energy distribution of electrons, indicating, in turn, that strong magnetic fields play an active role in this system.

If the optically thin regime would hold until frequencies as low as 1.4 GHz, we should have detected radio emission in VHS 1256–1257 with a flux density above 300 μJy (actually, this was the motivation for the 1.6 GHz VLBI observations reported); however, no flux above 20 μJy is detected at the nominal position of VHS 1256-1257 at *L*-band. Ultracool dwarfs have shown to be strongly variable source in radio (Bower et al. 2016), therefore arguments of variability could explain this lack of detection. However, the persistent non-detection in our VLBI observations (with a noise floor 10 times smaller than the expected 1.6 GHz flux density according to the spectral index derived) led us to formulate a different hypothesis consisting in considering that the radio emission is actually self-absorbed at the frequency of 1.4 GHz.

We have further explored this hypothesis following the analytic expressions developed by White et al. (1989, W89) for gyrosynchrotron radio emission of dMe stars in quiescent conditions, which provide estimates of the spectral index for the optically thick/thin components, and, therefore, the turnover frequency. We notice that synchrotron radio emission is not ruled out by our data, but gyrosynchrotron from midly relativistic electrons seems to be the preferred mechanism for previously studied M-dwarfs (i.e., Osten & Jayawardhana 2006; Osten et al. 2009), which in turn justifies the use of W89 formulation. These authors assume a dipolar magnetic field which scales as $B(r) \propto r^{-n}$, with $n = 3$ and r the distance measured from the dipole, and a power-law electron distribution $N'(E)$ which also scales as $N(E) \propto N'_o(E)\, r^{-m}$, where the index m varies from 0 (isotropic electron distribution) to $m = 3$ ($= n$, radial dependence of the electron distribution being the same as that of the magnetic field). Taking our measured optically-thin spectral index ($\alpha = -1.1 \pm 0.3$), which implies an energy index $\delta = 2.6$, W89 expressions provide two values for the spectral index of the optically thick component of the radiation, $\alpha = 0.6$, and $\alpha = 1.2$, corresponding to the two extreme cases of $m = 0$, and $m = 3$, respectively. With the constraints above, we can set lower bounds to the turnover frequency of ~8 GHz ($m = 0$) and ~5 GHz ($m = 3$), effectively limiting the turnover frequency to the range 5 – 8.5 GHz.

In addition, for gyrosynchrotron emission, the turnover frequency depends strongly of the magnetic field (and very weakly of the rest of the model parameters, m and n in particular; W89) in the form B$\sim$150 $\nu^{1.3}$, which provides magnetic field intensities for the previous turnover frequency range of 1.2–2.2 kG. Interestingly, the previous values agree with M-dwarf magnetic field estimates derived from theoretical models (Reiners & Christensen 2010): from the luminosity and mass reported for the components of VHS 1256-1257A and B (Stone et al. 2016; Rich et al. 2016), and using the radius of 0.12 $R_\odot$ the model of Reiners & Christensen (2010) provides values of the dipole field of ~1.7 kG, well within the range derived previously. This estimate is near the average value of the magnetic field intensity found in a sample of M7–9.5 dwarfs (Reiners & Christensen 2010).

5.3.2 The spectral energy distribution of VHS 1256-1257 AB

Figure 5.4 shows the complete spectral energy distribution (SED) of VHS 1256−1257AB covering from VLA through optical observations. The data at visible, near- and mid-

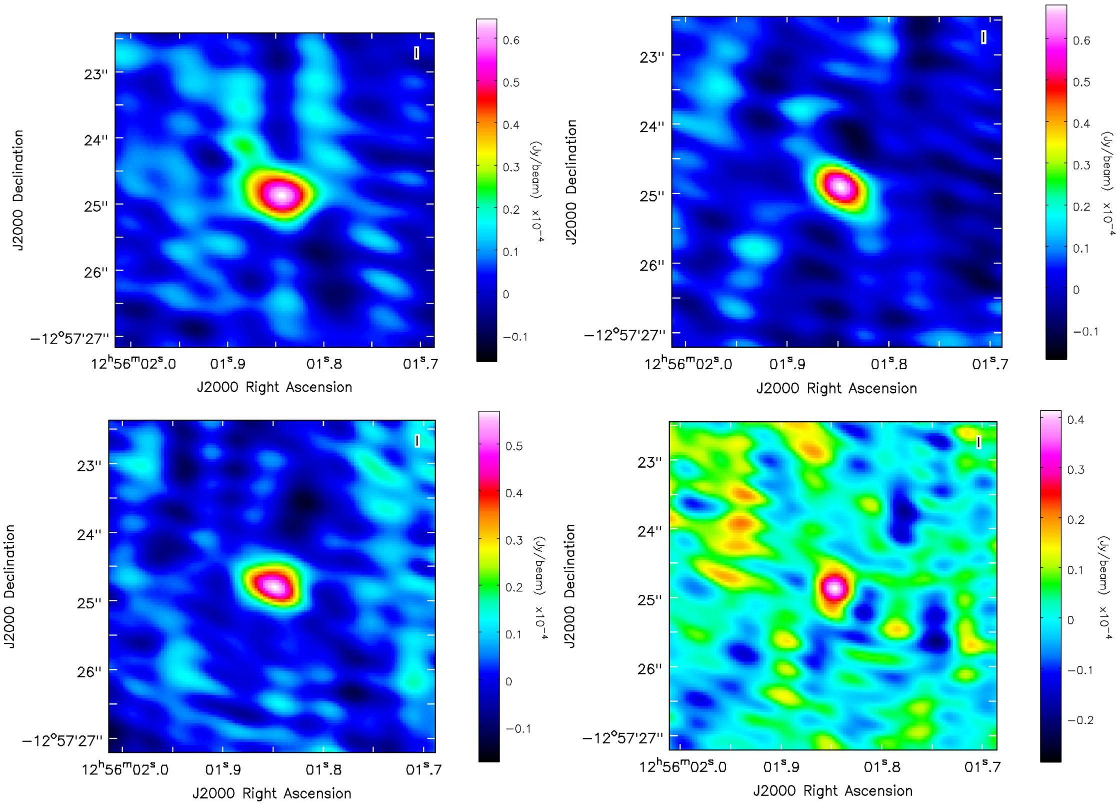

Figure 5.2: VLA images of the VHS 1256−1257 system (unresolved central binary AB) at X-band made from 1 GHz subsets of the total data. In the following order: top left, top right, bottom left, bottom right, the center frequency is 8.5, 9.5, 10.5, and 11.5 GHz, respectively. The peak flux density decreases from 63 μJy (top left) to 45 μJy (bottom right image).

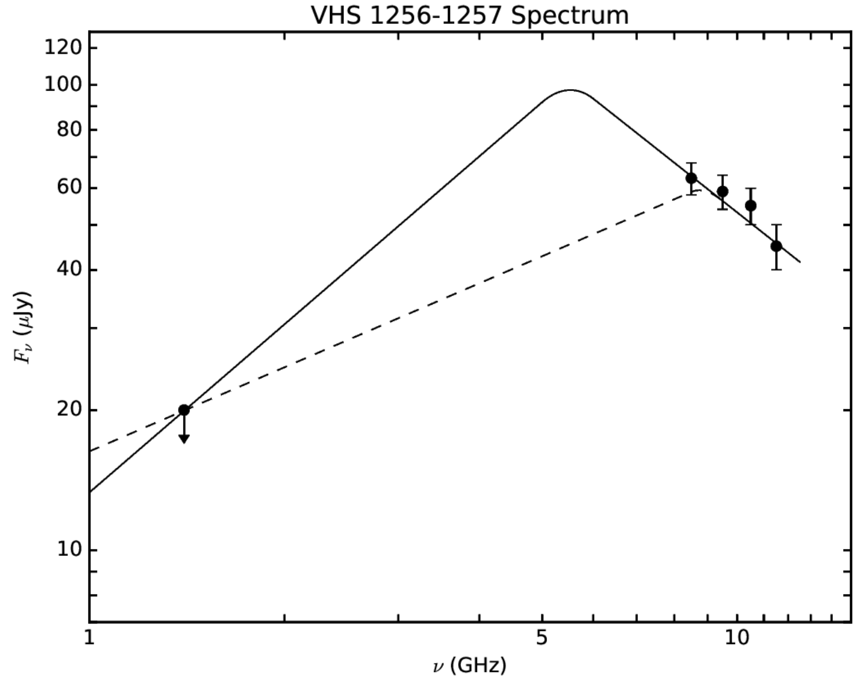

Figure 5.3: Spectrum of VHS 1256–1257 from VLA observations. The flux densities between 8 and 12 GHz correspond to the maps shown in Fig. 5.2. The upper bound resulting from the non-detection at *L*-band is denoted with a downwards arrow. The solid lines illustrate two possible spectra, each one made from a combination of the behaviour predicted by the White et al. (1989) model of gyrosynchrotron emission (optically thick regime, showing the two extreme cases, α=0.6 –dashed line– and 1.2 –solid line–), and a fit to our flux density measurements (optically thin regime, $\alpha = -1.1$).

infrared wavelengths are taken from Gauza et al. (2015). The observed spectrum is conveniently flux calibrated using the 2MASS *JHK* magnitudes and the zero points given in Cohen et al. (2003). The *W*4 photometry reported in Gauza et al. (2015) is affected by a large uncertainty indicative of S/N $\leq$ 4. Therefore, we adopt the nominal sensitivity limit of the *WISE* mission at 22 μm (Wright et al. 2010). The BT-Settl solar metallicity model atmosphere (Baraffe et al. 2015) computed for $T_{\rm eff} = 2600$ K and $\log g = 5.0$ [cm s^{-2}] is also included in Figure 5.4 to illustrate the expected photospheric emission at frequencies not covered by the observations. The synthetical spectrum is normalized to the *J*-band emission of VHS 1256−1257AB. This temperature and surface gravity are expected for dwarfs near the star–brown dwarf borderline with an age of a few hundred Myr (Chabrier et al. 2000). They also agree with the spectral type—$T_{\rm eff}$ relationship defined for high-gravity, ultracool dwarfs by Filippazzo et al. (2015) and Faherty et al. (2016). The BT-Settl photospheric model extends from ~300 up to ~ 7.5 × 10^5 GHz and does not overlap in the frequency axis with the VLA observations. A linear extrapolation of the theoretical SED down to 10 GHz yields a predicted photospheric flux of ~ 8.3 × 10^{-7} mJy. The observed VLA *X*-band flux is ~65,800 times higher than the expected photospheric emission suggesting that the mechanism responsible for the emission at 10 GHz is extremely powerful.

5.3.3 The radio emission of the very low-mass companion VHS 1256–1257 b

Our non-detection at *X*-band put a strong upper bound to the flux density of this L7 object of 9 μJy (3 σ). Certainly, the ultracool dwarf samples carried out by McLean et al. (2012) and Route & Wolszczan (2013) show that radio detections at GHz-frequencies are not frequent for objects later than L3.5, which could be expected by the declining activity of the cooler atmospheres of these objects. Despite this, auroral radio emission (based on electron cyclotron maser emission mechanism) has been detected in a number of late L and T dwarfs (i.e., Hallinan et al. 2015; Kao et al. 2016; Pineda et al. 2017). Could this emission be expected in VHS 1256-1257 b? At a distance of 15.8 pc, the reported luminosities of the coolest dwarfs detected in radio (Pineda et al. 2017) would produce a quiescent emission of ~4 μJy (below our 3 σ detection level). In case of auroral, pulsed emission, the radio flux would significantly rise up to peaks of 100 μJy, a factor of ~10 above our detection limit in *X*-band. However, we do not see such a peak in our data indicating that, at the moment of the VLA observations, VHS 1256−1257 b did not show strong levels of auroral activity similar to those seen in other ultracool dwarfs. Kao et al. (2016) found a strong correlation between radio aurorae and the presence of the H_α line; however, only 7–13% of the dwarfs with spectral types between L4 and T8 display H_α emission (Pineda et al. 2016). Given the absence of H_α in VHS 1256-1257 b, the statistics above do not favor the presence of auroral radio emission in this object.

On the other hand, considering the ~kG estimate of the magnetic field for VHS 1256 -

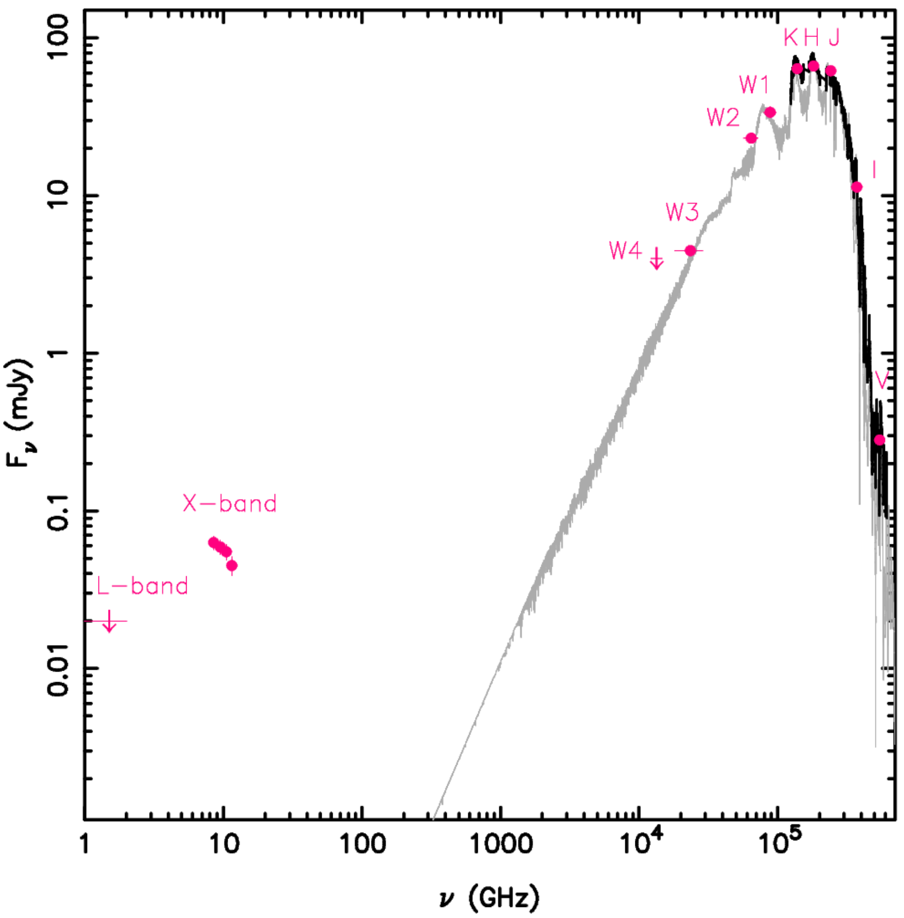

Figure 5.4: Observed spectral energy distribution of the unresolved binary VHS 1256−1257AB from optical wavelengths through 1 GHz. The optical and near-infrared observed spectra (Gauza et al. 2015) are shown with a solid black line, while the photometric observations are plotted as pink symbols: solid circles stand for actual detections with SNR $\geq$ 4 and arrows represent 4-σ upper limits. The filter and passband names are labeled. The horizontal error bars represent the width of the filters. Also plotted is the BT-Settl photospheric model (gray line, Baraffe et al. 2015) normalized to the J-band flux of VHS 1256−1257AB. This model corresponds to a cool dwarf with solar metallicity, $T_{\rm eff} = 2600$ K, and $\log g = 5.0$ [cm s^{-2}], which are the parameters expected for an M7.5 source (0.06–0.072 M$_\odot$) with an age of a few hundred Myr (Chabrier et al. 2000).

1257AB, along with the fact that this triple system could have formed from collapse and fragmentation of the same rotating cloud, component b may have also retained high levels of rotation and magnetic field, which eventually may produce sustainable radio emission, although variable, explaining our non-detection. Indeed, both the model of Reiners & Christensen (2010) and the scaling law reported in Christensen et al. (2009) (magnetic field $\propto$ energy flux, valid for fully convective, rapidly rotating objects) predict magnetic fields $>10^2$ G for an object with mass as low as 10–20 $M_{\rm Jup}$, and effective temperature of 800–1000 K (Gauza et al. 2015; Rich et al. 2016).

Additionally, we can estimate the possible radio emission of VHS 1256–1257 b from the Nichols et al. (2012) model. These authors consider the auroral emission as originating from magnetosphere-ionosphere coupling currents resulting from an angular velocity shear in a fast-rotating magnetized object. By assuming the fiducial parameters given in Nichols et al. (2012) (corresponding to a Jovian-like plasma), a magnetic field of ∼2 kG, and a rotation period of ∼2 hr (as extracted from the distribution of brown dwarf rotational periods given in Metchev et al. (2015)), we find that VHS 1256-157 b may present auroral emission with a peak flux density of $\sim100\mu$Jy, coincident with the estimate above resulting from Pineda et al. (2017) compilation. However, since the currents proposed by Nichols et al. (2012) are created through magnetic field reconnections, the cool atmosphere of VHS 1256–157 b may hamper the existence of auroral emission, as there are evidences that magnetic reconnections are not allowed or are suppressed at temperatures below ∼1500 K (Gizis et al. 2017).

5.4 Conclusions

We have reported the detection of radio emission from the VHS 1256–1257 system. Given the youthness of the system (∼300 Myr), its proximity, (15.8 pc), architecture (a possible triple substellar system), and presence of a very low-mass substellar object at 8″ from the primary, this detection appears relevant to study the role of the magnetic field in brown dwarfs. The radio emission is originated at the central system AB, likely consisting in non-thermal synchrotron or gyrosynchrotron emission in presence of kG-intense magnetic field. Further monitoring of the system at intermediate frequencies to those presented here should confirm our finding that the turnover frequency of the radiation is located between 5 and 8.5 GHz. The use of interferometers with higher resolution (eMERLIN or EVN at 5–8 GHz) should discriminate if the radio emission originates in one of the components (A or B), in both (A+B), or perhaps a sort of interaction between them. These higher resolution studies will open the door to a multiepoch astrometric study directed to the determination of the parallax of the system (modest 5-mas precise positions would result in a 1 pc-precise distance) and, additionally, to precise estimates of the masses of the internal pair via monitoring of its orbital motion (4.5 yr period for a face-on orbit). VHS 1256–1257 b is not seen in our maps; however, despite our non-detection at the level of 9 μJy, $\sim$100 G magnetic fields are expected in this 10–20 $M_{\rm Jup}$ object, therefore the presence of GHz-radio emission VHS 1256–1257 b should be further explored, as this would provide useful constraints to the emission mechanism in the coolest substellar objects.

Annex: A first look at VHS 1256-1257 K_a band data

We observed this system on 17 November 2018 and 26 November 2018 for a total time-on-target of 2 hours (1 hour each observation) using the VLA at K_a band (26-40 GHz). We intended to search for thermal emission that could reveal the possible presence of a dusty disk in this young system. Standard data reduction, very similar to that describe in Sect. 5.2.1, shows that radio emission is detected in both data sets. Once the data are combined using the CASA command *concat*, we found a peak of radio emission ~65 μJy (8-10σ) which is spatially coincident with the expected position of the central binary of the system. The resulting image is shown in Fig. 5.5.

To extract more information from this detection we tried to split the bandwidth of our observation into smaller portions following a similar procedure as the one described in Sect. 5.3.1. However, we only detected any emission in the lower portion of the K_a band. This might be a consequence of the lower sensitivity of the instrument at higher frequencies (see Fig. 5.6) and/or the fact that the spectra of the emission is not flat.

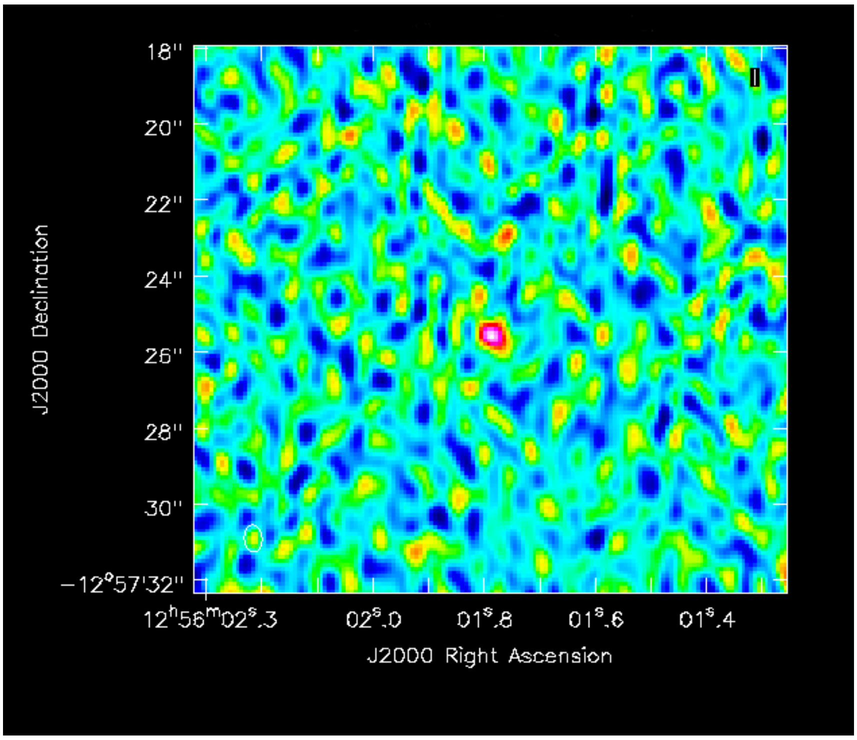

Figure 5.5: VLA K_a image of VHS 1256-1257. The detected emission is spatially coincident with the expected position of the central binary.

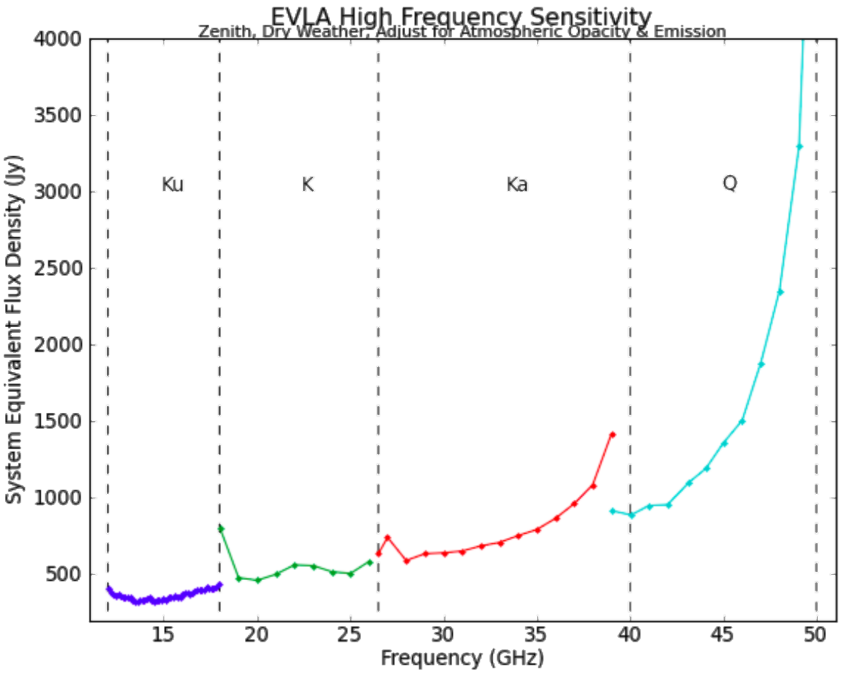

Figure 5.6: The system equivalent flux density as a function of frequency. Credit: NRAO

How does this detection fit the dusty disk model? Fig. 5.7 shows the SED of VHS 1256-1257 AB and, overlaid, the model of a dusty disk of a mass of 0.89 $M_{\rm moon}$, grain size of 100 μm, and temperature of 40 K combined with the BT-Settl model. Our detection has a flux density much greater than what would be expected from the presence of a dusty disk. Additionally, ALMA 7 band (275-373 GHz) data did not detect any emission from this object (Zapatero-Osorio, priv. communication) indicating that a dusty disk may not be the cause of the detected emission. Rather, flux density variability of the (gyro)synchrotron emission could explain the spectral behaviour in Fig. 5.7. A more detailed analysis and further observations are needed to better understand this intriguing object.

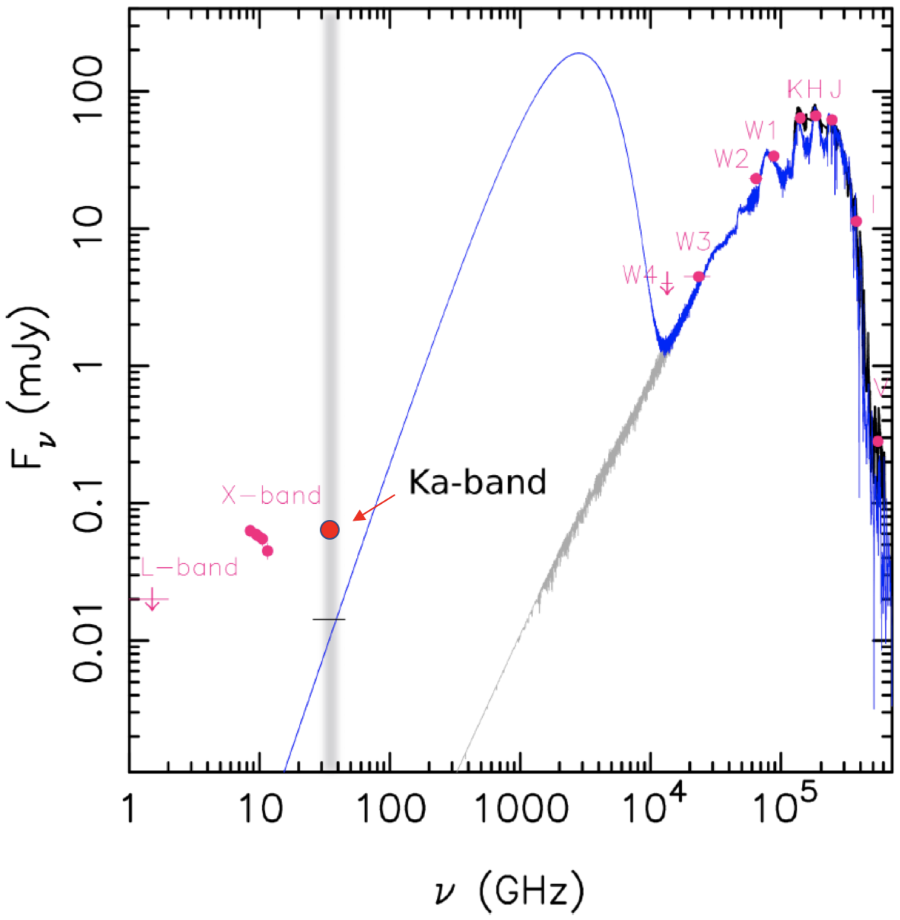

Figure 5.7: Same as Fig. 5.4 but including our new detection at K_a band. The gray shadowed area represents the bandwidth of our observations. The blue line represents the addition of a dusty disk of a mass of 0.89 $M_{\rm moon}$, grain size of 100 μm, and temperature of 40 K to the BT-Settl model.

Chapter 6

Evidence of a substellar companion to AB Dor C

This chapter is based on the homonymous publication that appeared on The Astrophysical Journal Letters, Volume 886, Issue 1, article id. L9, 7 pp. (2019), with DOI: 10.3847/2041-8213/ab5065 and published on November 2019.

6.1 Introduction

Stellar evolution models are essential to infer star fundamental parameters such as radius, mass, and/or age. Their reliability has long been tested and validated by the general good agreement between predictions and measurements. However, only recently have accurate measurements of stellar masses and radii become accessible in the case of low and very low-mass stars, thus allowing more stringent tests on stellar models. In the particular case of pre-main-sequence (PMS) stars, the models show an increasing difficulty in accurately reproducing some of the characteristics of star with masses below 1.2 $M_{\odot}$ (see, e.g., Hillenbrand & White 2004; Gennaro et al. 2012; Stassun et al. 2014).

Only stellar systems with dynamically determined masses can effectively be used to test and check the predictions of the models (see recent works of Dupuy & Liu (2017) and Mann et al. (2019)). AB Doradus (AB Dor) represents one such case. It is a PMS quadruple system formed by two pairs of stars separated by 9″, AB Dor A/C and AB Dor Ba/Bb (Close et al. 2005; Guirado et al. 2006), giving name to the AB Doradus moving group (AB Dor-MG). The main star of this system, the K0 dwarf AB Dor A (K_s = 4.686) has been extensively studied at all wavelengths, from the UV to radio (Gómez de Castro 2002; Guirado et al. 1997). Precise Hipparcos and very long baseline interferometry (VLBI) observations provided an accurate distance measurement (d = 15.06 ± 0.07 pc) and revealed the presence of AB Dor C, a low-mass companion with 0.090 $M_\odot$, orbiting AB Dor A at an average angular distance of 0.2″ (Guirado et al. 1997). The pair AB Dor A/C has also been observed by different near-infrared instruments at the VLT (Close et al. 2005, 2007; Boccaletti et al. 2008) allowing independent photometry of AB Dor C (K_s = 9.5) which, along with the dynamical mass determination, served as a benchmark for young, low-mass stellar evolutionary models (Azulay et al. 2017, and references therein).

Previous comparisons of observed magnitudes with theoretical mass-luminosity relationships suggested that the models tend to underpredict the mass of AB Dor C or, equivalently, overpredict the flux of the object, especially at the J and H bands (Close et al. 2005). This disagreement was also noted in studies of the other pair of the system, AB Dor Ba/Bb (Wolter et al. 2014; Janson et al. 2018). The authors argued that theoretical models tend to be consistent in the case of young moving groups but not in older associations such as the AB Dor moving group. This tendency was reinforced by the study of other members of this moving group, such as GJ 2060 AB (Rodet et al. 2018) or LSPM J1314+1320 AB (Dupuy et al. 2016). In the case of AB Dor C, most of the difficulty in validating the model predictions comes from the uncertainty in age and the possible binary nature of the object. Regarding the latter, Marois et al. (2005) pointed out that if AB Dor C were a binary brown dwarf, the overluminosity shown by the models, including the permanent disagreement in the J and H filters, could easily be corrected assuming reasonable mass ratios. Indeed, the determination of the possible binary nature of AB Dor C is an important issue for an object acting as calibrator of young, low mass objects that needs to be addressed.

In this work we present interferometric evidence of the presence of a low-mass com-

Table 6.1: Observation log of AB Dor C and calibrators.

Obs. Time	Target	Triplet	Mode	Seeing
28/12/2012 02:40	HD 35199	U1-U2-U4	Low JHK	0.79”
28/12/2012 03:17	AB Dor C	U1-U2-U4	Low JHK	0.63”
28/12/2012 03:43	AB Dor C	U1-U2-U4	Low JHK	0.72”
28/12/2012 04:17	AB Dor C	U1-U2-U4	Low JHK	0.74”
28/12/2012 04:40	AB Dor A	U1-U2-U4	Low JHK	0.74”

Note. Due to the nonstandard observing configuration (see the text), HD 35199 could only be observed at the beginning of the observation.

panion to AB Dor C from VLT Interferometer (VLTI) observations performed with the Astronomical Multi-BEam combineR (AMBER) focal instrument (Petrov et al. 2007), installed at the ESO facilities in Cerro Paranal, Chile. Attempts to observe this object with the GRAVITY instrument are also reported. We describe the observations and data reduction in Section 2. The analysis is presented in Section 3 and the comparison with stellar models and discussion are presented in Section 4. Finally, in Section 5 we present our conclusions.

6.2 Observations

The observations of AB Dor C were performed with the VLTI using the AMBER instrument with the external fringe tracker FINITO (Fringe-Tracking Instrument of NIce and TOrino) in low resolution mode at the J, H and K bands (programme 090.C-0559(A)). However, due to a technical problem, the J-band did not perform well and was not used in our analysis. The H-band was tested but finally also discarded in the analysis, as discussed below. The observations were performed on 2012 December 28 from 02:40 to 04:40 UT using the 8.2 m unit telescopes (UT) with the configuration UT1-UT2-UT4. Due to the faint magnitude of AB Dor C (K_s = 9.5), we used a nonstandard observing configuration that consisted of using AB Dor A as a fringe tracker to increase the integration time on AB Dor C. To achieve this, first we set AMBER in low-resolution mode with a DIT of 0.1 s; second, we found and locked the fringes of AB Dor A in the fringe tracker FINITO;

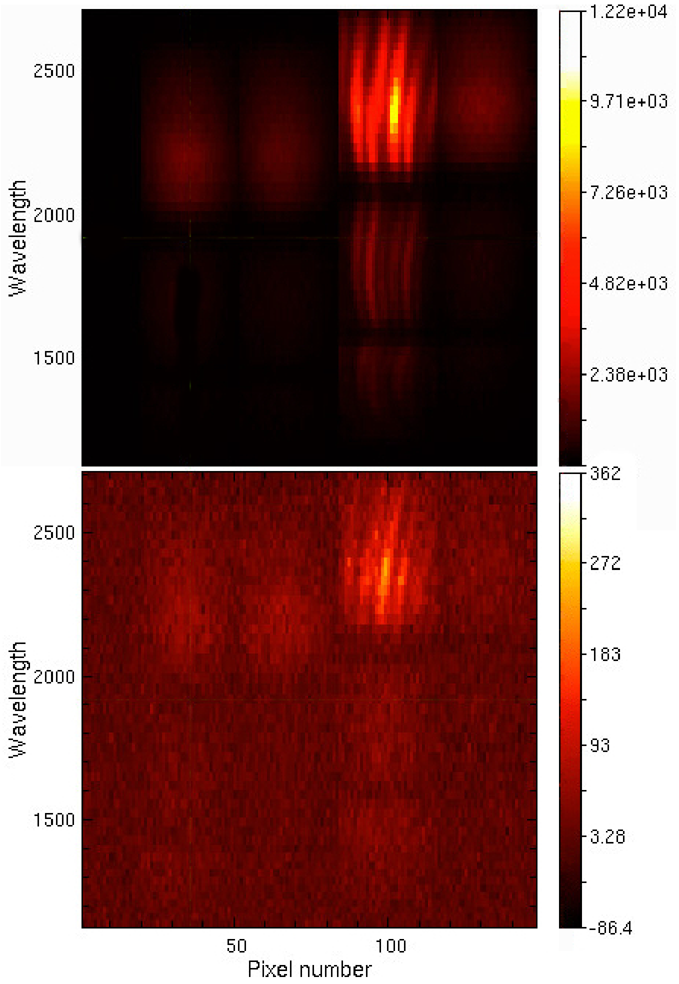

Figure 6.1: AMBER raw detector image (single frame) obtained with the triplet UT1-UT2-UT4 in low-resolution mode on AB Dor A (upper plot) and AB Dor C (lower plot), the latter taken with a non-standard, off-axis fringe-tracking configuration (see text). The upper (lower) half of the plots corresponds to K (H) band. From left to right, the first, second, and fourth columns represent the photometric beams for each one of the three telescopes, while the third column contains the interferometric signal. Notice the clear K-band detection on AB Dor C. The ratio between the intensity of both interferometric channels roughly indicates the flux ratio between AB Dor A and C.

and third, we offset AMBER (through tip/tilt correction) to find the fringes of AB Dor C. This "off-axis" fringe tracking allowed an exposure time on AB Dor C longer than that imposed by the atmospheric piston. Fringes were seen in every single frame (see Fig. 6.1), which could be properly averaged to obtain the visibility data. The procedure above benefited from (i) a precise knowledge of the orbit of AB Dor C (Guirado et al. 2006), which allowed us to predict with milliarcsecond precision the relative position AB Dor

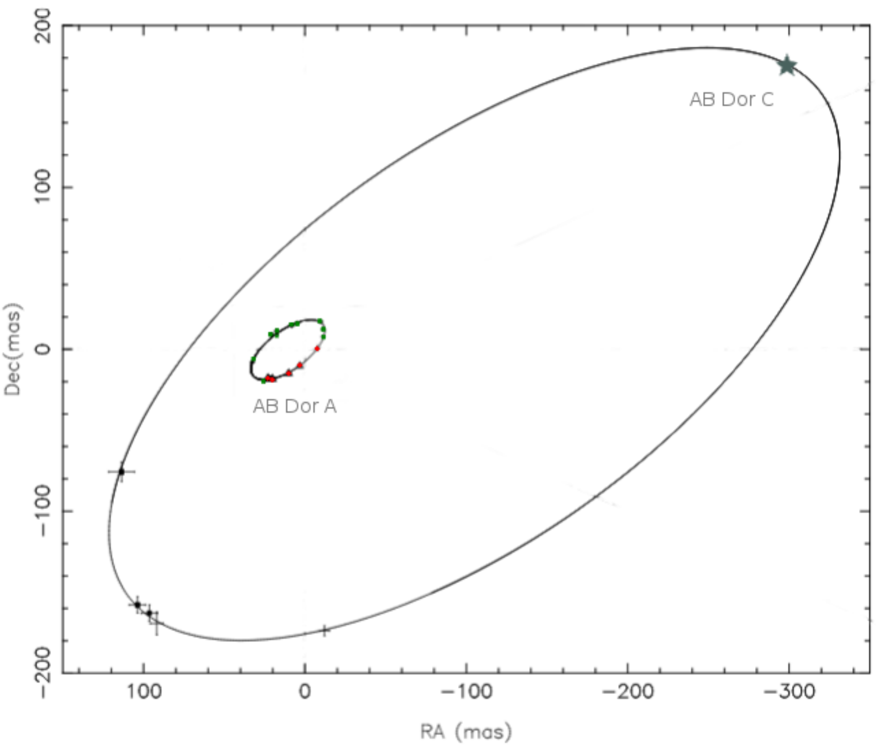

Figure 6.2: Absolute orbits of AB Dor A and AB Dor C, adapted from (Azulay et al. 2017). The map is centered at the center of mass of the system. Measured positions of AB Dor A are marked with red (Hipparcos data) and green (VLBI data) dots. Previous VLT/NACO measurements of AB Dor C are plotted with points while the expected position of AB Dor C at the time of our observation (2012.9918) is marked by a star.

A/C; (ii) an optimum observing epoch, 2012 December, with AB Dor C near apoastron (0.42” separated from A, see Fig. 6.2), thus minimizing the possible contamination from the brighter star AB Dor A; and (iii) good atmospheric conditions with a seeing of ~0.7”. The star HD 35199 (disk-equivalent diameter of 0.86 mas; Mérand et al. 2006) was also observed to calibrate the AB Dor C visibilities. The logs of these observations are shown in Table 6.1.

In addition to the AMBER data, 4 hr of VLTI/GRAVITY time were allocated (program 0102.C-0297, with the telescopes UT1-UT2-UT3-UT4) and scheduled on 2017 December 9 to confirm our findings. However, the proximity of the much brighter AB Dor A (located at 0.2” from C) during the observing epoch prevented AB Dor C to be properly identified in the GRAVITY acquisition camera, therefore making the observation technically unfeasible.

6.3 Data reduction and analysis

We obtained the raw visibility data using the software package amdlib v.3.0.8[a] (Tatulli et al. 2007; Chelli et al. 2009). We selected and averaged the resulting visibilities of each frame using different criteria for the baseline flux and for the fringe signal-to-noise ratio (S/N; for more information see the AMBER Data Reduction Software User Manual[b]. In particular, (i) we selected frames having a baseline flux with S/N larger than 1, 2, 3, 4, 5, 6, 7, 10, 15, and 20; (ii) for each of these selections, we kept the 5%, 10%, 20%, 30%, 40%, 50%, 60%, 70%, 80%, and 100% of the remaining frames with the highest fringe S/N, which effectively created a grid of 10 x 10 reduced data sets with different selection criteria; (iii) we made extensive tests to determine the robustness and consistency of each one of the data sets above (basically, we compared each data set to simulated visibilities of different source geometries, discarding those data sets producing unacceptable fits); and (iv) based on the previous tests, we selected the data set containing 5% of the frames with highest fringe S/N chosen from those with a baseline flux S/N larger than 6. The calibration of the transfer function was made using the calibrator star HD 35199.

The values of the squared visibilities panel (Fig 6.3 left) are far from corresponding to those of a pointlike source; rather, they indicate either the presence of an extended structure around AB Dor C, and/or the binary nature of the object. Actually, the sinusoidal behavior seen in the visibilities is a typical signature of a binary system (e.g., Millour et al. 2009). Supporting the previous statement, the closure phase (Fig.6.3 right) displays a nonnegligible departure from the null value, indicating that the contrast between binary components should be relatively high (Monnier 2003). The fact that the visibilities do not decrease with baseline suggests, in principle, that the components are not resolved.

We performed an exhaustive and systematic search for companions to AB Dor C using the software CANDID[c] (Gallenne et al. 2015). CANDID performs a least-squares fit of both the companion position and flux ratio at each starting position of a 2D grid using

---

[a] The AMBER reduction package amdlib is available at: `http://www.jmmc.fr/data_processing_amber.htm`

[b] `http://www.jmmc.fr/doc/approved/JMMC-MAN-2720-0001.pdf`

[c] [C]ompanion [A]nalysis and [N]on-[D]etection in [I]nterferometric [D]ata, available at: `https://github.com/amerand/CANDID`

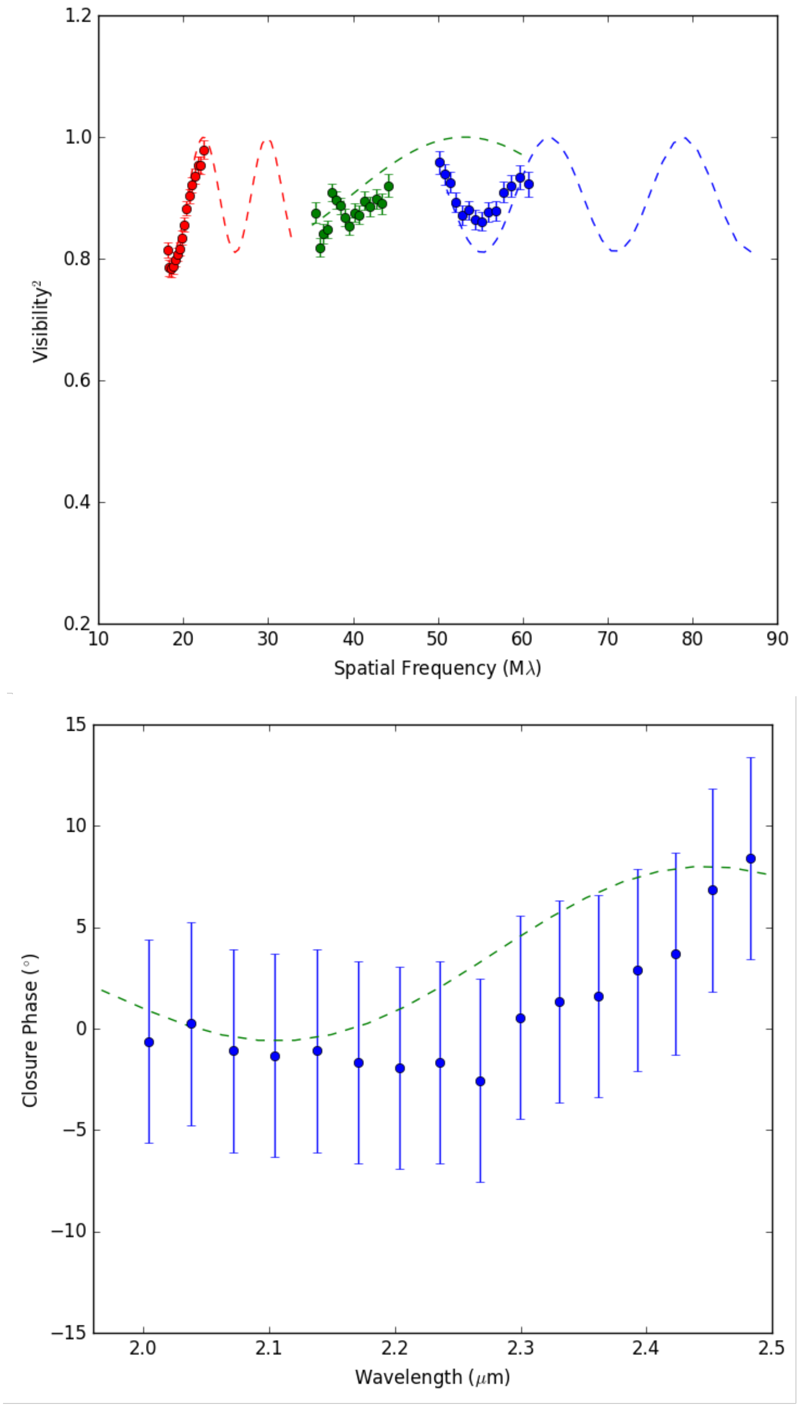

Figure 6.3: (*upper*): AMBER visibilities of AB Dor C. Different colors represent different baselines. The K-band observational data (circles) are best fitted by a binary system with the properties given in Table 6.2 with the CANDID K-band method and whose visibilities are plotted in colored discontinuous lines. (*lower*): AMBER K-band closure phases of AB Dor C. Blue dots correspond to observational data, while the dashed line represents the theoretical closure phases of the model given above. Indeed, the deviation from 0° suggests that AB Dor C is not a point source and possesses a more complex structure, modeled here by a binary.

Table 6.2: Best-fitting binary-model parameters for AB Dor C

Method	Flux ratio	Separation (mas)	P.A (°)
CANDID K band	0.054 ± 0.004	38.1 ± 0.2	178 ± 1
LITpro	0.05 ± 0.01	39 ± 1	177 ± 1

the interferometric observables, the squared visibilities, and the closure phases. We first used CANDID with only K-band data, revealing a companion to AB Dor C at a level of 24σ with separation and flux ratio detailed in Table 6.2, where the number of sigmas indicates how significant the binary model is compared to a single star and is computed using formula (8) in Gallenne et al. (2015). In agreement with this, the calculation of the corresponding χ^2 for both the single and binary scenarios yields a clear preference for the presence of a companion: $\chi^2_{single} = 14.07$ and $\chi^2_{binary} = 2.60$.

On the other hand, the quality of the fit is degraded (from 24σ to 16σ) when using both the K and H bands, adding, at least, another spurious solution. Moreover, no detection is found with CANDID when using only the H band. Given the results above, we conservatively restricted our interferometric data set to K-band only.

To assess the validity of the CANDID results, we also fitted the observed visibilities with LITpro (Lyon Interferometric Tool prototype), developed by the Jean-Marie Mariotti Center (JMMC Tallon-Bosc et al. 2008). We used a simple two-point model to simulate the suspected binary nature of AB Dor C. In contrast to the CANDID procedure, LITpro does not perform a systematic search of the parameters; therefore, aiming at identifying the best model, we initialized the fitting program with different sets of values for the free parameters, namely: flux ratio, binary separation, and position angle. In practice, we explore the following parameter space around the CANDID position: flux ratio between 2% and 8% in steps of 0.5%, separation between 25 and 50 mas in steps of 0.5 mas, and P.A. between 140° and 220° in steps of 0.5°. We selected as plausible fits the range of χ^2 values that correspond to a 95% confidence interval. The results of this parameter search are given in Table 6.2, and coincide, within uncertainties, with the position found with the CANDID software and the K-band, strengthening the validity of our binary hypothesis for AB Dor C. Given the plausibility of the results obtained with this binary model (and, admittedly, to avoid a possible overinterpretation of the data), we did not explore more complicated geometries with LITpro (i.e. binary with disks or envelopes).

From the analysis above, we conclude that AB Dor C is a binary system with components separated by 38 ± 1 mas, and a flux ratio at the K-band of 5% ± 1%, where the uncertainties have been conservatively enlarged to cover the results of both software.

6.4 Results and discussion

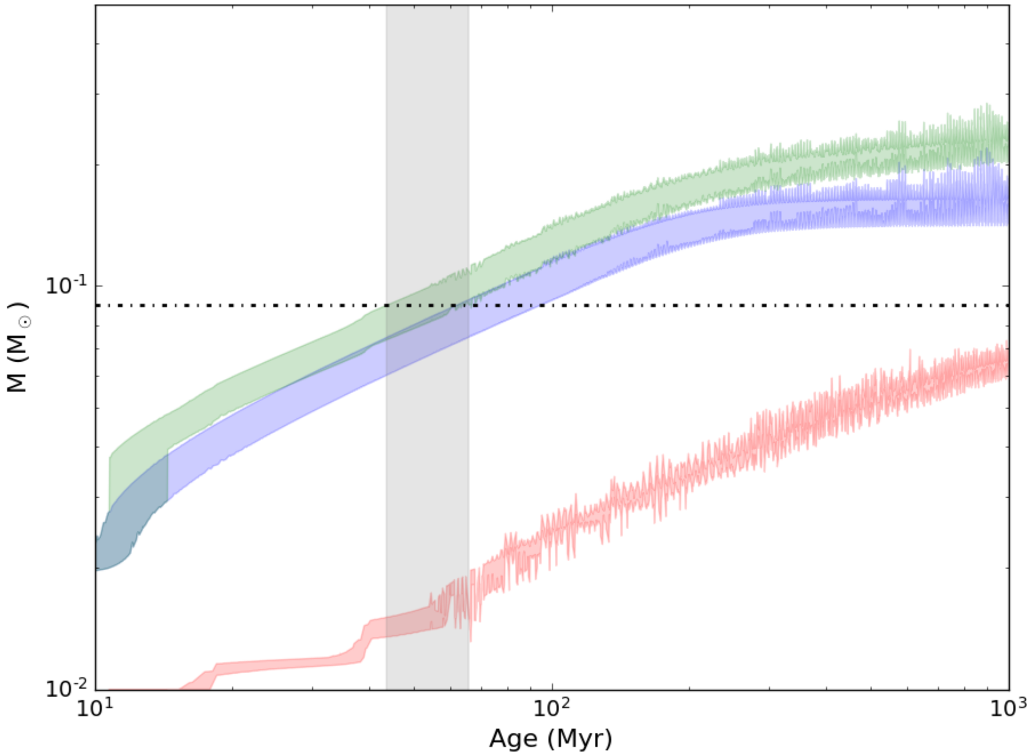

Figure 6.4: Mass versus age at constant K_s magnitude: 8.43 ± 0.16 (blue; Ca) and 11.7 ± 0.3 (red; Cb) and the corresponding binary system (green; Ca+Cb). A dashed-dotted line represents the measured dynamical mass of 0.090 $M_\odot$ (Azulay et al. 2017), while the shadowed gray area represents the age range (44-66 Myr) resulting from the intersection of this measured dynamical mass with the measured Ca+Cb magnitude, according to the models by Tognelli et al. (2018). The irregularities in the model are more likely a product of the interpolation than a real physical effect. The use of the DUSTY+BHAC15 models produces very similar results.

The interferometric results presented allow us to characterize the components of the tentative binary in AB Dor C (AB Dor Ca/Cb). The combination of the flux ratio (Cb/Ca), 5% ± 1%, with the total (Ca+Cb) K_s absolute magnitude of 8.38 ± 0.16 (Boccaletti et al. 2008) implies a binary with magnitudes K_s = 8.43 ± 0.16 and K_s = 11.7 ± 0.3 for Ca and Cb, respectively.

6.4.1 Comparison with evolutionary models

With the individual magnitudes of the components, an estimate of the individual masses can be obtained by using PMS evolutionary models. We computed the models using the Pisa stellar evolutionary code (Tognelli et al. 2018) for masses in the range 0.01–0.4 $M_\odot$ and solar metallicity ([Fe/H] = 0). We also used an interpolation of the DUSTY models (Chabrier et al. 2000) and BHAC15 models (Baraffe et al. 2015) to infer the dependence of the derived parameters on the adopted evolutionary tracks. The boundary between DUSTY and BHAC15 models was based on mass, with each model covering the ranges of 0.001–0.1 $M_\odot$ for the former and 0.01–1.4 $M_\odot$ for the latter.

Following the procedure described in Sect. 4.2 of Liu et al. (2008), we used these evolutionary models and our inferred magnitudes of Ca and Cb to estimate the mass of each one of the components; the sum of these masses is the the total mass of the system, which is represented against the age in Fig. 6.4. The shadowed gray area indicates the possible combinations of masses for Ca and Cb accomplishing that the total mass of the system lies within the measured dynamical mass of 0.090±0.008 $M_\odot$ for AB Dor C (Azulay et al. 2017). This implies masses of 0.072 ± 0.013 $M_\odot$ and 0.013 ± 0.001 $M_\odot$ for each one of the components of the binary, which interestingly lie near the hydrogen-burning limit for the case of AB Dor Ca, and near the deuterium-burning limit, straddling the boundary between brown dwarfs and giant planets, for the case of AB Dor Cb. Given the relatively large mass ratio between AB Dor Ca/Cb, we notice that the tentative binarity of AB Dor C would not result in a substantial change in the age range when compared with previous estimates based on the same evolutionary models (Azulay et al. 2017). Likewise, the presence of AB Dor Cb does not affect the age determinations based on model isochrones fitting to the members of the AB Dor moving group (Bell et al. 2015).

6.4.2 Binary hypothesis and photometry

How is the interpretation of published AB Dor C photometry affected by our binary hypothesis? In Fig. 6.5 we represent the cooling curves of AB Dor Ca/Cb (models by Tognelli et al. 2018) compared with published AB Dor C photometric measurements (Close et al. 2005; Luhman & Potter 2006; Close et al. 2007; Boccaletti et al. 2008) for the two scenarios considered: 1) the (old) single-object scenario (with AB Dor C as a single object of 0.090 $M_{\odot}$) and 2) the (new) binary scenario resulting from our detection (with AB Dor C as a binary with estimated masses of 0.072 $M_{\odot}$ and 0.013 $M_{\odot}$, according to the parameters given in Table 2). Published magnitudes at J, H, and K bands are shown for the two most-considered age ranges in the literature: 75 ± 25 Myr (Janson et al. 2007; Boccaletti et al. 2008) and 120 ± 20 Myr (Luhman et al. 2005; Ortega et al. 2007), being the latter being favored by the recent works of Bell et al. (2015) and Gagné et al. (2018).

For the discussion that follows we use solely the fact that AB Dor C may be a binary system with masses 0.072 $M_{\odot}$ and 0.013 $M_{\odot}$ (as obtained in Sect. 6.4.1) and previously reported photometric measurements. As we can see in Fig. 6.5, for an age of 75 Myr (left column plots), the binary hypothesis produced an overall better agreement considering all the three bands than the single-object hypothesis. In fact, the binary tracks are compatible (to within 1.2σ of the showed uncertainties), with all the photometric measurements, slightly favoring those reported by Close et al. (2007) and Luhman & Potter (2006). Turning to the age of 120 Myr (right column plots in Fig. 6.5), we found that the binary track nicely reproduces the J-band measurements; however, the tracks for this older age range seems to underestimate some of the H- and K- band measurements (especially those from Boccaletti et al. 2008). The most relevant result of the comparisons above is that the small disagreements in the J and H bands reported by Luhman & Potter (2006) and Close et al. (2007) are partially alleviated (for an age of 75 Myr), or completely removed (for an age of 120 Myr), considering AB Dor C as a binary system.

We also estimated the bolometric luminosity (L_{bol}) using the photometric published measurements and the bolometric corrections found in Pecaut & Mamajek (2013) and Filippazzo et al. (2015). Both corrections produce very similar results and are consistent within the errors. Conservatively we adopt the bolometric correction value of 3.10 ± 0.13 from Filippazzo et al. (2015) for an M7 dwarf. Differences in bolometric luminosity or in magnitudes could highlight two scenarios. On one hand, a discrepancy in luminosity would suggest problems in the fundamental physics used to compute very low-mass stars models, in particular due to the adopted equation of state, outer boundary conditions, magnetic fields, and surface spots (Siess 2001; Chabrier et al. 2007; di Criscienzo et al. 2010; Feiden & Chaboyer 2013; Somers & Pinsonneault 2015; Tognelli et al. 2018). On the other hand, a difference visible only in magnitudes should point out for the need for more accurate synthetic spectra, which, especially in the case of low- and very low-mass stars, still represents a challenging task. The top panels of Fig. 6.5 show that the binary scenario produces a slightly better agreement with the estimated bolometric luminosities. This is especially notable at the younger age of 75 Myr. Although small, this effect may be pointing to a problem in the fundamental physics used in very low-mass stars models, as previously stated.

Regarding the spectral type of AB Dor C, and according to the binary scenario, the M5.5 ± 1 classification reported by Luhman & Potter (2006) should be assigned to the heavier component of the system, AB Dor Ca. To obtain an estimate of the spectral features of the weaker component Cb we used the color-magnitude calibration provided by Zapatero Osorio et al. (2014), in turn based on the least massive population, brown dwarfs, and giant planets, belonging to the Pleiades cluster (age 120 Myr). Following this calibration, and for a K_s magnitude of 11.7 ± 0.3 (Sect. 6.4), a spectral type of L4–6 could be expected for component AB Dor Cb.

6.4.3 Orbit and stability of AB Dor Ca/Cb

Although our interferometric measurements do not provide any information about the orbit of Cb and Ca, we can derive estimates for the semimajor axis using the conversion factors from projected separation to semimajor axis provided by Dupuy & Liu (2011). The median values given in their Table 6 for very low-mass binaries range from 0.85 to 1.16, which, considering our Ca/Cb separation (38.1 mas) and the dynamical mass of AB

Dor C (0.090 $M_\odot$), translate to a semimajor axis for the Ca/Cb orbit of 32.4-44.2 mas with a period of 418-666 days. The Ca/Cb binary is, in turn, orbiting the 0.89 $M_\odot$ AB Dor A with a period of 11.78 yr (Azulay et al. 2017). It is obvious that the complete system is dynamically dominated by the presence of AB Dor A, and accordingly, its gravitational pull exerted on the inner orbit Ca/Cb should be evaluated to ascertain if the latter pair is in a stable orbit. For this purpose (and neglecting the effect of the 9" apart AB Dor Ba/Bb) we can consider AB Dor as a triple system (A, Ca, Cb) where AB Dor Cb is in an S-type orbit, that is, Cb is orbiting near one of the bodies (Ca) while the third body (AB Dor A) acts as a perturber. The critical semimajor axis at which the orbit of the system Ca/Cb is stable depends on the eccentricity of the binary A/C, the mass ratio A/C, and the separation between the host object (Ca) and the perturber (A). Assuming the estimated mass of AB Dor Ca, and adopting the orbital parameters of AB Dor C around AB Dor A given in Azulay et al. (2017), the formulae provided by Holman & Wiegert (1999) yield stable orbits for AB Dor Ca/Cb for separations <50 mas. This implies that our measured separation for the binary in AB Dor C (~38 mas) would correspond to a stable binary system. A similar conclusion can be reached following a different reasoning based on the simulations of Musielak et al. (2005): according to their Fig. 5, stable S-type orbits are obtained for the estimated distance ratio (d_{Ca-Cb}/d_{A-C} ~0.27) and mass ratio (M_C/M_A ~0.10) of the triple system AB Dor A/Ca/Cb.

Finally, should AB Dor Cb have been detected in previous observations? The presence of the solar-type star AB Dor A (K_s = 4.686) at only 0.2" made it extraordinarily difficult to detect and characterize AB Dor C (K_s = 9.5) (Close et al. 2005, 2007), given the high-contrast imaging needed in the vicinity of AB Dor A; as AB Dor Cb is about three magnitudes weaker, it is very likely that this newly discovered companion remained unnoticed in the observations reported by Close et al. (2007) or Boccaletti et al. (2008). Assuming a face-on, circular orbit and masses of 0.072 ± 0.013 $M_\odot$ and 0.013 ± 0.001 $M_\odot$ for AB Dor Ca/Cb, the radial velocity semi-amplitude produced in Ca would be ~2 km/s with a period of 418–666 days. At 2.3 μm of wavelength, the expected spectral shift due to the presence of the companion Cb would be ~0.02 nm while the finest spectral resolution achieved in the spectra of AB Dor C is 1.5 nm (Close et al. 2007) explaining why this radial velocity signal has not been discovered before.

6.5 Conclusions

We present interferometric evidence that AB Dor C is not a single pointlike star but most likely a binary system of very low-mass objects. Our results show that both squared visibilities and closure phases are in good agreement with a binary system of ~38 mas separation between the components and a K-band flux ratio of ~5%. This configuration implies masses for the tentative binary AB Dor Ca/Cb of 0.072 ± 0.013 $M_\odot$ and 0.013 ± 0.001 $M_\odot$, according to the PMS evolutionary models of Chabrier et al. (2000), Baraffe et al. (2015) and Tognelli et al. (2018). It is worth noting that, with these masses, one of the objects would lie near the hydrogen-burning limit (AB Dor Ca), while AB Dor Cb would lie at the frontier between brown dwarfs and planets. The binarity of AB Dor Ca/Cb may have gone unnoticed in previous observations given the three-magnitude difference between Ca and Cb and the great difficulty of discerning AB Dor C itself from the nearby, five-magnitude brighter AB Dor A. However, the binary hypothesis would alleviate the disagreement between observed magnitudes and theoretical mass-luminosity relationships. We considered the two most frequently used scenarios (75±25 Myr and 120±20 Myr) and found that especially at the *J* and *H* bands the binary hypothesis produces a better agreement than a single 0.090 $M_\odot$ object.

The perturbation caused by the more massive AB Dor A would destabilize a binary system of separation larger than 50 mas. With a separation of about 38 mas, the newly discovered binary AB Dor Ca/Cb appears stable under such perturbation. Yet, although our result defines a very plausible scenario for AB Dor C, it is based on a limited number of visibilities taken near the performance limit of AMBER and, therefore, further confirmation of our findings would be convenient. Advanced instrumentation (i.e. GRAVITY dual-field on-axis mode observations) will help to clarify the nature of this remarkable system.

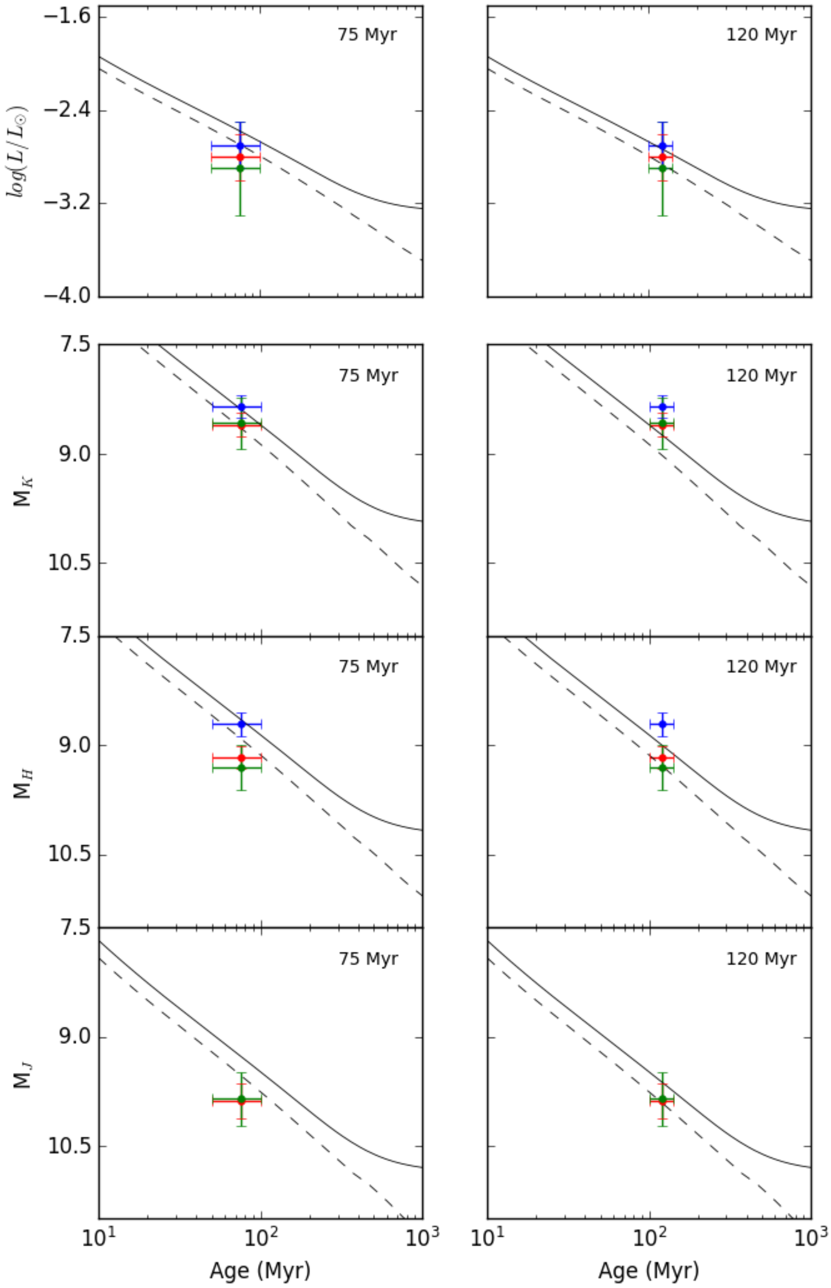

Figure 6.5: Evolutionary tracks of theoretical models (Tognelli et al. 2018) for a single object of 0.090 $M_\odot$ (solid) and a binary system of 0.072 ± 0.013 $M_\odot$ and 0.013 ± 0.001 $M_\odot$ (dashed) compared with photometric measurements of Luhman & Potter (2006) (green dots), those of Close et al. (2007) (red dots) and those of Boccaletti et al. (2008) (blue dots). The first row represents the bolometric luminosity derived from the photometric measurements and the bolometric corrections found in Filippazzo et al. (2015). The second, third, and fourth rows are for K, H, and J photometry, respectively. The left plots represent the first age scenario (75 ± 25 Myr) and the right plots represent the second one (120 ± 20 Myr). The DUSTY+BHAC15 models produce extremely similar results.

Chapter 7

VLTI-PIONIER imaging of the red supergiant V602 Carinae

This chapter is based on the homonymous publication that appeared on Astronomy and Astrophysics, 635, A160, 2020 with DOI: 10.1051/0004-6361/201936734 and published on March 2020.

7.1 Introduction

Red supergiants (RSGs) are cool evolved massive stars before their transition toward Wolf-Rayet (WR) stars and core-collapse supernovae. Their characterization and their observed location in the Hertzsprung-Russell (HR) diagram is important to calibrate stellar evolutionary models for massive stars and to understand their further evolution toward WR stars and supernovae (e.g., Dessart et al. 2013; Groh et al. 2013, 2014; Smith 2014; Meynet et al. 2015). Moreover, red supergiants are of importance in stellar synthesis models because of their high luminosities and high masses (e.g., Marco & Negueruela 2013).

The structure and morphology of the close circumstellar environment and wind regions, including the atmospheric molecular layers and dusty envelopes, are currently a matter of intense debate (e.g., Yoon & Cantiello 2010; Walmswell & Eldridge 2012). Knowledge on the circumstellar envelope and fundamental parameters is important to understand the matching of supernova (SN) progenitors to the different types of core-collapse SNe (Heger et al. 2003; Groh et al. 2013). The mass loss from red supergiants is, as well, one of the most important sources for the chemical enrichment of the interstellar medium.

The study of fundamental parameters and atmospheric extensions of RSGs in our neighborhood (Wittkowski et al. 2012; Arroyo-Torres et al. 2013, 2014, 2015; Wittkowski et al. 2017b), has shown that extended molecular atmospheres, with extensions comparable to Mira variable asymptotic giant branch (AGB) stars, are a common feature of RSGs stars and that, unlike for Miras, this phenomenon is not predicted by 3D radiative-hydrodynamics (RHD) or 1D pulsation models (Arroyo-Torres et al. 2015).

The onset of the mass-loss process, that is the levitation of the outer atmospheric layers to radii where dust can form, is currently not understood for RSG stars. The most commonly proposed mechanism has been an interplay of pulsation and convection (e.g., Yoon & Cantiello 2010). Josselin & Plez (2007) suggested that a decrease of the effective gravity, caused by convective motions, combined with radiative pressure on molecular lines, may initiate the mass loss in RSG stars. It was also suggested that magnetic fields could contribute to the heating of the outer atmosphere and to the mass loss (Aurière et al. 2010). Arroyo-Torres et al. (2015) showed that current 1D and 3D radiative-hydrodynamics models of pulsation and convection alone cannot levitate the molecular atmospheres of RSGs to observed extensions. They observed a correlation of atmospheric extension with luminosity, which may support a scenario that includes radiative acceleration on Doppler-shifted molecular lines. However, there are alternative mechanisms such as magnetic fields and Alfvén waves (e.g., Airapetian et al. 2010; Cranmer & Saar 2011; Thirumalai & Heyl 2012; Rau et al. 2019; Yasuda et al. 2019), differential rotation (Vlemmings et al. 2018), or the presence of giant dominating hot spots as recently observed by Montargès et al. (2016). Although the processes that initiate the mass loss from RSG stars are not currently known, it is well established that RSG stars show mass-loss rates between 2×10^{-7} $M_{\odot}yr^{-1}$ to 3×10^{-4} $M_{\odot}yr^{-1}$ (De Beck et al. 2010).

In this work, we aim at characterizing effects of convection on the stellar surface and at investigating the role that convection may play in the mass-loss process of RSGs. We compare VLTI-PIONIER image reconstructions of the stellar surface of V602 Carinae (V602 Car) with predictions by 3D simulations of stellar convection. We chose V602 Car as our main target which was part of our previous sample of VLTI-AMBER studies, that is targets of which we already established fundamental stellar parameters and the presence of extended molecular atmospheres. Arroyo-Torres et al. (2015) reported for V602 Car a radius of 1050±165 $R_\odot$, an effective temperature of 3432±280 K, a surface gravity $\log g$ = -0.30±0.16, and an initial mass of 20-25 $M_\odot$ corresponding to a current mass of 10-13 $M_\odot$.

Table 7.1: Observation log of V602 Car with the instrument PIONIER.

Date	Stations	Conf.[a]	Seeing ($''$)	Coh. time (msec)
2016-04-07	A0/G1/J2/J3	L	0.47	7.6
2016-05-23	A0/B2/C1/D0	S	0.63	4.4
2016-05-24	A0/B2/C1/D0	S	0.44	5.4
2016-05-25	A0/B2/C1/D0	S	0.47	3.3
2016-05-31	D0/G2/J3/K0	M	0.66	3.5
2016-06-01	A0/G1/J2/J3	L	0.66	2.5
2016-06-27	A0/B2/C1/D0	S	0.62	3.1
2019-04-29	A0/D0/G1/J3	L	0.75	5.3
2019-05-02	A0/G1/J2/J3	L	0.57	6.7
2019-05-03	A0/G1/J2/J3	L	0.46	13.5
2019-05-04	A0/G1/J2/J3	L	0.52	4.9
2019-05-10	A0/B2/C1/D0	S	1.09	2.2
2019-05-30	A0/B2/C1/D0	S	0.77	2.5
2019-05-31	A0/B2/C1/D0	S	0.70	2.6
2019-07-07	A0/G2/J2/J3	L	0.47	6.3
2019-07-08	D0/G2/J3/K0	M	0.46	6.9

Notes. [a] Short configuration (S): AT stations A0/B2/C1/D0, ground baselines 10-40 m; Medium configuration (M): D0/G2/J3/K0, 40-100 m; Large configuration (L): A0/G1/J2/J3, A0/G2/J2/J3 and A0/G2/J2/J3, 60-140m.

7.2 Observations and data reduction

We obtained interferometric observations of V602 Car employing the PIONIER instrument (Le Bouquin et al. 2011) of the Very Large Telescope Interferometer (VLTI) and its four auxiliary telescopes (ATs). The ATs were placed in 3 different effective configurations: short, medium and large (see Table 7.1). Observations were taken using ESO's service mode between 7 April 2016 and 27 June 2016 and between 29 April 2019 and 8 July 2019. The 2019 data were taken using the new NAOMI adaptive optics system (Woillez et al. 2019) at the ATs during NAOMI science verification, providing an improved precision and accuracy compared to 2016 (see Appendix A.1 for details). The data were dispersed over six spectral channels with central wavelengths $1.53\,\mu$m, $1.58\,\mu$m, $1.63\,\mu$m, $1.68\,\mu$m, $1.72\,\mu$m, $1.77\,\mu$m and widths of $\sim 0.05\,\mu$m. Observations of V602 Car were interleaved with observations of the interferometric calibrator HD 96566 with spectral type G8III and angular uniform disk diameter of 1.50 ± 0.11 mas (Lafrasse et al. 2010). A log of our observations can be found in Table 7.1. We initially divided the 2016 observation dates into 3 sub-epochs, where each epoch lasted not more than 9 days, because the V602 Car is a semi-regular variable. However, an analysis of the different sub-epochs showed that, within our accuracy and spatial resolution, there was no significant variability of the visibility data over the sub-epochs, so that in the following we analyzed the data of all sub-epochs together. We did not repeat the exact *uv* coverage within the full epoch so that variability on small scales might be present and would be smeared by combining the data. Indeed, 3D convection models of RSGs by Chiavassa et al. (2009) showed time variations of surface structures on time scales of one month in the H-band. However, we show later in Sect. 7.5.2 that snapshots of convection simulations remain similar at our spatial resolution, albeit not identical, on time scales of about 3 months, justifying our approach to combine the sub-epochs. The same reasoning was applied for the 2019 observations. The total *uv* coverage that we obtained for our observations is very similar for 2016 and 2019, as can be appreciated in Fig. 7.1.

We reduced and calibrated the data with the *pndrs* package (Le Bouquin et al. 2011). The resulting visibility data of our observations can be found in Fig. 7.2, together with model fits and synthetic visibilites of our image reconstructions as discussed below.

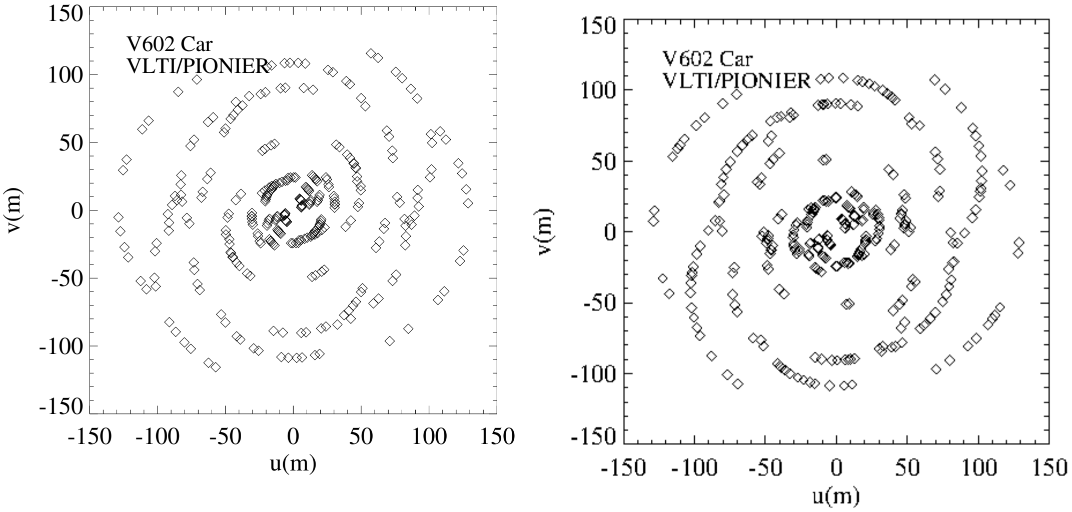

Figure 7.1: The *uv* coverage of our PIONIER observations of V602 Car (upper, 2016; lower, 2019), where *u* and *v* are the spatial coordinates of the baselines projected on sky.

7.3 Data analysis

The visibility data in Fig. 7.2 indicate an overall spherical stellar disk. However, deviations from a continuously decreasing visibility in the first lobe and closure phases different from 0/180° at higher spatial frequencies indicate the presence of inhomogeneities.

As detected in previous K-band observations (Arroyo-Torres et al. 2015), V602 Car possesses an extended molecular layer, in the near-IR most importantly of H_2O and CO, also called MOLsphere (Tsuji 2000). These same molecules are also present in the H-band, and such extended layers have been detected in the H-band, for example for the AGB star R Aquarii (Ragland et al. 2008). We thus have to expect the MOLsphere of V602 Car to be seen in our H-band data as well. In order to describe the stellar photosphere and this MOLsphere we used a two-component model: a PHOENIX model atmosphere (Hauschildt & Baron 1999) for the stellar photosphere and a uniform disk (UD) describing the MOLsphere, as it was done in Arroyo-Torres et al. (2015). We chose a PHOENIX model from the grid of Arroyo-Torres et al. (2013) with parameters close to the established values for V602 Car by Arroyo-Torres et al. (2015): 20 $M_\odot$, $T_{\rm eff}$ = 3400 K

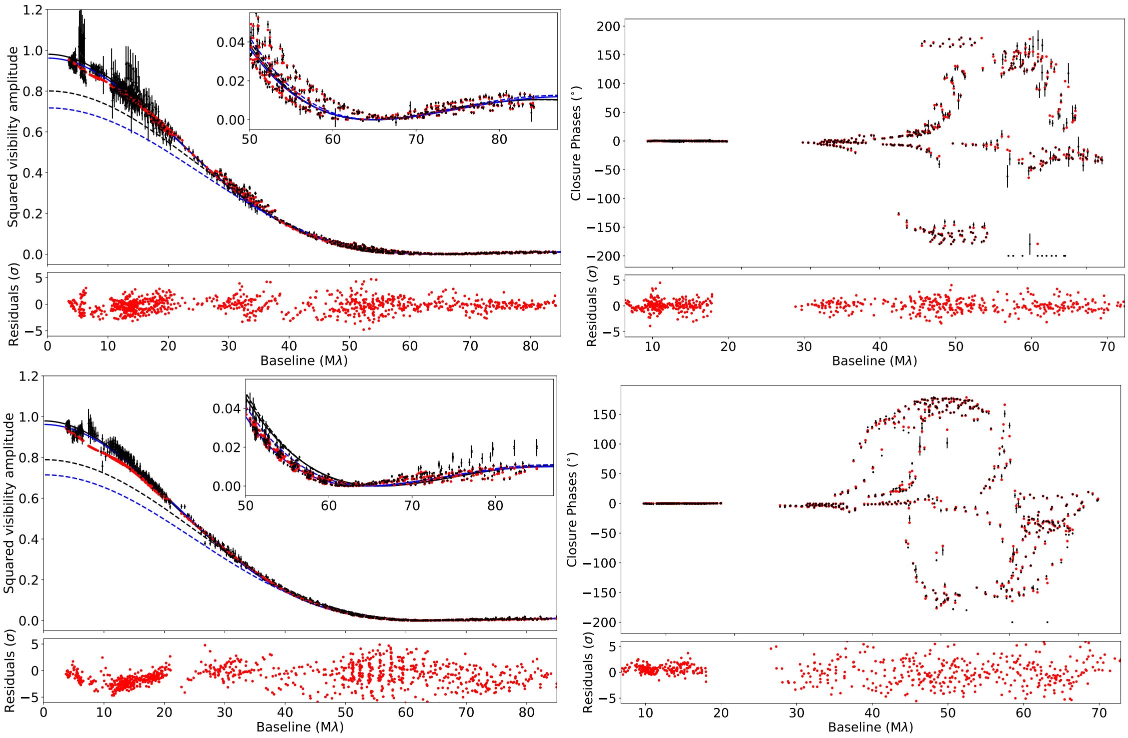

Figure 7.2: PIONIER visibility results of V602 Car of 2016 (top) and 2019 (bottom) as a function of baseline length. The left panel shows the squared visibility amplitudes, where the inlay enlarges the part of the low values. The right panel shows the closure phases. The vertical bars indicate the symmetric error bars. The black solid line denotes our visibility model including the stellar photosphere, represented by a PHOENIX model atmosphere, and a larger uniform disk indicating the extended atmosphere or MOLsphere. The black dashed line indicates the part of the PHOENIX model atmosphere alone without the added uniform disk (MOLsphere). Solid and dashed blue lines represent the same parts but for the selected 3D RHD snapshots for each epoch instead of the PHOENIX model (see Sect. 7.5). The synthetic values based on the reconstructed images are shown in red (SQUEEZE algorithm). The lower small panels provide the residuals between observations and reconstructed images.

and log(g) = -0.5. The fit was performed in the same way as in Wittkowski et al. (2017b) and separately for each spectral channel. We treated the flux fractions f_{Ross} and f_{UD} both as free parameters to allow for an additional over-resolved background component.

Table 7.2 lists the resulting best-fit parameters, together with the values averaged over the spectral channels. As expected for long-period variables, the flux contribution of the molecular layer is stronger in the water vapor bands toward the edges of the H-band. The angular diameter of the MOLsphere may not correlate well with its flux contribution, and may be less well constrained, in particular for low flux contributions. For the 2016 epoch, the best fit was found to be a photosphere with an angular diameter $\Theta_{\rm Ross}$ of 4.4±0.2 mas and a MOLsphere contributing on average ~10% of the total flux with an angular diameter of ~ 8 mas. For the 2019 epoch, we obtained consistent values with a $\Theta_{\rm Ross}$ of 4.5±0.2 mas and a MOLsphere with the same parameters as for 2016. For both epochs, the flux fraction of a larger unresolved component was negligible and our values of the Rosseland angular diameter are consistent with the estimate of $\Theta_{\rm Ross} = 5.08 \pm 0.75$ mas by Arroyo-Torres et al. (2015).

The synthetic squared visibility values are plotted in Fig. 7.2. The PHOENIX plus MOLsphere model successfully describes our visibility data. The effect of the UD representing the MOLsphere is clearly visible, since the PHOENIX model alone is unable to reproduce the measured shape of the visibility function.

A close inspection of the visibilities at baselines 50-90 Mλ (Fig. 7.2), in particular for the 2016 epoch, reveals the presence of more than one visibility minimum along different baseline angles, where visibility minima are separated by about 5% in baseline length. As discussed for Betelgeuse (Chiavassa et al. 2010a; Montargès et al. 2016), this feature may indicate that the star is seen by the interferometer as an overall slightly elongated disk, with differences of about 5% in radius across different angles, instead of a perfectly spherical disk. However, as shown by Chiavassa et al. (2009, 2010a), big intense convection cells within an overall spherical stellar disk can also be the origin of such dispersion of the spatial frequency at the visibility null. In order to probe this possibility, we reconstructed the observational images from these visibilities.

7.4 Aperture synthesis imaging

We used the reconstruction package SQUEEZE (Baron et al. 2010) to obtain aperture synthesis images.

We expect an overall (star plus stellar environment) source size beyond 8 mas in angular diameter based on the analysis in Sect. 7.3. As defined in Monnier (2003), the nominal spatial resolution of our imaging observations $\lambda/(2B_{\rm max})$ is 1.2 mas. We tested 3 different scenarios to select the best pixel size and field of view (FOV) for our image reconstruc-

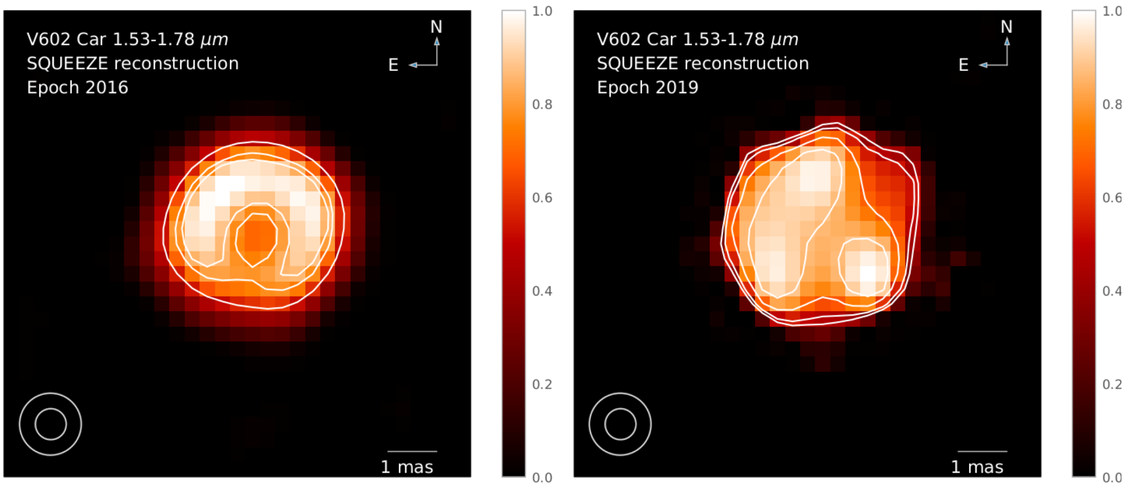

Figure 7.3: SQUEEZE reconstruction of V602 Car with spectral channels combined. (*Left*): 2016 data set. Contours are drawn at levels 55%, 77% and 85% of the peak intensity. (*Right*). 2019 data set. In this case, contours are drawn at levels 40%, 50%, 70% and 87% of the peak intensity. Here and hereafter, the pixel scale is 0.3 mas/pixel. The size of the circles in the lower left corners indicate our nominal angular resolution of 1.2 mas and the smallest circle represents our best estimate of the real resolution obtained, 0.6 mas (see Appendix A.2.3).

tions: 1) 0.6 mas/pixel with 64x64 pixel FOV; 2) 0.3 mas/pixel with 64x64 pixel FOV; 3) 0.3 mas/pixel with 128x128 pixel FOV. When restricting the field of view (comparing scenarios 2 and 3), the χ^2 of the reconstructed images clearly favored scenario 3, that with larger FOV. This is a good indication of extended flux that scenario 2 is not able to recover. The visual comparison of scenarios 1 and 3, that is same FOV with different resolutions, showed the same features in both images. Since no new information was created with the pixel size of 0.3 mas/pixel but χ^2 improves, we kept this as our final pixel size and field of view.

We performed SQUEEZE reconstructions for two main regularizations: Laplacian (*la*) and Total Variation (*tv*). We also included for both of these regularizations an L0-norm regularization (*l*0) to decrease the number of spurious point-like sources in the FOV. We also used a transpectral regularization (*ts*) to center all the images in the bandpass at the same position of the FOV (when working with combined channels). We tested two combinations of regularizations: *la* + *l*0 + *ts* and *tv* + *l*0 + *ts*. The optimum value of a given regularization's hyperparameter (μ) was selected in the following way. We created an L-curve characterizing the response of the prior term versus the χ^2 value of the image solution for several values of μ. The optimum value of μ is associated with the elbow of the L-curve. This procedure[a] was followed firstly for the L0-norm regularization, then for the transpectral regularization, and finally for the Laplacian and Total Variation regularizations.

We also tested the possible influence of an initial model on the image reconstruction process. The image reconstructions without an initial model were obtained by employing the procedure explained in Paladini et al. (2018), which consists of: i) Create a reconstructed image with a resolution of a quarter of pixels and four times the mas/pixel of the final image, with a simple Dirac delta function as a start image. ii) Use this image as initial guess for creating another one with half the number of pixels and two times the mas/pixel of the final image. iii) Using this intermediate image as initial model, reconstruct the final image at full resolution. The reconstructions with initial model used the best-fit models from the PHOENIX + UD model discussed in Sect. 7.3. The difference between these two methods of reconstruction (initial model vs no initial model) was negligible.

We first reconstructed images at the six spectral channels individually. When comparing the images, we did not find significant differences across spectral channels. The Structural Similarity Index (see Sect. 7.5.2) showed a very high similarity of SSIM = 0.99 across the spectral channels. Therefore, we combined the data of all spectral channels covering wavelengths of $1.53\,\mu$m to $1.78\,\mu$m.

We selected the SQUEEZE images with lowest χ^2, which, in the case of combined channels for 2016, corresponds to $\chi^2 = 1.57$ with $\mu_{tv} = 500$, $\mu_{l0} = 3$, $\mu_{ts} = 1$, using the initial model described in Sect. 7.3. The 2019 combined channels image has a $\chi^2 = 7.09$ with $\mu_{tv} = 2000$, $\mu_{l0} = 30$, $\mu_{ts} = 1$, using also an initial model. The reason of the larger χ^2 of the 2019 image compared to the 2016 image is not clear. It may be related to the smaller estimated errors of the measured visibility and closure phases in the 2019 data, so that systematic absolute calibration uncertainties have a larger relative contribution. Our

---

[a] See *Reconstruction test report and data processing cookbooks* by Sanchez-Bermudez et al. available at `http://www.jmmc.fr/oimaging.htm`

image reconstruction tests (see Sect. 7.4.2) confirm that the 2019 image reconstruction is as at least as reliable as the 2016 image reconstruction. The reconstructed images were not further convolved beyond the chosen pixel scale of 0.3 mas/pixel as discussed above.

7.4.1 The final reconstructed images

Figure 7.3 shows the final reconstructed images for the 2016 and 2019 epochs. The images of the individual spectral channels are shown in Appendix A.3 to illustrate that they are very similar across spectral channels. We obtained the synthetic visibilities of the final reconstructed images at our *uv* observational points using the OITOOLS package[b]. The comparison of the interferometric observables from the experimental data with those extracted from the reconstructed images (Fig. 7.3) shows a very good agreement (Fig. 7.2). This confirms that extended flux caused by the MOLsphere (Sect. 7.3) is present in the reconstructed images, as already indicated by the improved χ^2 values with increased FoV (Sect. 7.4). For the sake of clarity, we show in Fig. 7.2 only the visibility values based on the wavelength- and time-averaged reconstructions, while the observed visibilities are shown for individual observing dates and spectral channels. Some of the residual differences in Fig. 7.2 may be caused by this effect.

The reconstructed image of the 2016 epoch shows the stellar disk with an intriguing bright arc-like feature toward the northern rim of the stellar surface. In 2019, the orientation of the arc-like feature is different and a new peak of emission is detected at the opposite part of the stellar surface. The extended molecular layer or MOLsphere, although present in the reconstructed images, lies close to our achieved dynamic range (of about 1:10 to 1:20), so that it is not well visible. While the parameters of the MOLsphere show a dependence on wavelength, the photospheric structure is not expected to be wavelength dependent, which explains that the reconstructed images appear to be very similar across spectral channels. The double visibility null, as seen in the observed visibilities in Fig. 7.2 and described in Sect. 7.3, is reproduced by the image reconstructions, and is thus most likely caused by the surface features and not by an overall elongated stellar disk.

---

[b] Available at `https://github.com/fabienbaron/OITOOLS.jl`

7.4.2 Error estimates of the final reconstructed image

We characterized possible errors that may be introduced by the reconstruction process to assess the soundness of the detected surface features. We also used the IRBis reconstruction package (Hofmann et al. 2014, Image Reconstruction software using the Bispectrum) to test the dependency of our results on the reconstruction package employed. A detailed explanation of these tests can be found in Appendix A.2. Our analysis revealed that: i) No new features are introduced within SQUEEZE when altering the final reconstructed images by one standard deviation. ii) Synthetic observational data based on 3D snapshots at our *uv* points and with our level of noise recovers the substructure present in the original image, with maximum intensity losses of 26% for the 2016 and 30% for the 2019 epochs. iii) The difference between SQUEEZE and IRBis reconstructed images shows that the same structures are present in both image reconstructions. Therefore, we conclude that the detected structure is most likely real and not due to any artificial effect.

Fig. 7.4 shows the total error map, conservatively taking into account all these possible error sources, as described in detail in Appendix A.2. The average errors, in terms of original image flux, are 17% and 14% for 2016 and 2019, respectively. Most of these error sources are systematic extending across the images, so that the pixel-to-pixel error is significantly smaller.

Our tests using reconstructions of synthetic data (based on 3D RHD models and with our *uv* coverage and observational errors) with different convolution kernels (see Appendix A.2.3) revealed that original images and reconstructions match best with a convolution kernel of 0.6 mas. This suggests that we reach with our data and *uv* coverage a super-resolution of ~ 0.6 mas compared to the nominal resolution $\lambda/(2B_{\mathrm{max}})$ of 1.2 mas.

7.5 Comparison with 3D RHD simulations

In order to compare our PIONIER data of V602 Car to theoretical models, we used numerical 3D RHD simulations obtained with the CO^{5}BOLD code (COnservative COde for the COmputation of COmpressible COnvection in a BOx of L Dimensions; Freytag et al.

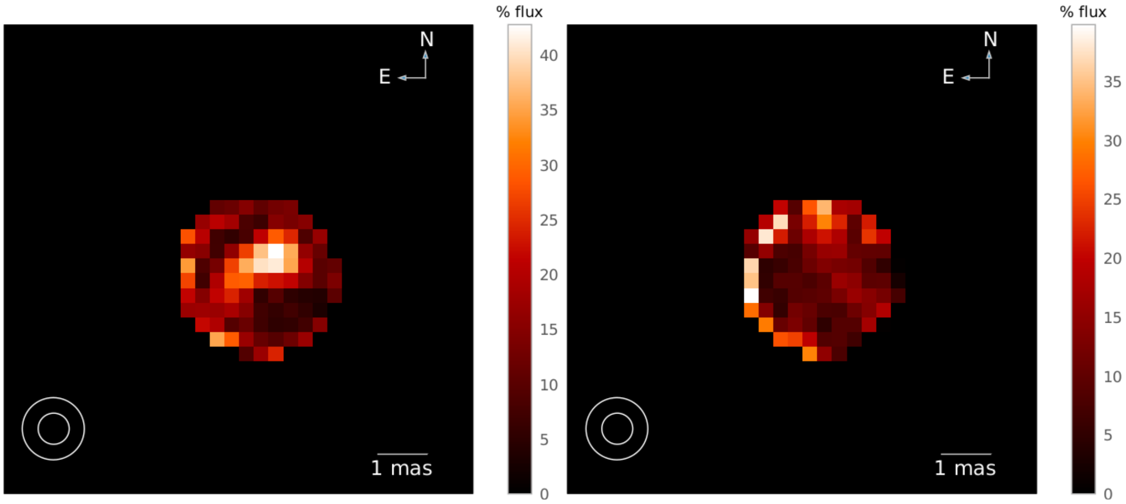

Figure 7.4: (*Left*). Error images for the (left) 2016 epoch and (right) 2019 epoch resulting conservatively from the addition of three possible sources of errors discussed in Appendix A.2. The errors are expressed in terms of the original image flux. Here and hereafter, the 3D-RHD-model-related images have being convolved with a 0.6 mas beam, our best estimate of the real resolution obtained.

2012). The simulation used was st35gm04n38 (401^3 grid points, $T_{\rm eff}$ = 3414 ± 17 K, log g = -0.39 ± 0.01, 5 $M_\odot$, 582 ± 5 $R_\odot$). The grid resolution is 4.055 $R_\odot$ with a total field of view of 1626 $R_\odot$. This model shows an effective temperature and surface gravity as established for V602 Car (see Sect. 7.1), while it has a smaller radius and a lower mass compared to the observational parameters. Due to the limited number of currently available 3D simulations of RSG stars, and in particular the computationally demanding calculation of higher-mass stellar models, 3D models of a current mass of 10–13 $M_\odot$, as expected for V602 Car, and corresponding larger radii are not yet available. Nevertheless, this 3D model represents typical properties of an RSG star, and distinctively different dynamical properties than lower-mass pulsating AGB star models (cf. the discussion by Kravchenko et al. 2019). This simulation reproduces the effects of convection and, additionally, non-radial waves (Chiavassa et al. 2011). This model was first used by Kravchenko et al. (2018) and Kravchenko et al. (2019) and a detailed discussion on the model can be found therein. We computed 81 temporal snapshots about 23 days apart and covering a stellar time of about 1863 days in total. Intensity images were then computed using the pure-LTE radiative transfer Optim3D (Chiavassa et al. 2009) at the bandpass of our PIONIER observation of 1.65±0.15 μm (averaged over 56 maps across the range 1.5-1.8 μm).

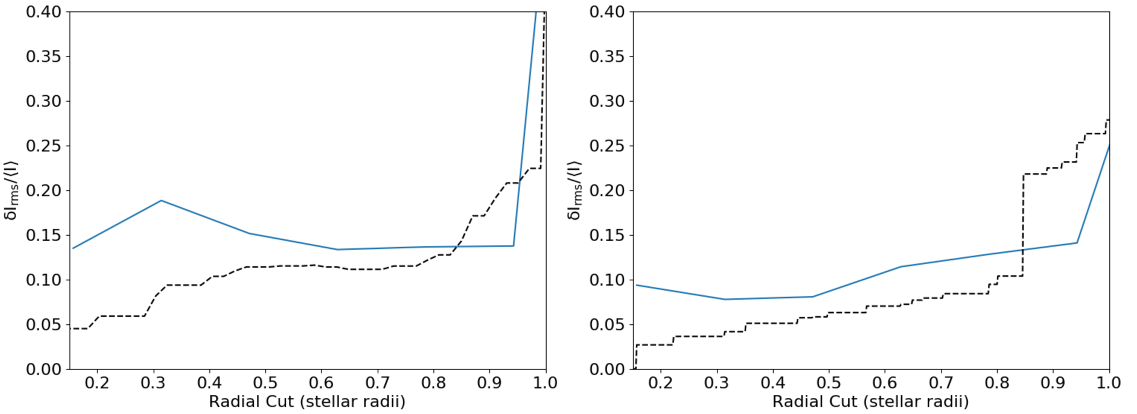

Figure 7.5: (*Left*). Contrast of the 2016 data set as a function of the radial cut considered. The black dashed line indicates the contrast of the SQUEEZE reconstructed image and the solid blue line represents one of the best simulated snapshot (065) for the 2016 data (see text). (*Right*). Same as (*Left*) but 2019 data and snapshot 67.

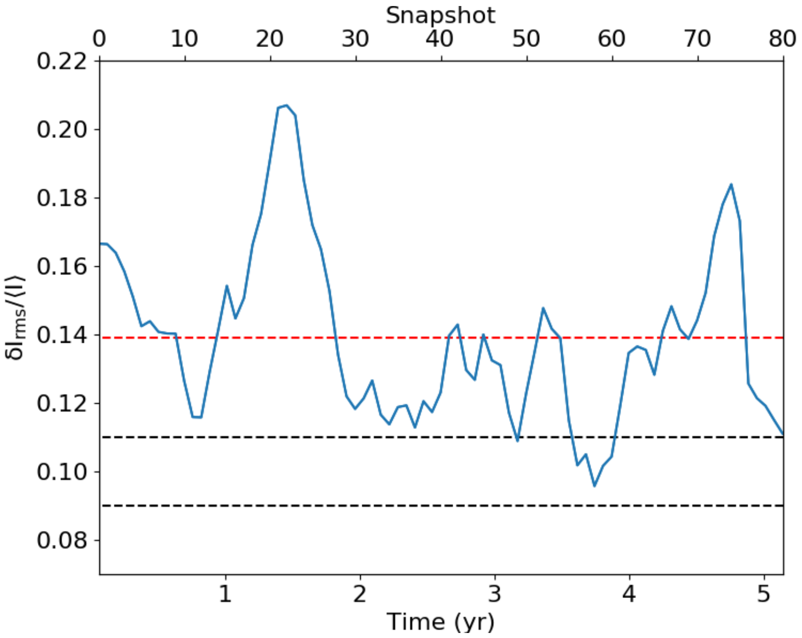

Figure 7.6: The blue line represents the contrast of the simulated snapshots after being corrected for limb-darkening (LD) with a radial cut of 0.75 stellar radii. The black dashed lines represent the contrasts measured in the final reconstructed images (11 ± 2% in 2016, 9 ± 2% in 2019) while the orange dashed line represents the average value over all the snapshots (14 ± 2%). The LD was corrected using the best-fit model image from Sect. 7.3.

7.5.1 Comparison in terms of contrast

We estimated the contrast of our reconstructed images, $\delta I_{rms}/\langle I \rangle$, as defined in Tremblay et al. (2013) to compare them to 3D RHD simulations. The contrast on the stellar surface is affected both by surface features and by the limb-darkening (LD) effect. We are interested in the contrast of the surface features themselves. In order to correct for the LD effect, we used two independent methods: i) dividing the reconstructed image by the best-fit model image described in Sect. 7.3. ii) applying Equation 2 found in Chiavassa et al. (2009) with parameters in Table 2 of the same text. In this second method, we created a high resolution image of the LD model (401×401 pixels) with the same field of view (FoV) as the reconstructed image. Then, we re-binned it to the same resolution and pixel size of our reconstucted image, so that the effectively both images (LD model and reconstructed) possessed the same FOV and resolution. Finally, we divided pixel by pixel in a similar fashion to the first method. Both of these methods resulted in a very similar correction. From now on the results exposed are valid for both of them.

We need to ensure that we do not include the stellar limb in our estimate of the contrast of surface features. We define a cut-off radius, i.e., the maximum radius adopted from the center of the star and for all angles, from which outer pixels are not considered to compute the contrast. Fig. 7.5 shows the contrast as a function of the chosen cut-off radius. For the 2016 data, the contrast increases with increasing radial cut up to ~0.5 stellar radii. This could be explained by an increasing number of included image patterns as the cut-off radius gets larger. For larger cut-off radii, between about 0.75 and 0.95 stellar radii, the contrast again shows a fast increase. This may be an effect of the limb-darkening that may not be perfectly corrected. When the radial cut surpasses the value of about 0.95 stellar radii we see a rapid and steep increase, which may be representative of the contrast between the stellar disk and the outside of the disk, which may also not be perfectly circular. A similar behavior is seen for the 2019 data, where more and more patterns and structures are included as the radial cut gets larger until a rapid increase occurs at ~0.85 stellar radii.

We will only consider the contrast below a radial cut of 0.75 stellar radii to avoid the bias of the uncertainty of the limb-darkening correction.The lower cut must include the arc-like feature present in Fig. 7.3 for 2016 and the more complex features of the 2019 data. Therefore, we establish a lower cut of 0.5 stellar radii in the 2016 data, implying a contrast value of 11% ± 2% which corresponds to the plateau found between these radii. Due to shape of the sub-structures present in 2019 data, no lower cut value can be easily determined for this epoch. Therefore, we assume as a radial cut the maximum value considered here, i.e., 0.75 stellar radii, with a contrast value of 9% ± 2%. Although the average pixel errors of the images were 17% and 14% for 2016 and 2019, as described in Sect. 7.4.1, and thus larger than the surface feature contrasts, we emphasize that the pixel errors are conservative values that take into account multiple sources of errors, as outlined in Appendix A.2, several of which are systematic. This does not mean that the pixel-to-pixel and the contrasts uncertainties are as large as this error map.

Following the same procedure, we calculated the contrast for the 81 snapshots of the simulated 3D RHD snapshots. Figure 7.6 shows how the contrast varies across different snapshots, assuming a radial cut of 0.75 stellar radii. The average contrast value over the 81 snapshots is 14% ± 2%. This value is slightly larger than that of our image reconstructions, but with individual snapshots that have consistent contrast values.

Considering that our observational epochs lasted about 70 days, we made a test in which we first averaged consecutive model snapshots over this time span, i.e., 2–3 snapshots, and then computed the contrasts of the averaged snapshots. The snapshot images were similar over this time spans, resulting in only marginal differences in the contrast curve shown in Fig. 7.6.

Previous works have found similar contrast values in RSGs. Wittkowski et al. (2017a) reported consistently a contrast of 10%±4% for the RSG V766 Cen, while Montargès et al. (2018) found a lower contrast of 5–6% ±1% for the RSG CE Tau. Both estimates were based on similar imaging of data obtained with the PIONIER instrument in the near-IR H-band.

7.5.2 Comparison in terms of morphology

We then investigated whether the 3D RHD simulations could reproduce the observed morphology of our reconstructed images, such as the arc-like feature discussed in Sect. 7.4.1.

The calculated snapshots of the 3D RHD simulations represent the stellar convection dynamics every ~23 days, covering a total of 1863 days. There is a fundamental problem in direct comparisons of such simulated snapshots to our data: The surface pattern changes in a stochastic way and never repeats itself. With a finite number of simulated snapshots, we cannot expect any snapshot to coincide exactly with the pattern at one of our observed epochs. If we cannot expect a model to describe the observational data, a formal χ^2 comparison between model and observation is not appropriate and may lead to spurious results. As a solution to this fundamental problem, we introduce the use of the Structural Similarity Index (SSIM; Wang et al. 2004) to find the most similar of the 81 model snapshots compared to our reconstructed image (Fig. 7.3). The SSIM of a pair of images represents a superior method for image comparison. It is typically used in order to quantify the differences between a distorted image and a reference image. It is based on the perceived change in the structural information from one image to the other and ranges from -1 to 1, where 1 indicates perfect similarity (Eq. A.1).

We first convolved the model images to our best estimate of the real resolution obtained, 0.6 mas (see Appendix A.2.3), re-sized the images to the pixel scale and field of view of our reconstructed images, and applied a cut-off radius of 0.75 stellar radii as in Sect. 7.5.1. To account for the unknown orientation on the plane of the sky, we rotated the model images every 5° around its center and estimated the SSIM for each rotation angle. As expected, none of the snapshots coincided with our observed epochs perfectly but several were equally similar. For the 2016 data, the most similar snapshots were (rotation angle in parenthesis): 003 (325° ± 5°), 004 (325° ± 5°), 005 (320° ± 5°), 006 (325° ± 5°), 064 (10° ± 5°), 065 (10° ± 5°), 066 (10° ± 5°) and 067 (10° ± 5°), all with SSIM = 0.85. All of these snapshots coincided with those that we, previously and visually, had selected to be most similar to our observed image. We selected snapshot 065 as a representative

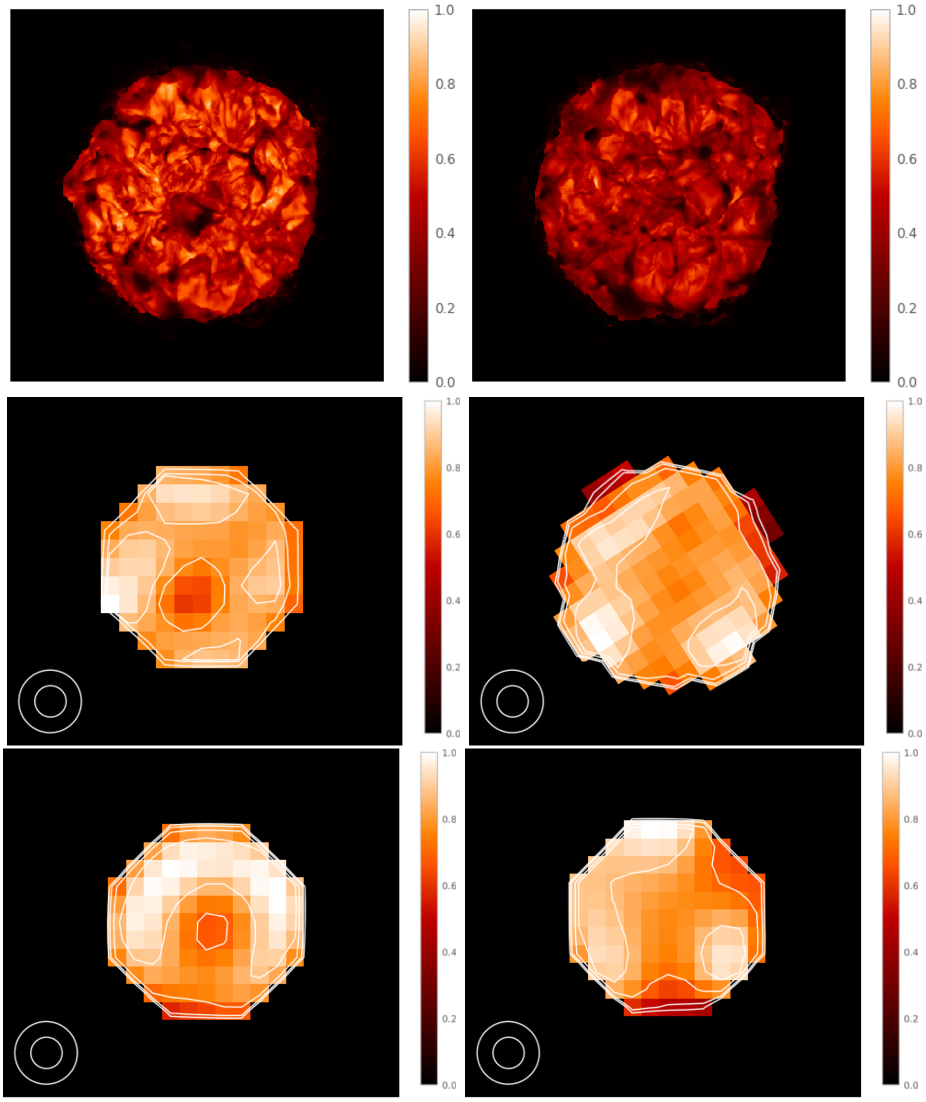

Figure 7.7: (*Top row*): Intensity image of one of the selected best snapshots (number 065) for 2016 in relative intensity (*left*), and for snapshot 067, which is the best choice for the 2019 data (*right*). (*Middle row*): The same snapshot images as in the *upper row* after being convolved with a 0.6 mas beam, rotated to match the observed morphology, and corrected for the limb-darkening effect with a cut-off radius of 0.75 stellar radii. (*Bottom row*): Reconstructed observational images after LD correction and with a cut-off radius of 0.75 stellar radii. In both *middle row* and *lower row*, the contours are drawn at levels of 55%, 77% and 85% of the peak intensity for 2016 (*left column*) and at 40%, 50%, 70% and 87% of the peak intensity for 2019 (*right column*).

of this subset of snapshots, in which the arc-like structure is visually clearest. Figure 7.7 (upper left panel) shows this model image at the original model resolution. Figure 7.7 (left middle and lower panels) shows a comparison of this model image to our image reconstruction after adjusting it to the pixel size of the reconstruction, and rotating it to best match the reconstruction.

The same procedure was followed for the 2019 data selecting, in this case, snapshots 067 (-30° ± 5°), 068 (-30° ± 5°), 069 (-30° ± 5°) and 070 (-35° ± 5°), all with SSIM = 0.87. As a representative of this subset of snapshots, we selected snapshot 067 (see Fig. 7.7 right panels). Adjacent snapshots for the 2016 and 2019 data are very similar to these selected representatives. Although visually not identical to each other, our limited spatial resolution and dynamic range render them equally similar to the observational image. Finally, we have tested the uncertainties when computing the SSIM by adding and subtracting the intensity error image (Fig. 7.4) to the observational images (Fig. 7.3) and computing the SSIM between these resulting images and the selected 3D RHD model images corresponding to each epoch. The SSIM value differs only 0.02 with respect to the case when no error image is considered.

The surface features seen in the model snapshots (Fig. 7.7, top row) are unlikely individual deep convection cells that reach out to the surface layers, as the time scale on which the structure changes in the models is too fast. The features in the model snapshots are, therefore, likely related to instationary convection, i.e., to pressure fluctuations (non-radial waves that do not exist long enough to produce a clear mode visible in a power spectrum), that are caused by sonic convective motions and are able to affect not only a single surface granule but a group of neighboring granules. With the limited spatial resolution of our observation (Fig. 7.7, middle and bottom row), the structure is further convolved to larger observed patches on the stellar surface. This means that we cannot determine sizes of individual granules or convection cells (see also Freytag 2003).

Each subset of the most similar snapshots to our 2016 data, 003 to 006 and 064 to 067, represent a time span of 69.5 days, indicating that the structure remains similar on time scales of ~2 months. A similar result is found in the 2019 analysis where snapshots 067 to 070 represent also 69.5 days. This confirms that, with our accuracy and spatial resolution, it was a valid approach to combine data obtained over about 70 days (see Sect. 7.2).

The agreement between our image reconstructions and the most similar snapshots of the 3D RHD simulations may indicate that, within our angular resolution and achieved dynamic range, the observed stellar surface features of V602 Car at two individual epochs can be reproduced by the physics accounted for in the simulations we considered (i.e., non-local radiation transport, shock waves, gray and non-gray opacities, see Chiavassa et al. (2011)).

We then computed azimuthally averaged intensity profiles and synthetic visibility values for the selected snapshots and compared them to our observed visibility spectra. We computed the intensity profiles using rings regularly spaced in μ, related to the impact parameter by $r/R_{\rm star} = \sqrt{1-\mu^2}$. We used 56 spectral maps between 1.5 μm and 1.8 μm at a spectral resolution of 300. Synthetic visibility values were then derived following the same procedure as in Wittkowski et al. (2017b), and in the same way as for the fit of a PHOENIX model in Sect. 7.3. Table 7.2 shows the resulting best-fit parameters. The synthetic visibilities based on this model are included in Fig. 7.2. In both the 2016 and 2019 data, the best-fit parameters are close to those obtained from the fit of the PHOENIX model together with a UD representing the MOLsphere. We adopt a resulting photospheric angular diameter of V602 Car of 4.4 ± 0.2 mas. This is the average of the photospheric angular diameters for 2016 and 2019, that are based on the fits including the PHOENIX model.

The best fits were achieved with an additional UD component and a free zero visibility scale, as for the 1D PHOENIX model atmosphere. The visibility plot of the best model for each epoch is included in Fig. 7.2. This shows that the 3D RHD simulations alone cannot reproduce the observed visibility values, but that an additional, more extended component is still required to re-produce the observed data. The presence of a MOLsphere on top of the photosphere may alter the contrast and morphology of the photospheric features to some extent (below about 4% in pixel value). This may explain a part of the residual differences between image reconstructions and 3D model images in terms of contrast and morphology.

Table 7.2: Fit parameters to the PHOENIX model and to the best snapshots from 3D RHD simulations, for each epoch.

Model	Epoch	Channel (μm)	Θ_1 (mas)	f_1 (%)	$\Theta_{\rm UD}$ (mas)	$f_{\rm UD}$ (%)	$f_{\rm free}$ (%)
PHOENIX	2016	1.53	4.4 ± 0.2	84.9	6.4 ± 0.2	12.3	2.8
		1.58	4.4 ± 0.2	86.6	6.3 ± 0.2	10.8	2.6
		1.63	4.4 ± 0.2	88.3	6.1 ± 0.2	8.4	3.3
		1.68	4.5 ± 0.2	94.2	12.3 ± 0.2	5.4	0.4
		1.72	4.4 ± 0.2	89.5	8.2 ± 0.2	9.8	0.7
		1.77	4.5 ± 0.2	88.7	8.3 ± 0.2	10.6	0.7
		Average	4.4 ± 0.2	88.7 ± 3.2	7.9 ± 2.3	9.5 ± 2.4	1.0 ± 1.2
PHOENIX	2019	1.53	4.5 ± 0.2	93.0	11.1 ± 0.2	7.2	0.0
		1.58	4.6 ± 0.2	94.2	11.7 ± 0.2	6.0	0.0
		1.63	4.5 ± 0.2	91.2	6.7 ± 0.2	6.5	2.2
		1.68	4.5 ± 0.2	90.5	6.3 ± 0.2	7.5	2.0
		1.72	4.4 ± 0.2	82.7	5.7 ± 0.2	16.0	1.3
		1.77	4.4 ± 0.2	80.8	6.2 ± 0.2	17.4	1.8
		Average	4.5 ± 0.2	88.8 ± 5.7	8.0 ± 2.7	10.1 ± 0.5	1.1 ± 1.0
3D RHD 065	2016	1.53	4.1 ± 0.2	79.3	6.0 ± 0.2	17.9	2.8
		1.58	4.1 ± 0.2	82.2	6.1 ± 0.2	15.3	2.5
		1.63	4.2 ± 0.2	84.2	6.1 ± 0.2	12.8	3.0
		1.68	4.2 ± 0.2	88.2	7.2 ± 0.2	10.1	1.7
		1.72	4.2 ± 0.2	87.8	7.9 ± 0.2	11.5	0.7
		1.77	4.2 ± 0.2	86.7	7.9 ± 0.2	12.5	0.8
		Average	4.2 ± 0.2	84.7 ± 3.5	6.9 ± 0.9	13.4 ± 2.8	1.9 ± 1.0
3D RHD 067	2019	1.53	4.2 ± 0.2	86.3	5.9 ± 0.2	10.8	2.9
		1.58	4.3 ± 0.2	88.7	6.0 ± 0.2	8.9	2.4
		1.63	4.3 ± 0.2	89.7	6.7 ± 0.2	8.7	1.6
		1.68	4.3 ± 0.2	88.8	6.3 ± 0.2	9.3	1.9
		1.72	4.2 ± 0.2	76.4	5.5 ± 0.2	22.3	1.3
		1.77	4.2 ± 0.2	77.4	6.0± 0.2	21.1	1.5
		Average	4.2 ± 0.2	84.5 ± 6.0	6.1± 0.4	13.5 ± 6.4	1.9 ± 0.6

Notes. Θ_1 represents the Rosseland angular diameter in the case of the PHOENIX model and the layer where r/R$_{star}$ = 1 in the 3D RHD model. $\Theta_{\rm UD}$ is the angular diameter of the uniform disk describing the MOLsphere. Finally, f_1, $f_{\rm UD}$ and $f_{\rm free}$ describe the relative flux of the PHOENIX/3D RHD, MOLsphere and a free zero visibility scale components.

7.6 Conclusions

Our new VLTI/PIONIER visibility data sets of V602 Car indicate an overall spherical stellar disk and an extended molecular layer, similarly to what has been detected in previous observations. The same data also indicate the presence of sub-structures within the stellar disk at both epochs 2016 and 2019. In order to further probe the stellar surface of V602 Car we obtained aperture synthesis images using two different reconstruction packages: SQUEEZE and IRBis. Both packages resulted in very similar results. The reconstructed images revealed a bright arc-like feature toward the northern rim of the stellar surface of the RSG V602 Car in 2016. Three years later, in 2019, an arc-like feature appeared at a different orientation and a new peak of emission emerged at the opposite side of the stellar surface. The flux contribution caused by the extended molecular layer is present in the reconstructed images, but not well visible because it lies close to our achieved dynamic range. We can therefore not constrain its morphology.

We compared the reconstructed images to latest 3D RHD simulations of RSGs. There is a fundamental problem in direct comparisons of such simulated snapshots to our data: The surface pattern changes in a stochastic way and never repeats itself. With a finite number of available simulated snapshots, we cannot expect any snapshot to coincide exactly with the pattern at one of our observed epochs. A classic χ^2 comparison between model and observation is thus not appropriate and may lead to spurious results. As a solution to this problem, we introduced the use of the SSIM to find the most similar of the model snapshots compared to our reconstructed image. This comparison resulted in the identification of 8 and 4 adjacent snapshots (out of 81 total) equally similar to the observational data obtained in 2016 and 2019, respectively. The SSIM was 0.85 and 0.87, respectively, indicating that none of the snapshots coincides perfectly with our observed epochs, but some show a high degree of similarity. We concluded that, within our limitations in angular resolution and dynamic range, the observed stellar surface features of V602 Car can be reproduced by the physics accounted for in the simulations we considered at two individual epochs. Further observations at higher spatial and temporal resolution are needed to confirm the agreement. We interpreted the observed surface features to be related to instationary convection. The structure is further convolved to larger observed patches on the stellar surface with our observational spatial resolution. As a result, we loose information on sizes of individual granules or convection cells. The time during which the structure of the most similar snapshots remains stable is ~70 days. As a more quantitative method of comparing observational data and simulations, we computed the contrast of the best snapshots and found agreement with the contrast of the reconstructed images (within the associated errors).

Although the observed stellar surface structure can be well explained by the 3D RHD models as such, the simulations alone are not able to reproduce the observed visibility data. An additional extended molecular component is still needed, pointing to the current limitations of RHD simulations of RSG stars, as found in Arroyo-Torres et al. (2015). While the effects of convection on the stellar surface may be well described by current 3D simulations and the physics they contain, convection alone may not be the only relevant process to levitate the atmosphere, that is the first step of the mass-loss process.

Chapter 8

Summary and outlook

8.1 Summary

In this dissertation, we have presented the results of radio and infrared interferometric observations of objects as varied as ultracool dwarfs and red supergiants. What has allowed for such diversity of objects is the backbone of this work: the interferometry technique. With the the ability to achieve such high angular resolutions, the applications in different fields that this technique can provide are countless. In our case, we have focused on:

1. Investigating the radio emission mechanisms and radio structure on AB Dor A. This PMS star is known to be a strong and persistent radio emitter. With VLBI observations lasting more than a decade using the LBA, our 8.4 GHz images showed a double core-halo morphology, similar at all epochs, with emission extending at heights between 5 and 18 stellar radii. What is even more intriguing is that, in these images, there is a clear variation of the source structure within the observing time. We have considered several models to explain these features: a possible companion to AB Dor A, emission from the stellar polar caps, a flaring, magnetically-driven loop structure, and the presence of helmet streamers. Our current observations can only discard the companion scenario. Detection of AB Dor A at 1.4 was also made with the image showing a structure compatible with an unresolved source. Finally, we placed strong upper limits of 0.11 mJy, 0.04 mJy, 0.10 mJy, 0.04 mJy and 0.07

mJy for the radio emission of AB Dor C in 2007 (8.4 GHz), 2010 (8.4 GHz), 2013 (8.4 GHz), 2017 (22.3 GHz) and 2018 (1.4 GHz), respectively.

2. Probing the radio emission of the substellar triple system VHS 1256-1257. Using multi-frequency, multi-epoch observations with the VLA and EVN, we have discovered radio emission at X band originating in the central binary. We also placed a strong upper limit for the radio emission at L band of 20 μJy. Additionally, we have been able to infer the possible origin of the detected emission by estimating the spectral index between 8 and 12 GHz. We found $\alpha = -1.1 \pm 0.3$, indicating a non-thermal, optically thin, synchrotron, or gyrosynchrotron radiation. The non-detection of radio emission at L band made us considered two hypothesis: either a strong variability weakened the radio emission in all of our epochs of observation, or the radio emission is actually self-absorbed at L band. The first hypothesis seems highly unlikely and, hence, exploring the second hypothesis, we constrained the turnover frequency to be in the interval 5-8.5 GHz, from which we infered the presence of strong magnetic fields ($\sim$ kG) in the M7.5 binary. The value of this magnetic field intensity is in agreement with theoretical models for M-dwarfs (Reiners & Christensen 2010) and with the average value of the magnetic field intensity found in a sample of M7-9.5 dwarfs (Reiners & Basri 2010). Our data also imposes a 3σ upper bound to the radio emission of the L7 object of 9 μJy at 10 GHz. Remarkably, we have also detected K_a band (26-40 GHz) radio emission coincident with the expected position of the central binary with a peak flux of 65 μJy. This value seems to be way above the flux expected for a dusty disk model. Additionally, this hypothesis does not seem to fit with ALMA band 7 (275-373 GHz) observations in which no emission from this object was detected (Zapatero-Osorio, priv. communication).

3. Exploring the nature of AB Dor C. From VLTI/AMBER observations at J,H and K infrared bands, we have found that both the visibilities and closure phases of this object at K band are compatible with a binary brown dwarf system. This is specially relevant because stellar evolution models have had some difficulties in their

predictions in the case of low- and very low-mass pre-main-sequence stars, and only well-known objects with dynamically determined masses and precise photometry can be used to test and check the predictions of such models. It is, therefore, critical to know if, indeed, AB Dor C is a binary system. Our measurements show supporting evidence for this hypothesis and, from them, we infered that the masses of components AB Dor Ca and AB Dor Cb would be $0.072 \pm 0.013 M_{\odot}$ and $0.013 \pm 0.001 M_{\odot}$, respectively. That is, AB Dor C could be formed by a brown dwarf near the hydrogen-burning limit in the case of AB Dor Ca, and an object straddling the boundary between brown dwarfs and giant planets in the case of AB Dor Cb. This binarity would alleviate the disagreement between observed magnitudes and theoretical mass-luminosity relationships.

4. Shedding some light on the responsible mechanisms for the great mass loss rates on red supergiants. It is thought that photospheric convection may be a crucial factor of the levitation of the outer atmospheric layers in RSG. To probe this, we observed V602 Car with infrared interferometry (VLTI/PIONIER) in a similar manner as we did with AB Dor C. However this time, the quality of the observations on this RSG allowed for image reconstruction at two different epochs (2016 and 2019) and so we were able to appreciate the features on the stellar surface of V602 Car. In the first epoch, the reconstructed image revealed a bright arc-like feature toward the northern rim of the photospheric surface. In 2019, an arc-like feature was also seen but at a different orientation and a new peak of emission was detected on the opposite side. When comparing these observational results to 3D RHD models we found that, indeed, the simulations predict substructures similar to the observed surface features of V602 Car at two different epochs. However, they failed to reproduce the observed visibility data. Therefore, an additional extended molecular component was still needed, and that points directly to the current limitations of RHD simulations of RSG stars. From this study we concluded that, convection alone may not be the only relevant process to levitate the atmospheres on RSGs.

8.2 Outlook

There are a number of research projects worth pursuing in the near future. Some of them are natural extensions of the research discussed in this thesis. Others are objects different than those discussed here but investigated through the same interferometry technique. Let us discuss these two projects separately.

Firstly, we have now ready-to-analyze observations of the intriguing system VHS 1256-1257 at 5 GHz with the EVN. These are of extreme importance since they should be able to confirm our finding that the turnover frequency of the radiation detected in the central binary is located between 5 and 8.5 GHz. Additionally, the great angular resolution offered by the EVN may allow us to discriminate if the radio emission originates in one of the components, in both, or perhaps a sort of interaction between them. These higher resolution observations will also open the door to a multiepoch astrometric study in order to determine the parallax of the system and, also precisely estimate the masses of the internal pair via monitoring of its orbital motion.

Secondly, the evidence we discovered in favour of the binarity of AB Dor C needs to be confirmed. To do this we have applied for GRAVITY/VLTI observations in dual-field on axis mode with the ATs. With this mode, the light of the brighter AB Dor A will go to the fringe-track (FT) fibre, meanwhile we would center AB Dor C in the science fibre (SC), the latter being possible thanks to the milliarcsecond-precise knowledge of its orbital position. With 10 hours of observing time we expect to improve the dynamic range to successfully detect the weak companion AB Dor Cb. This proposal is currently under evaluation.

In the third place, more data is needed to further investigate the mass loss mechanism in RSGs. New data on a sample of these stars is already available: MATISSE data on AH Sco, V766 Cen PIONIER data, and R Aqr data with GRAVITY monitoring and PIONIER and MATISSE imaging. R Aqr is a very interesting target. It is a symbiotic binary with the white dwarf moving in front of the primary every 44 years. Fortunately, the darkening starts again supposedly in 2022 and so these observations will be extremely valuable. This field of research is incredibly exciting and new spectacular results should be expected.

Finishing the natural extensions of the work presented in this thesis is the radio structure detected in AB Dor A. Here, new VLBI data has the difficult task of discerning which of the scenarios we proposed (if any) is responsible for such structure around this star. Additionally, new data will also be probing the possible radio emission of AB Dor C.

Beyond these projects, we are currently expanding and deepening our scientific fields of interest:

- We currently have new 8.4 GHz VLA observations of a sample of 5 binary low-mass objects in the AB Dor moving group. We intend to characterize the possible radio emission of these systems. Additionally, detection of radio emission would mean that they are suitable to be the target of further astrometric studies (using the VLA and/or VLBI arrays) addressed to determine the dynamical masses, essential to calibrate (sub-)stellar evolutionary models.
- We are expanding our observations to other UCDs using the EVN. We currently have a sample of four objects with previously detected radio emission with the VLA and now observed with the EVN at 5 GHz. One of these objects is actually a binary system, LP 349-25, of which we could potentially improve the accuracy of the dynamical masses of its components which, in turn, could serve as benchmarks for evolutionary models.
- We are also using the interferometry technique for exploring possible radio emission from exoplanets. Although no detection of exoplanet radio emission has occurred yet, there are a few proposed mechanisms for such emission. We intend to probe one of them, exoplanet induced radio emission (Turnpenney et al. 2018), in our sample of five M-dwarfs systems with known exoplanets. Additionally, our data will also provide valuable insights into the radio emission from the M dwarfs.

Appendix A

Complementary work on V602 Car

A.1 Comparison of the pre-NAOMI 2016 and post-NAOMI 2019 PIONIER data

We obtained pre-NAOMI PIONIER data in 2016 and post-NAOMI PIONIER data in 2019 during NAOMI Science Verification. Both data sets are very similar in terms of *uv* coverage, time span, and atmospheric conditions. The total number of *uv* points is 156 for both data sets, and their distribution is very similar (see Fig. 1.2). The 2016 data span over 81 days, while those of 2019 span over 70 days. The atmospheric conditions were similar (see Table 7.1) with an average seeing of 0.56″and average coherence time of 4.3 msec in 2016, and of 0.64″and 5.7 msec in 2019. Both datasets used the same interferometric calibrator and the same observational and data reduction strategies.

The average error of the squared visibility amplitudes $\sigma(V^2)/V^2$ is 10.2% in 2016 and 5.6% in 2019. The average error of the closure phases is 1.8° in 2016 and 0.9° in 2019. The scatter of the visibility points, in particular at short baselines is much reduced in the 2019 data set compared to the 2016 data set (cf. Fig. 7.2).

As otherwise the two data sets are very comparable, we attribute this improvement in precision and accuracy of the visibility data to the addition of the adaptive optics system NAOMI.

Consequently, our average estimated pixel errors of the reconstructed images, based on different tests as outlined in detail in Appendix A.2, has improved from 17% to 14% for 2016 and 2019, respectively.

A.2 Estimation of image errors

In order to ensure the validity of the substructures found in Fig. 7.3, we probe different systematic errors due to three effects:

i) Errors inside the SQUEEZE reconstruction package. Detailed in Appendix A.2.1.

ii) Errors due to the reconstruction package used. Detailed in Appendix A.2.2.

iii) Errors due to effects of our limited *uv* coverage. Detailed in Appendix A.2.3.

A.2.1 Errors within SQUEEZE

To obtain the image that is shown in Fig. 7.3, we computed 50 different SQUEEZE images and averaged them. In a similar fashion as Paladini et al. (2018), Fig. A.1 shows the images one standard deviation above (and below) the average image for 2016 and 2019 data. The persistence of the same features in these error images indicates that the substructures do not originate due to the averaging procedure we followed.

A.2.2 IRBis reconstruction and comparison with SQUEEZE

Following a similar way as for the carbon AGB star R Scl (Wittkowski et al. 2017c) we used the IRBis reconstruction package as follows:

i) We selected as start images the best-fit model from the PHOENIX + UD model discussed in Sect. 7.3.

ii) We used a flat prior and the six available regularization functions of IRBis. For each regularization we tested reconstructions with decreasing values of the hyperparameter μ and increasing radii of the object mask.

iii) We chose as the final image that with the best quality derived from the χ^2 values and residual ratio values of the visibility and closure phases (q_{rec} value). This image is based on regularization function 4 (edge preservation) both in 2016 and 2019 data.

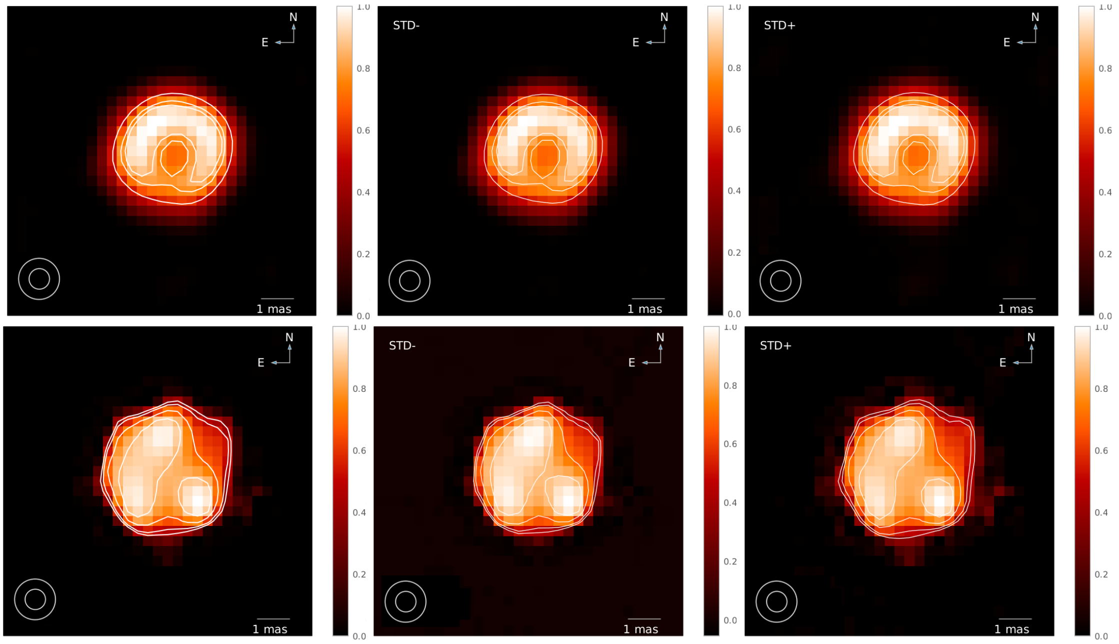

Figure A.1: Squeeze average images (left column), images one standard deviation below the average (middle column) and images one standard deviation above the average (right column). The top row represents 2016 data (contours at 55%, 77% and 85% of peak intensity) while the bottom row represents the 2019 data (contours at 40%, 50%, 70% and 87% of peak intensity).

Images obtained with regularization functions 1 (compactness), 3 (smoothness), 5 (smoothness), and 6 (quadratic Tikhonov), resulted in very similar images of similar quality parameter. Function 2 (maximum entropy) resulted in poorer reconstructions. The final images can be found in Fig. A.2.

For the same epoch, IRBis and SQUEEZE result in very similar images. Fig. A.3 shows the difference between both images (SQUEEZE - IRBis) evaluated pixel by pixel in terms of the flux of the SQUEEZE image. The results indicate that the same structures are present both in SQUEEZE and IRBis reconstruction images although some pixels differ in intensity value up to 24%. We applied a cut-off radius of 0.75 stellar radii (as stated in the main text) in order to avoid larger, not physical errors near the limb of the star.

When comparing two astronomical images of the same object that only vary in the reconstruction method employed, the image differences need to originate in these methods. This scenario is equivalent to that which the SSIM was constructed for: a reference image (e.g., SQUEEZE reconstruction) and a distorted image with respect to its reference (e.g., IRBis reconstruction). The value obtained for these two reconstructed images is SSIM = 0.99 both in 2016 and 2019 data.

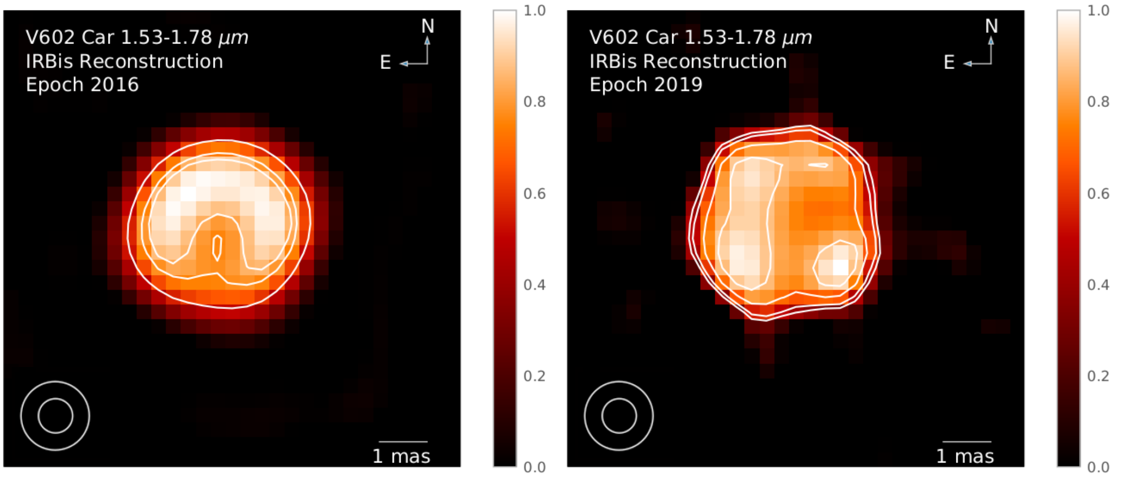

Figure A.2: Same as Fig. 7.3 but for the IRBis reconstruction package. Contours are drawn at levels 55%, 77% and 85% of the peak intensity in 2016 and at 40%, 50%, 70% and 87% of peak intensity in 2019.

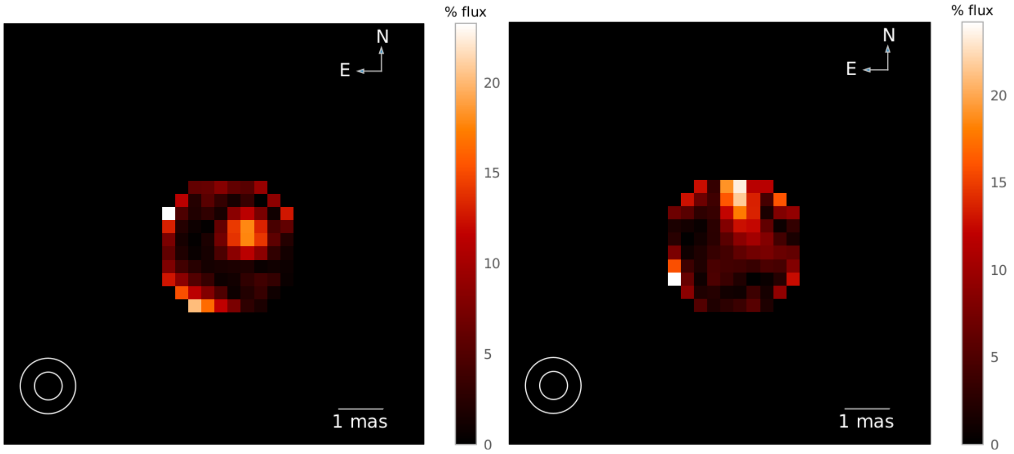

Figure A.3: Image resulting of the pixel by pixel difference between SQUEEZE and IRBis reconstructions shown in Fig. 7.3 and Fig. A.2. (*Left*): 2016 epoch. (*Right*): 2019 epoch. The scale represents the percentage of flux of the original SQUEEZE image. We have applied the same cut-off radius as presented in the main text, i.e., 0.75 stellar radii.

A.2.3 Errors due to limited uv coverage

A limited *uv* coverage might produce artificial effects that could be concealed in the final image. In order to test for these effects, we simulated visibilities from the 3D RHD model snapshots using OITOOLS at the same *uv* points of our observations. We then added a typical noise to the image and then reconstructed it using SQUEEZE in the usual way. Since we are interested in the validity of the surface features, no MOLsphere was added. We verified that an addition of a uniform MOLsphere, as modeled in Tab. 2, does not change the result.

Our results (see Fig. A.4) show that the reconstructions of the simulated visibilities (middle column of Fig. A.4) result in a very similar image to the original one (left column of Fig. A.4), with an SSIM = 0.90 in 2016 and SSIM = 0.89 in 2019. We computed these difference images with a convolved beam of 0.3, 0.6 and 1.2 mas and found that the resolution that best kept all the information about the substructures while reducing the errors is 0.6 mas, which is shown in Fig. A.4. Based on this analysis, we can estimate the super-resolution that we achieve with our *uv* coverage and our noise to 0.6 mas, as compared to the nominal resolution $\lambda/(2B_{\rm max})$ of 1.2 mas.

From this discussion, we conclude that the substructures found in Fig. 7.3 are probably not caused or altered by the limited *uv* coverages of our observations.

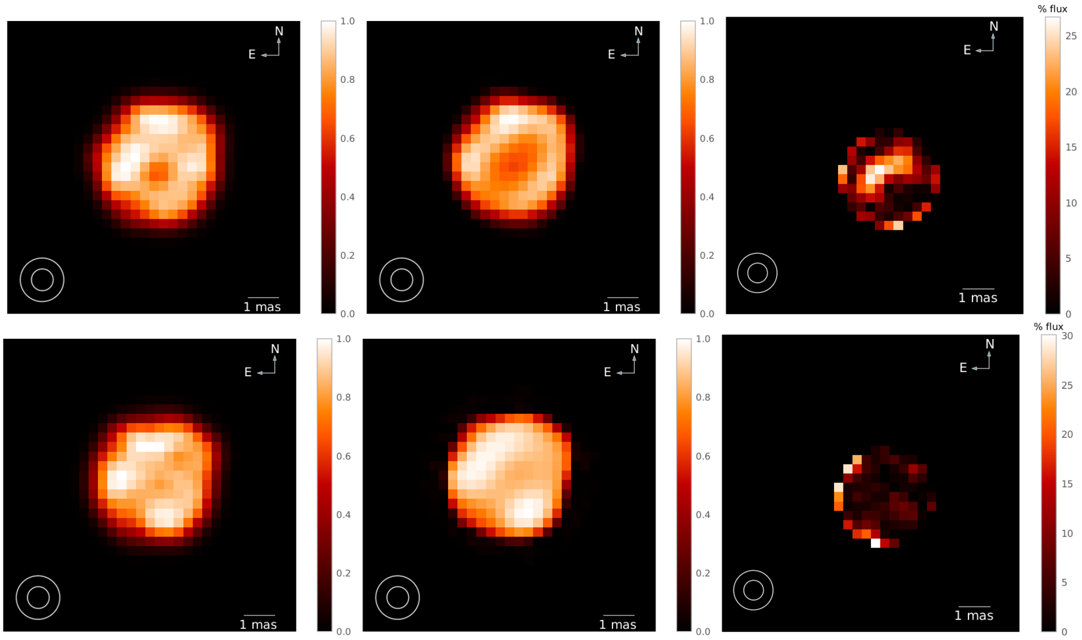

Figure A.4: Original snapshot image convolved to 0.6 mas resolution (left column), SQUEEZE reconstructed image from the synthetic visibilities of the left image (middle column; not further convolved beyond the pixel scale of 0.3 mas/pixel) and pixel by pixel difference image between *left column* and *middle column* images in terms of the original flux (right column). Top panel for snapshot 65 and bottom panel for snapshot 67. No rotation of the images was applied here. We have applied the same cut-off radii as presented in the main text, i.e., 0.75 stellar radii.

A.3 Spectral channel images of V602 Car

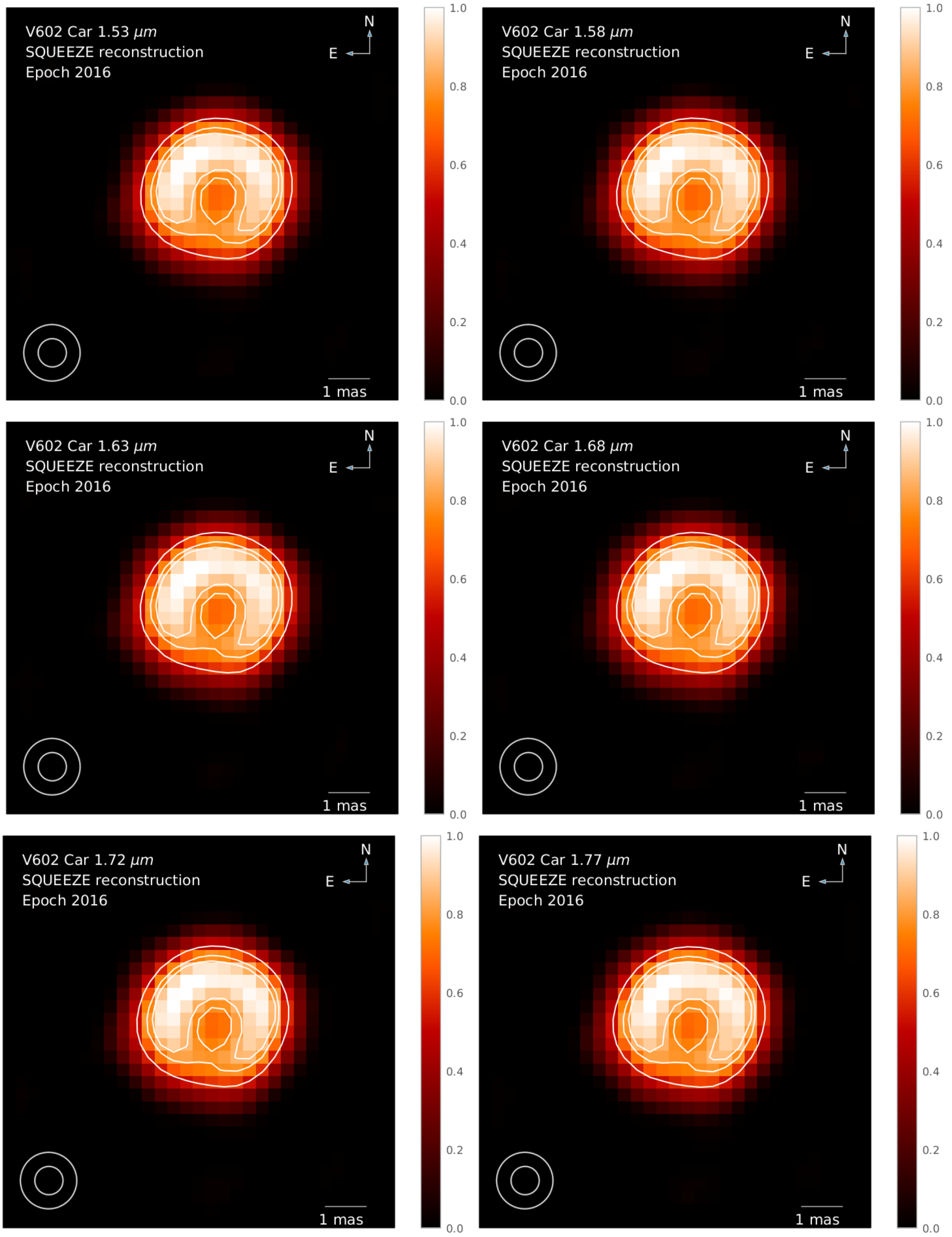

Figure A.5: SQUEEZE reconstruction of 2016 V602 Car data at each spectral channel. Contours are drawn at levels 55%, 77% and 85% of the peak intensity.

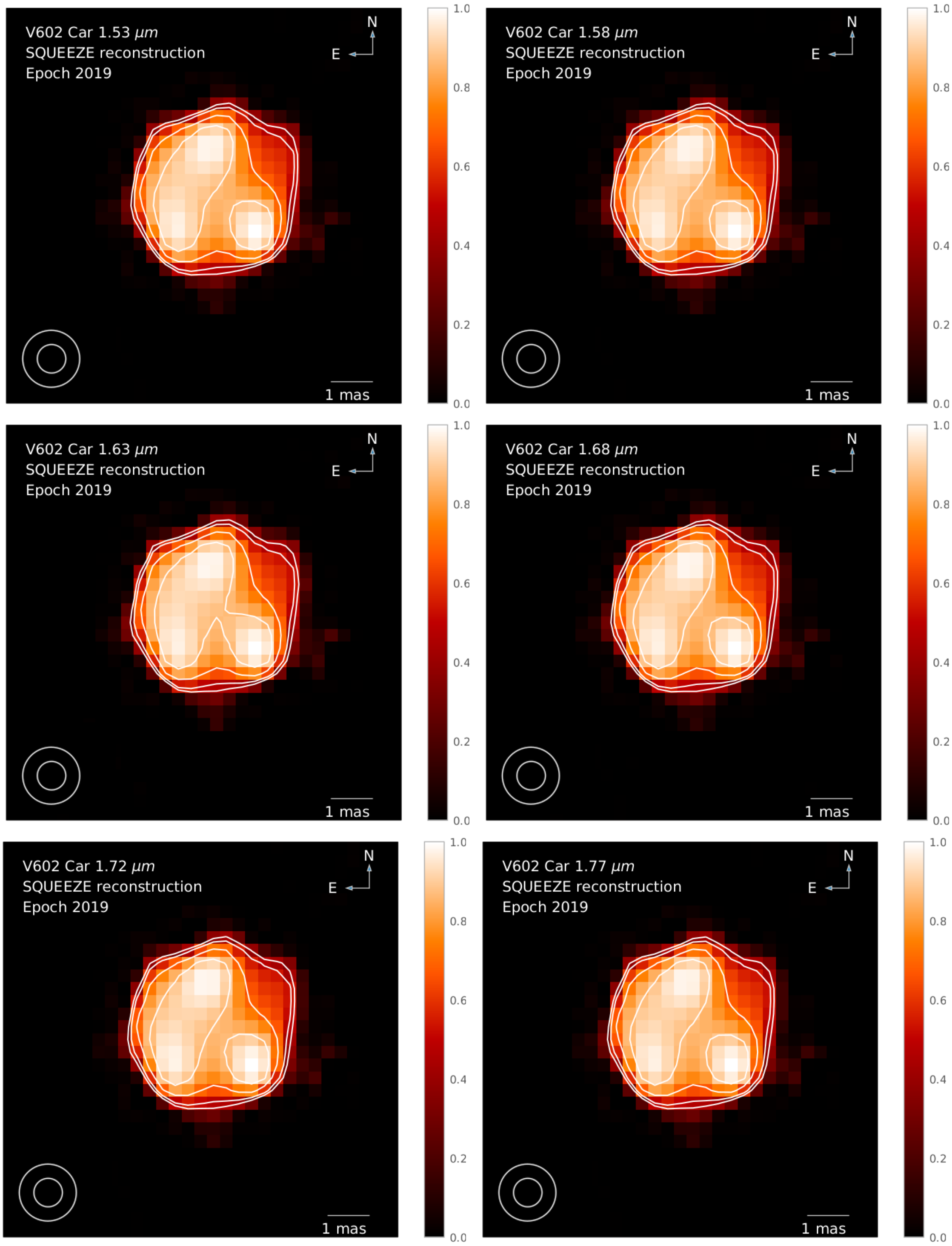

Figure A.6: SQUEEZE reconstruction of 2019 V602 Car data at each spectral channel. Contours are drawn at levels 40%, 50%, 70% and 87% of the peak intensity.

A.4 Mathematical definition of the SSIM

When calculated on various image windows (*x* and *y*) of the same size (N×N), the SSIM index is computed:

$$\mathrm{SSIM}(x,y) = \frac{(2\mu_x\mu_y + c_1)(2\sigma_{xy} + c_2)}{(\mu_x^2 + \mu_y^2 + c_1)(\sigma_x^2 + \sigma_y^2 + c_2)} \tag{A.1}$$

where,

μ_x is the average value of x.

μ_y is the average value of y.

σ_x^2 is the variance of x.

σ_y^2 is the variance of y.

σ_{xy} is the covariance of x and y.

$c_1 = (k_1L)^2$, $c_2 = (k_2L)^2$ are two variables to stabilize the division with weak denominator.

L represents the dynamic range of the pixel-values and is determined by the number of levels of luminance per pixel.

By default, $k_1 = 0.01$ and $k_2 = 0.03$.

Bibliography

Abbott, D. C. 1982, ApJ, 259, 282

Abbott, D. C., Bieging, J. H., & Churchwell, E. 1984, ApJ, 280, 671

Airapetian, V., Carpenter, K. G., & Ofman, L. 2010, ApJ, 723, 1210

Alencar, S. H. P., Bouvier, J., Walter, F. M., et al. 2012, A&A, 541, A116

Andre, P., Deeney, B. D., Phillips, R. B., & Lestrade, J.-F. 1992, ApJ, 401, 667

Andre, P., Montmerle, T., Feigelson, E. D., Stine, P. C., & Klein, K.-L. 1988, ApJ, 335, 940

Andre, P., Phillips, R. B., Lestrade, J.-F., & Klein, K.-L. 1991, ApJ, 376, 630

Antonova, A., Doyle, J. G., Hallinan, G., Golden, A., & Koen, C. 2007, A&A, 472, 257

Antonova, A., Hallinan, G., Doyle, J. G., et al. 2013, A&A, 549, A131

Arroyo-Torres, B., Martí-Vidal, I., Marcaide, J. M., et al. 2014, A&A, 566, A88

Arroyo-Torres, B., Wittkowski, M., Chiavassa, A., et al. 2015, A&A, 575, A50

Arroyo-Torres, B., Wittkowski, M., Marcaide, J. M., & Hauschildt, P. H. 2013, A&A, 554, A76

Aurière, M., Donati, J. F., Konstantinova-Antova, R., et al. 2010, A&A, 516, L2

Avison, A. & George, S. J. 2013, European Journal of Physics, 34, 7

Azulay, R., Guirado, J. C., Marcaide, J. M., et al. 2015, A&A, 578, A16

Azulay, R., Guirado, J. C., Marcaide, J. M., et al. 2017, A&A, 607, A10

Baldwin, J. E., Beckett, M. G., Boysen, R. C., et al. 1996, A&A, 306, L13

Baraffe, I., Homeier, D., Allard, F., & Chabrier, G. 2015, A&A, 577, A42

Barenfeld, S. A., Bubar, E. J., Mamajek, E. E., & Young, P. A. 2013, ApJ, 766, 6

Baron, F., Monnier, J. D., Kiss, L. L., et al. 2014, ApJ, 785, 46

Baron, F., Monnier, J. D., & Kloppenborg, B. 2010, in Society of Photo-Optical Instrumentation Engineers (SPIE) Conference Series, Vol. 7734, Optical and Infrared Interferometry II, 77342I

Basri, G. & Marcy, G. W. 1995, AJ, 109, 762

Bastian, T. S., Benz, A. O., & Gary, D. E. 1998, ARA&A, 36, 131

Beasley, A. J. & Conway, J. E. 1995, in Astronomical Society of the Pacific Conference Series, Vol. 82, Very Long Baseline Interferometry and the VLBA, ed. J. A. Zensus, P. J. Diamond, & P. J. Napier, 327

Bell, C. P. M., Mamajek, E. E., & Naylor, T. 2015, MNRAS, 454, 593

Benz, A. O., Conway, J., & Gudel, M. 1998, A&A, 331, 596

Berger, E. 2006, ApJ, 648, 629

Berger, E., Ball, S., Becker, K. M., et al. 2001, Nature, 410, 338

Berger, E., Rutledge, R. E., Phan-Bao, N., et al. 2009, ApJ, 695, 310

Berger, E., Rutledge, R. E., Reid, I. N., et al. 2005, ApJ, 627, 960

Berger, J. P. & Segransan, D. 2007, NAR, 51, 576

Boccaletti, A., Chauvin, G., Baudoz, P., & Beuzit, J. L. 2008, A&A, 482, 939

Bouvier, J., Alencar, S. H. P., Harries, T. J., Johns-Krull, C. M., & Romanova, M. M. 2007, in Protostars and Planets V, ed. B. Reipurth, D. Jewitt, & K. Keil, 479

Bouy, H., Martín, E. L., Brandner, W., & Bouvier, J. 2005, AJ, 129, 511

Bower, G. C., Loinard, L., Dzib, S., et al. 2016, ApJ, 830, 107

Budding, E., Erdem, A., Innis, J. L., Oláh, K., & Slee, O. B. 2009, Astronomische Nachrichten, 330, 358

Burgasser, A. J. & Putman, M. E. 2005, ApJ, 626, 486

Buscher, D. F. 1994, in IAU Symposium, Vol. 158, Very High Angular Resolution Imaging, ed. J. G. Robertson & W. J. Tango, 91

Buscher, D. F. & Longair, F. b. M. 2015, Practical Optical Interferometry

Chabrier, G., Baraffe, I., Allard, F., & Hauschildt, P. 2000, ApJ, 542, 464

Chabrier, G., Gallardo, J., & Baraffe, I. 2007, A&A, 472, L17

Chelli, A., Utrera, O. H., & Duvert, G. 2009, A&A, 502, 705

Chiavassa, A. & Freytag, B. 2015, in Astronomical Society of the Pacific Conference Series, Vol. 497, Why Galaxies Care about AGB Stars III: A Closer Look in Space and Time, ed. F. Kerschbaum, R. F. Wing, & J. Hron, 11

Chiavassa, A., Freytag, B., Masseron, T., & Plez, B. 2011, A&A, 535, A22

Chiavassa, A., Haubois, X., Young, J. S., et al. 2010a, A&A, 515, A12

Chiavassa, A., Lacour, S., Millour, F., et al. 2010b, A&A, 511, A51

Chiavassa, A., Plez, B., Josselin, E., & Freytag, B. 2009, A&A, 506, 1351

Chiosi, C., Nasi, E., & Bertelli, G. 1979, A&A, 74, 62

Chiosi, C., Nasi, E., & Sreenivasan, S. R. 1978, A&A, 63, 103

Christensen, U. R., Holzwarth, V., & Reiners, A. 2009, Nature, 457, 167

Chu, K. R. 2004, Reviews of Modern Physics, 76, 489

Climent, J. B., Berger, J. P., Guirado, J. C., et al. 2019, ApJ, 886, L9

Close, L. M., Lenzen, R., Guirado, J. C., et al. 2005, Nature, 433, 286

Close, L. M., Thatte, N., Nielsen, E. L., et al. 2007, ApJ, 665, 736

Cohen, M., Wheaton, W. A., & Megeath, S. T. 2003, AJ, 126, 1090

Cohen, M. H., Moffet, A. T., Romney, J. D., et al. 1975, ApJ, 201, 249

Cohen, O., Drake, J. J., Kashyap, V. L., Hussain, G. A. J., & Gombosi, T. I. 2010, ApJ, 721, 80

Collier Cameron, A. & Robinson, R. D. 1989, MNRAS, 236, 57

Cornwell, T. 1995, in Astronomical Society of the Pacific Conference Series, Vol. 82, Very Long Baseline Interferometry and the VLBA, ed. J. A. Zensus, P. J. Diamond, & P. J. Napier, 39

Cranmer, S. R. & Saar, S. H. 2011, ApJ, 741, 54

De Beck, E., Decin, L., de Koter, A., et al. 2010, A&A, 523, A18

De Loore, C., De Greve, J. P., & Lamers, H. J. G. L. M. 1977, A&A, 61, 251

De Loore, C., de Grève, J. P., & Vanbeveren, D. 1978, A&A Suppl., 34, 363

Deller, A. T., Forbrich, J., & Loinard, L. 2013, A&A, 552, A51

Dessart, L., Hillier, D. J., Waldman, R., & Livne, E. 2013, MNRAS, 433, 1745

di Criscienzo, M., Ventura, P., & D'Antona, F. 2010, APSS, 328, 167

Doyle, J. G., Antonova, A., Marsh, M. S., et al. 2010, A&A, 524, A15

Drake, J. J., Chung, S. M., Kashyap, V. L., & Garcia-Alvarez, D. 2015, ApJ, 802, 62

Drake, J. J., Stern, R. A., Stringfellow, G., et al. 1996, ApJ, 469, 828

Dulk, G. A. 1985, ARA&A, 23, 169

Dupuy, T. J., Forbrich, J., Rizzuto, A., et al. 2016, ApJ, 827, 23

Dupuy, T. J. & Liu, M. C. 2011, ApJ, 733, 122

Dupuy, T. J. & Liu, M. C. 2017, ApJS, 231, 15

Faherty, J. K., Riedel, A. R., Cruz, K. L., et al. 2016, ApJS, 225, 10

Feiden, G. A. & Chaboyer, B. 2013, ApJ, 779, 183

Felli, M., Massi, M., & Churchwell, E. 1989, A&A, 217, 179

Ferreira, J. M. 2000, MNRAS, 316, 647

Filippazzo, J. C., Rice, E. L., Faherty, J., et al. 2015, ApJ, 810, 158

Fleming, T. A., Giampapa, M. S., & Schmitt, J. H. M. M. 2000, ApJ, 533, 372

Fomalont, E. B. 1999, in Astronomical Society of the Pacific Conference Series, Vol. 180, Synthesis Imaging in Radio Astronomy II, ed. G. B. Taylor, C. L. Carilli, & R. A. Perley, 301

Forbrich, J., Osten, R. A., & Wolk, S. J. 2011, ApJ, 736, 25

Forbrich, J., Preibisch, T., & Menten, K. M. 2006, A&A, 446, 155

Freytag, B. 2003, in Society of Photo-Optical Instrumentation Engineers (SPIE) Conference Series, Vol. 4838, Proceedings of SPIE Astronomical Telescopes + Instrumentation, ed. W. A. Traub, 348–357

Freytag, B., Steffen, M., Ludwig, H. G., et al. 2012, Journal of Computational Physics, 231, 919

Gagné, J., Fontaine, G., Simon, A., & Faherty, J. K. 2018, The Astrophysical Journal, 861, L13

Gagné, J., Lafrenière, D., Doyon, R., Malo, L., & Artigau, É. 2014, ApJ, 783, 121

Gallenne, A., Mérand, A., Kervella, P., et al. 2015, Astronomy and Astrophysics, 579, A68

Gaponov, A. V. 1959, Izv VUZ Radiofizika, 2, 450

Gary, D. E. & Hurford, G. J. 1994, ApJ, 420, 903

Gauza, B., Béjar, V. J. S., Pérez-Garrido, A., et al. 2015, ApJ, 804, 96

Gennaro, M., Prada Moroni, P. G., & Tognelli, E. 2012, MNRAS, 420, 986

Gillon, M., Jehin, E., Lederer, S. M., et al. 2016, Nature, 533, 221

Gillon, M., Triaud, A. H. M. J., Demory, B.-O., et al. 2017, Nature, 542, 456

Gizis, J. E., Paudel, R. R., Mullan, D., et al. 2017, ApJ, 845, 33

Glindemann, A. 2011, Principles of Stellar Interferometry

Golimowski, D. A., Leggett, S. K., Marley, M. S., et al. 2004, AJ, 127, 3516

Gómez de Castro, A. I. 2002, MNRAS, 332, 409

Gontcharov, G. A. 2006, Astronomy Letters, 32, 759

Gray, M. D., Baudry, A., Richards, A. M. S., et al. 2016, MNRAS, 456, 374

Groh, J. H., Meynet, G., Ekström, S., & Georgy, C. 2014, A&A, 564, A30

Groh, J. H., Meynet, G., Georgy, C., & Ekström, S. 2013, A&A, 558, A131

Güdel, M. 2002, ARA&A, 40, 217

Guirado, J. C., Azulay, R., Gauza, B., et al. 2018, A&A, 610, A23

Guirado, J. C., Marcaide, J. M., Martí-Vidal, I., et al. 2011, A&A, 533, A106

Guirado, J. C., Martí-Vidal, I., Marcaide, J. M., et al. 2006, A&A, 446, 733

Guirado, J. C., Reynolds, J. E., Lestrade, J. F., et al. 1997, ApJ, 490, 835

Hajian, A. R., Armstrong, J. T., Hummel, C. A., et al. 1998, ApJ, 496, 484

Hallinan, G., Antonova, A., Doyle, J. G., et al. 2006, ApJ, 653, 690

Hallinan, G., Antonova, A., Doyle, J. G., et al. 2008, ApJ, 684, 644

Hallinan, G., Bourke, S., Lane, C., et al. 2007, ApJ, 663, L25

Hallinan, G., Littlefair, S. P., Cotter, G., et al. 2015, Nature, 523, 568

Harding, L. K., Hallinan, G., Boyle, R. P., et al. 2013, ApJ, 779, 101

Haubois, X., Perrin, G., Lacour, S., et al. 2009, A&A, 508, 923

Hauschildt, P. H. & Baron, E. 1999, Journal of Computational and Applied Mathematics, 109, 41

Heger, A., Fryer, C. L., Woosley, S. E., Langer, N., & Hartmann, D. H. 2003, ApJ, 591, 288

Hillenbrand, L. A. & White, R. J. 2004, ApJ, 604, 741

Hofmann, K. H., Weigelt, G., & Schertl, D. 2014, A&A, 565, A48

Holman, M. J. & Wiegert, P. A. 1999, AJ, 117, 621

Innis, J. L., Nelson, G. J., Coates, D. W., & Thompson, K. 1985, Information Bulletin on Variable Stars, 2667, 1

Innis, J. L., Thompson, K., Coates, D. W., & Evans, T. L. 1988, MNRAS, 235, 1411

Ireland, M. J., Monnier, J. D., & Thureau, N. 2006, in Society of Photo-Optical Instrumentation Engineers (SPIE) Conference Series, Vol. 6268, Proceedings of SPIE Astronomical Telescopes + Instrumentation, 62681T

Jakosky, B. M., Grebowsky, J. M., Luhmann, J. G., et al. 2015, Science, 350, 0210

Janson, M., Brandner, W., Lenzen, R., et al. 2007, A&A, 462, 615

Janson, M., Durkan, S., Bonnefoy, M., et al. 2018, A&A, 620, A33

Jardine, M. & Collier Cameron, A. 2019, MNRAS, 482, 2853

Jardine, M., Collier Cameron, A., Donati, J. F., & Hussain, G. A. J. 2019, MNRAS, 2779

Jardine, M. & van Ballegooijen, A. A. 2005, MNRAS, 361, 1173

Josselin, E. & Plez, B. 2007, A&A, 469, 671

Kao, M. M., Hallinan, G., Pineda, J. S., et al. 2016, ApJ, 818, 24

Kao, M. M., Hallinan, G., Pineda, J. S., Stevenson, D., & Burgasser, A. 2018, ApJS, 237, 25

Kazarovets, E. V., Samus, N. N., Durlevich, O. V., Kireeva, N. N., & Pastukhova, E. N. 2006, Information Bulletin on Variable Stars, 5721, 1

Kellermann, K. I. & Pauliny-Toth, I. I. K. 1966, ApJ, 145, 953

Kellett, B. J., Bingham, R., Cairns, R. A., & Tsikoudi, V. 2002, MNRAS, 329, 102

Kravchenko, K., Chiavassa, A., Van Eck, S., et al. 2019, A&A, 632, A28

Kravchenko, K., Van Eck, S., Chiavassa, A., et al. 2018, A&A, 610, A29

Kudritzki, R. P., Pauldrach, A., Puls, J., & Abbott, D. C. 1989, A&A, 219, 205

Kuerster, M., Schmitt, J. H. M. M., & Cutispoto, G. 1994, A&A, 289, 899

Kurucz, R. L. 1993, VizieR Online Data Catalog, VI/39

Labeyrie, A. 1975, ApJ, 196, L71

Labeyrie, A., Lipson, S. G., & Nisenson, P. 2006, An Introduction to Optical Stellar Interferometry

Lafrasse, S., Mella, G., Bonneau, D., et al. 2010, VizieR Online Data Catalog, II/300

Lalitha, S., Fuhrmeister, B., Wolter, U., et al. 2013, A&A, 560, A69

Lamers, H. J. G. L. M. & Cassinelli, I. P. 1996, in Astronomical Society of the Pacific Conference Series, Vol. 98, From Stars to Galaxies: the Impact of Stellar Physics on Galaxy Evolution, ed. C. Leitherer, U. Fritze-von-Alvensleben, & J. Huchra, 162

Lanza, A. F. 2018, A&A, 610, A81

Le Bouquin, J. B., Berger, J. P., Lazareff, B., et al. 2011, A&A, 535, A67

Leitherer, C. & Robert, C. 1991, ApJ, 377, 629

Lestrade, J. F., Jones, D. L., Preston, R. A., et al. 1995, A&A, 304, 182

Liebert, J., Kirkpatrick, J. D., Reid, I. N., & Fisher, M. D. 1999, ApJ, 519, 345

Lim, J., Carilli, C. L., White, S. M., Beasley, A. J., & Marson, R. G. 1998, Nature, 392, 575

Lim, J., Nelson, G. J., Castro, C., Kilkenny, D., & van Wyk, F. 1992, ApJ, 388, L27

Lindegren, L. & Kovalevsky, J. 1995, A&A, 304, 189

Linsky, J. L., Wood, B. E., Brown, A., Giampapa, M. S., & Ambruster, C. 1995, ApJ, 455, 670

Liu, M. C., Dupuy, T. J., & Ireland, M. J. 2008, ApJ, 689, 436

López-Santiago, J., Crespo-Chacón, I., Flaccomio, E., et al. 2016, A&A, 590, A7

López-Santiago, J., Montes, D., Crespo-Chacón, I., & Fernández-Figueroa, M. J. 2006, ApJ, 643, 1160

Luhman, K. L. & Potter, D. 2006, ApJ, 638, 887

Luhman, K. L., Stauffer, J. R., & Mamajek, E. E. 2005, ApJ, 628, L69

Lynch, C., Murphy, T., Ravi, V., et al. 2016, MNRAS, 457, 1224

Maggio, A., Pallavicini, R., Reale, F., & Tagliaferri, G. 2000, A&A, 356, 627

Malbet, F., Cotton, W., Duvert, G., et al. 2010, in Society of Photo-Optical Instrumentation Engineers (SPIE) Conference Series, Vol. 7734, Proceedings of SPIE Astronomical Telescopes + Instrumentation, 77342N

Malbet, F. & Perrin, G. 2007, NAR, 51, 563

Malo, L., Doyon, R., Lafrenière, D., et al. 2013, ApJ, 762, 88

Mann, A. W., Dupuy, T., Kraus, A. L., et al. 2019, ApJ, 871, 63

Marco, A. & Negueruela, I. 2013, A&A, 552, A92

Marois, C., Macintosh, B., Song, I., & Barman, T. 2005, arXiv e-prints, astro

Massi, M., Felli, M., Pallavicini, R., et al. 1988, A&A, 197, 200

Massi, M., Ros, E., Menten, K. M., et al. 2008, A&A, 480, 489

Mathieu, R. D., Baraffe, I., Simon, M., Stassun, K. G., & White, R. 2007, in Protostars and Planets V, ed. B. Reipurth, D. Jewitt, & K. Keil, 411

Matthews, L. D. 2013, PASP, 125, 313

Mauron, N. & Josselin, E. 2011, A&A, 526, A156

McLean, M., Berger, E., Irwin, J., Forbrich, J., & Reiners, A. 2011, ApJ, 741, 27

McLean, M., Berger, E., & Reiners, A. 2012, ApJ, 746, 23

Meimon, S., Mugnier, L. M., & Le Besnerais, G. 2008, Journal of the Optical Society of America A, 26, 108

Melrose, D. B. & Brown, J. C. 1976, MNRAS, 176, 15

Mérand, A., Bordé, P., & Coudé du Foresto, V. 2006, A&A, 447, 783

Metchev, S. A., Heinze, A., Apai, D., et al. 2015, ApJ, 799, 154

Meynet, G., Chomienne, V., Ekström, S., et al. 2015, A&A, 575, A60

Millour, F., Chesneau, O., Borges Fernandes, M., et al. 2009, A&A, 507, 317

Mohanty, S., Basri, G., Shu, F., Allard, F., & Chabrier, G. 2002, ApJ, 571, 469

Monnier, J. D. 2003, Reports on Progress in Physics, 66, 789

Monnier, J. D. 2007, NAR, 51, 604

Monnier, J. D., Berger, J.-P., Le Bouquin, J.-B., et al. 2014, in Society of Photo-Optical Instrumentation Engineers (SPIE) Conference Series, Vol. 9146, Proceedings of SPIE Astronomical Telescopes + Instrumentation, 91461Q

Monnier, J. D., Berger, J. P., Millan-Gabet, R., et al. 2006, ApJ, 647, 444

Montargès, M., Kervella, P., Perrin, G., et al. 2016, A&A, 588, A130

Montargès, M., Norris, R., Chiavassa, A., et al. 2018, A&A, 614, A12

Moran, J. M. & Dhawan, V. 1995, in Astronomical Society of the Pacific Conference Series, Vol. 82, Very Long Baseline Interferometry and the VLBA, ed. J. A. Zensus, P. J. Diamond, & P. J. Napier, 161

Musielak, Z. E., Cuntz, M., Marshall, E. A., & Stuit, T. D. 2005, A&A, 434, 355

Mutel, R. L., Molnar, L. A., Waltman, E. B., & Ghigo, F. D. 1998, ApJ, 507, 371

Nichols, J. D., Burleigh, M. R., Casewell, S. L., et al. 2012, ApJ, 760, 59

Nielsen, E. L., Close, L. M., Guirado, J. C., et al. 2005, Astronomische Nachrichten, 326, 1033

O'Gorman, E., Harper, G. M., Brown, A., et al. 2015, A&A, 580, A101

O'Gorman, E., Kervella, P., Harper, G. M., et al. 2017, A&A, 602, L10

Ortega, V. G., Jilinski, E., de La Reza, R., & Bazzanella, B. 2007, MNRAS, 377, 441

Ortiz-León, G. N., Loinard, L., Kounkel, M. A., et al. 2017, ApJ, 834, 141

Osten, R. A. & Jayawardhana, R. 2006, ApJ, 644, L67

Osten, R. A., Phan-Bao, N., Hawley, S. L., Reid, I. N., & Ojha, R. 2009, ApJ, 700, 1750

Pakull, M. W. 1981, A&A, 104, 33

Paladini, C., Baron, F., Jorissen, A., et al. 2018, Nature, 553, 310

Pauls, T. A., Young, J. S., Cotton, W. D., & Monnier, J. D. 2005, PASP, 117, 1255

Pecaut, M. J. & Mamajek, E. E. 2013, ApJS, 208, 9

Peterson, W. M., Mutel, R. L., Güdel, M., & Goss, W. M. 2010, Nature, 463, 207

Petrov, R. G., Malbet, F., Weigelt, G., et al. 2007, A&A, 464, 1

Phillips, R. B. & Lestrade, J. F. 1988, Nature, 334, 329

Phillips, R. B., Lonsdale, C. J., & Feigelson, E. D. 1991, ApJ, 382, 261

Phillips, R. B., Lonsdale, C. J., Feigelson, E. D., & Deeney, B. D. 1996, AJ, 111, 918

Pineda, J. S., Hallinan, G., & Kao, M. M. 2017, ApJ, 846, 75

Pineda, J. S., Hallinan, G., Kirkpatrick, J. D., et al. 2016, ApJ, 826, 73

Puls, J., Springmann, U., & Lennon, M. 2000, A&A Suppl., 141, 23

Quirrenbach, A., Mozurkewich, D., Buscher, D. F., Hummel, C. A., & Armstrong, J. T. 1996, A&A, 312, 160

Radigan, J., Jayawardhana, R., Lafrenière, D., et al. 2013, ApJ, 778, 36

Ragland, S., Le Coroller, H., Pluzhnik, E., et al. 2008, ApJ, 679, 746

Ramaty, R. 1969, ApJ, 158, 753

Ransom, R. R., Bartel, N., Bietenholz, M. F., et al. 2002, ApJ, 572, 487

Ransom, R. R., Bartel, N., Bietenholz, M. F., et al. 2003, ApJ, 587, 390

Rau, G., Ohnaka, K., Wittkowski, M., Airapetian, V., & Carpenter, K. G. 2019, ApJ, 882, 37

Readhead, A. C. S., Walker, R. C., Pearson, T. J., & Cohen, M. H. 1980, Nature, 285, 137

Reid, I. N., Kirkpatrick, J. D., Gizis, J. E., & Liebert, J. 1999, ApJ, 527, L105

Reiners, A. & Basri, G. 2010, ApJ, 710, 924

Reiners, A. & Christensen, U. R. 2010, A&A, 522, A13

Rich, E. A., Currie, T., Wisniewski, J. P., et al. 2016, ApJ, 830, 114

Richards, A. M. S. 2012, in IAU Symposium, Vol. 287, Cosmic Masers - from OH to H0, ed. R. S. Booth, W. H. T. Vlemmings, & E. M. L. Humphreys, 199–208

Richards, A. M. S., Impellizzeri, C. M. V., Humphreys, E. M., et al. 2014, A&A, 572, L9

Robertson, P., Mahadevan, S., Endl, M., & Roy, A. 2014, Science, 345, 440

Rodet, L., Bonnefoy, M., Durkan, S., et al. 2018, A&A, 618, A23

Route, M. & Wolszczan, A. 2013, ApJ, 773, 18

Rutledge, R. E., Basri, G., Martín, E. L., & Bildsten, L. 2000, ApJ, 538, L141

Rybicki, G. B. & Lightman, A. P. 1979, Radiative processes in astrophysics

Saha, S. K. 2011, Aperture Synthesis

Samus, N. N., Kazarovets, E. V., Durlevich, O. V., Kireeva, N. N., & Pastukhova, E. N. 2009, VizieR Online Data Catalog, B/gcvs

Schmitt, J. H. M. M., Ioannidis, P., Robrade, J., Czesla, S., & Schneider, P. C. 2019, A&A, 628, A79

Schneider, J. 1959, PRL, 2, 504

Scholz, M. 1997, in IAU Symposium, Vol. 189, IAU Symposium, ed. T. R. Bedding, A. J. Booth, & J. Davis, 51–58

Schwab, F. R. & Cotton, W. D. 1983, AJ, 88, 688

Schwarzschild, M. 1975, ApJ, 195, 137

Shao, M. & Staelin, D. H. 1977, Journal of the Optical Society of America (1917-1983), 67, 81

Shepherd, M. C., Pearson, T. J., & Taylor, G. B. 1994, in BAAS, Vol. 26, 987–989

Shields, A. L., Ballard, S., & Johnson, J. A. 2016, Phys. Rep, 663, 1

Siess, L. 2001, in Astronomical Society of the Pacific Conference Series, Vol. 243, From Darkness to Light: Origin and Evolution of Young Stellar Clusters, ed. T. Montmerle & P. André, 581

Slee, O. B., Erkan, N., Johnston-Hollitt, M., & Budding, E. 2014, PASA, 31, e021

Slee, O. B., Haynes, R. F., & Wright, A. E. 1984, MNRAS, 208, 865

Slee, O. B., Nelson, G. J., Innis, J. L., et al. 1986, PASA, 6, 312

Smith, N. 2014, ARA&A, 52, 487

Somers, G. & Pinsonneault, M. H. 2015, ApJ, 807, 174

Stassun, K. G., Feiden, G. A., & Torres, G. 2014, NAR, 60, 1

Stassun, K. G., Mathieu, R. D., Vaz, L. P. R., Stroud, N., & Vrba, F. J. 2004, ApJS, 151, 357

Stauffer, J., Cody, A. M., Baglin, A., et al. 2014, AJ, 147, 83

Stone, J. M., Skemer, A. J., Kratter, K. M., et al. 2016, ApJ, 818, L12

Tallon-Bosc, I., Tallon, M., Thiébaut, E., et al. 2008, in Society of Photo-Optical Instrumentation Engineers (SPIE) Conference Series, Vol. 7013, Proceedings of SPIE Astronomical Telescopes + Instrumentation, 70131J

Tatulli, E., Millour, F., Chelli, A., et al. 2007, A&A, 464, 29

Taylor, G. B., Carilli, C. L., & Perley, R. A. 1999, in Astronomical Society of the Pacific Conference Series, Vol. 180, Synthesis Imaging in Radio Astronomy II

Thiébaut, E. 2008, in Society of Photo-Optical Instrumentation Engineers (SPIE) Conference Series, Vol. 7013, Proceedings of SPIE Astronomical Telescopes + Instrumentation, 70131I

Thirumalai, A. & Heyl, J. S. 2012, MNRAS, 422, 1272

Thompson, A. R., Moran, J. M., & Swenson, George W., J. 2001, Interferometry and Synthesis in Radio Astronomy, 2nd Edition

Tognelli, E., Prada Moroni, P. G., & Degl'Innocenti, S. 2018, MNRAS, 476, 27

Torres, C. A. O., Quast, G. R., da Silva, L., et al. 2006, A&A, 460, 695

Torres, C. A. O., Quast, G. R., Melo, C. H. F., & Sterzik, M. F. 2008, Young Nearby Loose Associations, ed. B. Reipurth, Vol. 5, 757

Torres, R. M., Loinard, L., Mioduszewski, A. J., et al. 2012, ApJ, 747, 18

Tremblay, P. E., Ludwig, H. G., Freytag, B., Steffen, M., & Caffau, E. 2013, A&A, 557, A7

Treumann, R. A. 2006, AAPR, 13, 229

Trigilio, C., Buemi, C. S., Umana, G., et al. 2001, A&A, 373, 181

Tsuji, T. 2000, ApJ, 540, L99

Turnpenney, S., Nichols, J. D., Wynn, G. A., & Burleigh, M. R. 2018, ApJ, 854, 72

Twiss, R. Q. 1958, Australian Journal of Physics, 11, 564

Villarreal D'Angelo, C., Jardine, M., Johnstone, C. P., & See, V. 2019, MNRAS, 485, 1448

Villarreal D'Angelo, C., Jardine, M., & See, V. 2018, MNRAS, 475, L25

Vlemmings, W. H. T., Khouri, T., De Beck, E., et al. 2018, A&A, 613, L4

Walker, R. C. 1995, in Astronomical Society of the Pacific Conference Series, Vol. 82, Very Long Baseline Interferometry and the VLBA, ed. J. A. Zensus, P. J. Diamond, & P. J. Napier, 247

Walker, R. C. 1999, in Astronomical Society of the Pacific Conference Series, Vol. 180, Synthesis Imaging in Radio Astronomy II, ed. G. B. Taylor, C. L. Carilli, & R. A. Perley, 433

Walmswell, J. J. & Eldridge, J. J. 2012, MNRAS, 419, 2054

Wang, Z., Bovik, A. C., Sheikh, H. R., Simoncelli, E. P., et al. 2004, IEEE transactions on image processing, 13, 600

Waugh, R. F. P. & Jardine, M. M. 2019, MNRAS, 483, 1513

Weigelt, G. P. 1977, Optics Communications, 21, 55

West, A. A. & Hawley, S. L. 2008, PASP, 120, 1161

White, S. M., Kundu, M. R., & Jackson, P. D. 1989, A&A, 225, 112

Williams, P. K. G., Berger, E., Irwin, J., Berta-Thompson, Z. K., & Charbonneau, D. 2015, ApJ, 799, 192

Wittkowski, M., Abellán, F. J., Arroyo-Torres, B., et al. 2017a, A&A, 606, L1

Wittkowski, M., Arroyo-Torres, B., Marcaide, J. M., et al. 2017b, A&A, 597, A9

Wittkowski, M., Aufdenberg, J. P., Driebe, T., et al. 2006, A&A, 460, 855

Wittkowski, M., Aufdenberg, J. P., & Kervella, P. 2004, A&A, 413, 711

Wittkowski, M., Hauschildt, P. H., Arroyo-Torres, B., & Marcaide, J. M. 2012, A&A, 540, L12

Wittkowski, M., Hofmann, K. H., Höfner, S., et al. 2017c, A&A, 601, A3

Wittkowski, M., Hummel, C. A., Johnston, K. J., et al. 2001, A&A, 377, 981

Woillez, J., Abad, J. A., Abuter, R., et al. 2019, A&A, 629, A41

Wolszczan, A. & Route, M. 2014, ApJ, 788, 23

Wolter, U., Czesla, S., Fuhrmeister, B., et al. 2014, A&A, 570, A95

Wright, E. L., Eisenhardt, P. R. M., Mainzer, A. K., et al. 2010, AJ, 140, 1868

Wright, J. T. & Howard, A. W. 2009, ApJS, 182, 205

Yasuda, Y., Suzuki, T. K., & Kozasa, T. 2019, ApJ, 879, 77

Yoon, S.-C. & Cantiello, M. 2010, ApJ, 717, L62

Zapatero Osorio, M. R., Gálvez Ortiz, M. C., Bihain, G., et al. 2014, A&A, 568, A77

Zarka, P., Treumann, R. A., Ryabov, B. P., & Ryabov, V. B. 2001, APSS, 277, 293

Zuckerman, B., Song, I., & Bessell, M. S. 2004, ApJ, 613, L65